

# Synchrotron x-ray diffraction studies of bulk metallic glass forming liquids and glasses

Dissertation  
zur Erlangung des Grades  
des Doktors der Ingenieurwissenschaften  
der Naturwissenschaftlich-Technischen Fakultät  
der Universität des Saarlandes

vorgelegt von  
Moritz Stolpe

Saarbrücken  
2019



**Tag des Kolloquiums:** 17. Juli 2020

**Dekan:** Prof. Dr. Guido Kickelbick

**Berichterstatter:** Prof. Dr. Ralf Busch  
Prof. Dr. Rainer Birringer

**Akad. Mitglied:** Dr.-Ing. Florian Schaefer

**Vorsitz:** Prof. Dr.-Ing. Dirk Bähre



# Abstract

Bulk metallic glasses (BMGs) are rapidly quenched, frozen metallic liquids, which due to the absence of a long-range ordered atomic structure, as typical for conventional crystalline materials, show a unique spectrum of physical properties, rendering them promising candidates for various applications in multiple technological fields. Thermophysical, dynamical and functional material properties are closely linked to the structure of these alloys and can be optimized based on theoretical concepts and empirically proven criteria. In this work the structural evolution of multicomponent BMG-forming alloys is investigated using synchrotron X-ray diffraction. The experimentally obtained diffraction data are investigated in terms of their significance to deduce changes in macroscopic physical properties, notably changes in the volume or density. Moreover, it is analyzed how the structural information obtained from the diffraction data can be related to changes in the dynamic properties, in particular their sensitivity (fragility) with respect to changes in temperature. A special focus is laid on the interplay of local and global density changes and the formation of structure and order in the amorphous phase, as well as its implications on the viscous behavior in the liquid phase.

# Zusammenfassung

Metallische Massivgläser (MMGs) sind im Zuge rascher Erstarrung eingefrorene multikomponentige metallische Schmelzen. Aufgrund des Fehlens einer langweitreichig geordneten atomaren Struktur, wie sie für konventionelle kristalline Werkstoffe typisch ist, weisen MMGs ein einzigartiges Spektrum physikalischer Eigenschaften auf, welches eine Vielzahl an potentiellen Anwendungen in verschiedenen technologischen Feldern ermöglicht. Thermophysikalische, dynamische und funktionelle Materialeigenschaften stehen dabei in engen Zusammenhang mit dem strukturellen Aufbau der Legierungen und lassen sich auf Basis theoretischer Konzepte und empirisch validierter Kriterien gezielt optimieren. Im Rahmen dieser Arbeit wird die Strukturentwicklung multikomponentiger MMG-bildender Systeme mittels Synchrotron-Röntgen-Streuexperimenten untersucht. Die gewonnenen Streudaten werden im Hinblick auf ihre direkte Aussagekräftigkeit bezüglich makroskopischer physikalischer Eigenschaften insbesondere der auftretenden Volumenänderungen analysiert. Zudem wird untersucht, inwieweit sich die auf Basis der Streudaten abgeleiteten strukturellen Veränderungen in Relation zur Veränderung dynamischer Größen setzen lassen, allen voran deren Temperaturabhängigkeit (Fragilität). Eine spezielle Rolle kommt der Wechselwirkung zwischen lokalen und globalen Dichteänderungen und damit einhergehender Struktur- und Ordnungseinstellungen in der amorphen Phase sowie deren Auswirkungen auf das viskose Verhalten der flüssigen Phase zu.

# Publications

During the time as a Ph.D. student and employee at the Chair of Metallic Materials at Saarland University, the following work has been published. The articles are presented in chronological order in the list below. Only a part of this work has been included in this Ph.D.-thesis. The main articles related to the work presented in this thesis are [3] and [7]. The results published in article [3] are recapitulated in chapter 9. The results published in article [7] are reproduced in chapter 10 along with some additional studies, and further extended in chapter 11, and chapter 12. The findings presented in chapter 6, 8, 11, and 12 are considered for future publications.

## 2014

- [ 1 ] M. Stolpe\*, J. J. Kruzic, R. Busch, “*Evolution of shear bands, free volume, and hardness during cold rolling of a Zr-based bulk metallic glass*”, Acta Materialia 64, 231-240 (2014), DOI: 10.1016/j.actamat.2013.10.035
- [ 2 ] M. Weinmann\*, M. Stolpe, O. Weber, R. Busch, H. Natter, “*Electrochemical dissolution behaviour of Ti90Al6V4 used for ECM applications*”, Journal of Solid State Electrochemistry 19, 2, 485–495 (2014), DOI:10.1007/s10008-014-2621-x

## 2015

- [ 3 ] S. Wei\*, M. Stolpe\*, O. Gross, Z. Evenson, I. Gallino, W. Hembree, J. Bednarcik, J. J. Kruzic, R. Busch, “*Linking structure to fragility in bulk metallic glass-forming liquids*” Applied Physics Letters 106, 181901 (2015), DOI: 10.1063/1.4919590
- [ 4 ] A. Bachmaier\*, M. Stolpe, T. Mueller, C. Motz, “*Phase decomposition and nanostructure evolution of metastable nanocrystalline Cu-Co solid solutions during thermal treatment*”, IOP Conference Series Materials Science and Engineering 89, 1, 012017 (2015), DOI: 10.1088/1757899X/89/1/012017
- [ 5 ] A. Bachmaier\*, M. Pfaff, M. Stolpe, H. Aboulfadl, C. Motz, “*Phase separation of a supersaturated nanocrystalline Cu-Co alloy and its influence*

on thermal stability”, Acta Materialia 96, 1, 269-283 (2015), DOI: 10.1016/j.actamat.2015.05.053

- [ 6 ] Z. Evenson\* , B. Ruta, H. Hechler, M. Stolpe, E. Pineda, I. Gallino, R. Busch, “X-ray photon correlation spectroscopy reveals intermittent aging dynamics in a metallic glass”, Physical Review Letters 115, 17, 175701 (2015), DOI: 10.1103/PhysRevLett.115.175701

## 2016

- [ 7 ] M. Stolpe\*, I. Jonas, S. Wei. Z. Evenson, W. Hembree, F. Yang, A. Meyer, R. Busch “Structural changes during a liquid-liquid transition in the deeply undercooled  $Zr_{58.5}Cu_{15.6}Ni_{12.8}Al_{10.3}Nb_{2.8}$  bulk metallic glass forming melt”, Physical Review B 93, 014201 (2016), DOI: 10.1103/PhysRevB.93.014201
- [ 8 ] D. Baehre, A. Ernst\*, K. Weißhaar, H. Natter, M. Stolpe, R. Busch “Electrochemical dissolution behavior of titanium and titanium-based alloys in different electrolytes”, Procedia CIRP 42, 137-142 (2016), DOI:10.1016/j.procir.2016.02.208

## 2017

- [ 9 ] S. Wei\*, M. Stolpe, O. Gross, W. Hembree, S. Hechler, J. Bednarcik, R. Busch, P. Lucas, “Structural evolution on medium-range-order during the fragile-strong transition in  $Ge_{15}Te_{85}$ ”, Acta Materialia, 129, 259-267 (2017), DOI:10.1016/j.actamat.2017.02.055
- [ 10 ] O. Gross\*, B. Bochtler, M. Stolpe, S. Hechler, W. Hembree, R. Busch, I. Gallino, “The kinetic fragility of Pt-P- and Ni-P-based bulk metallic glass forming liquids and its thermodynamic and structural signature”, Acta Materialia, 132, 118-127 (2017), DOI:10.1016/j.actamat.2017.04.030
- [ 11 ] S. Hechler, B. Ruta\*, M. Stolpe, E. Pineda, Z. Evenson, O. Gross, W. Hembree, A. Bernasconi, R. Busch, I. Gallino, “Liquid-liquid transition revealed by quasi-static cooling of an ultra-viscous metallic liquid”, <https://arxiv.org/ftp/arxiv/papers/1704/1704.06703.pdf>
- [ 12 ] I. Gallino\*, D. Cangialosi, Z. Evenson, L. Schmitt, S. Hechler, M. Stolpe, B. Ruta, “Activation energy spectrum for relaxation and polyamorphism in an ultra-viscous metallic glass former”, <https://arxiv.org/ftp/arxiv/papers/1706/1706.03830.pdf>
- [ 13 ] O. Gross, S. S. Riegler, M. Stolpe, B. Bochtler, A. Kuball, S. Hechler, R. Busch, I. Gallino, “On the high glass-forming ability of Pt-Cu-Ni/Co-P-based liquids”, Acta Materialia 141, 109-119 (2017), DOI: 10.1016/j.actamat.2017.09.013

- [ 14 ] A. Kuball\*, M. Stolpe, R. Busch, “*Crystallization behavior of the  $Al_{86}Ni_8Y_6$  metallic glass forming alloy upon rapid cooling*”, Journal of Alloys and Compounds 737, 398-404 (2017) DOI: 10.1016/j.jallcom.2017.12.044
- [ 15 ] D. Mettus\*, M. Deckarm, A. Leibner, R. Birringer\*, M. Stolpe, R. Busch, D. Honecker, J. Kohlbrecher, P. Hautle, N. Niketic, J. R. Fernández, L. F. Barquín, A. Michels\*, “*Magnetic small-angle neutron scattering on bulk metallic glasses: A feasibility study for imaging displacement fields*”, Physical Review Materials 1, 074403 (2017), DOI: 10.1103/PhysRevMaterials.1.074403

## 2018

- [ 16 ] I. Gallino\*, D. Cangialosi, Z. Evenson, L. Schmitt, S. Hechler, M. Stolpe, B. Ruta, “*Hierarchical aging pathways and reversible fragile-to-strong transition upon annealing of a metallic glass former*”, Acta Materialia 144:400-410 (2018), DOI: 10.1016/j.actamat.2017.10.060
- [ 17 ] S. Hechler\*, I. Gallino, M. Stolpe, F.-T. Lentz, R. Busch, “*Analysis of thermophysical properties of lead silicates in comparison to bulk metallic glasses*”, Journal of Non-Crystalline Solids 485 (2018) DOI: 10.1016/j.jnoncrsol.2018.01.041
- [ 18 ] B. Bochtler\*, M. Stolpe, B. Reiplinger, R. Busch, “*Consolidation of amorphous powder by thermoplastic forming and subsequent mechanical testing*”, Materials and Design 140:188-195 (2018), DOI: 10.1016/j.matdes.2017.11.058
- [ 19 ] A. Kuball\*, B. Bochtler, O. Gross, V. Pacheco, M. Stolpe, S. Hechler, R. Busch, “*On the bulk glass formation in the ternary Pd-Ni-S system*”, Acta Materialia 158 (2018), DOI: 10.1016/j.actamat.2018.07.039
- [ 20 ] S. Hechler, B. Ruta\*, M. Stolpe, E. Pineda, Z. Evenson, O. Gross, A. Bernasconi, R. Busch, I. Gallino, “*Microscopic evidence of the connection between liquid-liquid transition and dynamical crossover in an ultraviscous metallic glass former*”, Physical Review Materials 2, 085603, (2017), DOI: 10.1103/PhysRevMaterials.2.085603

# Acknowledgement

Zuallererst möchte ich mich bei meinem Doktorvater Prof. Dr. Ralf Busch für seine Betreuung über die letzten Jahre bedanken. Ohne seine Gedult, sein mir entgegengebrachtes Vertrauen, und die Freiheit meine Ideen verwirklichen zu können, wäre diese Arbeit nicht zustande gekommen. Die Jahre an seinem Lehrstuhl zählen für mich nicht nur in wissenschaftlicher Hinsicht zu den lehrreichsten meines Lebens, und lassen mich auch heute noch gerne auf diese Zeit zurückblicken. An dieser Stelle möchte ich mich ebenfalls herzlichst bei Herrn Prof. Dr. Rainer Birringer für die gemeinsame Zusammenarbeit sowie die Zweitkorrektur meiner Dissertation bedanken. Ganz besonders bedanken möchte ich mich auch bei meinem ehemaligen Office-mate und Freund Shuai Wei für das Korrekturlesen der Arbeit, für unzählige erhellende Diskussionen, die fruchtbare Zusammenarbeit und seine Treue in meiner Zeit am Lehrstuhl und darüber hinaus.

Ebenfalls danke ich allen anderen Kollegen und Freunden am Lehrstuhl für metallische Werkstoffe für Ihre Hilfe und Unterstützung über die vergangenen Jahre, ohne die meine Zeit am Lehrstuhl nie das geworden wäre, was sie heute für mich bedeutet. Sigrid Neusis für ihre liebevolle und warmherzige Art und Unterstützung, viele Stunden gemeinsamen Schäkerns und Lachens, und für zahlreiche Gespräche über das Leben fernab der Wissenschaft. Und natürlich auch für die leckere Hühnersuppe in der Grippezeit! Dr. Isabella Gallino für die Leitung des Labors, für die Einführung in thermophysikalische Messmethoden und zahlreiche Diskussionen weit über die wissenschaftliche Ebene heraus. Dr. Frank Aubertin für sein stes offenes Ohr, und seine weisen Ratschläge zu diversen Problemen in verschiedensten Bereichen der Physik und Materialwissenschaft. Unseren beiden Technikern Jörg Eiden und Herrman Altmeyer und dem Rest der Werkstatt für die unermüdliche Hilfe bei technischen Problemen, der Umsetzung zahlreicher Modifikationen bestehender Anlagen sowie bei der Konstruktion neuer Anlagen, die einen Großteil der getätigten Versuche überhaupt erst möglich gemacht haben. Unseren beiden Exil-Amerikanern Zach Evenson und William Hembree für ihr stetes Bemühen meine teils "weirden" englischen Formulierungen in a "more common shape" zu bringen, und für zahlreiche feuchtfröhliche Nächte bei Bier und Whiskey an diversen Orten der Welt. Zach Evenson für seine unnachahmliche und ehrliche Art, und sein Vermögen mir stes ein Lächeln ins Gesicht zu zaubern. William Hembree für die Hilfe bei der Probenpräparation, der Durchführung und



Hilfe bei der Analyse der 3-Punkt Biegeversuche. Simon Hechler für die gemeinsame Zeit in unserem Büro, seine unermüdliche Ausdauer und Zielgerichtetheit über den Sport hinaus, und dafür stets einen gesunden Abstand zur Arbeit und den Blick auf das Lebens abseits der Wissenschaft zu bewahren. Oliver Gross für seine umfassende Hilfe und Koordination bei der Herstellung von Proben, dem Erstellen und Auswerten von Messdaten, sowie für unzählige erhellende Diskussionen über wissenschaftliche und alltägliche Probleme im Leben eines Doktoranden. Alexander Kuball für seine Hilfe und Zusammenarbeit in meiner Zeit am Lehrstuhl, der Herstellung von Proben und dem Erstellen von Messdaten, für zahlreiche Diskussion über wissenschaftliche Aspekte und darüber hinaus, und für die vielen gemeinsamen Stunden abseits der Arbeit beim Basketball und in unserem gemeinsamen Freundeskreis. Benedikt Bochtler für die Unterstützung beim Sammeln von Messdaten und die Weiterführung der Projekte nach meiner Zeit am Lehrstuhl. Nico Neuber, Maximilian Frey, Lisa-Yvonne Schmitt für ihre Hilfe bei der Probenpräparation und der Assistenz beim Durchführen von Messungen. Markus Kelkel, Stefan Gärtner und Yan Ming für ihre Unterstützung bei der Bearbeitung der Industrie-Projekte. Jochen Heinrich für die wissenschaftliche Begleitung in der Zeit vor meiner Zeit als Doktorand, und dafür den Blick auch auf die industriellen Aspekte der Materialforschung zu richten. Miriam Eisenbart für den Einblick in die Welt der Edelmetalle, sowie für zahlreiche ermunternde Gespräche über Themen in und ausserhalb der Materialwissenschaft. Martina Stemmler für die Durchführung von XRD-Messungen. Sanja Stanojevic für ihre liebevolle und kümmernde Persönlichkeit. Gabriele Krug, Yifat Okashi, und Heike-Eva Krieger für ihre Hilfe bei bürokratischen Aspekten während meiner Zeit am Lehrstuhl. Sowie allen anderen ehemaligen Kollegen, die mich in meiner Zeit an der Universität des Saarlandes begleitet und unterstützt haben.

Darüber hinaus möchte ich mich herzlichst bei allen Kooperationspartner für die gemeinsame Zusammenarbeit bedanken, die es mir ermöglicht hat auch in andere Bereiche der Materialwissenschaft einzutauchen und somit dazubeigetragen hat meinen wissenschaftlichen Horizont zu erweitern. Ohne sie wäre eine Vielzahl der getätigten Arbeiten nicht möglich gewesen. Besonderer Dank geht dabei an Prof. Dr. Andreas Meyer, Dr. Fan Yang, Dr. Isabell Jonas und Dr. Dirk Holland-Moritz vom Deutschen Zentrum für Raumfahrt (DLR) für die Einführung in den Elektrostatischen Levitator (ESL), für die konzeptionelle und technische Unterstützung der gemeinsamen Messungen am Deutschen Elektronensynchrotron (DESY) und an der European Synchrotron Radiation Facility (ESRF), für die Unterstützung und Hilfe beim Schreiben von Anträgen, und bei Fragen zur Auswertung und Interpretation der Messdaten, sowie für die Durchführung und Bereitstellung der Messdaten der Volumenmessungen im ESL.

Abschließend, aber umso herzlicher möchte ich mich bei meiner Familie, meinen Freunden und meiner großen Liebe Hanadi bedanken. Eure Treue, Unterstützung, Zuversicht und der Glaube an mich haben mir stets die nötige Kraft und Motivation gegeben, mich den Herausforderungen des Lebens entgegenzustellen. Ich

danke euch für euer Verständnis und eure Gedult über die letzten Jahre. Ich bin froh und unglaublich dankbar euch zu kennen und in meinem Leben zu haben.

# Contents

<b>1</b>	<b>Introduction</b>	<b>1</b>
<b>2</b>	<b>Metallic Glasses, Liquids, and Crystallization</b>	<b>6</b>
2.1	Crystalline vs. amorphous - structure and diffraction patterns . .	6
2.2	Glass formation . . . . .	7
2.3	Historical development of metallic glasses: alloys and technology .	10
2.4	Properties of metallic glasses . . . . .	12
2.5	Crystallization . . . . .	18
2.6	The glass transition . . . . .	24
2.7	Structure of metallic liquids and glasses . . . . .	27
2.7.1	Voronoi tessellation . . . . .	27
2.7.2	Formation of order in metallic liquids: local vs. global structure . . . . .	27
2.7.3	Random packing of equal sized spheres . . . . .	29
2.7.4	Multicomponent systems . . . . .	32
2.7.5	Metallic glass forming systems . . . . .	32
2.7.6	Medium-range ordering in metallic liquids and glasses . . .	33
2.8	Interplay of structure, thermodynamics and dynamics in metallic glass forming liquids . . . . .	36
<b>3</b>	<b>Liquid dynamics</b>	<b>46</b>
3.1	Diffusion and the Nernst-Einstein-Equation . . . . .	46
3.2	Viscosity . . . . .	47
3.3	The Stokes-Einstein relation . . . . .	48
3.4	Structural relaxation and aging . . . . .	49
3.5	The Viscous Slowdown and Fragility . . . . .	57
3.5.1	Fragility . . . . .	57
3.5.2	The volume perspective . . . . .	61
3.5.3	The Entropy Perspective . . . . .	65
3.5.4	The Energy Landscape Perspective . . . . .	71
3.6	The big picture of glass forming liquids . . . . .	75

<b>4</b>	<b>Scattering and Diffraction of amorphous substances</b>	<b>77</b>
4.1	Scattering from a point scattered - Insights from Huygens' Principle	78
4.2	The scattering amplitude- Born's approximation	80
4.3	Scattering form multiple scatterers	80
4.4	Scattering Cross sections	81
4.5	Scattering of Photons - a closer look	82
4.5.1	Scattering of photons with isolated atoms	83
4.5.2	The electron density description	84
4.5.3	The atomic density description	84
4.6	Corrections for the observed intensity	85
4.7	The total structure factor $S(Q)$	89
4.8	From reciprocal space to real-space	89
4.9	Pair Correlation functions	91
4.9.1	The radial distribution function	91
4.9.2	The pair density function	91
4.9.3	The pair distribution function	92
4.9.4	The reduced pair distribution function	92
4.10	Multi-component systems	93
4.11	Structural information provided by correlation functions	94
<b>5</b>	<b>Materials, Methods and Experiments</b>	<b>97</b>
5.1	X-ray Synchrotron Diffraction Studies	97
5.1.1	Synchrotron radiation	97
5.1.2	Synchrotron Sources - Storage Rings, Wiggler, and Undulators	100
5.1.3	Experimental Conduct	102
5.1.4	Details on Data Treatment	105
5.2	Thermophysical analysis	107
5.2.1	Calorimetry	107
5.2.2	Thermomechanical analysis	112
5.2.3	Volume measurements in ESL	114
<b>6</b>	<b>On the Thermal Dilatation of Metallic Glasses and Liquids</b>	<b>116</b>
6.1	Bragg's Law and the Ehrenfest Relation	116
6.1.1	Crystalline materials	116
6.1.2	Amorphous materials	117
6.2	Thermal Expansion of Metallic Glasses	119
6.3	Thermal Expansion in the Liquid state	124
6.4	Length-scale Dependence of the Thermal Expansion in Glasses and Liquids	128
6.5	Summary	135

<b>7</b>	<b>On the transformation of information between the reciprocal and real space</b>	<b>137</b>
<b>8</b>	<b>Structure-Fragility Relations in Reciprocal Space</b>	<b>142</b>
8.1	Empirical correlations between fragility and the first sharp diffraction peak . . . . .	142
8.2	Connection to the free volume model . . . . .	146
8.3	Summary . . . . .	148
<b>9</b>	<b>Structure-Fragility Correlations in Real Space</b>	<b>149</b>
9.1	The peak position approach . . . . .	150
9.2	The local dilatation approach . . . . .	152
9.3	Summary . . . . .	155
<b>10</b>	<b>On liquid-liquid phase transitions in bulk metallic glass forming liquids</b>	<b>157</b>
10.1	Liquid-liquid transitions . . . . .	157
10.1.1	Phenomenology of LLTs . . . . .	158
10.1.2	Critical points, the Widom line, and Jagla Potentials . . .	160
10.2	On fragile-to-strong transitions in Zr-based bulk metallic glass forming liquids . . . . .	165
10.2.1	Previous work and motivation . . . . .	165
10.2.2	ESL-synchrotron studies on the Vitreloy106a bulk metallic glass forming liquid . . . . .	166
10.3	Summary . . . . .	181
<b>11</b>	<b>Ornstein Zernike Analysis of bulk metallic glass formers</b>	<b>182</b>
11.1	Decay of density fluctuations according to Ornstein and Zernike .	182
11.1.1	The classical Ornstein Zernike approach . . . . .	183
11.1.2	The cluster approach . . . . .	183
11.1.3	Comparison of the two models - Ornstein-Zernike vs. the cluster approach . . . . .	184
11.2	Ornstein Zernike analysis of a Zr-Cu-Ni-Al-Nb BMG former in the liquid state . . . . .	186
11.3	Ornstein Zernike Analysis of the glass transition . . . . .	200
11.3.1	Evolution of the correlation length during the glass transition	202
11.3.2	The complete picture . . . . .	206
11.4	Summary . . . . .	206
<b>12</b>	<b>Structural order parameter analysis of a bulk metallic glass forming liquid</b>	<b>208</b>
12.1	Structural order parameters - Translational and bond-orientational ordering . . . . .	208

12.2	Evolution of structural order parameters during a liquid-liquid phase transition - insights from simulations . . . . .	212
12.3	Translational Structural Order Parameter Analysis for the LLT in Vitreloy106a . . . . .	214
12.4	Length-scale dependence of translational structural ordering: SRO vs. MRO . . . . .	216
12.5	Implications to the dynamics . . . . .	219
12.6	Correlations between translational order parameters and the correlation length . . . . .	220
12.7	TSOP analysis of BMG formers around the glass transition . . . .	222
12.8	Summary . . . . .	225
<b>13</b>	<b>Summarizing Remarks and Outlook</b>	<b>227</b>



# Chapter 1

## Introduction

Manifesting a unique spectrum of physical properties, glasses have played a crucial role in the technological evolution and are indispensable for modern civilization. They accompany us in our everyday day life and are essential parts of many applications, reaching far beyond the usage as window glasses, jars and optical devices. Owing to their specific structure, glasses combine a variety of advantageous properties, i.e. high strength, high hardness, high elasticity, high resilience, good wear behavior, good corrosion resistance, bio-compatibility, thermoplastic formability, and excellent magnetic properties<sup>1</sup>, rendering them suitable for numerous high-tech applications including e.g. communication technology (glass fibres), astronomy (modern telescopes), or medicine (bioactive implants). Already at Stone Age humans used sharp edged-pieces of a dark, glassy mineral called Obsidian to produce knives or arrow heads. Obsidian, also referred to as black lava glass, is formed naturally during the latest stage of volcanic eruptions, when silica-rich lava is ejected and rapidly chilled to surface temperature [1]. The natural formation of black Lava glass reveals one of the fundamental principles to produce glasses: quenching a liquid rapidly enough to avoid crystallization, so as to freeze its disordered (= amorphous) structure.

The propensity of liquids to form glasses differs considerably among different systems. In general, liquids composed of larger structural units tend to form glasses more readily than simple liquids such as metallic melts, as in the latter structural units (atoms) are more mobile, facilitating structural transformations into highly ordered crystalline structures. Accordingly, it was longtime assumed that metals do not form glasses under technological relevant conditions - a conception that was challenged by the pioneering work of David Turnbull [2–5] and later on proven to be wrong by the formation of the first metallic glass by the research group around Paul Duwez at the California Institute of Technology in 1960 [6]. Since this discovery considerable progress has been achieved in developing and understanding this class of materials. New alloy systems with improved

---

<sup>1</sup>The occurrence of magnetism naturally requires a sufficiently concentration of magnetic elements such as *Fe*, *Co*, *Ni*.



properties emerge constantly, opening new applications as structural or functional materials. While earlier metallic glass formers required cooling rates of the order of  $10^6$  K/s, modern alloys can be quenched into glasses at cooling rates in between  $10^0$ - $10^3$  K/s. As a result, metallic glass products are no longer restricted to micrometer-thin foils or ribbons but can be manufactured with thicknesses in the range of millimeters to a few centimeters by using specially-adapted conventional processing methods such as pressure-assisted casting (die casting or injection molding) and thermoplastic forming (blow molding, extrusion, imprinting). In addition, fully amorphous powders with particle sizes up to hundreds of micrometers can be produced by inert gas atomization which can serve as feed-stock to produce metallic glass coatings via cold and thermal spraying. Recently, it was demonstrated that new additive manufacturing techniques such as powder bed-based laser beam melting, wire extrusion, or laser foil printing make it possible to overcome the limitations in size and geometry inherent to conventional processing technologies, extending the range of metallic glass products.

The key to implementing these new alloys lies in identifying their strengths and weaknesses with respect to the respective applications and processing technologies, and to optimize their physical properties accordingly. This requires a clear understanding on the interplay of structure, dynamics, thermodynamic as well as mechanical and functional properties. Crucial to all is the question of how the structure of the liquid state evolves during undercooling, as the configurational state that is finally frozen at the glass transition eventually determines the properties of the glasses formed.

The present work aims to find correlations between the evolution of structure, thermodynamics, and dynamics in multicomponent bulk metallic glass forming liquids during the viscous slow-down towards the glass transition. Particular focus is laid on the relation between the structural evolution in the liquid and the temperature dependence of its dynamic properties, i.e. the fragility. A variety of different bulk metallic glass formers that markedly differ in terms of their fragilities is investigated using synchrotron x-ray diffraction and their the structural evolution of the alloys in the liquid and glass is studied in reciprocal and real space. Structural characteristics are defined and analyzed from the diffraction patterns and their Fourier transforms, and their evolution is set in relation to property changes in the amorphous state obtained from rheological and thermo-mechanical measurements. The theoretical background including the fundamental concepts and ideas required for understanding the present work are reviewed in chapter 2 to 4. Chapter 5 gives an overview of the materials and methods, including details on experimental setups and the conduct of experiments. In chapter 6 to 12 the results of the measurements are presented, discussed, and set in the context of previous work. A more detailed description of the individual chapters is given below.

## Chapter overview

*Chapter 2* gives an overview of the fundamental aspects of metallic glasses and their formation. Starting from a short distinction of the crystalline and amorphous state, the transition from the liquid to crystalline phase is reviewed. In the framework of *classical nucleation theory* equations for the nucleation rate and growth of the crystalline phase from the liquid phase are derived, enabling to deduce the stability of a liquid against crystallization, and thus to derive its *glass forming ability*. Different aspects defining the propensity of a liquid to form a glass are reviewed including thermodynamic, dynamic as well as structural aspects. A closer look on the structure of metallic liquids and glasses is presented, and finally the interplay between the formation of order, thermodynamics and dynamics is discussed.

*Chapter 3* gives an overview of dynamic properties in the liquid and glassy state. The phenomenology of the viscous slowdown that a liquid experiences when it is undercooled towards the glass transition is reviewed, along with the most prominent approaches to explain the different temperature behavior observed for different glass formers. Among them the *free volume models* might be the intuitively most amenable, stating that the mobility of a particle scales with its available space. At lower temperatures and high densities, structural rearrangements require cooperative motions including numerous particles, while at the same time the number of thermally accessible structural configurations decreases. These considerations will lead to the *Adam-Gibbs theory*, providing a quantitative link between the dynamics and thermodynamics, namely the changes in configurational entropy  $S_c$  of the liquid. Its general validity is discussed in terms of the experimentally accessible excess entropy of the liquid over the crystalline phase. The concept of the *potential energy landscape* is introduced, and it is argued that the temperature dependence of the (configurational) entropy as well as the activation energy for atomic rearrangements, determining the fragility, directly manifest the landscape topography of the liquid. The chapter ends with a discussion of the “big picture” of glass forming liquids, giving the theoretical fundamentals of the phenomenology of dynamic crossovers as a consequence of an underlying order-disorder transition in the liquid phase (liquid-liquid transitions).

*Chapter 4* equips the reader with the fundamental theory and equations of scattering and diffraction. Starting from Huygen’s principle, the scattering event of a plane wave with a point scatterer is introduced and set in relation to the Born approximation originally derived from a quantum mechanical treatise of the scattering event. The expression for the scattered amplitude of an ensemble of scatterers is derived and related to the physical quantity that is accessible in a diffraction experiment, i.e. the scattering cross section. A closer look on the interaction between photons and matter is presented. The definition of the structure factor is introduced, and the transformation of the reciprocal space data to real space data is discussed. Necessary corrections to extract the coherent part of the

scattered intensity are presented and described. The most prominent pair correlation functions are introduced and discussed in terms of their meaningfulness. Finally, the extension to multi-component systems is made, and the information that can be drawn from the pair correlation functions is debated.

*Chapter 5* gives an overview on the methods and details on the experimental conduct used for the determination of the data presented in this thesis. The generation of synchrotron radiation, the principle of storage rings, and properties of synchrotron radiation are described. The production of the materials and samples used in this study is explained. Details on the experimental setups and acquisition of data are presented along with details on the treatment of the diffraction data. The principals of thermal and thermomechanical analysis are explained and the fundamental equations of each method are introduced.

*Chapter 6* deals with the thermal dilation of liquids and glasses. Starting from the Bragg's law, the relation between the periodicity of the real-space structure in crystalline materials and their manifestation in reciprocal space are discussed. An extension to amorphous systems leads to the so-called Ehrenfest relation, linking the position of the principal diffraction peak to the mean interatomic spacing. The corresponding expression for thermal expansion is derived and tested against available experimental data in the glassy and liquid state. Using real space data obtained from the diffraction studies, the length-scale dependence of the thermal expansion for a variety of bulk metallic glass formers is investigated and set in relation to macroscopic volume changes.

*Chapter 7* is a very brief digression on the transmission of information from reciprocal to real space in a multicomponent bulk metallic glass forming liquid. The real space information stored in the principal diffraction peak is calculated and set in relation to the overall real space information obtained from Fourier transformation of the total structure factor. The main objective of this chapter is to provide the reader with a better intuition on the relation between structural features in reciprocal and real space which might be useful for an understanding of the following chapters.

*Chapter 8* aims to find correlations between the fragility and signatures of the structural evolution in reciprocal space. The thermal-induced shift of the principal diffraction peak in the glassy and liquid state for a variety of bulk metallic glass forming alloys is analyzed and compared. Relying on the results of the former chapters the structural changes in reciprocal space are translated into volume changes and discussed in terms of the free volume model.

*Chapter 9* is an attempt to find correlations between thermal-induced changes in the real space structure and the fragility. To this end structural changes of a variety of bulk metallic glass forming liquids are analyzed and related to the viscous slow down near their glass transitions. Structural signatures of fragility are extracted and parameters enabling to quantify them are introduced. Distinct length scales whose structural signatures correlate with fragility are identified and compared. Empirical correlations providing a link between the derived structural

parameters and the viscous behavior are derived and presented.

*Chapter 10* deals with the phenomenon of liquid-liquid phase transition (LLTs) in bulk metallic glass forming liquids. Starting from a short overview on the phenomenology and the underlying conceptions of LLTs, the motivation for the present work is deduced from previous findings in this area. Electrostatic levitation synchrotron studies are performed to study the structural changes of a zirconium-based bulk metallic glass forming liquid, whose rheological data suggest a fragile-to-strong transition in the supercooled liquid region. Thermodynamic and structural anomalies that indicate an underlying phase transition are identified and discussed in terms of their implications to the dynamics. Using the empirical correlations established in chapter 9 the structural changes are converted into changes in the dynamics and compared with experimental viscosity data.

In *Chapter 11* the structural coherence of bulk metallic glass forming liquids is investigated based on an Ornstein-Zernike analysis (OZA) of the decay of density fluctuations. The classical approach and a cluster-adapted modified version of the Ornstein-Zernike equations are introduced and discussed in terms of their applicability to the experimental data obtained from synchrotron diffraction studies. Details on the fit procedure used to extract the fit parameters are explained and the physical meaning of the fit parameters is debated. The OZA is performed on  $g(r)$  and  $G(r)$  and the results are compared. The evolution of the correlation length in the Zr-based bulk metallic glass forming alloy (Vit106a) in the liquid state is extracted and set in relation to the viscous behavior. The OZA is extended to the lower temperatures including the glassy state and the glass transition and the data sets are combined to yield an overall view of the evolution of the correlation length from the high temperature liquid phase down to the glassy state at around ambient temperatures. Moreover, the evolution of the correlation length is set in relation to evolution of the full-width of half maximum (FWHM) of the principal diffraction peak.

In *Chapter 12* the experimental evidences for a liquid-liquid phase transition in the *Vit106a* bulk metallic glass forming alloy are challenged against predictions and findings made in numerical simulations for a Jagla liquid. Translational structural order parameters (TSOP) are introduced and the evolution of the TSOPs during cooling is evaluated, enabling to make statements on the formation of order averaged over distinct length scales.

*Chapter 13* gives a concluding summary of the insights and findings gained in this thesis and provides an outlook to further studies along this direction.

## Chapter 2

# Metallic Glasses, Liquids, and Crystallization

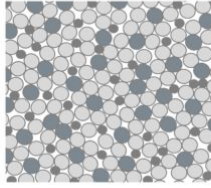
### 2.1 Crystalline vs. amorphous - structure and diffraction patterns

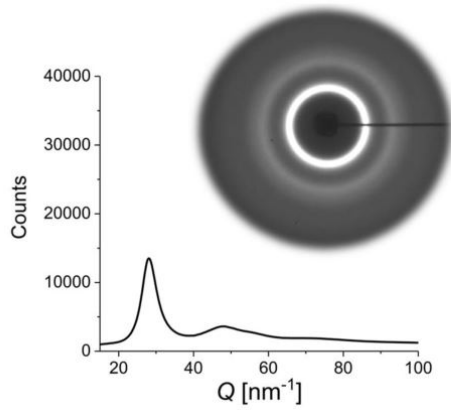
Crystalline solids are characterized by highly ordered, periodic 3D atomic or molecular structures called *lattice structures*. The arrangement of the particles follows well-defined construction rules. The local structural arrangement of particles is maintained throughout the entire crystal by repetition of the smallest unit that contains all geometrical information to build the lattice, i.e. the unit cell. Crystalline lattice structures have broken symmetry, i.e. their translational and rotational invariance is limited to well-defined vectors. The local packing density and average atomic separation varies along different crystallographic direction causing anisotropy of mechanical and functional properties.

In contrast, liquids and glasses are characterized by a high degree of structural disorder. Like liquids, glasses exhibit no long range order. Their amorphous (disordered) structure is translational and rotational invariant, leading to isotropic behavior. A closer examination reveals that the atomic structure in fact is not fully random. Instead undercooled liquids and glasses often show ordering tendencies on short- and intermediate length scales, a phenomenon referred to as short-range order (SRO) or medium-range order (MRO).

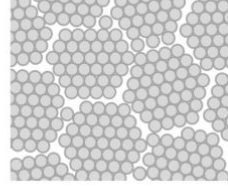
The different atomic structure of amorphous and crystalline metals results in characteristic diffraction patterns (cf. figure 2.1). In crystalline materials, the long-range periodicity of the highly ordered domains in the microstructure leads to the occurrence of sharp Bragg peaks, whose positions can be associated with well-defined interplanar atomic spacings. In contrast, amorphous metals exhibit diffraction patterns that are characterized by the appearance of diffuse, concentric diffraction rings (halos) centered around the primary beam (cf. figure 2.1). The fact that the scattered intensity shows local maximas around the incident beam

### Amorphous metals

- amorphous/liquid structure ■
  - atomic cluster assembly ■
  - short- to medium-range order ■
  - no long-range order ■
- 



### (Poly-)crystalline metals

- periodic lattice structures ■
  - long-range order ■
  - microstructure (e.g. phases, grains,...) ■
  - lattice defects (e.g. dislocations, grain boundaries,...) ■
- 

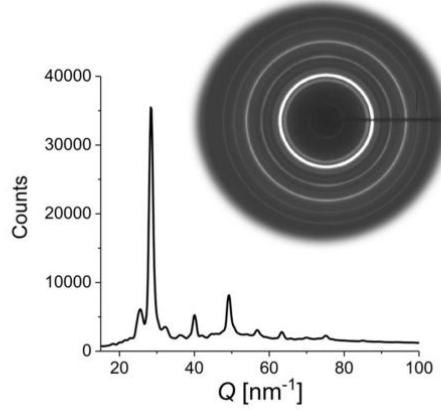


Figure 2.1: Crystalline vs. amorphous: atomic structure and diffraction patterns. The upper figures summarize the main feature of the distinct atomic structures. The lower figures show the corresponding diffraction patterns obtained from synchrotron X-ray transmission measurements. Note that the primary beam, normally appearing in the center of the concentric rings ( $Q = 0$ ), is shadowed by a beam stop.

reveals that the structure of liquids and glasses cannot be fully random<sup>1</sup>, but that there must be a preference for particular interatomic distances which are repeated throughout the structure. The latter can be understood by the formation of order on short- and medium-range length scales arising from the natural tendency to lower the Gibbs free energy by forming energetically preferred, dense-packed cluster structures.

## 2.2 Glass formation

Glasses can be formed via multiple routes: by direct deposition from the vapor phase, by solid state amorphization, or by quenching a liquid. Although all routes

<sup>1</sup>For fully random systems such as a monatomic gas, where each atomic distance is found with the same probability, the scattered intensity decreases monotonically with increasing scattering vectors  $Q$ .

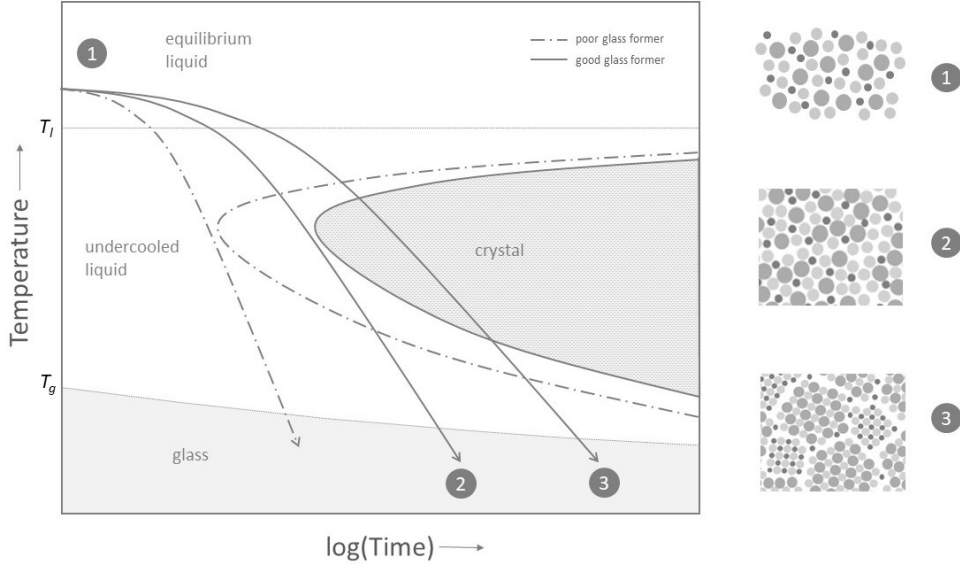


Figure 2.2: Schematic comparison of good and poor glass formers. In case of poorer glass formers the “crystallization nose” is shifted to shorter times, requiring to cool the liquid faster in order to avoid crystallization. The “critical cooling rate” corresponds to the minimum cooling rate necessary to bypass the crystallization nose and to form a fully amorphous structure (path 2). For any lower cooling rate the system will (partially) crystallize (path 3). Note that the onset of the glass transition during cooling, indicated by the solid line at  $T_g$ , is rate-dependent. For faster cooling the liquid will freeze to a glass at higher temperatures and vice versa. This can have drastic effects on the structure and properties of the glasses formed.

have been proven successful, from a technological point of view, glass formation from the liquid may be considered the most relevant. The ability of a system to form a glass, i.e. its glass forming ability (GFA), as well as its ability to maintain its amorphous structure, i.e. its thermal stability, are strongly coupled to the mobility of the structural units. The GFA differs considerably among different liquids, and the majority of (metallic) liquids does not form a glass readily.<sup>2</sup> Liquids which under technically reasonable conditions can be brought into the glassy state are referred to as “glass formers”. In case that the majority of the constituents are metallic elements, the system is referred to as “metallic glass”.

The essential step to obtain a glass from a liquid is to avoid nucleation and growth of a long-range ordered crystal structure. This requires to quench the liquid rapidly enough to bypass the crystalline phase region in its time-temperature

<sup>2</sup>It is assumed that every liquid may be formed into a glass. In many cases this however requires conditions that technically cannot be met easily.

transformation diagram, as shown schematically in figure 2.2. The position of the “crystallization nose” thus defines a *critical cooling rate* (CCR) at which crystallization can be avoided and a glass is formed. Poorer glass formers are characterized by faster crystallization kinetics; their nose of crystallization is shifted to lower times, and accordingly, a higher CCR is required to bypass crystallization. Considering that the heat stored in the liquid must be transferred from its center to its outer surface, it is clear that the CCR is essentially determined by the heat capacity  $c_p$ , the thermal conductivity  $\lambda_{th}$ , as well as the thickness of the cast sample. As in metallic liquids  $\lambda_{th}$  and  $c_p$  are basically of the same order of magnitude, the CCR determines the maximum thickness of a part that can be cast with a fully amorphous structure. The latter is usually referred to as the *critical casting thickness* (CCT). Just as the CCR, the CCT is a material-specific property that indicates the GFA of the system. If the maximum thickness that can be cast is larger than one millimeter, a liquid is said to be a “bulk glass former”.

The ability of a liquid to form a glass strongly depends on its constitution. In general, a liquid composed of larger more complex structural tends to form a glass more readily than a simple atomic liquid, as its structural complexity makes rearrangements of the particles more difficult, stabilizing the amorphous phase from a kinetic point of view. Besides, thermodynamic factors play a crucial role for the GFA of a liquid. In a simplified view, it can be stated that a lower energetic difference between the amorphous phase and its competing crystalline phases enhances the GFA.<sup>3</sup> In case of metallic glass formers several key empirical criteria that lead to an increased GFA have been identified. The recipe to stabilize the liquid against crystallization combines the following “ingredients”[7] :

- (I) use multicomponent near-eutectic alloys of three or more elements
- (II) mix elements with sufficiently large atomic size mismatches ( $> 12\%$ ) at the right proportions
- (III) take main elements with negative heat of mixing

This can be understood as follows. Point (I) thermodynamically stabilizes the amorphous structure with respect to competing crystalline phases. Due to the low liquidus temperature  $T_l$  of deep eutectics the amorphous phase is stable up to low temperatures, and the temperature interval  $T_l - T_g$  that needs to be passed until the onset of the glass transition  $T_g$  is lowered, facilitating glass formation. Moreover, a larger number of components often increases the complexity and size of the crystal unit cell, and the formation of multiple phases with differences in chemistry requires segregation of chemical species by long-range diffusion. Mixing elements with large atomic size differences in the right proportion (point (II))

---

<sup>3</sup>For a more detailed treatise on the influence of dynamic and thermodynamics on crystallization and glass formation the reader is referred to section "Crystallization".



increases the packing density of the amorphous phase. Due to the reduced free volume atomic mobility becomes more sluggish, leading to slower crystallization kinetics. A negative heat of mixing between the main elements (point (III)) favors short- and medium-range ordering in the liquid, leading to a dense-packed, energetic stabilized amorphous structure, and furthermore increases the energetic barrier at the liquid-solid interface [7].

Often the above recipe is used as a starting point to optimize or develop new glass forming alloys. In addition to it, minor alloying is found to be an effective tool to optimize glass forming alloys. The addition of a small amounts ( $< 5\%$ ) of additional elements not only can enhance the GFA but also can lead to significant increase in the thermal stability of the supercooled liquid phase or markedly improve the functional properties of the glasses [8, 9].

## 2.3 Historical development of metallic glasses: alloys and technology

The ongoing research over the last decades has resulted in a continuous improvement metallic glass forming alloys. With the transition from binary alloys to complex multicomponent near-eutectic alloys the critical casting thickness has been increased by about three orders of magnitude, as shown in figure 2.3. While the earliest binary alloys required cooling rates of the order of one million Kelvin per second, today's bulk metallic glasses can be formed at moderate cooling rates of the order of a few Kelvin per second. In consequence, the dimensions of glassy samples are no longer limited to foils or ribbons. Glassy products with dimensions of the order of centimeters can be produced via conventional casting, such as tilt casting, die casting or injection molding, opening new applications and markets. Recently, additive manufacturing routes have boosted the interest of metallic glasses for commercial applications. These new manufacturing methods can circumvent the limitations in shape and size inherent to conventional processing methods (see e.g. [10–15]). In particular powder-bed based technologies have been proven to be promising processing techniques for economic manufacturing of larger and more complex metallic glass components (cf. figure 2.4). Amorphous parts are formed layer-wise by selectively melting powders with a focused heat source (most commonly lasers) with spot sizes ranging from 10 - 100  $\mu\text{m}$ . Since only a small volume is melted, the process inherently generates high cooling rates, usually in the range of  $10^4$  -  $10^5$   $K/s$ , facilitating glass formation. The major challenge is not to produce an amorphous layer, but to maintain its amorphous structure throughout the layer-wise formation process, as the heat of the uppermost layer that is molten is dissipated through the lower lying previously formed layers, making them prone to crystallize. Nonetheless, by careful adjustment of process parameters, the accumulated heat inside a layer can be

significantly reduced, making it is possible to produce fully X-ray amorphous, complex bulk metallic glass component with dimensions exceeding the critical casting thickness of the alloy by far [15].

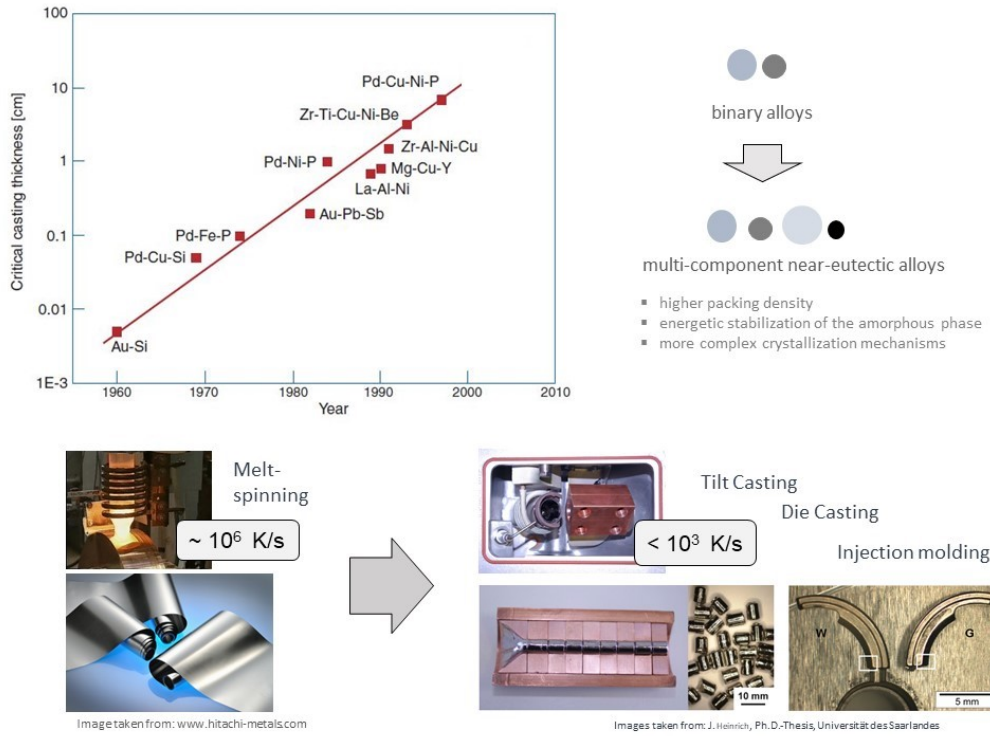
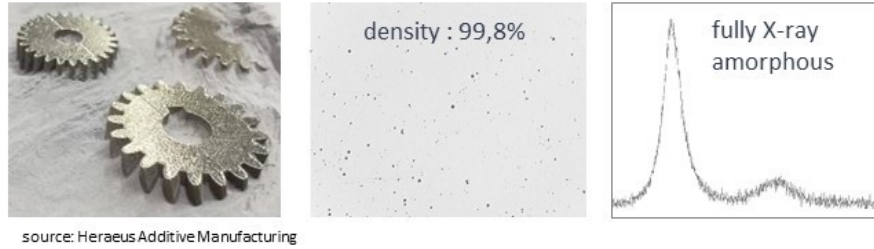


Figure 2.3: Historical development of metallic glass formers. Upper left figure: The critical casting thicknesses (CCTs) of the numerous metallic glass forming alloy systems are plotted versus the year of their discovery. The figure is taken from [7]. With the transition from simple binary alloys to multi-component, near-eutectic alloys the critical cooling rates could be steadily decreased over the last decades, enabling to produce bulk amorphous parts with dimensions up to the centimeter scale by using conventional casting techniques such as tilt casting, die casting, or injection molding.



source: Heraeus Additive Manufacturing

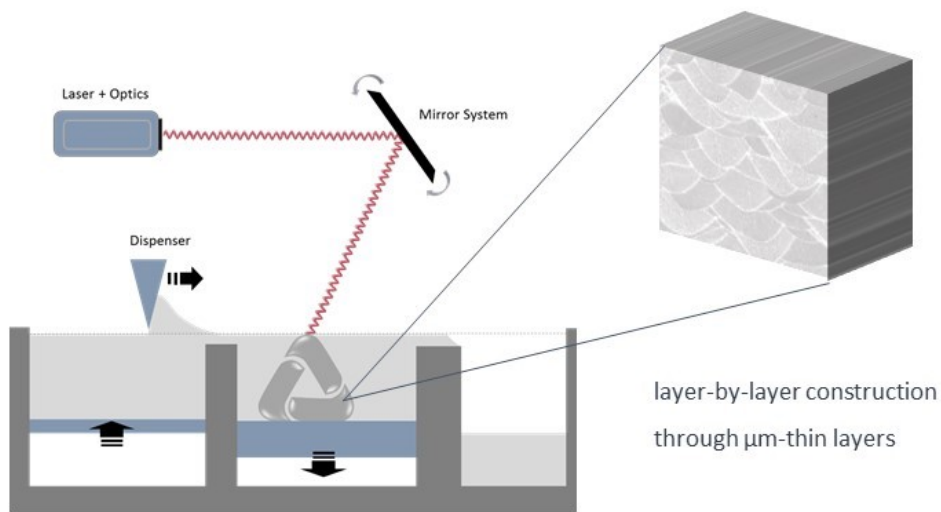


Figure 2.4: Laser Beam Melting of Bulk Metallic Glasses. Additive manufacturing techniques such as laser beam melting enable the production of fully X-ray amorphous, complex components from metallic glass forming powders without any limitation in size.

## 2.4 Properties of metallic glasses

Defects in the periodic lattice structure often degrade the performance of crystalline materials. Due to the absence of a crystalline microstructure and its corresponding defects metallic glasses exhibit properties that often outperform those of conventional crystalline metals. In the following a brief summary of the properties of metallic glasses is given. It is noted that not all of the characteristics are found concurrently. Like for crystalline metals, the individual properties can vary considerably among different metallic glass forming alloys. The present summary thus should be considered as a generalized description of this class of materials.

**Mechanical properties** Due to the absence of a periodic lattice structure, the classical deformation mechanisms of crystalline metals (e.g. dislocation motion, grain boundary sliding, etc.) no longer apply. As a consequence, metallic glasses exhibit high strengths, much closer to the theoretical strength than polycrystalline metals. This often goes along with a high hardness, improving the resistance to wear. Due to the particular atomic deformation mechanism, the onset of plastic deformation is postponed to markedly higher elastic strain limits of the order of 2%. Metallic glasses thus combine strengths exceeding that of conventional crystalline metals with the elasticity of polymers (cf. figure 2.5), resulting in a huge capacity to store elastic energy (resilience). Since energy-dissipating mechanisms as in crystalline materials (dislocation motion, grain boundary sliding) are absent, metallic glasses show low mechanical damping, rendering them the ideal spring material.

**Deformation and failure** - At temperatures around the glass transition temperature the atomic structure unfreezes, and the materials behave like a high-viscous fluid. At moderate strain rates plastic deformation occurs homogeneously over the entire volume, enabling high degrees of deformation at low forces up to plastic strains of several 1000% - a behavior referred to as superplasticity [16, 17]. At lower temperatures and high stresses, plastic deformation in metallic glasses occurs inhomogeneously [17–20]. Accordingly, only a small volume fraction of the material is involved and plastic deformation occurs highly localized. The outer applied strain is accommodated by the formation of thin bands (shear bands) that appear close to the direction of the maximum shear stresses. The strong localization via shear banding is a natural consequence of strain softening, stemming from the underlying atomistic deformation mechanism [18, 19], which in the absence of counteracting strain hardening mechanisms, proceeds in auto-catalytic manner. As an effect, metallic glasses appear to show brittle fracture behavior around room temperature although the deformed regions have undergone vast amount of plastic flow [17]. The different deformation and failure behavior of metallic glasses can be explained as follows.

Due to the non-uniform distribution of excess volume that is frozen during the glass transition, the structure of glasses on the atomic level is mechanically heterogeneous [21]. Regions of local (free) volume concentrations are characterized by lower stiffness and cohesion, and hence act as preferential initiation sites for plastic flow [18, 19]. Once the local stress threshold is reached, shear-induced atomic rearrangements take place [18, 19]. Since deformation in these so-called shear transformation zones (STZ) is dilatative [17–19], the local density decreases [22–24], leading to further softening. At low temperatures, the shear-induced local volume increase cannot be effectively redistributed by diffusive processes and hence remains localized, making a once perturbed region making more prone to further deformation [18]. Under further deformation the STZs grow and coagu-

late into nm-thin shear bands which normally propagate from the surface towards the inside [25] in stick-slip manner[22, 26]. In absence of mechanisms that hinder the propagation of shear bands, deformation stays confined onto one or a few bands. Under tensile loading this leads to an apparent brittle deformation behavior, although the material inside the bands itself undergoes large plastic flow [17, 27]. On the other hand, if the propagation of active shear bands is blocked, new shear band are formed in order to accommodate the outer imposed deformation (shear band multiplication) [17]. In compression under geometrical restraints such as cold rolling, or in bending where the neutral fibre acts a barrier to shear band propagation, some metallic glasses exhibit room temperature plasticity [20]. The consecutive formation of shear bands (shear band multiplication) leads to flow serrations in their stress-strain diagrams, where each serration can be attributed to a slipping event along a single or multiple shear bands [22, 26]. An effective way to hinder shear band propagation is the introduction of a second phase which acts as a barrier to propagating shear bands, triggering shear band multiplication throughout the material [28]. As a result deformation occurs less localized and the material becomes more ductile. Amorphous-matrix composites combine the high strength of metallic glasses with the ductility of conventional crystalline metals and even show necking under tensile loading [28].

At higher temperatures diffusive processes can redistribute or annihilate the deformation-induced local increase in free volume [18, 19]. Moreover, a larger number of STZs is thermally excited and available for plastic flow. As a consequence, deformation occurs homogeneously and the material behaves like a highly viscous liquid, showing superplastic behavior [18, 19]. This enables to fabricate metallic products via processing routes that are normally only known for oxide glasses or polymers [16, 29, 30], as further discussed below.

**Corrosive behavior -** Metallic glasses in general show a good corrosion resistance. In crystalline metals, dislocations or grain boundaries can act as preferential initiation sites for chemical attacking. Furthermore, phases of different chemical constitution and hence different electro-chemical potentials form local galvanic cells, leading to galvanic corrosion. By contrast, metallic glasses have no typical microstructure and their elements are distributed homogeneously, so that the electro-chemical potential is uniform throughout the material. This results in a higher resistance to corrosion compared to corresponding crystalline alloys, and often goes along with bio-compatibility, making metallic glass a promising material for medical applications.

**Aesthetic properties -** The fact that there are no grains or different phases in metallic glasses enables to produce very smooth and shiny surfaces [31]<sup>4</sup>, which due to their high hardness are often resistant against scratches. This makes metal-

---

<sup>4</sup>In principle, metallic glasses can be polished down to the atomic scale.

lic glasses attractive for applications such as mirrors, watch cases, or housings for electronic devices.

**Magnetic properties** - Provided that a sufficiently high amount of the alloy consists of magnetic elements, metallic glasses normally show a pronounced soft-magnetic behavior. The origin again lies in their special atomic structure. In crystalline alloys, defects in the lattice structure such as impurities, inclusions, dislocations, grain or phase boundaries act as barriers hindering the re-orientation of the magnetic domains towards the outer applied field, making the material "harder" to magnetize and demagnetize and larger hysteresis losses. As these defects are absent in metallic, the direction of the magnetic polarization can be switched much easier. Metallic glasses therefore show low coercivity leading to small hysteresis losses, rendering them interesting for applications such as high efficiency transformers, electric motors and generators, or electronic article surveillance.

**Processability** - Heating a metallic glass to its glass transition and above, its structure unfreezes and the material behaves like a highly viscous liquid, enabling to deform the material up to very high plastic strains at relatively low forces. This allows to produce metallic glasses similar to oxide glasses or thermoplastics, for example by blow molding, injection molding or imprinting [16, 29, 30, 32]. Fine-patterned structures with geometrical features ranging down to nanometer scale can be formed by squeezing the supercooled liquid into cavities, enabling to produce durable nanomolds [32]. Moreover, due to the fact that the liquid becomes frozen and does not undergo a phase transition upon solidification into the glassy phase, metallic glass formers show no solidification shrinkage as typical for conventional crystalline alloys. This enables to produce near net shape, high precision cast parts, making die casting of metallic glasses a competitive alternative to investment casting [33].

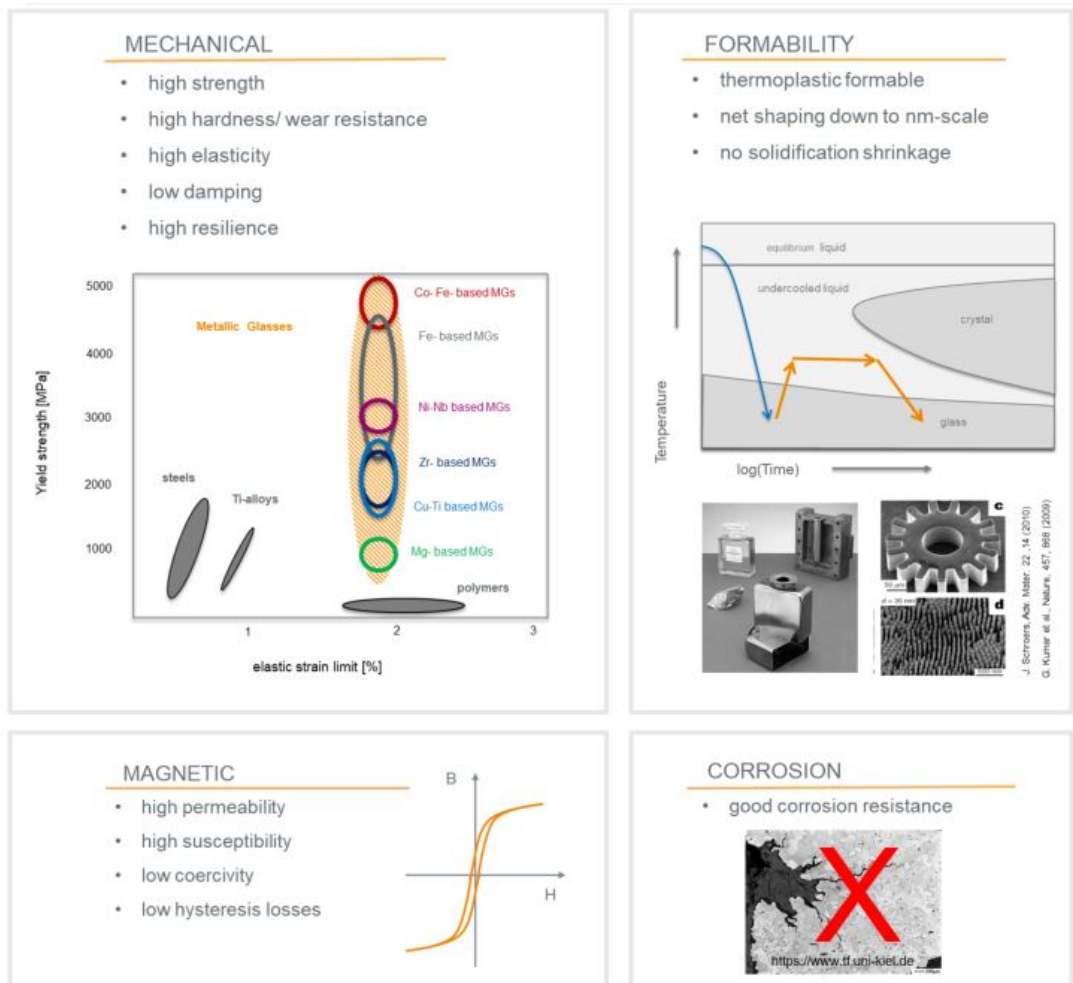


Figure 2.5: Overview of metallic glasses properties. The absence of a crystalline lattice structure results in a number of advantageous properties. Metallic glasses generally combine high strengths, high hardness, large elasticity, good wear and corrosion behavior, excellent soft magnetic behavior, and thermoplastic formability.

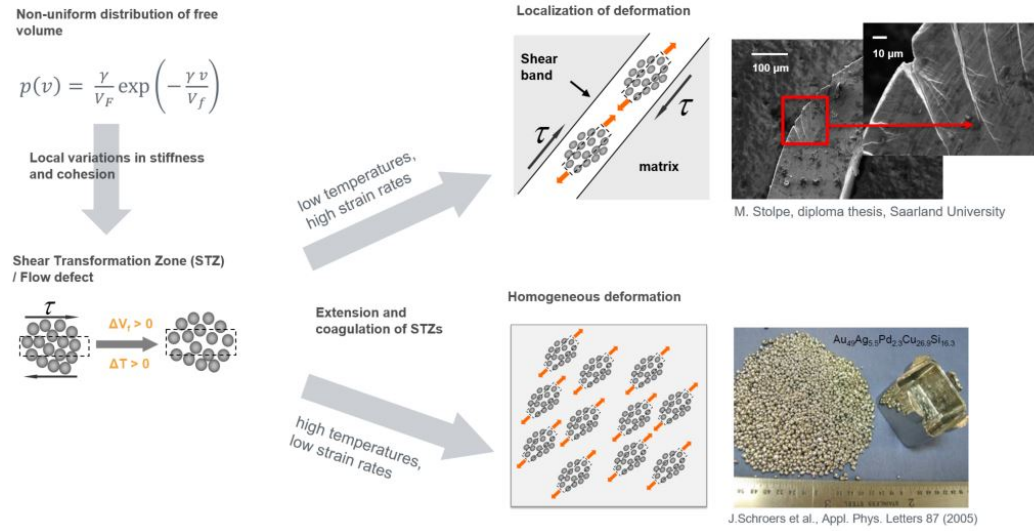


Figure 2.6: Deformation of metallic glasses. At low temperature and high strain rates metallic glasses show inhomogeneous deformation behavior via shear banding. At higher temperatures and lower strain rates deformation occurs homogeneously and metallic glasses can be processed like polymers or silicate glasses. The two macroscopically different deformation modes result from the same atomic deformation mechanism. The non-uniform distribution of the excess (free) volume leads to local variations in stiffness and cohesion. Regions of higher free volume concentrations act as initiation sites for plastic deformation (shear transformation zones). Once activated shear-induced atomic rearrangements lead to a local enrichment of free volume, making a once perturbed regions more susceptible for further plastic flow. Upon ongoing deformation the STZs extend and coagulate. Depending on how effectively the local strain-induced free volume increase can be redistributed by thermally-activated (diffusive) processes, deformation occurs homogeneously or inhomogeneously.



## 2.5 Crystallization

A liquid that is cooled below its liquidus temperature becomes unstable and normally transforms into a crystalline solid. Starting from numerous initiation sites, nuclei of the crystalline phase are stochastically formed by energy fluctuations. Once they reach a critical size, the nuclei grow until they ultimately collide and build a long-range ordered polycrystalline structure. On the other hand, if nucleation and growth of the crystalline phase can be avoided, the amorphous structure of the liquid can be frozen to room temperature and a glass is formed. To understand what makes a good glass former and to develop new systems with improved glass forming abilities, a detailed understanding of the nucleation and growth of crystalline phases from an undercooled liquid is required. In what follows a brief recapitulation of the classical nucleation theory is given.

At constant pressure  $p$  and temperature  $T$ , the equilibrium of a physical system is characterized by the minimum in its Gibbs free energy  $G = H - TS$ . Above the melt temperature  $T_m$  the Gibbs Free Energy of the liquid is lower than the Gibbs free energy of the crystalline phase(s),  $G_l(T) < G_x(T)$ , so that only the liquid phase is stable (see figure 2.7). At the melting point the liquid and the crystalline phase take the same value of  $G$ , i.e.  $G_l = G_x$  and hence coexist. If the liquid is cooled below  $T_m$ , its Gibbs free energy becomes larger than that of the crystalline phase  $G_l > G_x$ , leading to a natural *driving force*  $G_{xl} = G_x - G_l < 0$  that pushes the liquid to transform into a crystalline solid. When a small volume  $\Delta V$  of the liquid transforms into a crystal its Gibbs free energy will change about  $\Delta G_V = \Delta g_{xl} \Delta V$ , where  $\Delta g_{xl}$  corresponds to the difference in the Gibbs free energy density between the liquid and crystalline phase. Since the liquid and crystalline phase differ in structure (and potentially in chemistry), the formation of the crystalline phase inside the liquid requires the formation of an interface. Its energy  $\gamma_{xl}$  must be “paid” from the gain in energy associated with the formation of the crystalline phase. The total Gibbs free energy balance for the formation of a crystalline nucleus of volume  $V$  therefore is given by

$$\Delta G = \Delta G_V + \Delta G_\gamma = \Delta g_{xl} \Delta V + \gamma_{xl} \Delta A \quad (2.1)$$

with  $\Delta A$  being the area of the interface created. In case of a spherical solid cluster with radius  $r$ , equation 2.1 becomes

$$\Delta G = \frac{4}{3} \pi r^3 \Delta g_{xl} + 4 \pi r^2 \gamma_{xl} \quad (2.2)$$

Equation 2.1 is the fundamental equation for homogeneous nucleation and states that below a critical temperature, where  $\Delta g_{xl} < 0$ , there is a competition between the decrease in  $G$  caused by the transformation from the liquid into the crystalline phase,  $\Delta G_V$ , and the increase in  $G$  associated with the formation of the solid/liquid interface,  $\Delta G_\gamma$ . As the contribution from the interface scales with  $r^2$  while the volume free energy scales with  $r^3$ ,  $\Delta G$  passes a maximum. To

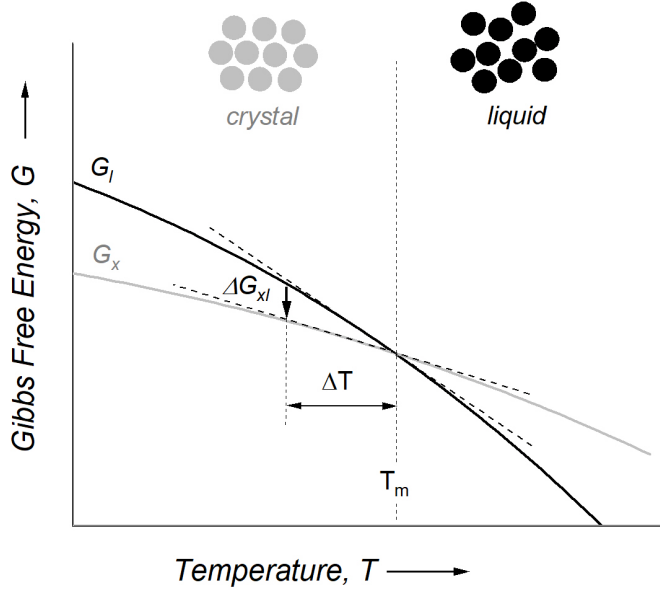


Figure 2.7: Temperature dependence of the Gibbs free energy of the crystalline,  $G_x$ , and the liquid state,  $G_l$ . Below the equilibrium temperature,  $T_m$ , there is thermodynamic driving force  $\Delta G_{xl}$  for the transition from the amorphous liquid into the ordered crystalline state.

develop into a stable nucleus, a crystalline cluster must reach a critical size  $r^*$  in order to climb the *nucleation barrier*  $\Delta G^*$ . Setting the derivative of equation 2.2 equal to zero, yields

$$r^* = -\frac{2\gamma}{\Delta g_{xl}} \quad (2.3)$$

and

$$G^* = \frac{16\pi}{3} \frac{\gamma^3}{(\Delta g_{xl})^2} \quad (2.4)$$

For  $r < r^*$  the clusters formed are unstable and dissolve; only for  $r > r^*$  it can transform into a stable nucleus that grows, since  $\Delta G$  decreases with increasing cluster radius  $r$  (cf. figure 2.8). Equation 2.4 shows that for a larger undercooling  $\Delta T = T_m - T$  the barrier for homogeneous nucleation  $\Delta G^*$  progressively decreases (cf. figure 2.7). From a thermodynamic point of view the propensity of a liquid to crystallize therefore continuously increases with decreasing  $T$  or increasing  $\Delta T$  respectively. Within first approximation  $\Delta g_{xl} = V^{-1} \Delta S_{xl}(T_m) \Delta T$ , where  $\Delta S_{xl}$  is the difference in entropy between the liquid and the crystalline phase given by the slope of the  $G$ -curves in figure 2.7.

Apart from these thermodynamic considerations, the rate of crystallization and hence the stability of the liquid phase is determined by the kinetics, which in

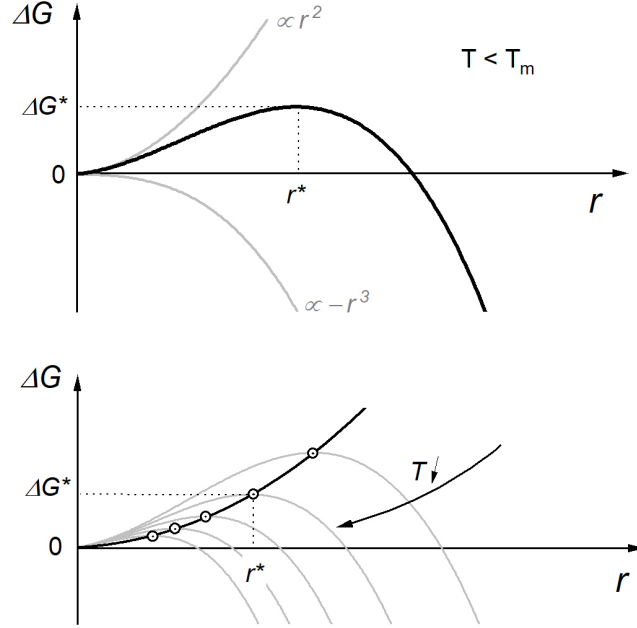


Figure 2.8: Energetic perspective of spherical nucleation. Below the equilibrium temperature  $T_m$  the competition between the free energy release due to the transformation of a small volume  $V$ , i.e.  $\Delta G_V \propto r^3$ , and the free energy needed to establish an interface  $A$ , i.e.  $\Delta G_\gamma \propto r^2$  results in a maximum in the Gibbs free energy (upper figure). Nucleation thus requires to overcome an energy barrier  $\Delta G^*$  whose amplitude decreases with decreasing temperature (lower figure).

turn is linked to the mobility of the particles. According to the *transition state theory*, the formation of a critical cluster of size  $r^*$  can be treated a thermally activated process. The probability that a spontaneous fluctuation yields a cluster associated with an increase in free energy of  $\Delta G^*$  is given by the Boltzmann factor  $\exp(-\Delta G^*/k_B T)$ . The number of critical clusters of size  $r^*$  therefore is given by

$$N^* = N_0 \exp\left(-\frac{\Delta G^*}{k_B T}\right) \quad (2.5)$$

where  $N_0$  is the total number of atoms per unit volume. Once the barrier is crossed, further growth will lower the Gibbs free energy and the crystalline cluster will transform into a stable nucleus by attaching atoms from the liquid phase. Consequently, the rate of formation of stable nuclei depends on the rate  $j$  at which atoms are transported to the nucleus and attach to its surface. According to the *classical nucleation theory* (CNT) the homogenous nucleation rate therefore

becomes

$$I = ZjN_0 \exp\left(-\frac{\Delta G^*}{k_B T}\right) \quad (2.6)$$

where  $Z$  is the so-called Zeldovich factor, which essentially can be regarded as the efficiency that a clusters reaching the top of the barrier will transform into a stable nucleus of the new phase [34]. Obviously the transport rate  $j$  is determined by the atomic mobility and hence must be related to the diffusivity  $D$  and the viscosity  $\eta$ , so that equation 2.6 can be expressed alternatively as

$$I \propto D_{eff} \exp\left(\frac{-\Delta G^*}{k_B T}\right) \quad (2.7)$$

Both  $j$  or  $D_{eff}$  themselves are thermally activated processes whose temperature dependence is associated with a factor  $\exp(-G_a/k_B T)$ , with  $G_a$  being the effective energy barrier for the atomic transport. In dense metallic liquids the effective diffusivity  $D_{eff}$  is piecewise-defined: At high temperatures a connection to the viscosity  $\eta$  can be established through the Stokes-Einstein relation  $D_{eff} = k_B T / (3\pi d \eta)$ , yielding  $I \propto T/\eta \exp(-\Delta G^*/k_B T)$ , while it is found that at lower temperatures the assumption of an Arrhenius behavior  $D_{eff} = D_{eff,0} \exp(-E_a/k_B T)$  is often more suitable [35]. The growth of the nucleus requires the liquid-crystal interface to migrate. It can be shown that the crystal growth rate  $u(T)$  is given by [35]

$$u(T) \propto D_{eff}/d \left[ 1 - \exp\left(-\frac{n\Delta g_{xl}}{k_B T}\right) \right] \quad (2.8)$$

Just like the nucleation rate  $I(T)$ , the temperature dependence of the growth velocity  $u(T)$  is determined by two contributions: a thermodynamic factor and a dynamic factor. In fact the thermodynamic factors  $I(T)\eta$  and  $u(T)\eta$  increase continuously during undercooling as shown in figure 2.9, indicating that thermodynamics consistently favor the nucleation of crystals and their growth during undercooling. On the other hand dynamics become more and more sluggish, restraining nucleation and growth. This opposite temperature dependence of the two factors leads to a maximum in the nucleation and growth rate as illustrated in figure 2.10. The nucleation rate and the growth rate enable to calculate rate at which the liquid crystallizes. According to the Johnson-Mehl-Avrami-Kolmogorow model [36], the fraction of the transformed phase,  $f$ , during an isothermal transformation is given by

$$f(t) = 1 - \exp(-kt^n) \quad (2.9)$$

where  $k$  is a constant that depends on the nucleation rate  $I$  and the growth rate  $u$ , and therefore is temperature dependent. The Avrami exponent  $n$  is a number between 1 and 4 and depends on the dimension of the system. Assuming

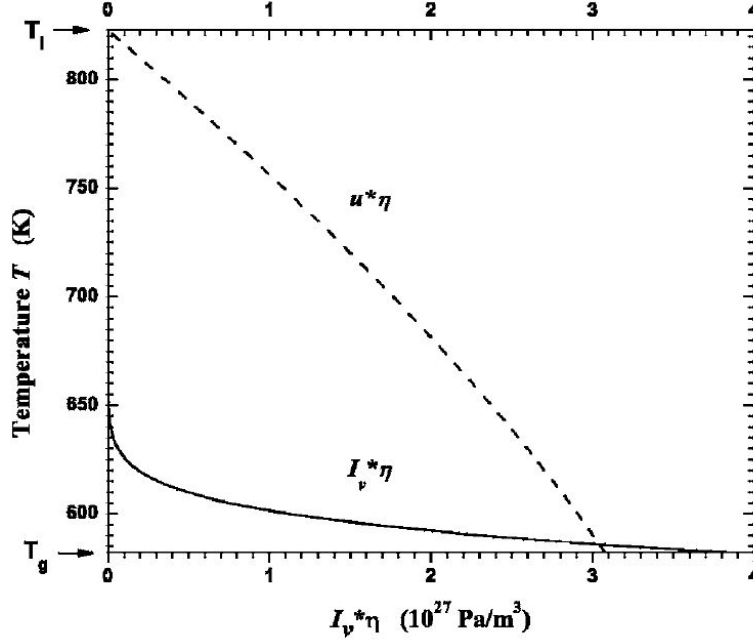


Figure 2.9: Temperature dependence of the thermodynamic factors controlling nucleation,  $I\eta$ , and crystal growth,  $u(T)\eta$  for the a Pd-based bulk metallic glass former. Figures are taken from [35].

randomly distributed spherical nuclei in a three dimensional system, equation 2.9 becomes

$$f(t) = 1 - \exp\left(-\frac{\pi}{3} I u^3 t^4\right) \quad (2.10)$$

In the beginning of the transformation  $f \ll 1$ , so that equation 2.10 can be approximated as

$$f(t) = \frac{\pi}{3} I u^3 t^4 \quad (2.11)$$

The temporal evolution of phase transformations is illustrated in *time-temperature-transformation diagrams* (TTT-diagrams). TTT-diagrams give a graphical overview about how long a phase is stable under the given conditions, when it will become unstable, and when it will transform into a new phase. There are two types of TTT-diagrams: continuous cooling and isothermal TTT diagrams. An isothermal TTT-diagram gives the temporal evolution of the amount of the new phase formed at a given (constant) temperature. It shows how fast the reaction proceeds when the system is held at constant temperature. In contrast, a continuous cooling TTT-diagram gives the evolution of the new phase at a given cooling rate. According to the JMAK equation (equation 2.9), the rate of formation of the new phase  $\dot{f} = \partial f / \partial t$  is determined by the rate at which nuclei are formed  $I(T)$  and the rate at grow  $u(T)$ . As  $I(T)$  and  $u(T)$  both exhibit a maximum with

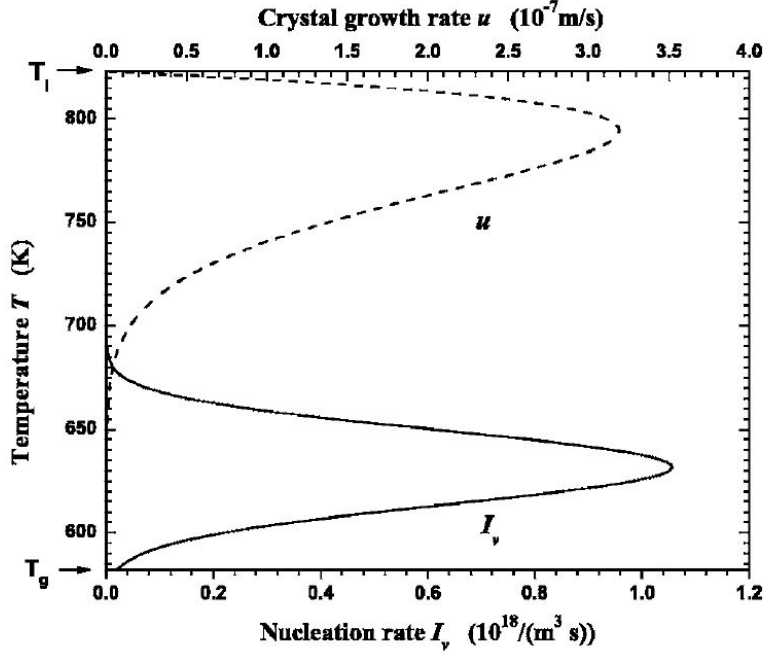


Figure 2.10: Temperature dependence of the nucleation rate  $I$  and the crystal growth rate  $u$  for a Pd-based bulk metallic glass former. Figures are taken from [35]

respect to temperature, it is clear that  $\dot{f}$  passes a maximum as well, leading to a C-shaped temperature dependence of the crystallization time. Figure 2.11 shows the experimental TTT-diagram of a PD-based glass former taken from reference [35]. Note that the nose of crystallization is situated in a temperature range where  $I$  and  $u$  show opposing trends in their temperature dependence (cf. figure 2.10). This has direct implications on the microstructure formed during solidification. For larger undercooling, the energy barrier becomes smaller, and nuclei are formed at higher rates. On the other hand, with decreasing temperature the atomic mobility reduces drastically, and so the growth rate of nuclei is lowered. Crystallization at low temperatures therefore occurs by a large number of nucleation sites that grow moderately leading to a finer microstructure. In contrast, at higher temperatures the driving force is low and the energetic barrier is high, and so the rate of the formation of nuclei is slow. On the other hand, the atomic mobility is high, so that once a stable (supercritical) nucleus has formed, it grows quickly. Crystallization at higher temperatures therefore occurs by fast growth of a smaller number of nucleation sites, leading to a coarser microstructure.

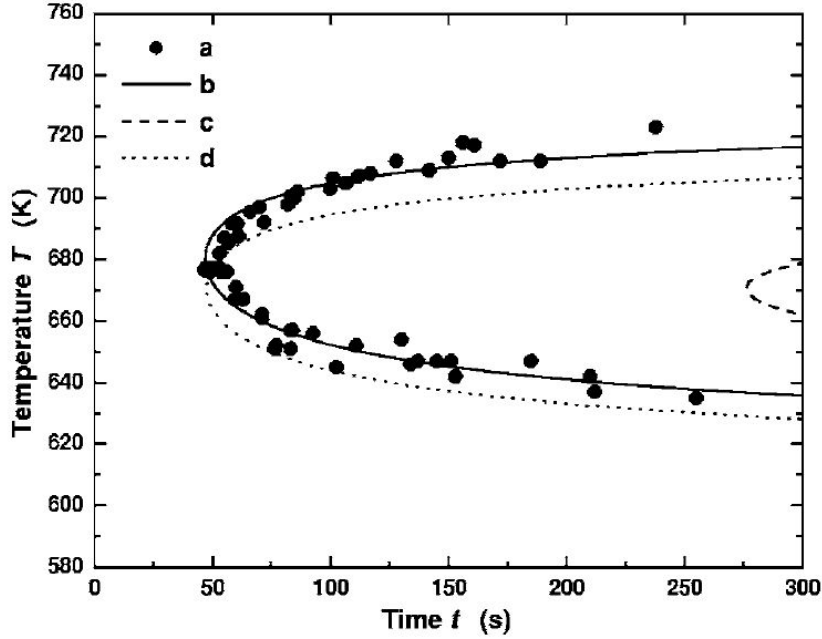


Figure 2.11: Experimental TTT-diagram of a Pd-based bulk metallic glass forming alloy corresponding to the nucleation and crystal growth rate depicted in figure 2.10. The figure taken from [35].

## 2.6 The glass transition

With decreasing temperature, the kinetic energy of the particles decreases, and the structure is more and more influenced by the interatomic forces. Below a critical temperature, the ordered crystalline phases becomes thermodynamically favored over the disordered (amorphous) liquid phase and the liquid ultimately transforms into a (poly-)crystalline solid, manifesting as a more or less sudden decrease in enthalpy  $H$ , entropy  $S$ , as well as the volume  $V$  (cf. figure 2.12). Since the transformation into the crystalline phase requires the formation of an interface, crystallization requires a certain amount of undercooling  $\Delta T$ , as illustrated by the dashed line below  $T_m$  in figure 2.12. With the transition into a crystalline solid the thermodynamic response functions, i.e. the thermal expansion coefficient  $\alpha = V^{-1}\partial V/\partial T$ , and the specific heat capacity  $c_p = \partial H/\partial T$  become smaller, reflecting a less pronounced temperature dependence of  $H$ ,  $S$ , and  $V$ .

Provided that crystallization is avoided, the metastable equilibrium state of the liquid can be preserved at lower temperatures. Upon cooling the liquid contracts and order is formed, leading to a continuous decrease in  $V$ ,  $H$ , and  $S$ . Above a critical packing fraction atomic motion becomes influence by its neighbors and structural rearrangements require collective atomic motions (cf. section

3.4 and section 3.5). With a further descent in its energy landscape (cf. section 3.5.4), the number of thermally accessible structural states in the liquid decreases, and energy barriers for collective atomic rearrangements can be less readily overcome, resulting in a marked increase in the structural relaxation time  $\tau$ . Macroscopically this is reflected by a tremendous increase of the viscosity  $\eta$ . In a temperature range of usually not more than a few hundreds of Kelvins, the viscosity increases by about 14 orders of magnitudes, while the volume decrease at the same time is of the order of a few per cent only ( cf. figure 3.11). Ultimately, the dynamic slowdown leads to a structural freezing and the system falls out of its metastable equilibrium <sup>5</sup>. This occurs approximately at a viscosity of about  $10^{12}$  Pas, corresponding to structural relaxation time  $\tau$  of the order of 100 - 1000 s, as the latter crosses the observation time of the experiment, i.e.  $\tau \approx \tau_{obs}$ . Below this point, the time scale needed for the system to adapt on the outer imposed changes, given by  $\tau$ , becomes much longer than the experimental time scale, given by  $\tau_{obs}$ , so that the properties observed in an experiment lag behind with respect to the properties expected from an extrapolation of the supercooled liquid state (cf. dashed lines in figure 2.9). The liquid now appears to be frozen and essentially behaves like a solid in the sense that its properties ( $H$ ,  $V$ ,  $S$ ,  $\alpha$ ,  $c_p$ ) mimic the behavior of the crystalline state. The temperature range of the transition from liquid to solid behavior is called the *glass transition*. Its corresponding onset or end temperature are derived from the positions where the measured properties, e.g.  $\eta$ ,  $V$ , or  $c_p$ , show a change in their temperature dependence.

Since the laboratory glass transition is a purely kinetic phenomenon arising from a crossing of time scales, its position (temperature) depends on the experimental conduct. For higher cooling rates the crossover occurs already at higher temperatures, while slower cooling shifts the transition to lower temperatures (cf. figure 3.11). For an infinitely slow cooling, no kinetic transition would be observed at all, and the supercooled liquid would keep its trend. As the heat capacity of the liquid phase is larger than that of the crystalline phase this would lead to a situation where the entropy of the liquid equals and finally becomes lower than the entropy of the crystalline phase. This conflicting scenario brought up by W. Kauzmann has been a subject of intense debate, and has stimulated the discussion of a real thermodynamic "ideal glass transition" hidden below the laboratory glass transition [37, 38].

The kinetic nature of the laboratory glass transition has significant implications on the structure and properties of the glass. In fact, there is no distinct glassy state but rather a vast plurality of states that can be established depend-

---

<sup>5</sup>In fact, the structural freezing is not a real freezing in the sense that the structural units no longer can move at all. They still possess a certain degree of mobility enabling the system to evolve towards the equilibrium state - a process called relaxation. However, the time constant for the relaxation, i.e. the structural relaxation time, is much longer than the time scale of observation, yielding an apparent freezing of the liquids properties.



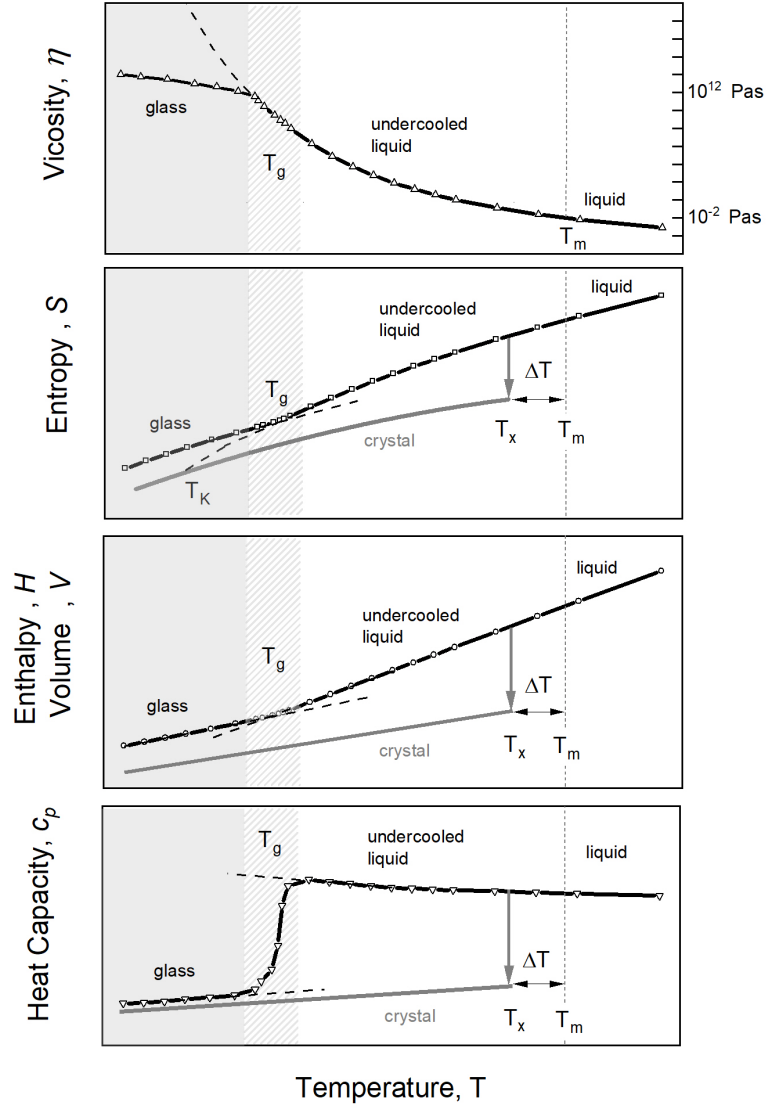


Figure 2.12: Schematic illustration of the evolution of the viscosity  $\eta$ , the entropy  $S$ , the enthalpy  $H$ , the volume  $v$ , and the heat capacity  $c_p$  during the glass transition.

ing on the thermal history. For examples, by changing the cooling rate, different structural and thermodynamic states can be quenched from the liquid. On the other hand, annealing the system below the glass transition will lead to so-called relaxation (aging) effects during which the system progressively descends in its energy landscape until it reaches its metastable equilibrium state given by the extension of the supercooled liquid lines (cf. section 3.4). The physical properties of a glass strongly depend on its configurational state. For instance, configurational states characterized by larger amounts of frozen excess volume and disor-

der are potentially more ductile, while structurally more-relaxed, more-ordered structures usually show a more brittle mechanical behavior. Understanding the interplay between the structure and properties of metallic glasses is therefore inevitable for their use as structural or functional materials.

## 2.7 Structure of metallic liquids and glasses

In contrast to conventional crystalline materials, a single structural unit like the unit cell that contains all relevant information on the atomic arrangement is missing in the amorphous materials, making their description more intricate. The structure of amorphous metals rather must be considered as a distribution of different atomic clusters, that vary in terms of the number, distances, and orientation of nearest neighbors.

### 2.7.1 Voronoi tessellation

A method often used to describe the 3D configuration of the amorphous structure is the Voronoi tessellation, where the space tiling is made by cells defined by a central atom and the spatial arrangement of its nearest neighbors [9]. The cell is constructed by connecting the central atom with its neighboring atoms and drawing planes perpendicular to the bonding direction at half distance between the atoms. The space enclosed between the closest planes and the central atom defines the local cell. In crystalline materials the Voronoi cells are equal for all atoms, and so the entire information of the lattice structure can be deduced from a single cell<sup>6</sup>. Figure 2.13 shows the Voronoi tessellation of an amorphous structure. The geometry of the cells is described by the so-called Voronoi indices  $\langle i, j, k, l \rangle$ . Each of the indices refers to a specific type of plane. Their values indicate the frequency of the planes present in the cell. The first index  $i$  refers to triangles, the second index  $j$  to quadrangles, the third index  $k$  to pentagons, and the fourth index  $l$  to hexagons. A  $n$ -edged polygon between the bonding atoms  $A$ - $B$  is associated with  $n$  common neighbors surrounding the pair, and therefore such a configuration constitutes a “ $n$ -fold bond”, as shown in figure 2.13c. The Voronoi cell thus bears useful information on the local environment, and studying their distribution yields valuable insights in the structural evolution of the amorphous state.

### 2.7.2 Formation of order in metallic liquids: local vs. global structure

The formation of order results from of the natural propensity of a physical system to minimize its Gibbs free energy  $G = H - TS$ . At high temperatures far beyond

---

<sup>6</sup>The Voronoi cell of the real space lattice is referred to as the Wigner-Seitz cell.

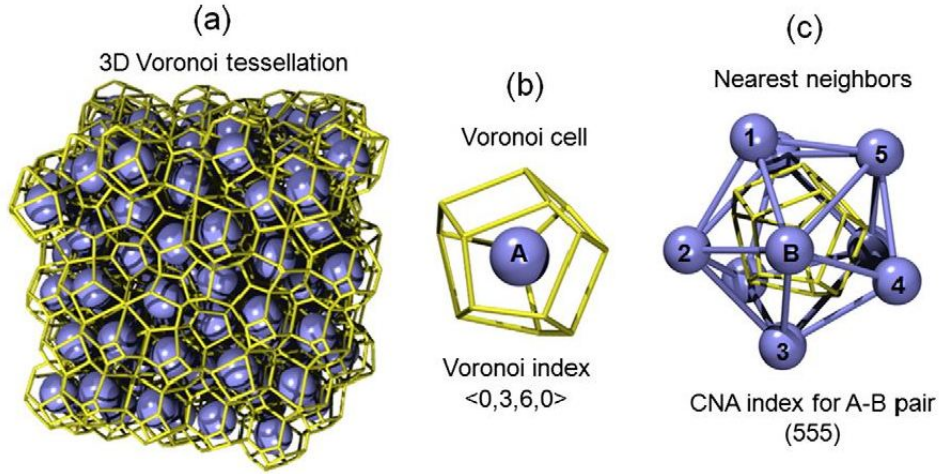


Figure 2.13: (a) 3D Voronoi tessellation of the amorphous state. (b) (c) Each atom can be considered as the center of a cell whose surrounding edges and faces reveal details on the local atomic environment as described in the main text. The figure is taken from [9].

the melting point the structure is determined by entropy, so that the liquid phase is highly disordered. With decreasing temperature enthalpy  $H$  more and more prevails over entropy  $S$ , leading to the formation of order. Normally lower enthalpy states coincide with more densely-packed structural configurations so that the system contracts upon cooling. This is in particular true for most metallic materials due to their non-directional bonding character.<sup>7</sup> Driven by topological and chemical factors specific atomic configurations become energetically more favorable than others when the liquid is cooled, leading to the formation of more densely-packed, more-ordered atomic clusters in a sea of other energetically less favorable local structures [39, 40]. Upon cooling the concentration of locally favored cluster structures increases. The clusters extend and tend to aggregate, building up larger blocks or networks that act as “islands” of lower mobility [41, 42].

In case that the locally favored structures have symmetry axis that are incompatible with a 3D-tiling of space, long-ranged periodic repetition would go along with increased “mismatch strains”<sup>8</sup> so that larger domains composed of these structures become energetically less favorable compared to long-ranged periodic repetition of clusters structures whose symmetry is compatible with a tiling of

<sup>7</sup>In case of more directional bonding between the constituents the lowest enthalpy/energy states do not necessarily coincide with the state of minimal volumes and, thus, lower packed structures can be more preferable. Nevertheless, with a few exceptions the crystalline state normally has the highest global density, being a few percent larger than the density of the liquid state.

<sup>8</sup>The term “mismatch strain” here refers to a temporally-averaged stretching of atomic bonds in the corresponding regions in order to “glue” the individual domains.

3D space, e.g. face-centered cubic (*fcc*), body-centered cubic (*bcc*), or hexagonal-close packed (*hcp*). The incompatibility of specific locally favored structures to tile 3D space therefore can lead to geometrical “frustration”, preventing the formation of a long-range order periodic structure.

The previous discussion shows that the structural evolution of metals upon cooling is determined by two (potentially) competing tendencies: (I) the formation of dense-packed locally favored (cluster) structures and (II) a striving to minimize the overall Gibbs free energy. The natural selection of close packed crystalline structures at lower temperatures can thus be viewed as a consequence of the incompatibility of other dense-packed clusters structures, e.g. icosahedra, to form larger domains without provoking “mismatch strains” that raise the overall (Gibbs) free energy - even though the latter can be energetically more favorable on local length scales.

### 2.7.3 Random packing of equal sized spheres

In the 1960’s Bernal [43, 44], Scott [45] and Finney [46, 47] investigated how space can be efficiently filled by hard spheres without introducing long-range crystalline order. Bernal proposed five types of polyhedral holes with edges of equal length to be the fundamental structural units of monatomic liquids [9, 44]. These so-called Bernal’s holes are shown in figure 2.14. Among them, equilateral tetrahedra have the highest packing efficiency and hence should have a natural prevalence in density-driven systems, once the macroscopic density reaches a critical value. However, a 3D space tiling by equilateral tetrahedron only cannot be obtained [48] and hence requires the emergence of other structural motifs or distortion of the tetrahedra to prevent the formation of larger holes in the structure [9]. In close-packed fcc or hcp crystalline structures the “issue” is solved by the occurrence of a well-balanced amount of octahedra  $N(octahedra)/N(tetrahedra) = 2 : 1$  [9]. By placing two tetrahedra on opposite faces of the octahedron, 3D space-tiling structural unit is formed whose periodic repetition results in the formation of a long-range ordered lattice structure. For dense random hard sphere packing (DRHSP) Bernal experimentally found that the structure consists of 70 % tetrahedra, 20 % half octahedra, and about 10 % of the other Bernal holes depicted in figure 2.14 [44].

The two examples yield a fundamental insight in the formation of structure in general. Although a specific structural unit may be locally favored, its spatial repetition may lead to geometrical frustration, requiring other structural motifs to emerge in order to prevent the formation of larger holes in the structure. Trying to model the structure of a monatomic system by equilateral tetrahedra only (polytetrahedral packing), one realizes that (I) the maximum number of atoms that can be placed around the central atom, i.e. the coordination number (CN), is twelve, and (II) the nearest neighbor shell exhibits a gap. This packing frustration can be avoided by two ways [48]: Either, the atoms are redistributed around the

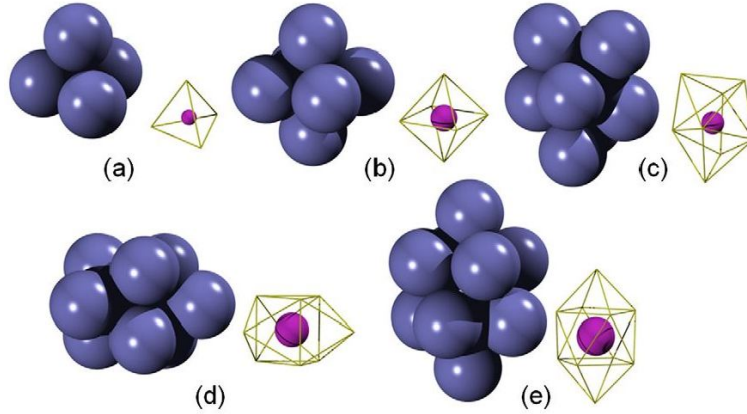


Figure 2.14: Bernal’s canonical holes: (a) tetrahedron, (b) octahedron, (c) tetragonal dodecahedron, (d) trigonal prism capped with three half octahedra, (e) Archimedean antiprism capped with two half octahedra. The left figures show the hard sphere packing surrounding the hole. The holes in the center of each packing scheme is shown in the right figures by the pink spheres. The figure is taken from [9].

shell to form eight tetrahedra while the remaining space is accommodated by six half octahedra, this is the classical fcc/hcp packing of crystalline materials already mentioned above, or, the twelve atoms are redistributed equally among the shell (cf. figure 2.15). In this latter scenario the atom in the coordination shell no longer touch each other, and a regular icosahedral cluster consisting of 20 distorted tetrahedra is obtained. Compared to the fcc arrangement, a regular icosahedron has a higher symmetry, and a shorter average bond length. It is energetically favored compared to the fcc arrangement and thus should be predominant in monatomic liquids as postulated by Frank [49]. However, its five-fold symmetry elements act against the formation of long-range translational order. To tile 3D space without forming larger holes (diamond shaped regions in figure 2.15), the regular icosahedron must be distorted, raising the overall Gibbs free energy. Although the regular icosahedron is the energetically preferred local structure compared to fcc, long-range frustration renders the latter globally more favorable (cf. figure 2.15). The fact that the crystalline and the amorphous phase have different preferred local structures is considered as structural origin of an increased “supercoolability” of metallic liquids [49].

The above considerations and observations are based on hard spheres. A more realistic description of the atomic interaction can be given by soft sphere pair potentials e.g the Lennard-Jones or the Morse potential. Similar to the case of hard spheres it is found that icosahedral ordering is energetically favored with respect to fcc/hcp packing [39, 49, 50], and hence should be the locally favored in metallic liquids. Numerous experimental studies give indirect evidence for

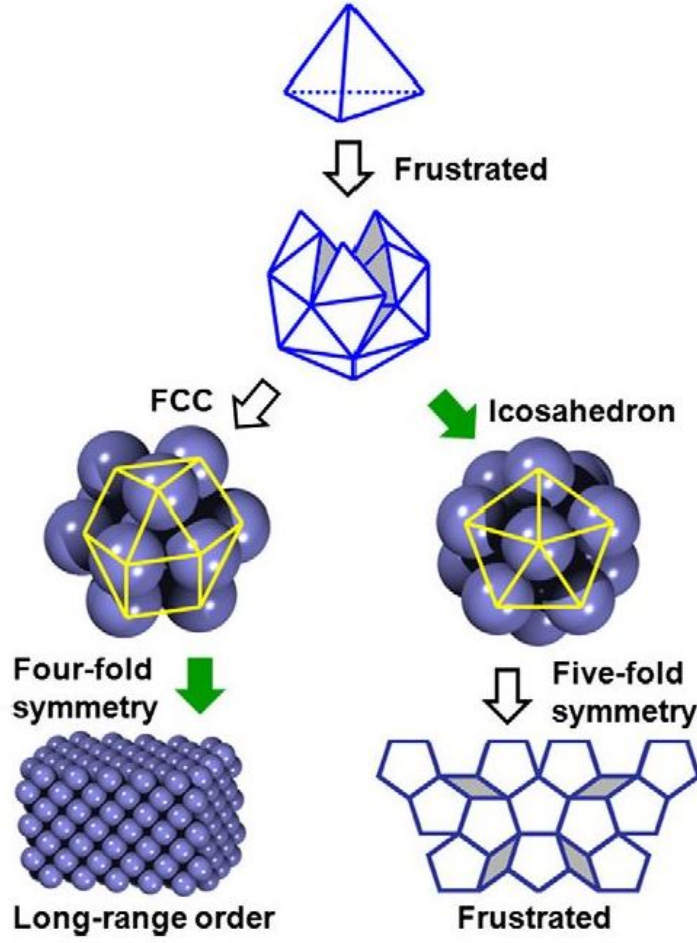


Figure 2.15: Frustration map of polytetrahedral packing of identical hard spheres according to Ma et al. [9]. The green arrows show the optimal choice at each stage. The figure is taken from [9].

the existence of icosahedral order in monatomic metallic liquids, although these elements have different crystalline structures [51–55]. The existence of icosahedra is further corroborated by *ab initio* density functional theory (DFT) simulations [9]. Yet, the extent and the distinct nature of topological order can vary markedly in different systems [9, 53–55], and there may be other structural motifs that compete with icosahedral ordering, e.g. bcc-type order in supercooled Zr [56]. Irrespective of their exact nature, there is a general consensus that energetically favored, high-symmetry structural motifs play a crucial role in the viscous slowdown towards the glass transition [9, 39, 50].

### 2.7.4 Multicomponent systems

The previous considerations strictly only apply for monatomic systems. In multicomponent systems the different atomic sizes of individual species strongly influence the efficiency of particular packing schemes. For example, if the central atoms of an icosahedron is replaced by a much larger atom, the highest packing density will be obtained for local structure with a coordination number  $CN > 12$ . On the other hand, if the central atom is much smaller, a local high packing density can only be achieved if the number of nearest neighbors is reduced, i.e.  $CN < 12$ . Thus, depending on the ratio of atomic sizes there can be other local structural motifs (cluster types) that are more suitable to increase the local packing density, and hence may be more energetically more preferable. In addition, there may be a tendency for chemical ordering. For example, in a system composed of two atomic species there may be a preference to form either unlike (A-B) or alike (A-A, B-B) bonds. The Gibbs free energy is then no longer determined by topological aspects only, but also by the propensity to create or replace A-B bonds, and hence will depend on the enthalpy of mixing between A and B. Accordingly, locally favored structures in multi-component alloys are not necessarily icosahedral but other cluster structures may be more efficient to lower the Gibbs free energy of the amorphous phase and hence may form in preference [9, 57–60].

### 2.7.5 Metallic glass forming systems

Based on their constitution, metallic glass forming systems can be classified into several families. The main families along with some prominent examples are summarized in table 2 in figure 2.16.<sup>9</sup>

A closer inspection of the alloy systems reveals numerous commonalities that appear to favor glass formation. Metallic glass formers often are near-eutectic multicomponent alloys characterized by a large size mismatch and negative heat of mixing between the constituents (cf. figure 2.17). Along with their high density in the liquid state the empirically found glass formers are in agreement with the conception that their structure is constituted of dense-packed atomic clusters with an increased number of unlike bonds between the solvent species and the solutes. Indeed, computational studies confirm that topological and chemical differences between the constituent favor the formation of energetically preferred clusters (ECPs) where the solutes are surrounded by the solvent species, as shown in figure 2.18 for the computed structure of three binary metallic glasses [62]. Note that the clusters often have five-fold symmetry elements, as indicated by their Voronoi indices. The numerical results of Sheng et al. [62] shown in the figure thus confirm solute-solute avoidance and a preference for chemically ordered,

---

<sup>9</sup>Recently, it has been shown that there exists a variety of bulk metallic glass forming systems bearing the non-metal sulfur [61], previously neglected as an alloy constituent.



**Table 1**

Classification of common constituent elements of MGs.

Abbreviation		Description	Examples
AM		Metals in groups IA and IIA	Mg, Ca, (Be <sup>a</sup> )
SM		Metals in groups IIIA and IVA	Al, Ga
TM	ETM	Metals in IVB to VIIB groups	Ti, Zr, Hf, Nb, Ta, Cr, Mo, Mn
	LTM	Metals in VIIIB, IB, IIB groups	Fe, Co, Ni, Cu, Pd, Pt, Ag, Au, Zn
RE		Sc, Y, Lanthanides (Ln)	Sc, Y, La, Ce, Nd, Gd
NM		Nonmetals and metalloids	B, C, P, Si, Ge

<sup>a</sup> Although element Be is an AM per this classification, its role in MG formation is often unique. See discussion in Section 3.4.4.**Table 2**

Classification of typical MGs based on the binary prototypes.

Prototype	Base metal	Examples
LTM + NM	LTM	Ni-P, Pd-Si, Au-Si-Ge, Pd-Ni-Cu-P, Fe-Cr-Mo-P-C-B
ETM + LTM	ETM or LTM	Zr-Cu, Zr-Ni, Ti-Ni, Zr-Cu-Ni-Al, Zr-Ti-Cu-Ni-Be
SM + RE	SM or RE	Al-La, Ce-Al, Al-La-Ni-Co, La-(Al/Ga)-Cu-Ni
AM + LTM	AM	Mg-Cu, Ca-Mg-Zn, Ca-Mg-Cu

Figure 2.16: Main families of metallic glass forming systems according to [9] with some prominent examples. The tables are taken from [9].

	Ti	Zr	Nb	Hf	Ta	Ni	Cu	Pd	Ag	Al	Be
Ti	1.46	0	2	0	1	-35	-9	-65	-2	-30	-30
Zr	0	1.49	4	0	3	-49	-23	-91	-20	-44	-43
Nb	2	4	1.46	4	0	-30	3	-53	16	-18	-25
Hf	0	0	4	1.67	3	-42	-17	-80	-13	-39	-37
Ta	1	3	0	3	1.58	-29	2	-52	15	-19	-24
Ni	-35	-49	-30	-42	-29	1.28	4	0	15	-22	-4
Cu	-9	-23	3	-17	2	4	1.27	-14	2	-1	0
Pd	-65	-91	-53	-80	-52	0	-14	1.41	-7	-46	-8
Ag	-2	-20	16	-13	15	15	2	-7	1.42	-4	6
Al	-30	-44	-18	-39	-19	-22	-1	-46	-4	1.43	0
Be	-30	-43	-25	-37	-24	-4	0	-8	6	0	1.13

Figure 2.17: Heat of mixing between elements according to the Mediema model. The atomic sizes are given in the diagonal cells. The figure is taken from [9].

dense-packed cluster types. Local atomic order in metallic glasses has also been observed directly using nanobeam electron diffraction [60, 63]. The experimental results confirm the formation of dense-packed atomic clusters and larger cluster assemblies, and are in good agreement with structures predicted from ab initio molecular dynamics simulations [60, 63], as shown in figure 2.19.

## 2.7.6 Medium-range ordering in metallic liquids and glasses

The results presented in figure 2.18 further reveal that solute-centered clusters tend to build dense-packed aggregates whose atomic correlations extend to length scales corresponding to medium range ordering. If more than two species are in-



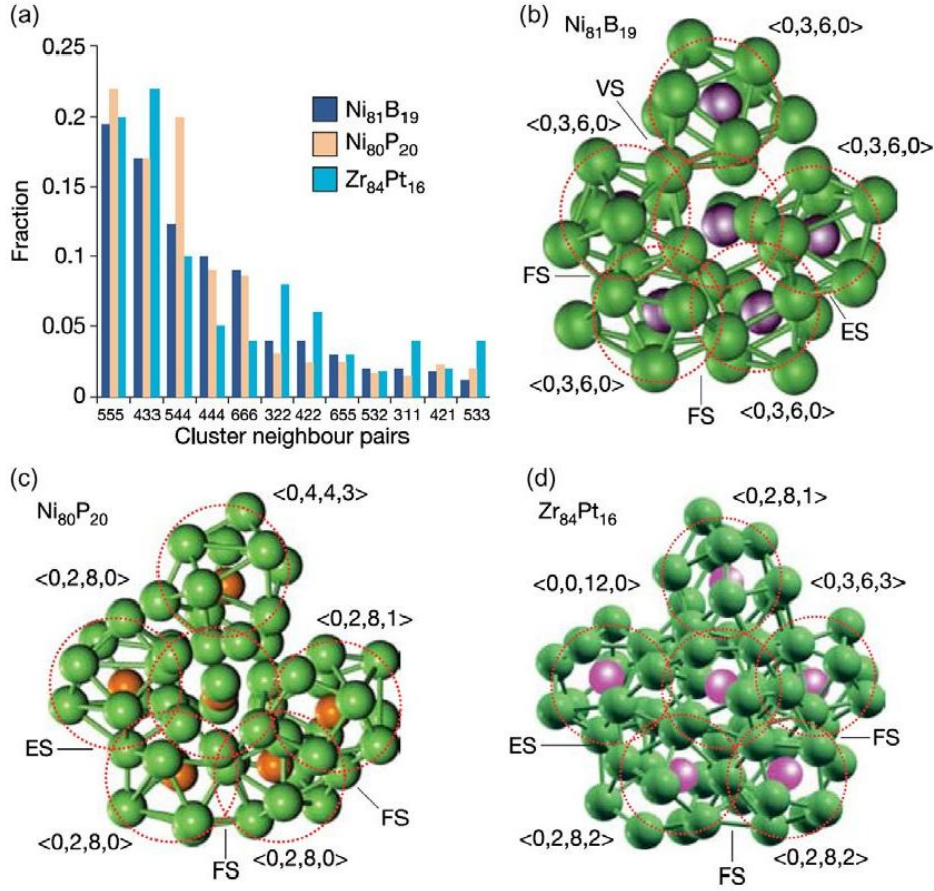


Figure 2.18: Atomic structure of binary metallic glasses. The structure is composed by efficient packing of solute-centered clusters including fivefold and icosahedral-like features. The figure is taken from [62].

involved a higher packing density can be achieved by placing the individual solute-centered clusters onto a lattice structure [57] as shown in figure 2.20 for the case of a fcc-superstructure. The model known as the efficient cluster packing model provides an explanation for the high packing densities observed for multicomponent BMG formers. The individual solute-centered clusters can but not necessarily need to be connected by sharing solvent atoms (interconnecting cluster shells) as shown for the (100) plane of a  $\langle 12, 10, 9 \rangle_{fcc}$  type structure in figure 2.20. The numbers classifying the specific packing scheme correspond to the number of solvent atoms belonging to a particular cluster species. The first number corresponds to the computed ideal number of solvent atoms around the  $\alpha$  solute, i.e. usually the biggest solute species. The second number corresponds to the  $\beta$  solutes, usually of intermediate size, and the third number corresponds to the  $\gamma$  solutes, i.e. normally the smallest solute species involved. The  $\alpha$ -clusters

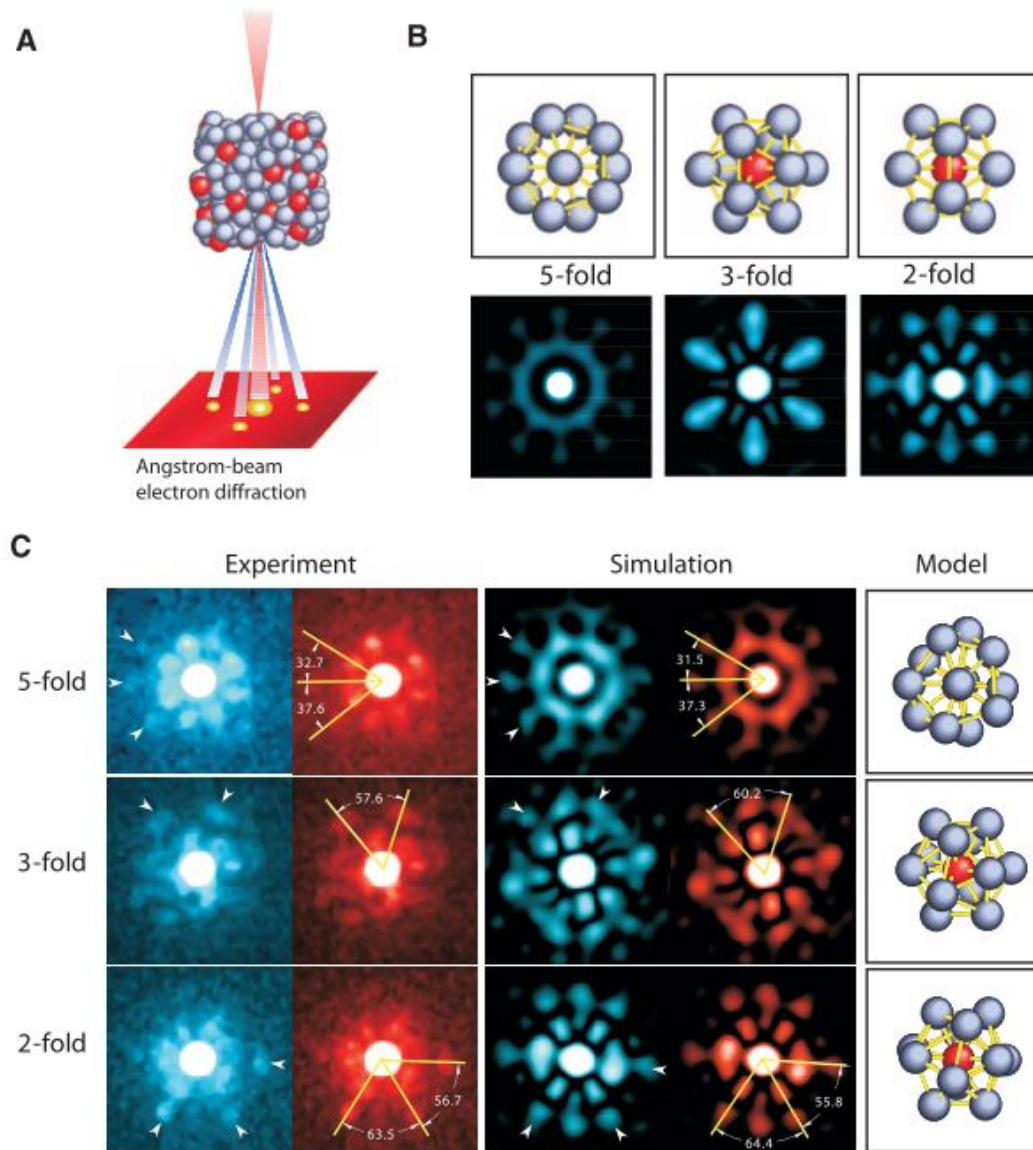


Figure 2.19: Direct observation of local order in metallic glasses by nanobeam electron diffraction. The experimental results confirm the formation of icosahedral ordering in agreement with *ab initio* MD simulation. The figure is taken from [63].

sit on the lattice sites of the underlying superstructure, while the  $\beta$  solutes occupy octahedral holes, and the  $\gamma$  solutes fill tetrahedral holes. The numbers of the nearest-neighbor solvent atoms surrounding a given solute species are determined by steric aspects alone, and can be computed from the size ratio  $R^*$  of the solvent and solute atoms. The ECP model allows to deduce a range of favorable glass-forming compositions based on (I) the radii of the constituents,

(II) the assumed model for the superstructure, (III) the degree of overlap of the distinct clusters, (IV) the site occupancy of the tetra- and octahedral holes, and (V) topological defects in the structure. A comparison with existing glass formers shows that the predictions made by the ECP model yield a good agreement with the experimentally obtained compositions [57]. Moreover, the ECP model provides an explanation for the occurrence of medium-order correlations in real-space diffraction data of metallic glass formers up to a length scale of  $\approx 0.7$  nm to 1 nm [57]. Beyond this length scale orientational and size mismatches lead to geometrical frustration precluding a long-range ordered structure [57].

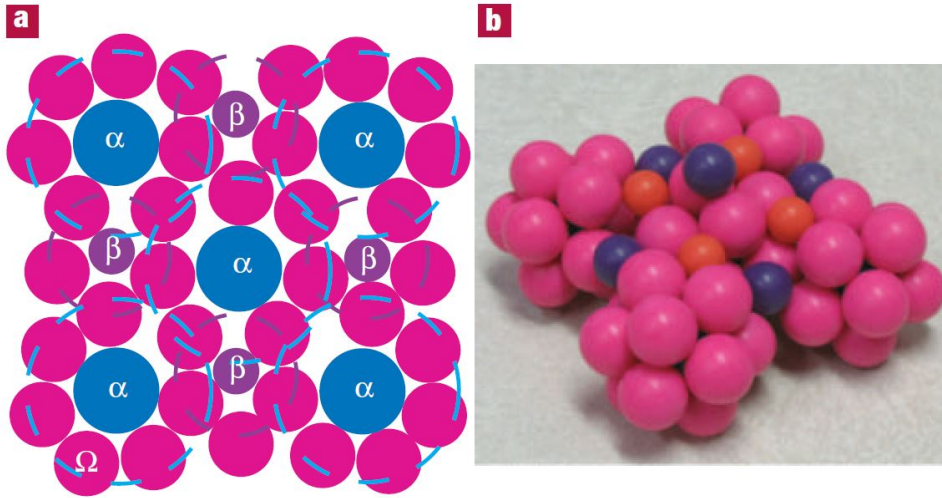


Figure 2.20: Efficient cluster packing model of medium-range ordering in metallic glasses according to Miracle [57]. The figure shows an example of a  $\langle 12, 10, 9 \rangle_{fcc}$  type-superstructure of (interpenetrating) solute-centered clusters. The left figure shows a 2D-representation of the (100) plane. The right figure shows a portion of a cluster unit cell. The figure is taken from [57].

## 2.8 Interplay of structure, thermodynamics and dynamics in metallic glass forming liquids

The formation or order in (metallic glass forming) liquids is directly reflected by its configurational entropy  $S_c$ . The configurational entropy measures the number of possible configurations that are available to a liquid in its energy landscape at a given temperature. With decreasing temperature the liquid descends in its potential energy landscape and less configurations become available, leading to a pronounced slowdown of its dynamics (cf. section 3.5.4). At high temperatures, usually far above the melting point, the liquid is characterized by a large amount

of disorder (entropy). Atoms can easily overcome energetic barriers and move more or less independently by free diffusion. The system is able to sample its entire energy landscape without “feeling” the topography of the energy landscape (cf. figure 3.15), and exhibits an almost temperature-independent activation energy for structural relaxation [38]. Within this regime, the enthalpy and entropy decrease moderately, indicating that the formation of order is moderate as well. Upon cooling the kinetic energy of the particles decreases and under pressure the systems contracts. Structural rearrangements become more and more collective, and the dynamics are more and more influenced by the energy landscape. The system no longer is able to sample its highest energy barriers and hence is forced to sample much rarer, deeper-lying configurations [38]. With the transition to the landscape-influenced regime, the kinetics of structural relaxation change from exponential to stretched exponential behavior, and the activation energy as well as the entropy become super-Arrhenius, meaning that their temperature dependence is stronger than exponential [38]. With a further descent in the energy landscape the height of the barriers separating sampled adjacent energy minima increases abruptly (landscape-dominated regime) [38]. Within this regime, atoms execute rare jumps over distances roughly equal to interatomic separations [38], indicating that they become caged by their neighbours. The temperature of the crossover from landscape-influenced to landscape dominated behavior corresponds closely with the mode-coupling transition temperature [38]. The fast decrease of the potential energy and the entropy in these temperature regimes is accompanied by a tremendous slowdown of the dynamics. How sensitive the dynamics in a liquid behave against changes in temperature is dictated by how strong the configurational entropy changes (cf. section 3.5.3). Ultimately, the increase in the structural relaxation time will lead to a kinetic arrest, i.e. the glass transition. This happens once the time scale of observation  $\tau_{obs}$  becomes much larger than the structural relaxation time  $\tau$ . Below the crossover, the liquid appears to be frozen on the time scale of observation and behaves like a solid.

The previous discussion clearly demonstrates the key role of the configurational entropy during the slowdown of dynamics that a liquid experiences upon descending in its energy landscape. The strong interplay between the temperature dependence of the configurational entropy  $S_c$  and the dynamics, i.e. the structural relaxation time  $\tau$ , and the dynamic shear viscosity  $\eta$ , can be understood in the framework of the Adams-Gibbs theory [64] (cf. section 3.5.3). According to the Adam-Gibbs theory the increase in the temperature dependence of cooperative relaxation processes is explained by the temperature variation of the size of (independent and equivalent) cooperatively rearranging regions, which in turn is determined by the available configurational entropy. Changes in  $S_c$  can thus be linked to changes in  $\tau$  or  $\eta$ , providing a quantitative explanation for the different temperature dependence of the dynamics observed among different glass formers. However,  $S_c$  is not directly accessible from experiments. The quantity usually measured in experiments is the excess entropy  $S_{ex}$  of the liquid over the

glass which is related to  $S_c$  via  $S_{ex} = S_c + S_{vib}$ , where  $S_{vib}$  denotes the excess vibrational. Despite this difficulty, it is found that the evolution of  $S_{ex}$  in general yields a good description for the evolution of the dynamics, even among different glass formers (cf. section 3.5.3). Considering that the “rate” of entropy change is given by

$$\left(\frac{\partial S}{\partial T}\right)_p = \left(\frac{\partial H}{T\partial T}\right)_p = \frac{c_p(T)}{T} \quad (2.12)$$

it is evident that a larger excess heat capacity of the liquid over the glass,  $\Delta c_p = (c_p(\text{liquid}) - c_p(\text{glass}))$  reflects a stronger ordering tendency upon cooling. The larger  $\Delta c_p(T)/T$ , the “faster” the entropy surplus of the liquid over the glass is consumed,

$$S_{ex}(T) = S_{ex}(T_{ref}) - \int_T^{T_{ref}} \frac{\Delta c_p}{T} dT \quad (2.13)$$

so that a higher sensitivity of the dynamics with respect to temperature, i.e. a higher fragility, can be expected, provided that the change in  $S_{ex}$  scales with the changes in  $S_c$ .<sup>10</sup> As the specific heat in the glass  $c_p(\text{glass})$  and crystalline state  $c_p(\text{crystal})$  are basically identical, and normally show a similar temperature dependence, often  $c_p(\text{glass})$  is substituted by  $c_p(\text{crystal})$  in equation 2.12, and the temperature dependence of the excess entropy of the liquid over the crystalline phase  $S_{ex}(T)$  is calculated based on its difference at the liquidus temperature ( $T_{ref} = T_l$ ) demanding  $S_{ex}(T_{ref}) = S_f$ , with  $S_f$  being the entropy of fusion that is obtained by integration of the melting peak(s). Alternatively, it has been proposed to leave  $S_{ex}(T_{ref})$  as a free fitting parameter that reflects the entropy of a liquid at a reference temperature  $T_{ref}$ , arbitrarily chosen as the temperature where the viscosity has a value of 1 Pa s [65].

According to these considerations the course of  $c_p$  in the liquid phase should mirror the formation of topological and chemical order on the atomic level. By forming locally favored structures (LFS) the enthalpy and entropy of the liquid are lowered, and its packing density increases. This is exemplarily shown for the case of icosahedral ordering in figure 2.21. The LFS are characterized by a lower energy  $E_S$ , a lower volume  $v_S$ , and a lower degeneracy of states  $g_S$  (higher symmetry, lower entropy). The LFS formed within the “sea” of normal liquid structures are longer-lived [50], as discussed further below, and can aggregate. However, due to their incompatibility to tile 3D space, their formation leads to geometrical frustration. Depending on their difference  $\Delta E$  with respect to the normal liquid structures, and the degree of frustration that is induced by their formation, different phase diagram including liquid-liquid transitions are obtained [39]. Obviously, the formation of LFS should go along with more pronounced increase in  $c_p$ , and more pronounced decrease in the enthalpy  $H$  and entropy  $S$  upon cooling. Indeed numerical studies [66] show that a steeper rise in the excess

---

<sup>10</sup>An assumption which generally seems to hold for many glass forming liquids.



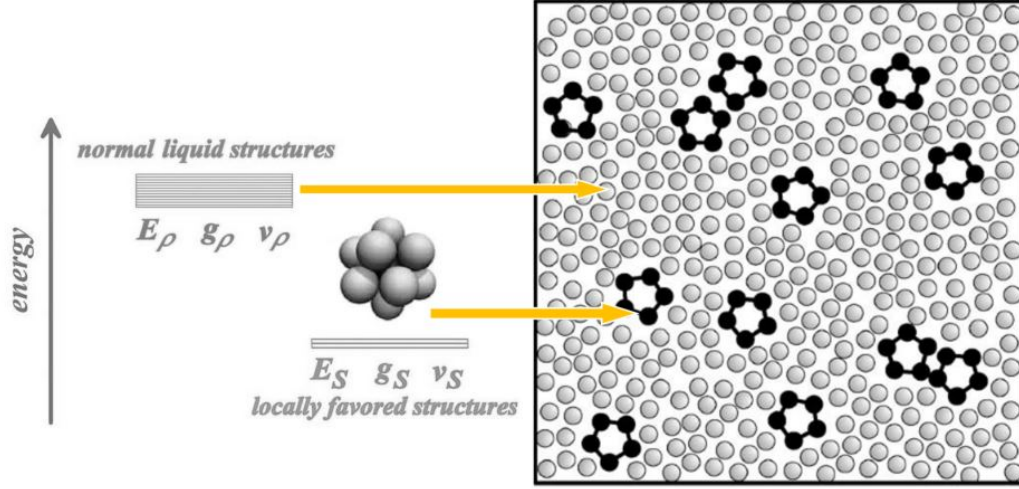


Figure 2.21: Locally favored structures vs. normal liquid structures according to Tanaka [50]: Compared to normal liquid structure, locally favored structures are characterized by lower energy  $E_S$ , lower volume  $v_S$ , and a lower degeneracy of states  $g_S$  (higher symmetry, lower entropy). The figures are taken from [50].

specific heat capacity is accompanied by a more pronounced structural ordering, in particular the formation energetically favored, low-symmetry structural motifs, e.g. icosahedral short-range ordering. This is shown in figure 2.22 and figure 2.23 for two simulated binary metallic glass formers. Upon cooling the locally favored structures such as full icosahedra ( $\langle 0,0,12,0 \rangle$ ) are formed at the expense of other energetically less-preferable structural motifs (cf. figure 2.23), leading a marked rise of  $c_p$  and a larger  $\Delta c_p$  in the deeply undercooled liquid around the glass transition (cf. figure 2.22). Accordingly, the excess entropy of the liquids is faster consumed during cooling, which according to the Adam-Gibbs theory should result in a more pronounced temperature dependence of the dynamics. Indeed, the simulations show that the  $\alpha$ -relaxation times of the individual species in the Cu-Zr alloy exhibit a more pronounced temperature dependence than in the Pd-Si alloy (cf. figure 2.24), i.e. a higher kinetic fragility.

With decreasing temperature the concentration of LFS increases, and the clusters aggregate, building string-like networks throughout the liquid structure [59, 67, 68], as shown in figure 2.25 for the case of icosahedral short range order packing (ISRO) in a simulated Cu-Zr binary metallic glass former [59]. Upon further cooling the networks expand and percolate. The strong aggregation tendency leads to a packing in a spinodal-like morphology, as shown in figure 2.26 for the case of ISRO packing in the 2D lattice [68].

The previous results imply that the formation of LFSs is accompanied by

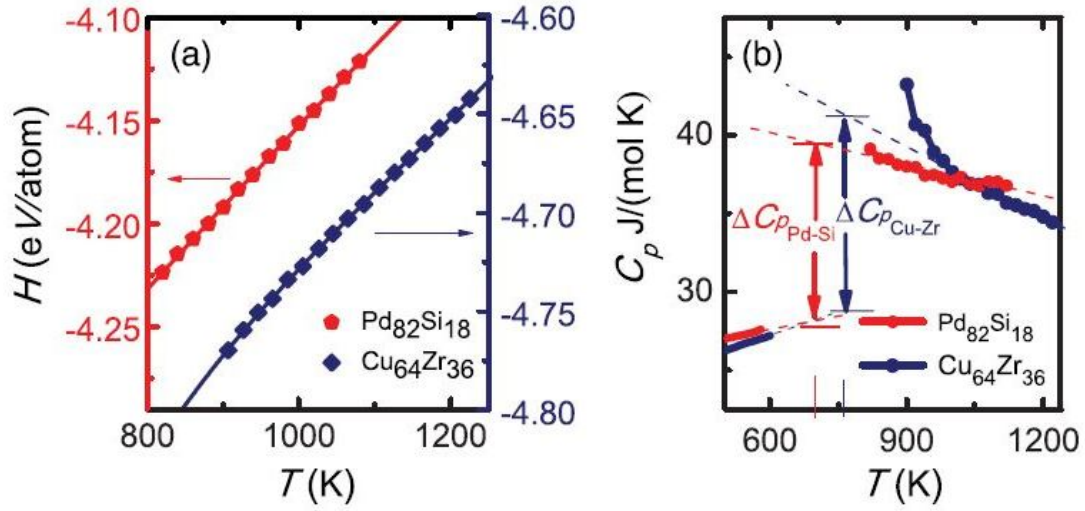


Figure 2.22: Enthalpy (left) and specific heat capacity (right) of  $\text{Cu}_{64}\text{Zr}_{36}$  and  $\text{Pd}_{82}\text{Si}_{18}$  obtained from computer simulations. The figure is taken from [66].

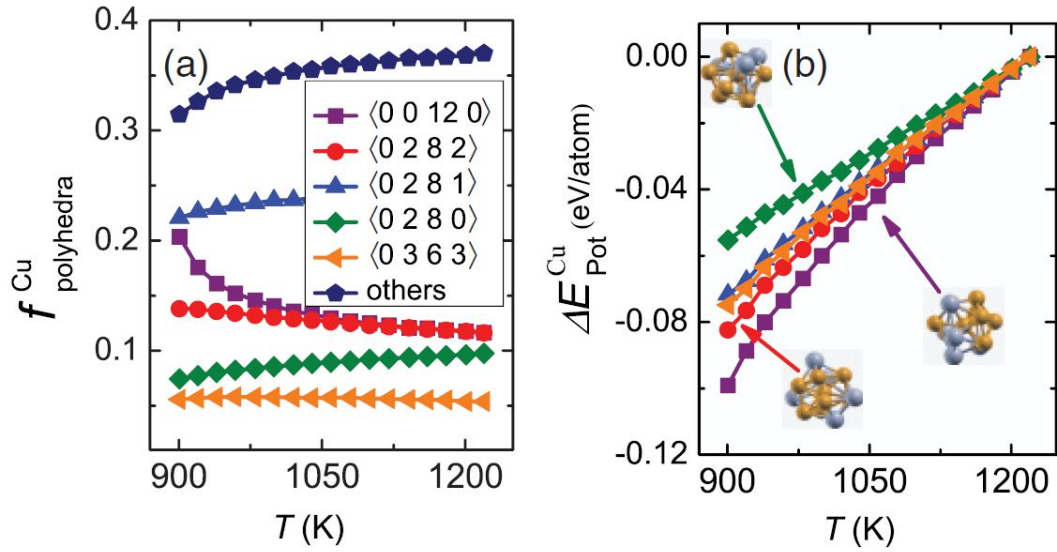


Figure 2.23: Evolution of cluster species in the  $\text{Cu}_{64}\text{Zr}_{36}$  supercooled liquid. During undercooling energetically-preferred cluster species such as icosahedra ( $\langle 0, 0, 12, 0 \rangle$ ) are formed at the expense of other cluster species (left subfigure). Due to their lower potential energy (right subfigure) and their higher symmetry, this results in a more pronounced decrease in enthalpy and entropy upon cooling. The figure is taken from [66].

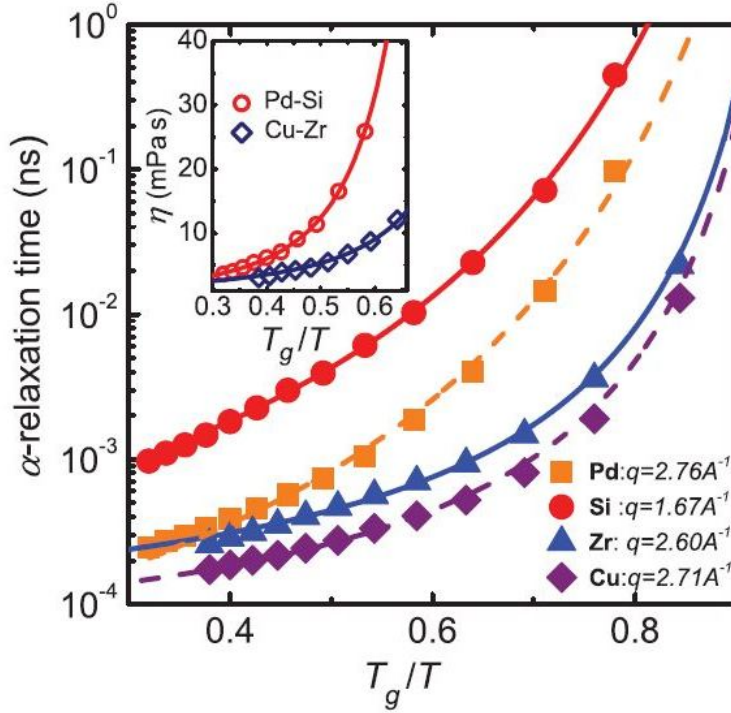


Figure 2.24:  $\alpha$ -relaxation times for  $\text{Cu}_{64}\text{Zr}_{36}$  and  $\text{Pd}_{82}\text{Si}_{18}$  obtained from computer simulation. The main figure shows the temperature dependence of the  $\alpha$ -relaxation times for each species together with VFT-fits of the data points. The inset shows the temperature dependence of the viscosity. For details on the calculation the reader is referred to reference [66]. The figure is taken from [66].

a tremendous increase in the structural relaxation time, and results in slower dynamics of the species involved. Indeed, further numerical simulation reveal that energetically preferred cluster structure of higher symmetry, e.g. full icosahedra (Voronoi index  $\langle 0,0,12,0 \rangle$ ), exhibit lifetimes that are larger than the average (cf. figure 2.27). Their lifetime further increases if the cluster belong to larger aggregates/ networks of locally favored structures. Atoms involved in stabilized clusters exhibit slower diffusion, as can be seen by the temporal evolution of their mean square displacement (MSD). Both findings indicate that aggregates or networks of locally preferred cluster species can act as islands of lower atomic mobility, implying that these networks are possible structural origins of low-mobile dynamic regions.

Once a critical packing fraction is obtained the structural relaxation time in undercooled liquids shows a stretched exponential behavior, suggesting a distribution of relaxation times as discussed in more depth in section 3.4. The latter can be seen as evidence for a dynamic heterogeneous behavior on the microscopic level [41]. Indeed, numerous computational and experimental studies indicate



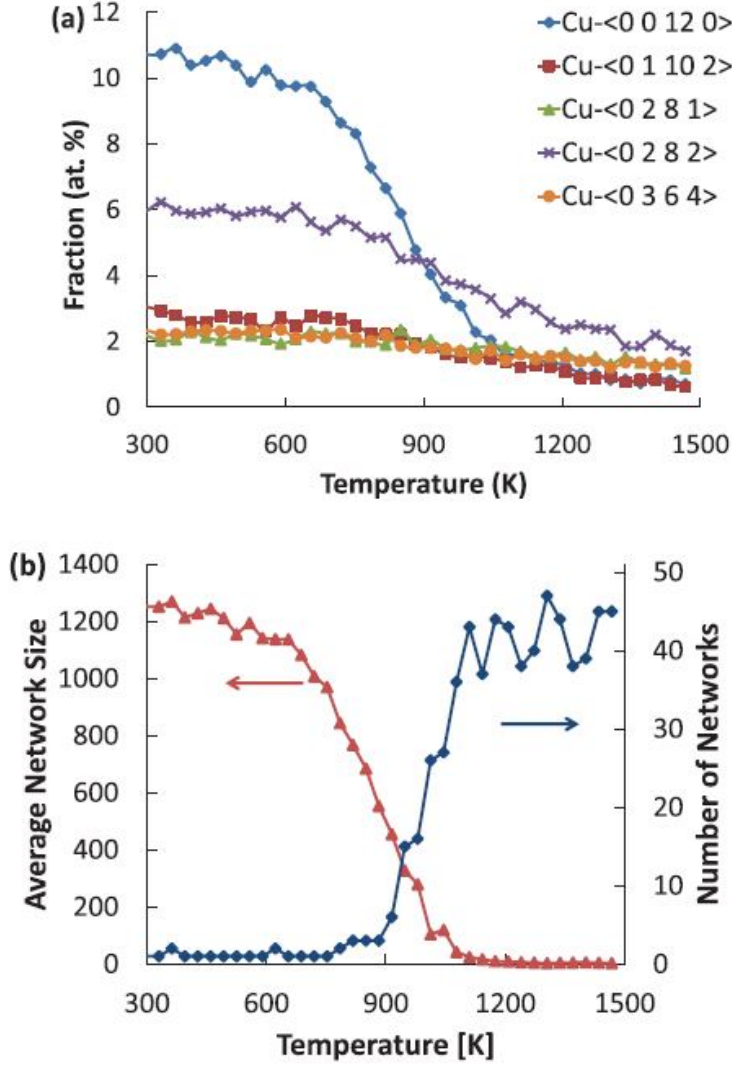


Figure 2.25: Cluster connectivity in a simulated  $\text{Cu}_{64.3}\text{Zr}_{35.7}$  binary glass former. With decreasing temperature the fraction of locally favored structures with higher symmetry (here icosahedral ordering) increases. The figure is taken from [59].

that the dynamics in supercooled liquid are spatially heterogeneous, in the sense that dynamics in some regions of the sample can be orders of magnitudes faster than the dynamics in other regions only a few nanometer away [41, 42, 69, 70], as shown in figure 2.28.

Experiments suggest that the characteristic length scale is about 5 to 20 molecular diameters around the glass transition [69]. Recently, direct experimental visualization of the spatially heterogeneous dynamics as a function of temperature in the supercooled liquid state of a metallic glass was provided by

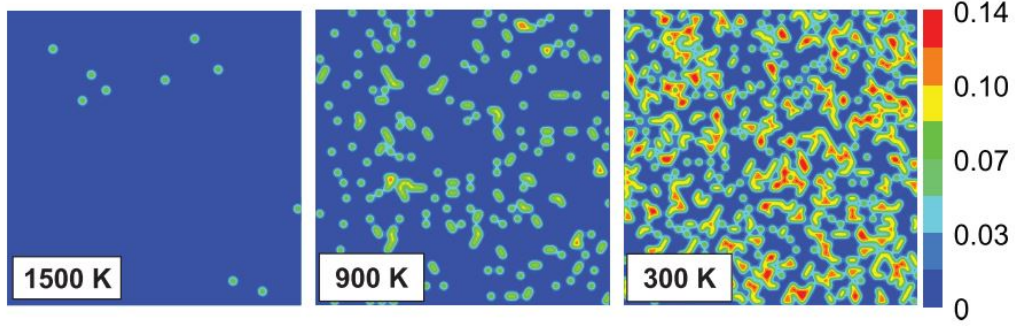


Figure 2.26: Morphology of icosahedral short range order (ISRO) packing density in the 2D lattice in a simulated  $Cu_{65}Zr_{35}$  binary metallic glass former. With decreasing temperature the amount of icosahedral packed clusters increases. The clusters aggregate building a spinodal-like network of ISRO packing density. The figure is taken from [68].

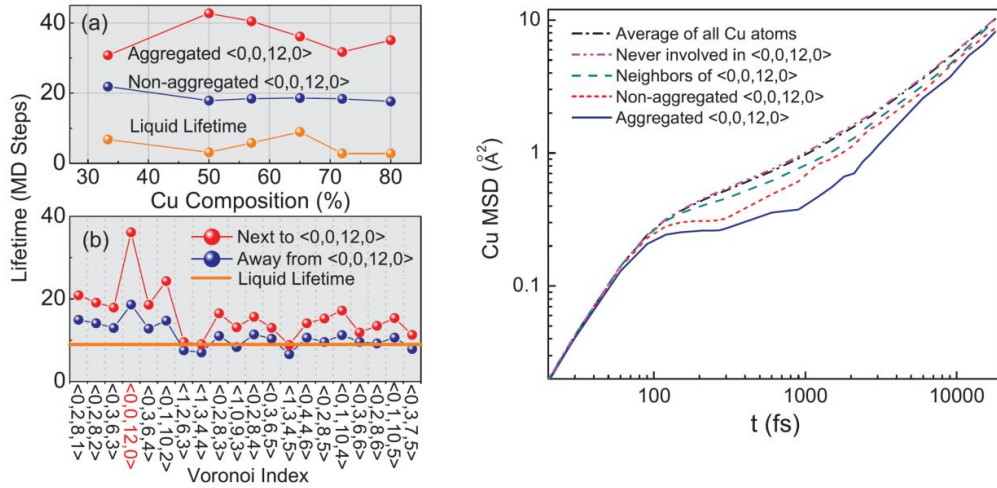


Figure 2.27: Left: Lifetime of cluster species in a simulated Zr-Cu metallic glass. Energetically preferred cluster structures of higher symmetry such as full icosahedra  $\langle 0,0,12,0 \rangle$  shown an increased lifetime compared to the average liquid structure. In case that the icosahedra are aggregated, their lifetime is even increased. Right: Mean square displacement of Cu atoms in different environments. Compared to the average, Cu atoms involved in full icosahedra show slower diffusion dynamics, in particular if they belong to aggregates. The figures are taken from [68].

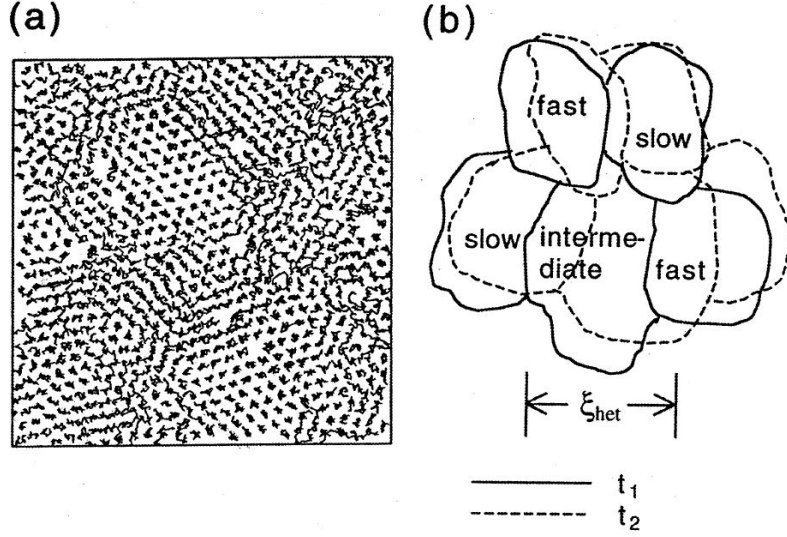


Figure 2.28: Spatially heterogeneous dynamics in supercooled liquids. Left: Overlaid maps of particle positions at various times from a two-dimensional simulation of soft disks. Right: Schematic illustration of dynamic heterogeneities near  $T_g$ . The spatial extension of these regions  $\eta_{het}$  is typically a few nanometers. The regions are not static but evolve in time. The figure is taken from [41].

[71]. Using electron correlation microscopy with sub-nanometer resolution on nanowires of a Pt-based bulk metallic glass, the authors were able to determine spatial maps of the structural relaxation time in the deeply undercooled liquid at temperatures around the glass transition. The results are shown figure 2.29). Near-surface regions exhibit substantially faster dynamics than regions in the bulk. With increasing temperature the average relaxation time decreases as expected and its temperature dependence is found to be in reasonable agreement with the Adam-Gibbs theory, the inhomogeneous mode-coupling theory as well as the random first order theory [71]. The maps further reveal that the spatial extension of the dynamic heterogeneities increases with decreasing temperature. Around  $T_g$  some of the less mobile domains reach spatial extension up to 10 nm. The average correlation length increases from 0.8 nm at 523 K to about 1.4 nm at 507 K ( $T_g$ ).

The spatial extension derived from the structural relaxation time maps are in good agreement with the spatial extension of medium-range order expected from the efficient cluster packing model of multicomponent bulk metallic glass formers [57], suggesting a direct link between the formation of medium-range order and dynamic heterogeneities. This is in line with earlier numerical simulations performed on polydisperse 2D colloidal systems [42]. However, it remains open whether the dynamic heterogeneities observed indeed originate from

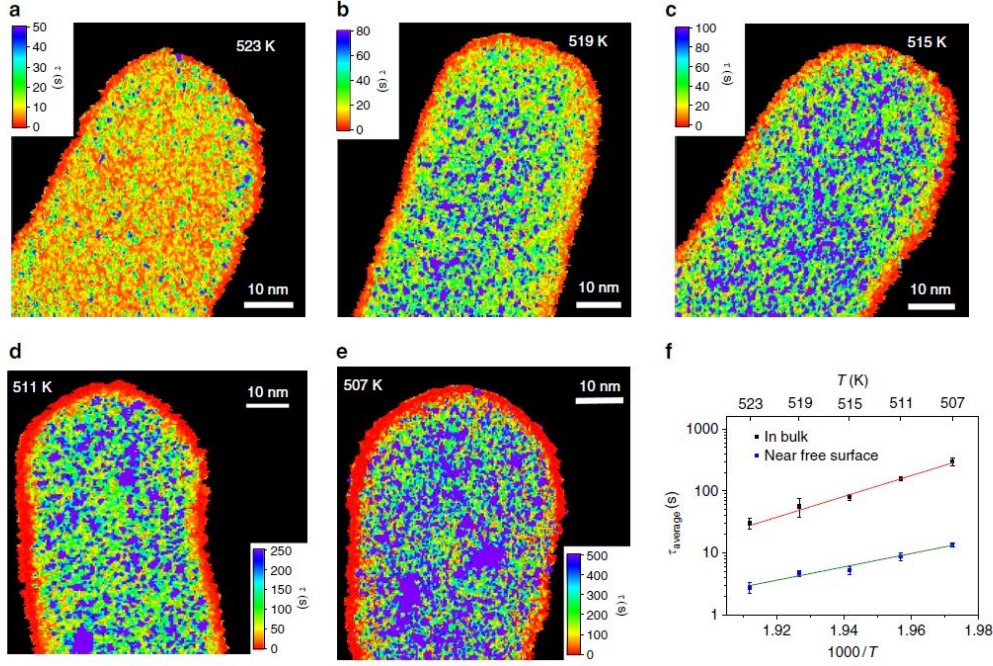


Figure 2.29: Spatial maps of the structural relaxation time in a Pt-based metallic glass nanowire in the deeply supercooled liquid region near the glass transition ( $T_g = 507\text{K}$ ). The experiments reveal the existence of domains with varying relaxation time at the nanometer scale. With increasing temperature the average time in the supercooled liquid decreases as expected as shown in the subfigure f. The spatial extension of the dynamic heterogeneities is found to increase with decreasing temperature. The average correlation length increases from 0.8 nm at 523 K to about 1.4 nm at 507 K (results not shown here). The figure is taken from [71].

time-evolving structural heterogeneities in the nanowires. If so, low-mobile domains should correspond to networks of atomic clusters with increased lifetime compared to the average (locally favored structures), while high-mobile regions should be characterized by higher concentrations of short-life clusters (normal liquid structure).

# Chapter 3

## Liquid dynamics

Liquids at temperatures around their melting points are dense fluids with densities close to that of solids. They are almost incompressible, i.e. they retain a nearly constant volume independent of pressure.<sup>1</sup> The kinetic energy of the particles is of the order of the potential energy, enabling particles to frequently change their positions and move around in their environment. The mean free path of a particle  $\lambda$ , i.e. the distance that a particle can move without interacting with another, is about the size of the particles themselves. A “travelling” particle thus constantly experiences collisions with other particles in its surrounding in which momentum and energy are exchanged. At very short time scales and distances, the dynamics are determined by classical or quantum mechanics (deterministic mechanics). On larger time scales and distances, the particles motion can be sufficiently well described by appropriate stochastic models, e.g. random walk, without invoking details on the individual collisions that a particle has experienced along its path. At even larger distances and times scales, the stochastic nature becomes indistinct and the hydrodynamics can be described by continuum descriptions such as the Navier-Stokes equation or the diffusion equation.

### 3.1 Diffusion and the Nernst-Einstein-Equation

Diffusion denotes the molecular transport due to a gradient in concentration or more precisely a gradient in the chemical potential. The diffusion equation relates the rate of changes in the local concentrations of particles to its spatial distribution. According to Fick’s second law the change in concentration with time,  $\partial c/\partial t$  is proportional to the curvature of the concentration profile  $\partial^2 c/(\partial x)^2$ , i.e.

$$\frac{\partial c}{\partial t} = D \frac{\partial^2 c}{\partial x^2} \quad (3.1)$$

---

<sup>1</sup>In fact, liquids are compressible to a very small degree. Metallic liquids around their melting points have compressibilities of the order of  $10^{-11} \text{ Pa}^{-1}$  to  $10^{-10} \text{ Pa}^{-1}$  [72].

The proportionality constant is called the *diffusion constant* or *diffusivity*  $D$ . It is a measure of how fast matter is transported by the stochastic motion of the particles, and therefore determines how fast fluctuations, such as local concentration peaks, will cease with time. The diffusion equation describes the mass transport without focusing on the details of the interaction between the individual particles or the individual trajectories of the particles. What counts is the average outcome of these processes, usually described by the *mean square displacement*  $\langle r^2 \rangle$  that a particle has traveled in a given time. A statistical mechanical treatise shows that

$$D = \frac{\langle r^2 \rangle}{6t} = 1/3 \int_0^\infty \langle v(t)v(0) \rangle dt \quad (3.2)$$

Equation 3.2 states that  $D$  is a measure of how strong a particle's velocity at time  $t$  is correlated to its initial velocity, and makes clear that  $D$  is close related to the mobility of a particle in its surrounding.

From the Langevin equation, which describes the dynamics of large (Brownian) particles suspended in a continuum fluid (small particles) as a consequence of randomly fluctuating force  $F_r(t)$  and a systematic frictional force  $F_f = \zeta v$ , it can be inferred that the diffusion constant is coupled to the friction coefficient  $\zeta$  via  $D = \frac{kT}{\zeta}$ . The larger is the friction that a particle experiences when moving, and the lower is the temperature, the lower is its diffusivity. In the presence of a force  $F_+$  that drags the particle, a stationary motion (constant drift  $v$ ) of the particle requires  $F_+ = F_f = \zeta v$ . Defining the mobility as  $\mu = F_+/v$ , it follows  $\mu = 1/\zeta$  which finally leads to

$$D = \mu kT \quad (3.3)$$

Equation 3.3 is referred to as the *Nernst-Einstein equation* and states that the atomic mobility  $\mu$  is directly proportional to the diffusivity divided by the temperature.

## 3.2 Viscosity

Viscosity is a measure of the fluidity of a liquid and quantifies its resistance to flow. Like the diffusivity, the viscosity is sensitive to variations in the outer conditions such as temperature, pressure, or the density, and further depends on the rate at which the liquid is deformed.<sup>2</sup> The lower is the temperature, the larger is the viscosity and vice versa. The viscosity and its temperature dependence have a tremendous influence of how readily a glass can be formed from the liquid state. Studying viscosity and its temperature dependence is therefore a key aspect in understanding glass formation.

---

<sup>2</sup>For dense packed systems like metallic liquids the effect of pressure is relatively small compared to changes in temperature or density.

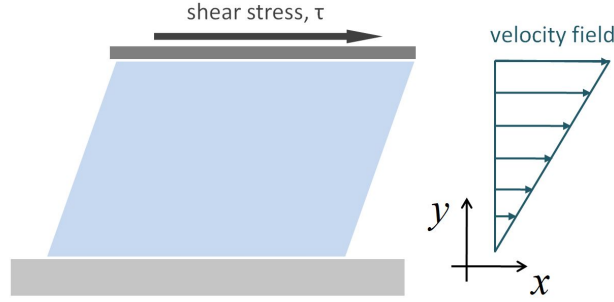


Figure 3.1: Dynamic shear viscosity. Shearing a liquid between two plates (upper plate: moving, lower plate: stationary) requires a force (shear stress) whose magnitude depends on the shear velocity and on the viscosity of the liquid.

The dynamic shear viscosity  $\eta$  is defined as<sup>3</sup>:

$$\tau_{xy} = \frac{F_x}{A_y} = \eta \frac{dv_x}{dy} = -\eta \dot{\gamma} \quad (3.4)$$

The shear viscosity of a liquid relates the shear force  $F_x$  required to move a plate of area  $A_y$  on top of a fluid film of thickness  $y$  to the velocity  $v_x$  at which the plate is moved. This is shown in figure 3.1 for the case of a linear velocity field, i.e. a constant velocity gradient  $v/y$  throughout the different layers of the liquid. More accurately  $\eta$  couples the shear stress  $\tau_{xy} = F_x/A_y$  to the velocity gradient  $dv_x/dy$ , i.e. the shear rate  $\dot{\gamma}$ . The faster the plate is moved, the larger is the velocity gradient throughout the liquid layers and thus the larger is the force needed to displace the plate. The dynamic shear viscosity can be viewed as a measure of the friction between the different liquid layers. A closer inspection reveals that  $\tau_{xy}$  represents the momentum transfer of the component  $x$  with respect to  $y$  showing that equation 3.4 is in fact a transport equation. Just like a temperature gradient induces a transfer of heat, or a concentration gradient induces a transport of matter, the velocity gradient between the different layers induces a transfer of momentum. Accordingly,  $\eta$  is in fact the transport coefficient for the momentum - just as the diffusion constant  $D$  is the transport coefficient for mass, and the thermal conductivity  $\lambda$  is the transport coefficient for heat.

### 3.3 The Stokes-Einstein relation

The internal friction and the atomic mobility are related to the diffusivity via the Nernst-Einstein relation (see equation 3.3). To find an analytical expression that relates the viscosity to the diffusivity, a hydrodynamic estimate of the friction

<sup>3</sup>The dynamic shear viscosity is discriminated from the volume viscosity (bulk viscosity) which is a measure of internal friction of liquids under isostatic deformation.

coefficient is needed. According to Stokes a rigid sphere with diameter  $d$  that moves through a stationary fluid at constant velocity  $v$  experiences a friction force  $F_f = -3\pi\eta vd$ . Inserting this into the equation 3.3 yields

$$\eta = \frac{kT}{3\pi dD} \quad (3.5)$$

Equation 3.5 is referred to as the *Stokes-Einstein relation*. It relates the viscosity of a liquid to the diffusive motion of the particles. Although derived for larger microscopic particles that move in a fluid of continuum properties, the SE-relation (surprisingly) well describes the molecular transport of particles whose size is of the order of the size of the particles constituting the surrounding fluid. Its predictions are reasonable accurate even for self-diffusion. This is mostly true for liquids in their thermodynamic stable regimes, i.e. above their melting points. The validity of the SE-relation is remarkable considering that, besides the approximations made for its derivation, it relates a quantity describing the single particle transport on the atomic scale to a quantity describing the macroscopic transport of momentum due to the collective motion of particles. However, there is growing experimental evidence that under certain circumstances  $\eta D/kT$  is no longer independent of temperature. The origin of this “breakdown” of the SE-relation is still a subject of debate [73–77]. Often the Stokes-Einstein relation holds in the equilibrium state but breaks down in the metastable state [73, 76]. It has been reported that in densely packed metallic melts the SE relation breaks already in the vicinity to the melting temperature [74, 75]. Recently, a violation of the SE-relation above the melting points was also observed for tetrahedrally-bonded PCM alloys [77], indicating that a densely packed structure is not a prerequisite for a breakdown of the SE-relation. It is proposed that the breakdown occurs as a consequence of the formation of dynamical heterogeneities which in turn might be linked to the occurrence of density fluctuations or structural heterogeneities [73]. These latter may arise when the liquid approaches a critical point or an underlying phase transition [77].

### 3.4 Structural relaxation and aging

When a system in equilibrium is disturbed by outer influences it moves out of equilibrium and a certain time is required until the equilibrium is restored. The disturbance may be caused by external fields or forces that are applied and/or switched off, or can be a consequence of a rapid temperature changes. Provided that the disturbance from equilibrium is small in the sense that it does not “destroy” its fundamental properties, the changes imposed to the system are reversible. Once the perturbing forces are removed, the system evolves back,



aiming to restore its initial equilibrium state.<sup>4</sup> This process is called *relaxation*. The characteristic time constant describing how fast the system moves back towards equilibrium is called the *relaxation time*  $\tau$ . An out-of-equilibrium system such as a glass therefore shows a natural dynamic evolution of its structure and properties towards its equilibrium states, a phenomenon commonly referred to as *aging*. Obviously, the relaxation rate is strongly coupled to the mobility of the structural units. The lower is the temperature, the lower is the mobility of the individual particles, and the larger is the cooperativity required for a structural rearrangement to take place. Depending on the temperature regime, relaxation thus can proceed by individual or collective atomic motion. In the deeply supercooled liquid or the glassy state, structural relaxation and aging occurs via cooperative motion involving numerous particles (cf. section AGT).

### Structural relaxation time and viscosity

Considering a liquid as a viscoelastic material, whose rheological behavior can be idealized by a Maxwell element, the (shear) viscosity  $\eta$  is proportional to average relaxation time  $\tau$ .

$$\tau = \frac{\eta}{G_{\infty}} \quad (3.6)$$

Here  $G_{\infty}$  denotes the high-frequency shear modulus, characterizing the response in the limit of an infinite loading frequency. Equation 3.6 is the so-called *Maxwell relation* and can be used to convert viscosity data into relaxation times.

### Relaxation, aging and stretched exponential decay functions

Let  $\Phi(t)$  be the quantity of interest in a system out-of-equilibrium and  $\Phi_{eq}$  be its equilibrium value. At the start of observation,  $\Phi$  has a “distance”  $\Delta\Phi(0) = \Phi(0) - \Phi_{eq}$  from equilibrium. Left at itself, the system has a natural tendency to evolve back into its equilibrium, so the distance  $\Delta\Phi(t) = \Phi(t) - \Phi_{eq}$  will cease with time. If the rate of the change  $\partial\Phi(t)/\partial t$  at any moment  $t$  is proportional to the current perturbation  $\Delta\Phi(t)$ , a simple exponential decay of can be expected  $\Delta\Phi(t) = \Delta\Phi(0) \exp(-t/\tau)$ . The quantity  $\Phi$  may describe for example, the temperature of a system, the charge of a capacitor during charging or discharging, the strain or stress during mechanical relaxation, or the viscosity (or even the average structural relaxation time itself) when the system has been subjected to a sudden temperature change.

In the majority of cases the relaxation or aging behavior of glass-forming liquids does not follow the simple exponential decay behavior described above but shows stretched or compressed relaxation dynamics that can modeled by a

---

<sup>4</sup>The initial and the final state may not be same microstate, however they both belong to the ensemble of equilibrium states, and in this sense can be viewed as equal.

stretched exponential decay function,

$$f_{\beta,\tau}(t) = \frac{\Delta\Phi(t)}{\Delta\Phi(0)} = \exp\left(-\left(\frac{t}{\tau}\right)^\beta\right) \quad (3.7)$$

where the constant  $\beta$  is the so-called *stretch exponent*, usually determined from data fits. Equation 3.7 is commonly referred to as the *Kohlrausch-Williams-Watts* (KWW) equation. Established by R. Kohlrausch [78], it was later applied by G. Williams and D.C. Watts [79] to explain the experimentally observed dielectric spectra of polymers. Up to date the KWW equation is the most prominent equation used to quantify the non-exponential relaxation behavior that is observed for many disordered systems, i.e. liquids, supercooled liquids and glasses.

Even though the KWW equation is actually an empirically motivated function its use is justified by its ability to properly describe the experimentally observed decay of many physical properties of disordered systems. The stretched exponential character ( $\beta < 1$ ) is considered to arise from a continuous sum of exponential decays, reflecting a distribution (spectrum) of relaxation times in the system (cf. figure 3.2 and figure 3.3).

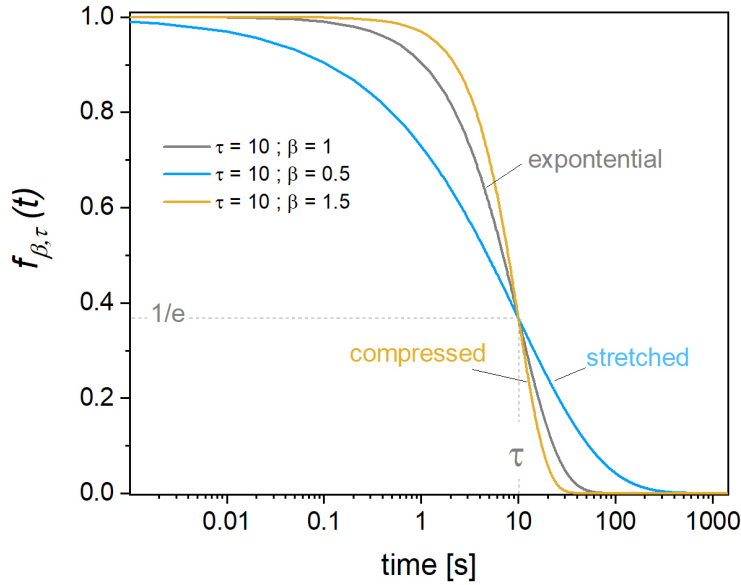


Figure 3.2: Comparison of different aging dynamics: exponential ( $\beta = 1$ ) vs. stretched exponential ( $\beta < 1$ ) vs. compressed ( $\beta > 1$ ).

Whether this dynamic heterogeneity originates from structural inhomogeneities is still a subject of debate. If so, the connection might be understood as follows. Assuming that the local dynamic response, i.e. the relaxation behavior, is linked

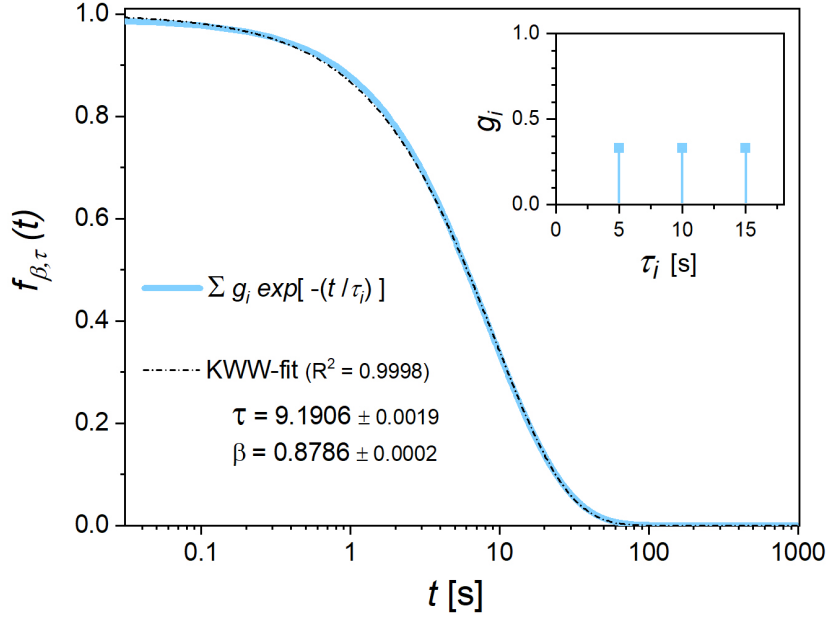


Figure 3.3: Stretched exponential vs. spectrum of relaxation times. The decay behavior of a fictive system composed of dynamic units that each follow a simple exponential decay behavior with a characteristic time constant  $\tau_i$  (blue line) can equally well modeled with a stretched exponential behavior (dashed-dotted line). In real systems the distribution of relaxation times  $g_i$  is more complex and rather continuous. However, even in this simple case it is seen that a weighted sum of exponential decays is virtually identical to a stretched exponential behavior.

to the local structural configuration, in the sense that the latter determines the activation energy barrier for a structural rearrangements, the distribution of relaxation times  $P[\tau(x)]$  implies a spectrum of activation energies  $P[E_A]$ , recognizing that  $\tau_i = \tau_0 \exp(-E_{A,i}/kT)$ . This is in agreement with the finding that in particular disordered condensed systems often show a non-exponential relaxation behavior, while structural reconfiguration mechanisms in ordered structures usually have well-defined energy barriers and thus obey exponential relaxation dynamics.

Recent x-ray photon correlation spectroscopy (XPCS) studies reveal that the decay of density correlations (or more accurately the decay of the autocorrelation of intensity speckles), at length scales corresponding to the maximum of the first sharp diffraction peak, can exhibit stretched ( $\beta > 1$ ) or compressed relaxation dynamics ( $\beta < 1$ ) [80–83], depending on the constitution of the system and its temperature. This is interpreted in terms of a transition from diffusive motion in the liquid state towards ballistic atomic motion mediated by stresses in the glassy state [80–83]. Furthermore, latest XPCS studies reveal that relaxation processes

in glasses not necessarily follow a simple continuous, monotonic decrease but occur as a series of relaxation events separated by still periods, a phenomenon referred to as *intermittent aging dynamics* [83]. Long term annealing studies below the glass transition also show that enthalpy or volume relaxation can occur in multiple steps. In this case the response function of the system can be modeled as a sum of individual (stretched) exponential decays [84]. This observation has been related to the observation that the diffusion of different species is decoupled in deeply undercooled liquids or metallic glasses [76, 85]. In general smaller atoms have lower activation energies for diffusive motions and thus retain higher mobility (diffusivities) at lower temperatures [76]. Phenomenologically, this can be anticipated by the conception that smaller atoms can maintain their mobility even in the presence of a slower (backbone-) structure composed by the larger species [76, 86]. A faster decay can be expected for any relaxation processes whose mechanisms requires mainly the motion or rearrangement of the smaller species. On the other hand, processes that require strongly collective motion, e.g. viscous flow, should rather be determined by the mobility of the slower species. In this conception the viscous slowdown and the structural relaxation time  $\tau$  would be determined by the formation of slower structural subsystems during cooling.

### Relaxation spectra - $\alpha$ vs. $\beta$ relaxation

In dense systems, the eradication of perturbations often requires a collective motion of particles. Depending on the structural architecture of a substance, multiple relaxation mechanism can occur. Different relaxation processes corresponding to translation, rotation, and internal motion can take place. The *structural relaxation time* characterizes the “slow” processes on the molecular scale involving diffusional and cooperative motion. It is directly related to the viscous flow and often referred to as the  *$\alpha$ -relaxation time*,  $\tau_\alpha$ , in order to discriminate it from the  *$\beta$ -relaxation time*, which is a measure of faster molecular processes. The discrimination is based on their occurrence in the frequency domain (see figure 3.4). Historically,  $\beta$ -relaxations were first found in internal friction measurements in polymer glasses and assumed to originate from rotations of side-chains or functional groups of polymers [87]. Later on it was shown by Johari and Goldstein [88, 89] that even polymers without side chains or internal degrees of freedom exhibit  $\beta$ -relaxations, implying that  $\beta$ -relaxations may not necessarily involve intramolecular motions but can also result from motions of entire molecules [87]. Relaxation studies on supercooled metallic liquids and metallic glasses show that even atomic systems possess a multimodal distribution of relaxation spectra. Up to now a full understanding on the atomistic origin of  $\beta$ -relaxations in metallic glasses and liquids is missing [87]. Most commonly relaxation spectra are determined from dielectric spectroscopy. A schematic relaxation spectrum of a glass forming liquid as obtained from dielectric spectroscopy is shown in figure 3.4 taken from reference [87]. The conductivity of metallic liquids or glasses

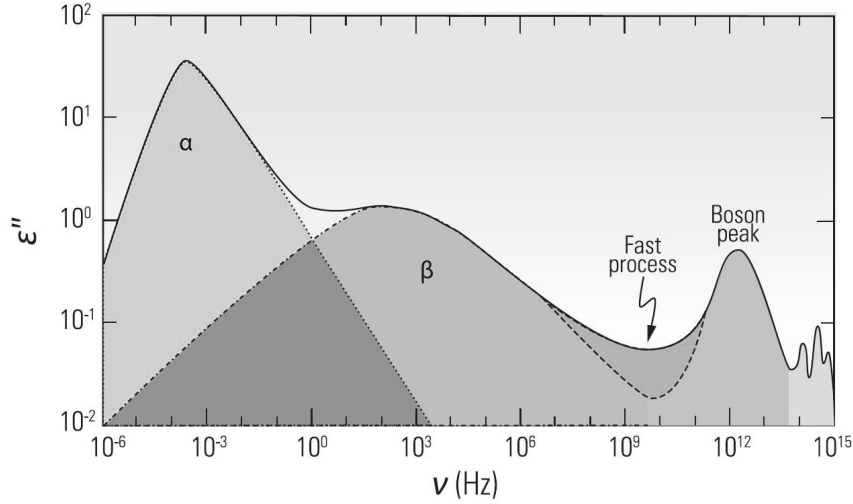


Figure 3.4: Schematic dielectric spectrum of relaxation dynamics of glass-forming liquids taken from [87].

prevents to apply the dielectric method, and thus other techniques are used to study their relaxation behavior. The relaxation spectra of metallic systems in the glassy or deeply undercooled liquid state are usually determined using dynamical mechanical analysis (DMA) or differential scanning calorimetry (DSC) [87, 90]. At higher temperatures around the melting point, the relaxation times are of the order of picoseconds. This ultrafast time or frequency domain can be probed using quasielastic neutron scattering by studying the decay behavior of the intermediate scattering function  $S(q, t)$  (see e.g. [75]).

The atomistic mechanism of  $\beta$ -relaxations is still unclear and its discovery is considered to be one of the most challenging issues in glass physics [87]. Apart from the question of how many actual degrees of freedom are involved, controversy remains about the exact nature of  $\beta$ -relaxations, i.e. whether they occur homogeneous or inhomogeneous, whether they occur cooperatively or non-cooperatively, if they are related to translational or reorientational motion<sup>5</sup>, and what is their corresponding length scale (nearest neighbors to several tens of nanometers)[87]. According to Stillinger [91]  $\beta$ -relaxations correspond to atomic reversible rearrangements between neighboring potential energy minima (basins) in the potential energy landscape, while the slower  $\alpha$ -relaxations are considered as irreversible transitions from one megabasin to another resulting from a series of *beta*-relaxation in cooperative manner (cf. figure 3.5). The connection to the mechanisms of plastic deformation in metallic glasses, (shear transformation zones (STZs) and plastic flow), is established by the cooperative shear model (cf. reference [87] and the references therein).

Although the actual underlying atomic mechanisms remains elusive, several

---

<sup>5</sup>The latter is obviously not directly applicable to atomar glass formers such as metallic

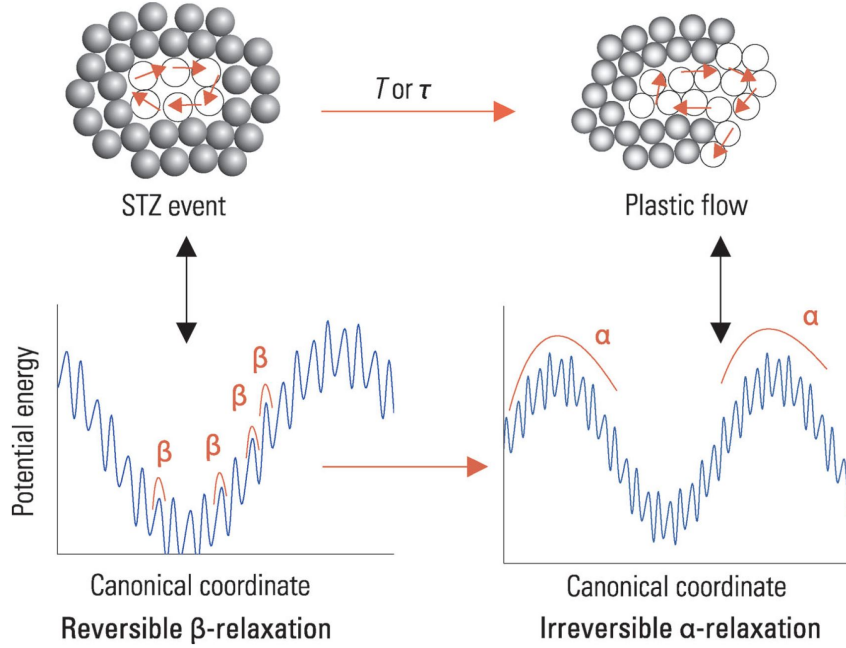


Figure 3.5: An energetic view of  $\alpha$ - and  $\beta$ -relaxations. The reversible  $\beta$ -relaxations are considered as a transition between neighboring local minima (basins), while the  $\alpha$ -relaxation is regarded as irreversible transition between megabasins in the potential energy landscape resulting from a series of *beta*-relaxations in cooperative manner. The connection to shear transformation zones (STZ), i.e. local regions of reduced density and stiffness, and to plastic flow is made based on the activation energy of the distinct mechanisms. The figure is taken from [87].

phenomenological models have been proposed. For example, Tanaka proposed that  $\alpha$ -relaxations correspond to the creation and annihilation of metastable solid-like islands in supercooled liquids, while  $\beta$ -relaxations correspond to a kind of restricted, jump-like, reorientational, and vibrational motion within these islands [40]. A similar conception was proposed by Stevenson and Wolynes who observed that the  $\alpha$ -relaxation occurs through activated events involving compact regions, while the  $\beta$ -relaxations are governed by more ramified, string-like clusters of particles [92]. Based on this Samwer et al. suggested that  $\beta$ -relaxations can be considered as string of atoms moving back and forth reversibly and cooperatively within the confinement of the surrounding elastic matrix [87]. In all of these models the presence of  $\beta$ -relaxations requires the formation of a “elastically rigid” or “solid-like” local surrounding that confines cooperative atomic motions. This suggests a critical temperature below which  $\beta$ -relaxations can exist at all.

---

glasses, questioning the existence of a universal mechanism among all types of glass formers.

Around the melting point, the  $\alpha$ - and  $\beta$ -relaxation coincide (see figure 3.6), implying that there is only a single relaxation mechanism in the equilibrium liquid [38], while at lower temperatures a decoupling of the  $\alpha$ - and  $\beta$ -relaxation is observed. Below a critical temperature  $T_c$  the  $\alpha$ -relaxation time deviates from its initial trend and exhibits a stronger than exponential, non-Arrhenius temperature dependence, while the  $\beta$ -relaxation persist on its initial trend maintaining Arrhenius behavior. The tremendous increase of the structural relaxation time  $\tau_\alpha$  with decreasing temperature reflects the increasing incapability of the system to perform collective structural rearrangements. Macroscopically this manifests as an enormous increase in the resistance to flow, i.e. the viscosity. Ultimately, the  $\alpha$ -relaxation vanishes and the supercooled liquid transforms into a glass. In the solid glass the  $\alpha$ -relaxation is frozen and only the  $\beta$ -relaxations remain. The persistence of  $\beta$ -relaxations down into the glassy state is a direct consequence of their lower activation energies arising from their specific atomistic mechanism. Experimentally it is found that  $E_\beta = 26(\pm 2)RT_g$  suggesting a close correlation between  $\beta$ -relaxations,  $\alpha$ -relaxations, and the glass transition [87].

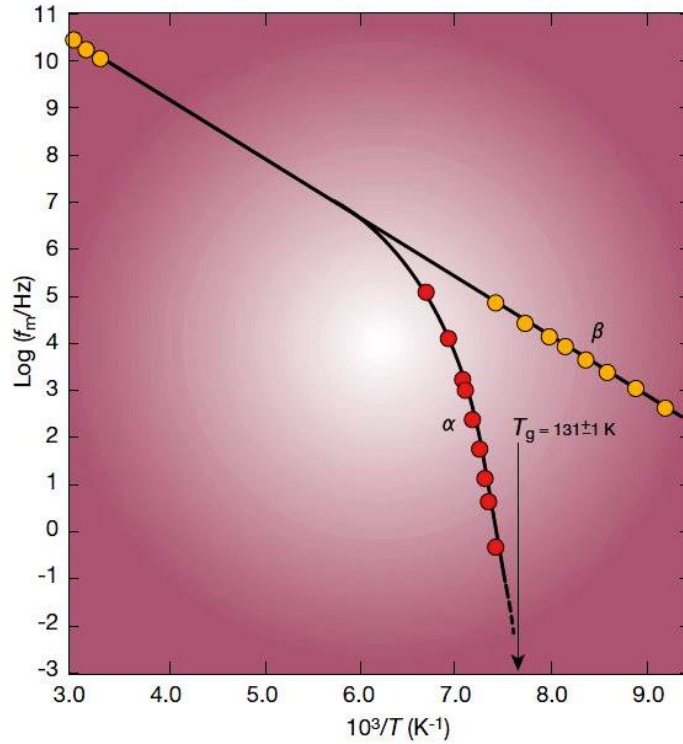


Figure 3.6: Decoupling of relaxation times. Temperature dependence of the peak dielectric relaxation frequency of the glass-forming mixture chlorobenzene/cis-decalin is shown. The figure is taken from [38].

## 3.5 The Viscous Slowdown and Fragility

Viscous flow in dense systems is a highly cooperative process. With decreasing temperature, the energy and mobility of the particles decreases. This goes along with a dramatic increase in the structural relaxation time and viscosity. The viscous slowdown can vary significantly between different liquids. The sensitivity of the dynamics with respect to temperature is treated by the concept of fragility, enabling a quantification among different types of glass formers. Its origin is among the most intensively studied topics in the field of liquid and glass science and its connection to the thermodynamics and structure is far from being fully understood. This is particularly true for the question of what leads to the drastic decrease in the atomic mobility that is observed during undercooling. In this section, some of the most common approaches and conceptions regarding the connections between structure, thermodynamics and dynamics are discussed. Rather than giving a complete overview of this subject, which would be out of the scope of the current work, the aim is to provide the reader with the underlying conceptual ideas that are relevant for the interpretation and discussion of the results obtained in this work.

### 3.5.1 Fragility

Viscous flow can be regarded as a stress-mediated thermally activated process. According to the *transition state theory*, the rate  $r$  of any thermally activated process is determined by the probability that the fundamental structural units (atoms, molecules, particles,...) can overcome energetic barriers. After Boltzmann this probability is proportional to the factor  $\exp(-E_A/kT)$ . Consequently, in case that  $E_A$  remains constant with  $T$ , the structural relaxation time  $\tau$  is expected to follow a simple exponential (Arrhenius) behavior  $\tau = \tau_0 \exp\left(\frac{E_A}{kT}\right)$ . In this case, plotting  $\log(\tau)$  over  $T^{-1}$  should yield a straight line with a slope  $E_A/k$ . In fact, the viscous slowdown of most, if not all<sup>6</sup>, liquids occurs “faster” than exponential. The non-Arrhenius behaviour can be understood in terms of a temperature dependent activation energy  $E_A(T)$  that increases with decreasing temperature.<sup>7</sup>

Measurements of the rheology, relaxation time or diffusivity show that the temperature dependence of dynamics varies considerably between different liquids. For instance, oxide glass formers, such as  $SiO_2$  or  $GeO_2$ , in general show a much less pronounced temperature dependence than organic liquids, like toluene or o-terphenyl, while metallic glass formers normally show an intermediate strong temperature dependence (cf. figure 3.8).

---

<sup>6</sup>Even the strongest liquids such as  $SiO_2$  show a slight deviation from Arrhenius behavior.

<sup>7</sup>Note that, the apparent activation energy graphically corresponds to the instantaneous slope  $E_A(T) = \partial \ln(\eta) / \partial (1/T)$  in the Angell plot (figure 3.7).



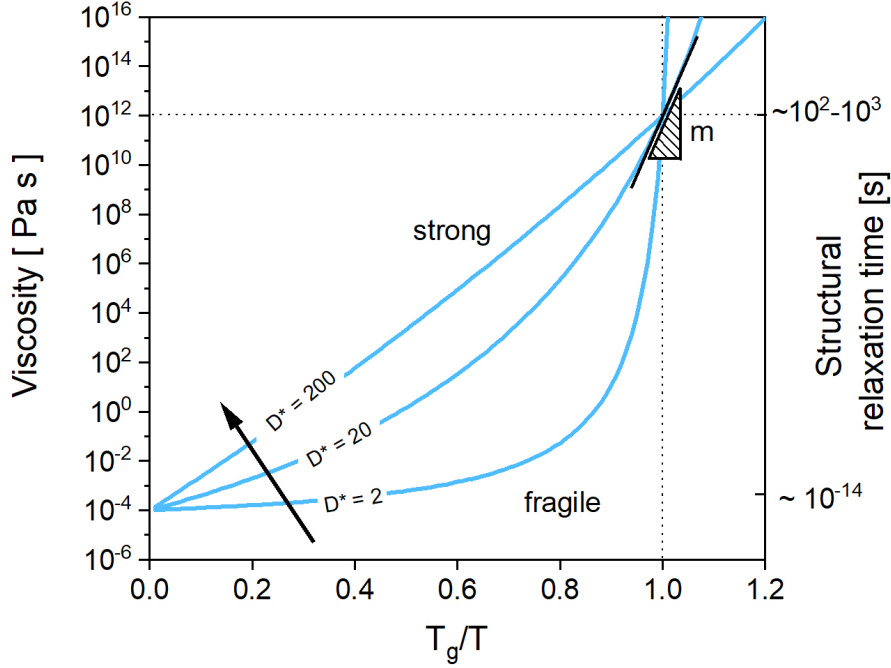


Figure 3.7: Schematic illustration to visualize the concept of fragility. The dynamic properties, e.g. the viscosity or relaxation time, are logarithmically plotted versus the inverse of temperature scaled by the glass transition temperature,  $T_g/T$ . Note that this graphical representation is essentially a  $T_g$ -scaled Arrhenius-plot - in the glass community commonly referred to as “Angell-plot”. The different sensitive of the dynamics between different glass formers can be quantified in terms of the fragility parameter  $D^*$  in the VFT equation 3.8. A larger  $D^*$  value correspond to a stronger, i.e. closer to Arrhenius behavior, and vice versa. The parameter  $D^*$  thus can be viewed as a measure of the curvature of the individual curves. Alternatively, the fragility can be defined by the steepness index  $m$ , being defined as the slope of the curves at  $T_g$ . Apparently, a larger  $m$  characterizes a more pronounced temperature-dependence of the dynamics around the glass transition, corresponding to a more fragile behavior (lower  $D^*$ ).

The sensitivity of liquid dynamics with respect to changes in temperature is quantified by the concept of *fragility* [94]. Similarly as the mechanical fragility relates to the susceptibility of a system to fracture in the presence of mechanical forces, the kinetic fragility is a measure of how stable the dynamic properties are against changes in temperature. Liquids whose dynamics follow a near exponential temperature dependence, i.e. close to Arrhenius behavior, are classified as *strong*, while liquids that show a distinct deviation from Arrhenius behavior are referred to as *fragile*. To compare the different sensitivity of the dynamics with

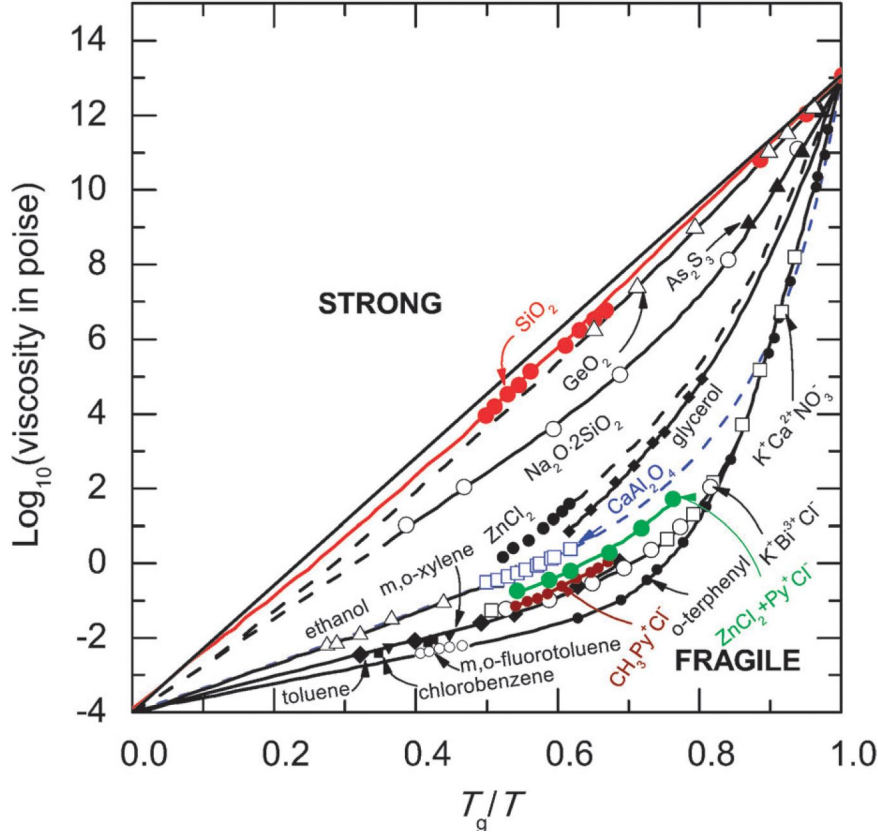


Figure 3.8: Comparison of the temperature dependence of the viscosity, i.e. the fragility, in different glass formers. Strong liquids, such as oxide glass formers, are characterized by a closer to Arrhenius behavior, while fragile liquids, such as organic glass formers, show a larger-than-exponential temperature dependence of their dynamics upon cooling towards the glass transition  $T_g$ . Metallic glass former show an intermediate behavior. The figure is taken from [93].

respect to temperature that is observed between different (glass forming) liquids it is useful to plot the dynamics in a  $T_g$ -scaled Arrhenius plot - in the glass community commonly referred to as the “Angell-plot” (cf. figure 3.7). The advantage of this representation is that the scaling of the ordinate by the glass transition temperature  $T_g$  enables to visualize and compare the temperature dependence of the dynamics of systems whose the interatomic forces differ considerably. Often, experimental data are best described by the empirical Vogel-Fulcher-Tamman (VFT) equation

$$f = f_0 \exp \left( \frac{D^* T_0}{T - T_0} \right) \quad (3.8)$$

in which  $D^*$  and  $T_0$  are system-specific parameters,  $f$  denotes a dynamical variable (e.g. diffusivity, viscosity or relaxation time),  $f_0$  is the value in the limit

$T \rightarrow \infty$ ,  $T_0$  is the temperature where  $f$  would approach infinity in the limit  $T \rightarrow T_0$ , and  $D^*$  is the so-called fragility parameter. In this description strong liquids are characterized by larger values of  $D^*$  and  $T_g/T_0$ , while fragile liquids exhibit lower  $D^*$  and  $T_g/T_0$ . Alternatively, fragility can be quantified based on the *steepness-index*  $m$  which is defined as

$$m = \left| \frac{\partial \ln(\eta(T))}{\partial (T_g/T)} \right|_{T \rightarrow T_g} \quad (3.9)$$

and graphically corresponds to the slope in the Angell-plot in vicinity to  $T_g$ . More fragile glass formers possess steeper slopes, and hence a larger  $m$ -value than strong ones (cf. figure 3.7).

Several key features regarding the dynamics of liquids can be deduced from figure 3.7 and figure 3.8. First, it appears that all liquids tend to form a glass at a temperature  $T = T_g$  where the viscosities are  $\approx 10^{12}$  Pas ( $10^{13}$  poise)<sup>8</sup> corresponding to structural relaxations times of the order of  $10^2 - 10^3$  s respectively.<sup>9</sup> This universality originates from the kinetic nature of the laboratory glass transition, namely the crossing of the laboratory time scale of observation and the intrinsic time scale of the dynamics inherent to the system. The system appears to be frozen when its inner time scale, expressed by its structural relaxation time  $\tau$  exceeds the observation time  $\tau_{obs}$  determined by the duration of the experiment. For  $\tau_{obs} < \tau$ , the system appears as frozen, although it actually is in an out-of-equilibrium state and slowly evolves towards lower energetic states. Second, it appears that the dynamics in the high temperature limit  $T \rightarrow \infty$  tend to a common viscosity value of approximately  $10^{-4}$  poise corresponding a structural relaxation time of approximately  $10^{-14}$  s. The latter observation can be explained as follows. Based on Eyring's considerations on the lower bound for viscosity [95], the pre-exponential factor in the VFT-equation of the viscosity can be estimated as  $\eta_0 = N_A h / v_m$  where  $h$  is Planck's constant,  $N_A$  is Avogadro's number and  $v_m$  is the molar volume. Typically,  $V_m$  of metals is of the order of  $10^{-5}$  m<sup>3</sup> per mole, yielding  $\eta_0 \approx 10^{-3}$  Pas to  $10^{-4}$  Pas. Alternatively, the high temperature limit can be estimated based on the attempt frequency, expected to be of the order of  $\tau_\infty = 10^{-13}$  s. By recognizing that  $G \approx 10^{10}$  Pas and applying the Maxwell relation 3.6 a similar value is found.

Accepting that the glass transition  $T_g$  occurs at a viscosity  $\eta = 10^{12}$  Pas and that liquids tend to a universal high temperature viscosity limit  $\eta_0 = 10^{-4}$  Pas, the parameters  $D^*$  and  $T_g/T_0$  are connected via  $D^* = \ln(10^{16}) (T_g/T_0 - 1) = 36.84 (T_g/T_0 - 1)$ . Given that  $T_g$  is known, the VFT-equation becomes essentially a one-parameter equation in which either of the parameters  $D^*$  or  $T_g/T_0$  is

<sup>8</sup>This is only a rule of thumb. In fact more fragile glass formers under laboratory conditions often "freeze" at lower viscosities. Nonetheless, it is common to assume that the transition from liquid to solid behavior occurs at  $10^{12}$  Pas. This observation is even used to define  $T_g$ .

<sup>9</sup>The conversion from  $\eta$  to  $\tau$  is possible by the use of the Maxwell relation 3.6, recognizing that the shear modulus of liquids is of the order  $10^{10}$  Pa.

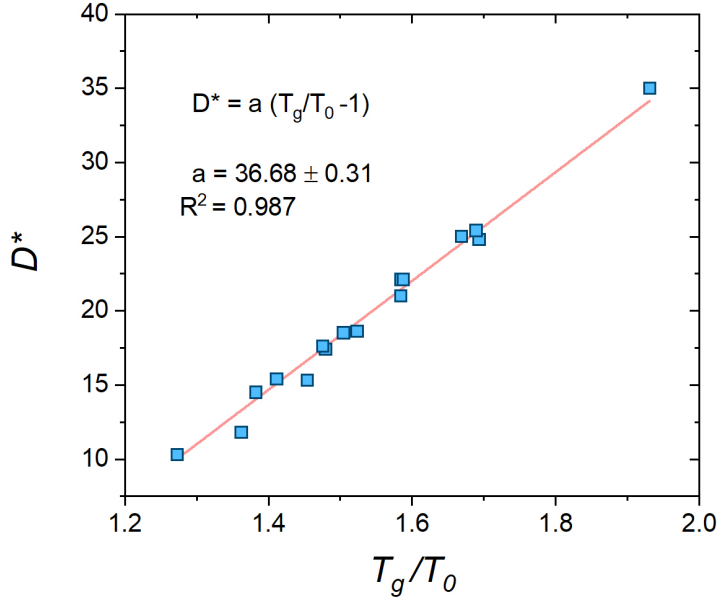


Figure 3.9: Correlation between  $D^*$  and  $T_g/T_0$  for several bulk metallic glass forming alloys. The straight line is a linear fit through the data points.

sufficient to describe the fragility. This is shown in figure 3.9 where the fragility index  $D^*$  of various metallic glass forming liquids is shown to obey a linear dependence with respect to the ratio  $T_g/T_0$  whose slope within the errors reproduced the above anticipated value  $\ln(10^{16}) = 36.84$ . Note that  $D^*$  and  $T_0$  are obtained from fitting of experimental viscosity data using the VFT equation 3.8, while  $T_g$  is normally determined from constant heating rate DSC scans, or by definition set as the temperature where  $\eta = 10^{12}$  Pa.s.

Up to the present day, the exact origin of the viscous slowdown and the differences in the fragility among different liquids remains vague. In the following, the most prominent approaches to explain the origin of the viscous slowdown are recaptured and summarized.

### 3.5.2 The volume perspective

With decreasing temperature, the liquid structure is more and more dominated by energy. The interaction among the particles, determined by interatomic pair potentials, acts against entropy and increasingly governs the structural formation. In consequence, most liquids tend to become denser and more ordered when the temperature is lowered. This is particularly true for metallic liquids, as metallic bonding is non- or weak-directional, so that the lowest energetic states often

coincide with states that are characterized by a maximum packing density.<sup>10</sup> The fact that both, density and viscosity, increase with decreasing temperature has stimulated the idea that the increase in viscosity is inherently linked to the decrease in the volume accessible to the particles. This conception is usually referred to as the *free volume model*.

Based on the earlier work of Fox and Flory [96], Doolittle [97] proposed an equation that relates the changes in viscosity to changes in the “free space” available to the particles in the system,

$$\eta(T) \propto \exp\left(\frac{bv^*}{v_f(T)}\right) \quad (3.10)$$

where  $b$  is a material specific constant which multiplied with the van-der-Waals volume  $v^*$  represents the critical volume required for viscous flow, and  $v_f(T)$  is the so-called *free volume* of a particle. The terminology “free” aims at emphasizing that it is the available excess volume, that is responsible for the fluidity. Equation 3.10 is commonly known as the *Doolittle equation*. Its underlying consideration is quite intuitive. The less “free” space is available, the more difficult it is for the particle to move in its surrounding, and hence the larger should be the energy required to displace particles against each other.

The free volume model was later on refined by Turnbull and Cohen [21]. Envisaging the amorphous structure as an assembly of cells or cages formed by an atom and its neighbors, the free volume  $v_f$  is defined as that part of the thermal expansion or excess volume  $\Delta v$  that can be redistributed among the cells without a free energy change. Based on the local potential energy attributed to the thermally induced cell expansion, the model heuristically predicts that, above a threshold volume  $v_{th}$ , a non-uniform distribution of the free volume among the structure becomes entropically favored over a uniform distribution. According to Turnbull and Cohen [21] the change in free volume with respect to a temperature  $T_{ref}$  is given by  $\Delta v_f(T) = \Delta\alpha_{lg}(T - T_{ref})$ , so that  $v_f(T)$  in equation 3.10 becomes  $v_f(T_{ref}) + \Delta\alpha_{lg}(T - T_{ref})$ , which together with the assumption that there exists a finite temperature  $T_{ref} = T_0$  at which the free volume ceases,  $T \rightarrow T_0 \Rightarrow v_f \rightarrow 0$  yields

$$\eta(T) \propto \exp\left(\frac{bv^*}{\Delta\alpha_{lg}(T - T_0)}\right) \approx \exp\left(\frac{const}{T - T_0}\right) \quad (3.11)$$

As can be seen from equation 3.11, the model, under the given assumptions, reproduces the VFT equation. The free volume model of Turnbull and Cohen

---

<sup>10</sup>In systems with more directional bonds, it can be energetically more efficient to form a structure that is characterized by a lower density or packing efficiency. Typical examples of this *anomalous behavior* are tetrahedrally bonded systems such as water, Si, Ge, and others. In these systems the lower energy states do not coincide with the lowest density states. The more ordered crystalline states can have a lower density than the corresponding disordered liquid states around the melting temperature, causing a so-called “density anomaly” upon melting.

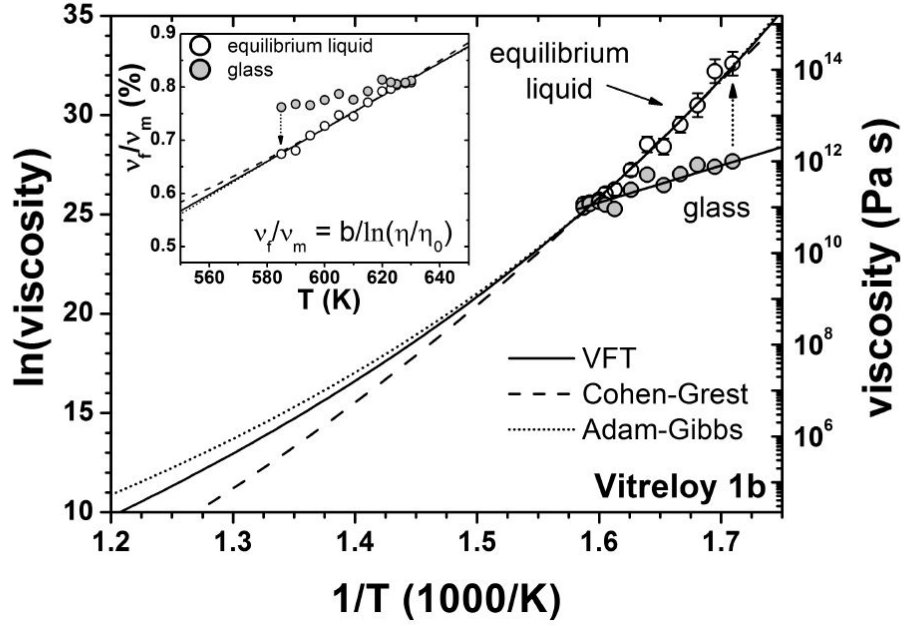


Figure 3.10: Comparison of different models to describe the experimental viscosity data of a Zr-based bulk metallic glass forming alloy close to the glass transition. The experimental data can be equally well described by all models. Differences become remarkable at higher temperatures only. Note that the VFT fit is equivalent to the Turnbull-Cohen free volume model, which in turn can be directly derived from the Doolittle equation 3.10. Figure taken from [98].

predicts a singularity of the viscosity at a finite temperature  $T_0$  arising from dearth of (free) excess volume.

Later on, Cohen and Grest further elaborated the free volume model [99]. In this later version the (undercooled) liquid phase is considered to be composed of two types of cells that differ in terms on their on the fluidity, namely solid- and liquid-like cells, whose free energy is a function of the cell volume. In contrast to the earlier model, the free volume does not vanish above 0 K, so that the viscosity remains finite at all temperatures for  $T > 0$  K. The transition from liquid to glassy dynamics is considered to result from a percolation of solid-like cells throughout the structure. Or vice versa, the system behaves like a liquid (unfreezes) when the number of liquid-like cells reaches the percolation limit. According to the Cohen-Grest-model [99] the free volume is given by

$$v_f = \frac{k_B}{2\psi} \left( T - T_q + \sqrt{(T - T_q)^2 + 4\psi v_a k_B^{-1} T} \right) \quad (3.12)$$

where  $T_q$ ,  $k_B(2\psi)^{-1}$  and  $4\psi v_a k_B^{-1}$  are constants obtained from fitting.

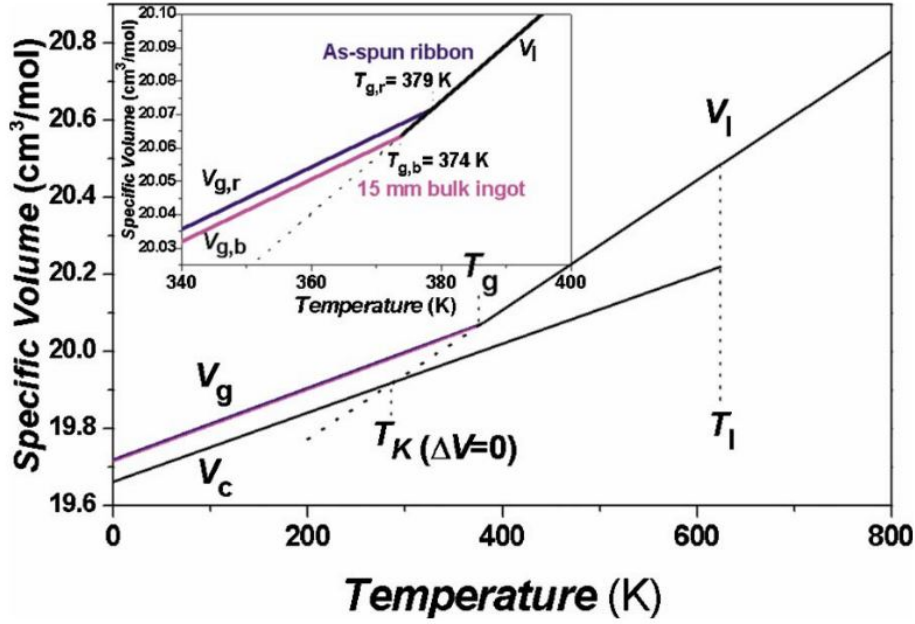


Figure 3.11: Specific volumes of the crystalline, glassy and liquid state as a function of temperature for the  $Ca_{65}Mn_{15}Zn_{20}$  bulk metallic glass forming alloy. The liquid shows a stronger temperature dependence of the volume than the glass, which essentially shows the same temperature dependence as the crystalline phase. The figure is taken from [100]. The inset shows a magnification of the different volume states of two glasses formed at different cooling rates  $R_c$ . The as-spun ribbon formed at  $R_c \approx 10^6 K/s$  has a slightly lower density than the structurally more ordered bulk sample formed at much lower cooling rates, i.e.  $R_c < 100 K/s$ . Although the difference of the frozen excess volume appears to be small compared to the overall volume changes, it may have a significant influence on the mechanical behavior of the glasses. In general, higher volume states are potentially more ductile, and vice versa.

In practice, experimental viscosity data close to  $T_g$  often can be equally well described by either of the models (cf. figure 3.10). Despite of the success in describing the course of experimental viscosity data as well as acting as a basis for models aiming to explain the deformation behavior of glasses [17, 18, 101], the physical correctness of the free volume model has been debated. Its phenomenological character and the idea of local open (or free) space in highly packed, dynamic systems can be criticized. Although intuitively amenable, the model bares the difficulty that the conception of free volume is ambiguous. There is no clear definition of what the free volume actually refers to. The term “free” only implies that there is some sort of reference state where the volume available to an atom reaches a minimum.

Finally, it is worth noting that the influence of volume changes on the viscosity is tremendous. The viscosity change from the liquidus temperature ( $T_g/T_l \approx 0.5 - 0.6$ ) down to the glass transition spans, depending on the fragility of the system, about 10 - 14 order of magnitudes (cf. figure 3.8), while the corresponding volume changes in metallic glass formers are often less than 2 percent (cf. figure 3.11).

### 3.5.3 The Entropy Perspective

#### The Adam Gibbs Theory

Molecular relaxation processes such as viscous flow in dense packed systems require cooperative motions or rearrangements of the particles. This suggests a direct link between the relaxation time and the structural configurations available to the system. In 1965 G. Adams and J. H. Gibbs proposed a theory to explain the non-Arrhenius temperature dependence of relaxation times observed for supercooled liquids near their glass transition temperature  $T_g$  [64]. Although originally developed to quantify the temperature dependence of relaxations times in polymer glass formers [64], the general formulation of the theory allows a much broader application including all kind of glass forming liquids, ranging from organic over metallic to oxide glass formers. The underlying idea of the Adam-Gibbs-Theory (AGT) is the conception that the increase in relaxation times towards the glass transition (viscous slowdown) is a consequence of the decreasing number of molecular configurations  $W$  available to the system, measurable by its configurational entropy  $S_c$ . In the following the main aspects and underlying considerations of this theory are reproduced from [64] and discussed.

The principal hypothesis of the AGT is that the structural relaxation time is determined by the probabilities of local cooperative structural rearrangements. To evaluate the temperature dependence of the transition probability, Adam and Gibbs consider a liquid or glass as a system composed of *cooperative rearranging regions* (CRR). The CCRs are subsystems consisting of  $z$  molecular units (atoms, particles, monomer segments) that upon sufficient energy fluctuations can rearrange into another configuration. The subsystems are in mechanical and thermal contact with each other and it is further assumed that they can undergo a structural rearrangement independently from their environments.

The isobaric-isothermal partition function of an ensemble consisting of  $N$  independent, equivalent and distinguishable subsystems of size  $z$ , is given by

$$\Pi(z, p, T) = \sum w(z, E, V) \exp\left(-\frac{E}{kT}\right) \exp\left(-\frac{pV}{kT}\right) \quad (3.13)$$

where the sum is taken over all possible energy and volume states ( $E, V$ ) that the subsystems can take, and  $w(z, E, V)$  is the degeneracy of the states. The Gibbs free energy of the subsystems is given by  $G = z\mu - kT \ln \Pi$  where  $\mu$  denotes the chemical potential. In order to perform a cooperative rearrangement



an energy barrier must be mounted, thus, only subsystems that are in excited states  $(E', V')$  can perform cooperative rearrangements. Summation over only these states yields the associated “partition function” of rearrangeable subsystems  $\Pi'(z, p, T)$ , corresponding to a “Gibbs free energy”  $G' = z\mu' = -kT \ln \Pi'$ . The probability that a subsystem of size  $z$  is in an energy state that allows a cooperative rearrangement is therefore given by

$$\frac{n_i}{N} = \frac{\Pi'(z, T)}{\Pi(z, T)} = \exp\left(-\frac{G' - G}{kT}\right) \quad (3.14)$$

where the pressure dependence has been dropped as in the following only the temperature dependence will be considered. Assuming that the transition rate  $P(z, T)$  is proportional to the fraction  $n_i/N$  of rearrangeable subsystems gives

$$P(T, z) = A \exp\left(-\frac{z\Delta\mu}{k_B T}\right) \quad (3.15)$$

where  $\Delta\mu = \mu' - \mu$  is the difference in chemical potential between subsystems that can undergo a cooperative rearrangements and the average, and  $A$  is frequency factor assumed as negligibly temperature dependent in comparison to the exponential factor. Note that  $\Delta\mu$  can be considered as largely the potential energy barrier hindering cooperative rearrangements per structural unit of the subsystem [64]. The average transition probability  $\langle P(T) \rangle$  can now be obtained by summing over all subsystem sizes  $z$  that have non-vanishing contributions  $P(T, z)$ . In recognizing that there must be a lower size limit  $z^*$ , corresponding to a lower limit for the configurational entropy  $s_c^*$ , that is necessary to yield a transition at all, the temperature dependence of the average transition probability becomes

$$\langle P(T) \rangle = A \sum_{z^*}^{\infty} \exp\left[\left(\frac{\Delta\mu}{k_B T}\right)^z\right] = \frac{A}{1 - \exp(-\Delta\mu/kT)} \exp\left(\frac{-z^*\Delta\mu}{kT}\right) \quad (3.16)$$

Adam and Gibbs argue that for  $\Delta\mu > kT$  “the denominator is nearly equal to unity, and therefore, negligible dependent on temperature in comparison with the numerator”[64]. This allows to absorb this factor into the frequency factor  $A$  enabling to write

$$\langle P(T) \rangle = A' \exp\left(-\frac{z^*\Delta\mu}{kT}\right) \quad (3.17)$$

with  $A'$  being a new prefactor, whose temperature-dependence is considered to be negligible compared to the exponential term [64]. Equation 3.17 states that, keeping the phrasing of Adam and Gibbs, “The overwhelming majority of transitions are undergone by regions that differ negligible from the smallest size  $z^*$  that permits a transition at all.” [64]. The evaluation of the temperature dependence of  $\langle P(T) \rangle$  is therefore transferred to the temperature dependence of  $z^*$ , which in

turn can be linked to the configurational entropy  $S_c$ . Realizing that there must be a lower limit for the number of configurations  $W^*$  corresponding to a critical size  $z^*$  required to yield a transition at all - which intuitively should be at least of the order of 2 - it follows  $W^* = W^{z^*/N_A}$  corresponding to a critical configurational entropy  $s_c^* = k \ln(W^*) = S_c z^*/N_A$ . Inserting this into equation 3.17 and considering that  $\tau \propto P(T)^{-1}$  finally gives

$$\tau = \tau_\infty \exp\left(\frac{s_c^* \Delta\mu}{S_{c,m} kT}\right) = \tau_\infty \exp\left(\frac{B}{S_{c,m} T}\right) \quad (3.18)$$

where  $S_{c,m}$  is the molar configurational entropy of the macroscopic system. Accordingly, the recognition of a critical configurational entropy  $s_c^*$  necessary for a structural rearrangement, demands that  $z^*$  increases when the overall entropy  $S_{c,m}$  decreases. With other words, the dearth of configurations available to the macroscopic system requires the subsystems to grow bigger in size in order to perform structural rearrangements. This leads to an increase in the activation barrier for the cooperative rearrangements  $E_A = z^* \Delta\mu$  upon cooling, explaining the super-Arrhenius increase in the structural relaxation time or viscosity observed for undercooled liquids.

### Validity of the Adam-Gibbs-Model: Configurational vs. Excess Entropy

The Adam-Gibbs-Theory provides a direct connection between the thermodynamics and kinetics of a liquid. The parameter  $B$  in equation 3.18, usually obtained from fitting [65, 102], acts as an effective activation energy, in the sense that for two liquids with the same molar configurational entropy, the system with the larger  $B$  will be more viscous. Although the Adam-Gibbs entropy model [64] has been questioned [103], its general applicability is corroborated by the strong empirical correlation found between the fragility and the evolution of excess entropy of the liquid over the crystalline phase  $S_{ex}$  [65, 104]. A comparison of the changes in entropy and changes in the dynamics for a large variety of glass forming liquids is shown in figure 3.12. A direct comparison of figure 3.12a and figure 3.12b implies a strong generic connection between the decrease of the excess entropy  $S_{ex}$  and the increase of viscosity  $\eta$  during cooling towards the glass transition. This observation is quantitatively evaluated in figure 3.13, where a strong positive correlation between the thermodynamic fragility index  $F_{3/4}$  and the kinetic fragility index  $F_{1/2}$  is found. For an explanation of the  $F_{1/2}$  and  $F_{3/4}$  the reader is referred to the caption of the figure.

However, the Adam-Gibbs equation 3.18 relates  $\tau$  (or  $\eta$ ) to  $S_c$  not  $S_{ex}$ . Strictly speaking the correlation between  $S_{ex}$  and the kinetic fragility shown in figure 3.13 does not necessarily imply a connection between the viscous slowdown and  $S_c$ . In fact, the total excess entropy of the liquid is given by the sum of the excess

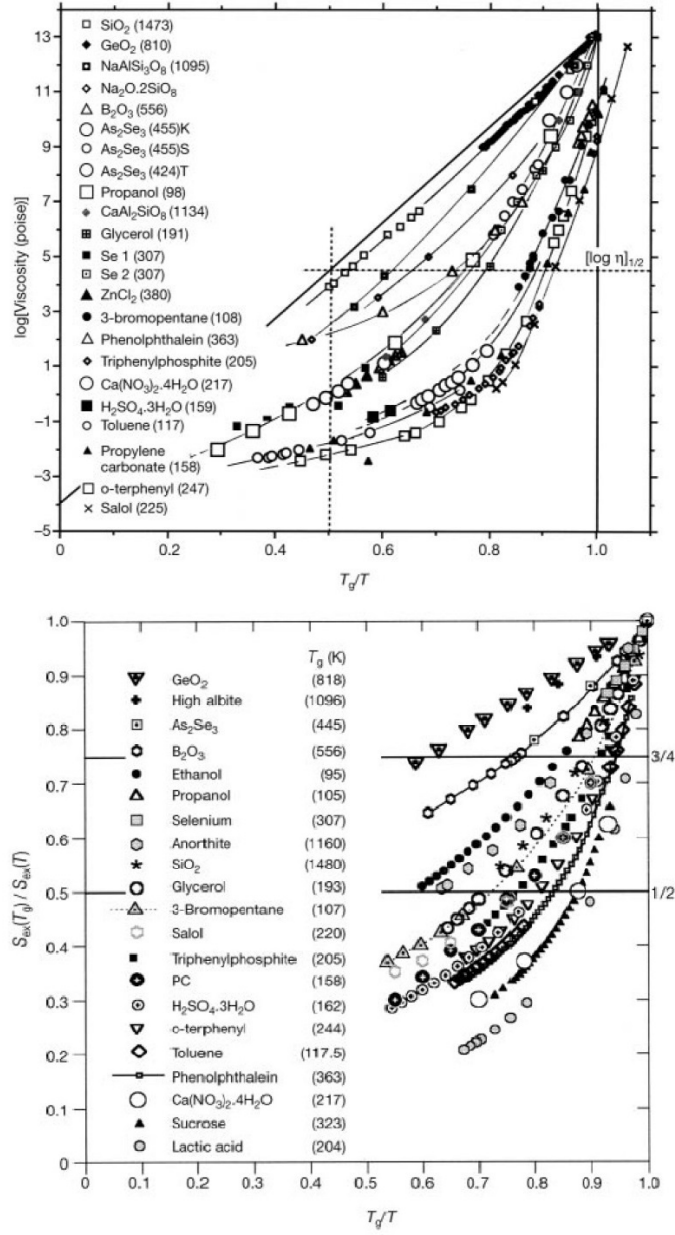


Figure 3.12: Relation between the fragility and changes in excess entropy of multiple glass formers. Upper panel:  $T_g$ -scaled Arrhenius plot (Angell-plot) of the change in viscosity  $\eta$  of a large variety of different glass forming liquids. Lower panel: The corresponding changes in excess entropy normalized to its value at  $T_g$ ,  $S_{ex}(T_g)/S_{ex}(T)$ , plotted against  $T_g/T$ . A comparison of the two figures suggests a close connection between the temperature dependence of the decrease of  $S_{ex}$  and the increase in  $\eta$ . The figures are taken from [104].

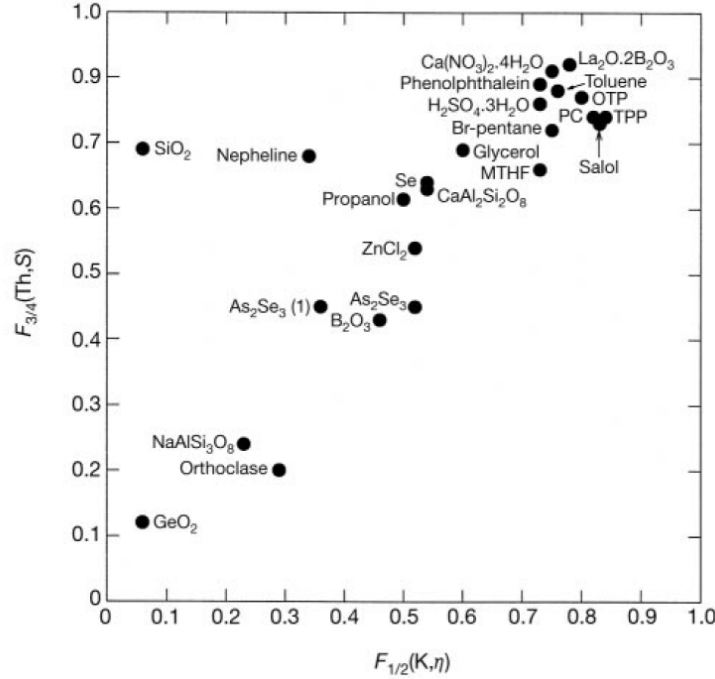


Figure 3.13: The thermodynamic fragility parameter  $F_{3/4}(Th, S)$  plotted versus the kinetic fragility  $F_{1/2}(K, \eta)$ . The parameter  $F_{3/4}(Th, S)$  is derived from the upper plot of figure 3.12 by drawing a horizontal line at  $3/4 = 0.75$  on the y-axis and taking the x-value of the intersection points for individual curves. Physically it corresponds to the temperature normalized to  $T_g$  where the system has an excess entropy  $S_{ex} = 4/3 S_{ex}(T_g)$ . On the other hand  $F_{1/2}(K, \eta)$  is obtained equally from the upper plot in figure 3.12 by drawing a horizontal at  $1/2 = 0.5$  on the y-axis. Accordingly,  $F_{1/2}(K, \eta)$  corresponds to the temperature normalized to  $T_g$  where the viscosity has dropped about half of its value at  $T_g$ . Except for the two outliers  $SiO_2$  and *Nepheline*, a good positive correlation is obtained, indicating that there is a direct link between the decrease of the excess entropy  $S_{ex}$  and the change in viscosity  $\eta$ . The figure is taken from [104].

configurational and the excess vibrational entropy,

$$S_{ex} = S_{ex}(vib) + S_c \quad (3.19)$$

Due to the difficulties to directly measure  $S_c$  in experiments, often the assumption is made that  $S_c$  in equation 3.18 can be replaced by  $S_{ex}$ . This however is only valid if the excess vibrational entropy of the liquid over the crystal,  $S_{ex}(vib)$  is negligible. In contrast, Goldstein's analysis of entropy changes in glasses between 0 K and  $T_g$  has shown that this approximation is rather poor as the contribution of configurational entropy to the excess entropy can be as small as 15 % and can vary considerably among different systems [105].

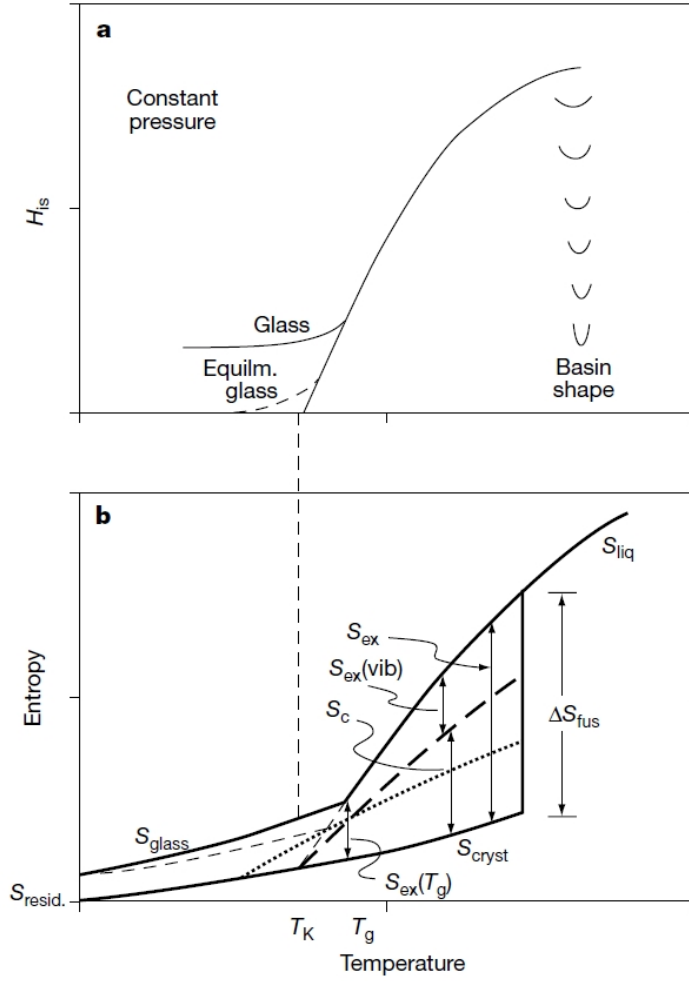


Figure 3.14: a) The inherent structure enthalpy  $H_{is}$  of a one-component system during heating from 0 K above the melting point at constant pressure. With higher temperature the basins that the liquid visits with greatest probability become shallower as the system expands. b) The entropy as a function of temperature. The glass has an additional residual entropy  $S_{resid}$  at  $T = 0$  K and a larger excess entropy  $S_{ex}$  with respect to the crystalline state due to an excess of low-frequency vibrational modes. Above  $T_g$  the excess vibrational entropy  $S_{ex,vib}$  shows a more rapid increase in a system that has access to energetically higher lying basins of different shapes (fragile system) as compared to a system where the basins have the same shape (stronger system). This yields an additional increase in entropy that must be balanced by a more rapid increase in the enthalpy. With the “faster” ascent in the energy landscape the system has access to larger number of basins  $W$ , and therefore a larger configurational entropy  $S_c = k_B \ln(W)$ . The figure is taken from [104].

So how to explain that the excess entropy yields reasonable descriptions of the course of viscosity (or relaxation time) [104] when inserted into equation 3.18? A solution is proposed by Martinez and Angell [104], namely, that the changes of  $S_c$  and  $S_{ex}$  with temperature must be (close to) proportional, i.e.  $\Delta S_{ex} \propto \Delta S_c$  (see figure 3.14). Obviously, in this case the viscous slowdown is equally well described by the Adam-Gibbs-Equation by either of the quantities; the only difference being a different proportionality constant  $B$  in equation 3.18. The latter is usually left as a free fitting parameter, and so the experimentally observed course of the viscosity over temperature can be reasonably well described by equation 3.18 relying on the experimentally measured excess entropy  $S_{ex}$ . According to Martinez and Angell [104] the proportionality of  $S_c$  and  $S_{ex}(vib)$  directly results from the topography of the potential energy hypersurface over the configuration-space of the liquid [104].<sup>11</sup> In general, the number of configurational states (basins)  $W$  that the system can access, increases with increasing height in potential energy landscape [38]. The more “rapidly” the system ascends the PEL, the “faster”<sup>12</sup> is therefore the increase in its configurational entropy  $S_c = k_B \ln(W)$ . In fragile liquids the shape of the inherent structure basins, i.e. the local minima’s in the potential energy landscape, becomes shallower at higher potential energies (see figure 3.14). This yields an extra increase in the number of accessible vibrational states, i.e. extra vibrational entropy in the liquid  $\Delta S_{ex}(vib, +)$ . In order to fulfill the equilibrium condition  $\Delta G = \Delta H - T\Delta S = 0$  the additional increase  $TS_{ex}(vib, +)$  must be balanced by a faster ascent in the potential energy landscape [104] (see figure 3.14). In contrast, in case of a strong liquid the drive to higher enthalpy states comes mainly (or only) from the increasing number of accessible configurations alone, thus  $TS_c$  [104]. Consequently, fragile liquids show a more rapid rising of the excess vibrational as well as configurational entropy in the liquid phase  $S_{liq}$  with respect to the crystalline phase  $S_{cryst}$ , and thus a larger temperature dependence of the total excess entropy  $S_{ex}$  usually combined with a higher entropy of fusion  $\Delta S_{fus}$  as shown in figure 3.14.

### 3.5.4 The Energy Landscape Perspective

The dynamic behavior of glass-forming liquids and decoupling of relaxation times can be explained in terms of the topography of the configurational (or potential) energy landscape [38]. The so-called potential energy landscape (PEL) is a topographic view of the potential energy function of a N-body system with respect to its coordinates (orientational and vibrational) [38]. The PEL is a multidimensional hypersurface, which for the simplest case of particles (no internal orientational and vibrational degrees of freedom) is embedded in a space with a

<sup>11</sup>For a more detailed description of the potential energy landscape, the reader is referred to the next section.

<sup>12</sup>The terms “faster” and “rapidly” need to be understood in terms of the corresponding changes with respect to temperature, not time.

dimensionality of  $3N + 1$ . This topographic viewpoint of condensed phases goes back to Goldstein [106] more than 30 years ago, and has been applied to numerous problems including protein folding, the mechanical properties of glasses, shear-enhanced diffusion and the dynamics of supercooled liquids [38]. Here its underlying concepts are reproduced based on reference [38].

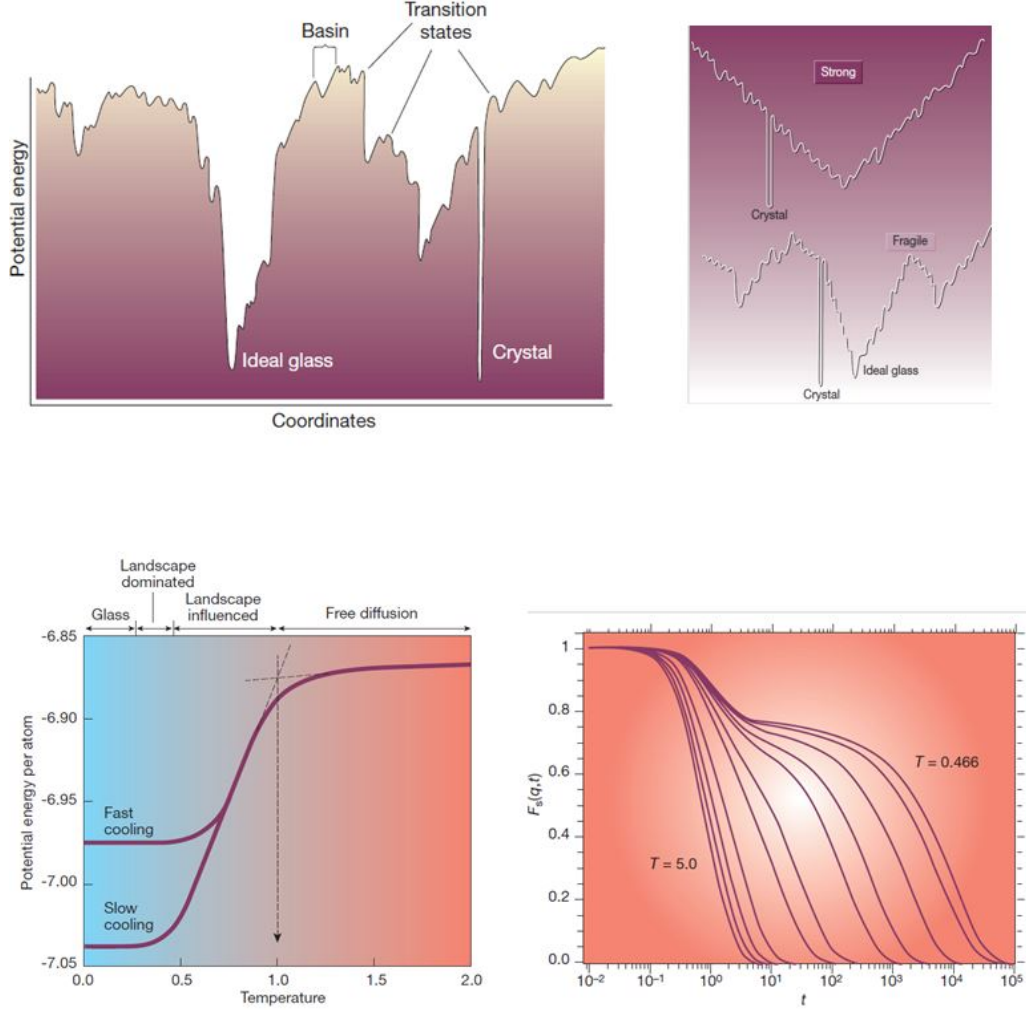


Figure 3.15: Landscape perspective of the dynamic behavior of glass forming liquids. Upper left figure: Schematic representation of the potential energy landscape (PEL) including its principal topological features, i.e. basins and transition states. Upper right figure: Comparison of the PEL between strong and fragile glass formers. Lower left figure: Energetic descent in the PEL as a function of temperature. Different dynamic regimes are passed during cooling. Lower right figure: Temporal evolution of the intermediate scattering function for different temperatures. At lower temperatures a shoulder or plateau develops indicating a decoupling of relaxation processes. Images are taken from [38].

The topography of the landscape is fixed for constant volume. The way that a system samples its landscape as a function of temperature provides information on its dynamic behavior, while the way that the landscape deforms with respect to changes in volume (or density) provides information on the mechanical properties [38]. To understand these relations it is useful to study the average energy of the inherent structure of the liquid as a function of the temperature. The inherent structures are local potential energy minima (basins) of a given depth that are separated by saddle points. Each basin in the potential energy landscape represents a local, mechanically stable equilibrium configuration. The lower left subfigure of figure 3.15 shows the average inherent structure energy plotted against the reduced temperature for the case of a binary mixture of unequal-sized atoms. At high temperatures ( $T > 1$ ) the potential energy per atom is almost constant (plateau) and the system is able to sample its entire energy landscape. The overwhelming number of the sampled basins are shallow, as deep minima are rare (see upper left subfigure). In this free diffusion regime, the system is expected to have a temperature-independent activation energy for structural relaxation [38]. At lower temperatures the system enters the landscape-influenced regime, where sampling of the mechanically stable configurations is strongly temperature-dependent [38]. At even lower temperature ( $T < 0.45$ ) the height of the barriers between adjacent minima increases abruptly, and the particles execute rare jumps over distances roughly equal to interparticle distances [38]. The transition to this landscape-dominated behavior occurs closely to the mode-coupling transition temperature [38]. The descent in the energy landscape through the different regimes is accompanied by a decoupling of the dynamics and can be probed by the decay behavior of the intermediate scattering function  $F(q, t)$ , which measures the temporal evolution of particle density fluctuations on a certain length scale associated to the wave number  $q$  (see lower right subfigure). At high temperatures, in the so-called free diffusion regime,  $F(q, t)$  exhibits a simple exponential decay, implying that there is only a single relaxation mechanism. With decreasing temperature the relaxation time increases until below a certain temperature a shoulder or plateau ( $F(q, t) = \text{constant}$ ) appears at intermediate times, indicating a transient freezing of the particles. The full decay now occurs in two steps: A faster exponential initial decay, the so-called  $\beta$ -relaxation, and a slower final decay referred to as  $\alpha$ -relaxation. Upon further cooling, the plateau becomes more pronounced, indicating that the two relaxation processes diverge (cf. figure 3.6). The divergence of the two relaxation processes observed in undercooled liquids suggests a heterogeneous landscape comprised of (at least) two subdomains. On the one hand there must be structural reconfigurations that corresponds to the fast initial decay. These  $\beta$ -relaxations possess a temperature-invariant activation energy and therefore follow an Arrhenius behavior. On the other hand there must be a second type of structural reconfigurations that emerges at lower temperatures. Their temperature dependence is more pronounced than for  $\beta$ -relaxations and normally does not follow an Arrhenius behavior. These slower



relaxations are referred to as  $\alpha$ -relaxations and only emerge below a critical temperature. The splitting of the two relaxation mechanisms has structural origin, as discussed in more details in section 3.4. The  $\beta$ -relaxations corresponds to elementary transitions between contiguous basins, while the  $\alpha$ -relaxation are envisioned as configurational sampling of neighboring megabasins corresponding to highly collective (cooperative) rearrangements (cf. figure 3.5). Their time constant, i.e. the structural relaxation time, is linked to the viscosity and thus characterizes the viscous slow down during cooling. At the glass transition temperature, the dynamics become so sluggish, that on the time-scale of observation, the alpha-decay is no longer observed and  $F(q, t)$  stagnates. The transitions normally occurs at a viscosity of  $10^{12}$  Pas or a structural relaxation time of about 100 s. On the time scale of observation, the system appears as frozen in its landscape. A further descent to lower energetic states now requires much longer waiting times and is only measurable if sufficient thermal energy is provided to move the system over its energetic barriers (saddle points) along its downwards path in the landscape (sub- $T_g$  relaxation).

The change of the landscape topography with respect to temperature and density also bears relation to the temperature-sensitivity of the liquid dynamics, i.e. their fragility. For fragile liquids the activation energy for cooperative structural rearrangements ( $\alpha$ -relaxations) is more temperature-sensitive than for strong liquids. This suggests that the landscape of fragile glass formers becomes progressively more rugged during undercooling. With a descent in its landscape a fragile system has to overcome increasing activation barriers in order to make the transition from one megabasin into another. On the other hand the landscape topography of strong glass formers maintains its ruggedness. In consequence the activation energy remains more or less constant when the system is cooled to lower temperatures and densifies, as shown in the upper right subfigure of figure 3.15.

### 3.6 The big picture of glass forming liquids

According to Angell’s “big picture” of glass forming liquids [107, 108] strong liquids differ from fragile liquids by occupying the different flank of an underlying order-disorder transition in the liquid state. In the following the phenomenology of this picture is discussed. A more detailed treatise on its connections to liquid-liquid transitions and liquid-liquid critical points is presented in chapter 10.

Thermodynamically, an order-disorder transition manifests as a peak in the heat capacity. Whether and at which temperature a strong or fragile behavior is observed for a liquid depends on the relative position of the transition temperature with respect to the melting temperature  $T_m$  and the glass transition temperature  $T_g$ . Under the terms of this conception, all liquids are considered to be fragile at high enough temperatures, and an increase in  $c_p$  (or  $\Delta c_p$ ) with decreasing temperature can be expected. On the other hand, at temperatures below the transition, any liquid is expected to show a stronger dynamic behavior. Glass formers can thus be divided into three types (cf. figure 3.16) [107, 108]:

(I) Systems with strong interatomic forces (bonding) between the individual species, such as network glass formers like  $SiO_2$  or  $BeF_2$ , exhibit a high degree of order even at high temperatures. In these systems the transition temperature, and so the  $c_p$ -peak, are located far above the melting point, often beyond the temperature range that is accessible by experimental studies. Consequently, experiments occur on the left flank of the transition and therefore only the strong behavior is detected. In experiments, these systems are characterized by modest and gradual changes in entropy, and small heat capacity jumps at the glass transition (see right panels in figure 3.16).

(II) In systems with weak intermolecular forces, such as organic glass forming liquids like 1-butene or toluene, the (first order) transition is occurs at low temperatures, often below the laboratory glass transition. As a consequence only the fragile behavior is observed in experiments. These liquids are characterized by a pronounced rise in the heat capacity during cooling, a large heat capacity jump at the glass transition, and a rapid decay of entropy with decreasing temperature.

(III) In systems with intermediate strong interatomic/intermolecular forces such as water,  $Si$  and  $Ge$ , the transition, is located in the undercooled liquid state, i.e. between the melting point and the glass transition. These liquids show a fragile behavior above and around  $T_m$ , but a stronger dynamic behavior around or below  $T_g$ . Due to the metastable nature of the undercooled liquid these glass formers have a high propensity to crystallize, making experimental studies difficult. However, even though direct experimental observations of the transition may be complicated by the occurrence of crystallization, indirect evidences for the existence of a phase transition in the liquid state can be drawn from a comparison of the high and low temperature dynamics.

The phenomenology of liquid-liquid transitions and their associated anomalies in the thermodynamic and dynamic properties is considered to be linked to the

existence of liquid-liquid critical points (LLCP) in the phase diagram [107–112]. In this context the appearance of the anomalies (peaks) in the thermodynamic response functions, e.g. the heat capacity, compressibility, is related to the distance of the system to its critical point [109, 110, 112]. Below the LLCP the transition is first order, and the response functions shows a sharp peak (divergence) at the transition temperature. Above the critical point, the transition is continuous, and the peaks are smeared. The larger is the distance of the system to its LLCP, the more smeared are the peaks.<sup>13</sup> In this light the big picture suggests that for type-I glass formers, such as organic glass formers like 1-butene or toluene, the LLCP is above ambient pressure, whereas the LLCPs for the two other cases (type-II and type-III) are located below ambient pressure. Obviously, at ambient pressure the strongest glass formers like  $BeF_2$  or  $SiO_2$  would be the farthest apart from their LLCPs.

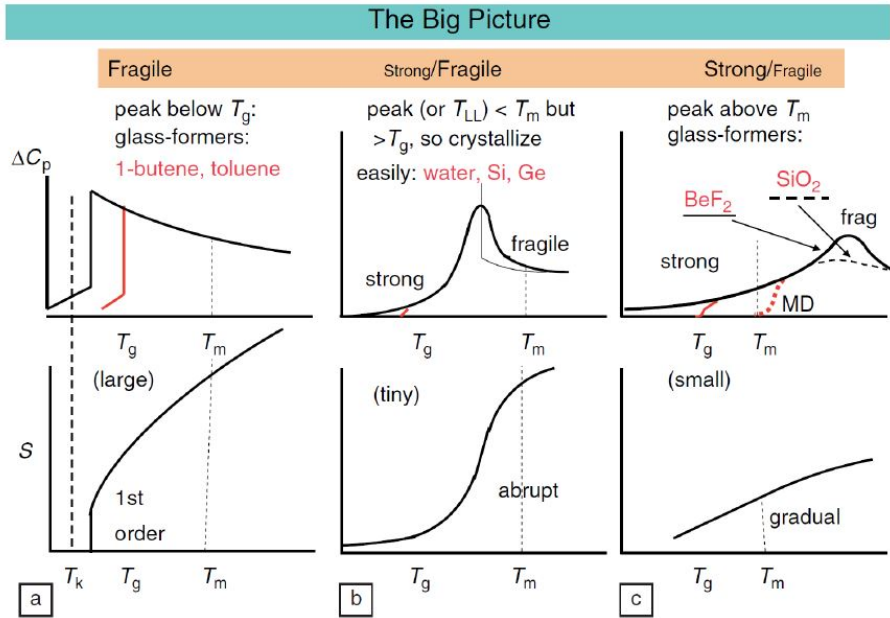


Figure 3.16: The big picture of glass forming liquids according to C. A. Angell [107, 108]: Strong liquids differ from fragile liquids by occupying different flanks of an underlying order-disorder transition in the liquid state. The order-disorder transition can be either first order or continuous. Thermodynamically it manifests either as a sharp or a more or less smeared-out  $c_p$ -peak and a characteristic temperature behavior of the entropy of the liquid phase. The image is taken from [107].

<sup>13</sup>This description is based on systems with a classical behavior, i.e. systems with a positive slope of the coexistence line in the p-T-phase diagram. For systems with negative slopes, e.g. water, the situation is vice versa (cf. figure 10.1).

## Chapter 4

# Scattering and Diffraction of amorphous substances

Scattering and diffraction are powerful methods to explore the structure of materials. To gain information about the structural arrangement the wavelength of the radiation used to probe the material must be of the size or smaller than the distance in between the structural units. In case of metals, wavelengths of the order of one atomic distance or less are thus required, so that the probing radiation requires wavelengths of the order of Angstroms, i.e.  $10^{-10}$  m. This condition is met by electrons, (thermal) neutrons or photons in the x-ray regime. X-rays and neutrons interact only weakly with atoms. This makes the scattered intensity weak, but on the other hand facilitates the description of the scattering event as compared to electrons whose interaction with matter is much stronger [113]. Due to the weaker interaction, multiple scattering occurs less frequently, so that x-rays and neutrons penetrate into matter much deeper than electrons, with penetration depths ranging from  $\mu\text{m}$  to  $\text{cm}$ . This enables to measure macroscopic samples in transmission.<sup>1</sup>

This chapter gives an introduction to scattering and diffraction. The purpose of this chapter is to provide the reader with the fundamental theory and equations of scattering and diffraction techniques. For a reader familiar with the underlying concepts of scattering and diffraction techniques, it is recommended to skip this chapter. For the sake of simplicity, in the following a non-relativistic, elastic scattering process is considered. Instead of a rigorous, complete quantum mechanical description of the scattering theory, a rather phenomenological introduction is chosen, as it facilitates to track the underlying considerations without the need to revert on physical and mathematical concepts whose treatise would be out of the scope for the current purpose.

In the following the discussion of the scattering process is based on the con-

---

<sup>1</sup>Due to their strong interaction, the penetration depth of electrons is much lower than for x-rays and neutrons. Thus, electrons are mainly used to study surfaces. To perform electron diffraction in transmission, samples must be thinned down to about 10 nm to 100 nm.

cept of an ideal radiation source. An ideal radiation source emits perfectly monochromatic plane waves characterized by a sharp wave vector  $k$ ,  $\Phi_k(r, t, ) = \exp(i(kr - \omega t))$ . This approach has the advantage that, in case of coherent elastic scattering, the time dependence can be separated out, enabling to consider the scattering process as a stationary problem. At this point it is emphasized that real physical radiation sources actually emit quantum particles corresponding to wave packets rather than ideal perfectly monochromatic plane waves. Nonetheless, the description and derivations on the basis of plane waves is justified by recognizing that any wave packet can be described by a Fourier series, i.e. a sum of plane wave which are eigenstates of the Hamiltonian [114]. It can be shown that for a small spread of wave numbers (highly coherent radiation) and under geometrical conditions that are usually fulfilled in a X-ray scattering experiment, a wave packet will not spread considerably during the course of experiment [114]. Together with the assumption that the scattering amplitude is varying slowly with the spread of the wave number  $\delta k$ , it is possible to separate out the time dependence, justifying a stationary description of the scattering process and facilitating its description [114].

## 4.1 Scattering from a point scattered - Insights from Huygens' Principle

Consider an incoming wave composed of a ideal plane wave with a sharp wave vector  $\mathbf{k}_0$ , i.e.  $\Phi_0(\mathbf{r}) = \exp(i\mathbf{k}_0\mathbf{r})$ .<sup>2</sup> When the incoming wave hits a scattering target, the wave and target interact with each other and the incident wave will be scattered. In order to describe the outcome of this scattering process, one is searching for a solution of the scattered wave that superimpose on the initial wave. This solution is now phenomenologically inferred from Huygens' principle, although it can be shown by a more rigorous treatment in the framework of *quantum scattering theory* that equivalent results are obtained from the asymptotic solution of the *Lippmann-Schwinger equation* under appropriate boundary conditions [114]. According to Huygens principle every point reached by a luminous disturbance becomes a source of a spherical wave that propagates from its origin. The secondary waves formed superpose and form the wave at any subsequent time. This motivates to express the wave function of a single target scatterer as [114]

$$\Phi = \Phi_0 + \Phi_s = \exp(i\mathbf{k}_0\mathbf{r}) + f(\theta, \phi) \frac{\exp(ikr)}{r} \quad (4.1)$$

where  $(\theta, \phi)$  describes the direction in space, and  $f(\theta, \phi)$  is the *scattering ampli-*

---

<sup>2</sup>Note that the time dependence has been separated out.

tude.<sup>3</sup> Equation 4.1 states that the outcome of a scattering event is a superposition of the incoming wave plus a scattered wave that emanates from the point-like target, removing some incoming particles from the incident beam [114] (see figure 4.1).

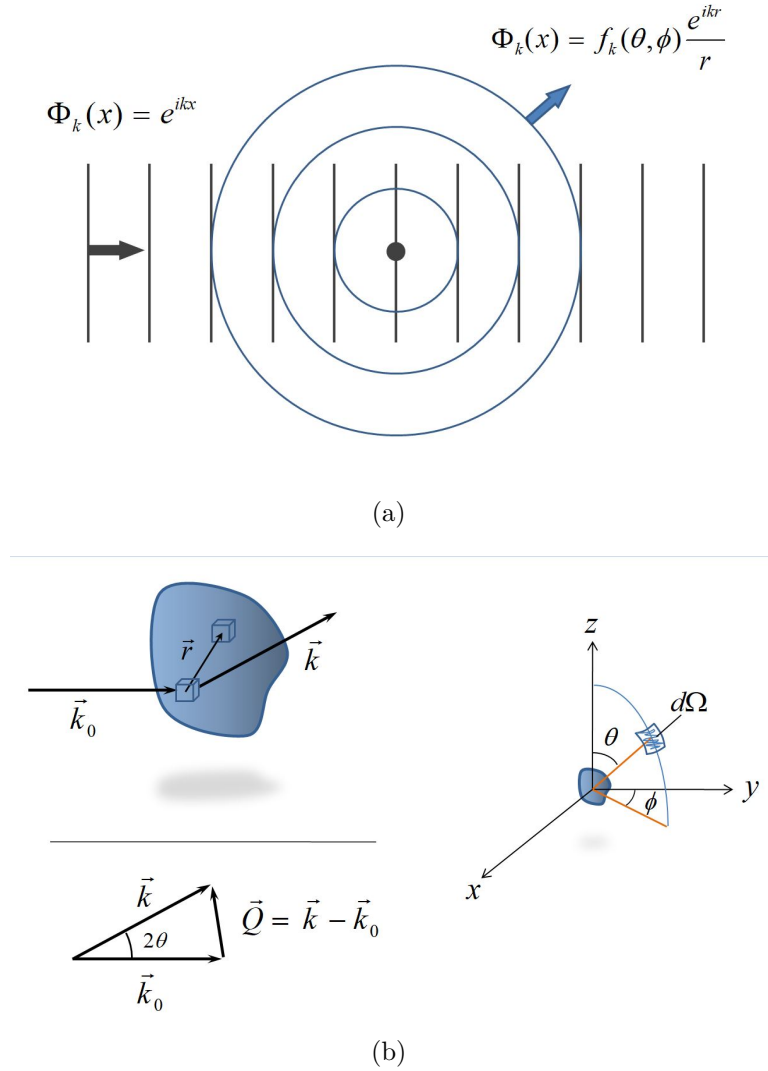


Figure 4.1: (a) Schematic view of the scattering process: A plane wave is scattered by a point scatterer at the origin. As a result a spherical wave emanates. (b) Definition of geometrical parameters used in the description of the scattering event.

<sup>3</sup>For the simplicity the scatterer has been placed at the origin, without a loss of generality.

## 4.2 The scattering amplitude- Born's approximation

The scattering amplitude  $f(\theta, \phi)$  determines the amplitude of the scattered wave along the direction  $(\theta, \phi)$  due to the presence of the interaction potential  $V(x)$ . The general aim of the scattering theory is to calculate  $f(\theta, \phi)$  for a given  $V(x)$  and to relate this to the experimentally accessible quantity measured in a scattering experiment, i.e. the differential scattering cross section (cf. section 4.4).

According to the Born<sup>4</sup>, the scattered wave that is emanated from a target due to the presence of  $V(x)$ , in first approximation, is given by [113]

$$\Phi_s = \frac{1}{4\pi} \int \frac{e^{ik|\mathbf{r}-\mathbf{r}'|}}{|\mathbf{r}-\mathbf{r}'|} V(\mathbf{r}') e^{i\mathbf{k}\mathbf{r}'} d\mathbf{r}' \quad (4.2)$$

At large distance ( $r \gg r'$ ) equation 4.2 becomes [113]

$$\Phi_s = \frac{e^{ikr}}{4\pi r} \int V(\mathbf{r}') e^{i(\mathbf{k}-\mathbf{k}')\mathbf{r}'} d\mathbf{r}' \quad (4.3)$$

Consequently, the scattering amplitude  $f(\theta, \phi)$  is given by the Fourier transform of the interaction potential  $V(\mathbf{x})$  with respect to the scattering vector  $\mathbf{Q} = \mathbf{k} - \mathbf{k}'$ . Born's first approximation physically corresponds to the assumption that the wave is only scattered once (single scattering), building the base of the *kinematic scattering theory*.

## 4.3 Scattering form multiple scatterers

Scattering experiments are often performed on samples consisting of multiple scattering units distributed in space, whose position can vary in time. The intensity measured stems from the superposition of all secondary waves emanating from the ensemble of scatterers. The scattered waves interfere constructively or destructively, yielding diffraction patterns that are characteristic for the structural arrangement of the scatterers.

The amplitude of the scattered wave emanating from a single scatter located around the origin is given by equation 4.3. Writing the total scattering potential  $V$  as a superposition of the potentials of the individual scatterers,  $V_i$ , located at the positions  $\mathbf{R}_i$ ,

$$V(\mathbf{r}) = \sum_i V_i \delta(\mathbf{r} - \mathbf{R}_i) \quad (4.4)$$

the wave emitted by the collection of scatterers becomes [113]

$$\Phi = \frac{\exp(ikr)}{r} \sum_i V_i \exp(i\mathbf{Q}\mathbf{R}_i) \quad (4.5)$$

---

<sup>4</sup>For a detailed treatise and a derivation the reader is referred to reference [113].

motivating to define a *sample scattering amplitude*

$$\Psi(\mathbf{Q}) = \langle V \rangle^{-1} \sum_i V_i \exp(i\mathbf{Q}\mathbf{R}_i) \quad (4.6)$$

so that the scattered wave can be written as

$$\Phi_s = \frac{\exp(ikr)}{r} \langle V \rangle \Psi(\mathbf{Q}) \quad (4.7)$$

where  $\mathbf{Q} = \mathbf{k}' - \mathbf{k}$  is the *scattering vector* describing the momentum transfer, and the angle brackets denote the ensemble average.

Although not explicitly stated in the equation,  $\Psi(\mathbf{Q})$  is actually a time dependent property as the locations of the scattering units  $\mathbf{R}_i$  can change in time. For example, in solids the atoms are not static but vibrate around their average positions, affecting the scattered intensity. In liquids atoms or particles are not fixed to specific sites but constantly move around. In case that the time resolution of a scattering experiment is too low to probe the instantaneous configuration of the scatterers, the outcome of a scattering experiment yields the temporal average of the structure. For example, if the exposure time taken to collect a detector image is much longer than the structural relaxation time of the samples, the measured detector image corresponds to an average over all configurations that are sampled during the exposure.

Apart from its time dependence,  $\Psi(\mathbf{Q})$  obviously depends on the interaction between the probing radiation (e.g. neutrons, x-rays) and the target, determined by  $V$ . Neutrons and x-rays interact differently with the scatterers (atoms). While neutrons mainly interact with the nucleus (protons and neutrons) via the strong interaction or the magnetic structure of the sample, x-rays most dominantly are scattered by electrons. As will be discussed later in section 4.5 it is useful to write the interaction potential in terms of *atomic form factors*, which describe the scattering amplitude of isolated atoms.

## 4.4 Scattering Cross sections

The fundamental physical quantity measured in a scattering experiment is the *double differential scattering cross section*

$$\frac{d^2\sigma}{d\Omega dE_f} \quad (4.8)$$

The double differential scattering cross section gives the number of particles having an energy  $E_f$  that is scattered into the solid angle  $d\Omega$  with respect to the incident flux of particles having an energy  $E_i$ . The double differential scattering cross section thus represents the probability that an incoming photon is scattered



with an energy transfer  $\Delta E = E_f - E_i$  into the solid angle  $d\Omega$ , and hence determines the number of particles measured with a detector at the position defined by the two angles  $\theta$  and  $\phi$  (see figure 4.1).

In most cases diffraction experiments are carried out using monochromatic radiation, so the incident wavelength  $\lambda_i$  and the energy  $E_i$  are fixed. More accurately, there is a natural, small spread in wavelength  $\delta\lambda$  and energy  $\delta E$ , and the distribution of wavelengths and energies are sharply peaked around  $\lambda_i$  and  $E_i$ . For ideal elastic scattering no energy is transferred among the probing particles (incident beam) and the sample, so that all scattered waves (particles) have the same energy as the probing radiation. Also, due to their finite energy resolution, detectors not always can discriminate particles of similar energies, and hence the counting is performed over the spread of energies. In this case the energy resolution is lost and the scattering experiment is described by the *differential cross section*

$$\frac{d\sigma}{d\Omega} = \int \frac{d^2\sigma}{d\Omega dE_f} W(E) dE_f \quad (4.9)$$

obtained by an integration of equation 4.8 over the band pass  $W(E)$  of the detector [113].

For an incident flux density  $i_0$ , the intensity of the scattered beam in the area  $dA$ ,  $I_s dA$  is given by [113]

$$I_s dA = i_0 |\Phi|^2 r^2 d\Omega = i_0 d\sigma \quad (4.10)$$

therefore

$$\frac{d\sigma}{d\Omega} = |\Phi|^2 r^2 = \langle V \rangle^2 |\Psi(Q)|^2 \quad (4.11)$$

Equation 4.11 states that the probability that a particle (wave) is scattered into the solid angle  $d\Omega$  is given by the square of the sample scattering amplitude  $\Psi(Q)$  multiplied by the square of the mean scattering potential  $V$ . Accordingly, the number of particles, i.e. the intensity, measured at the solid angle  $d\Omega$ , is proportional to the square of the sample scattering amplitude  $\Psi(Q)$ .

## 4.5 Scattering of Photons - a closer look

Photons mainly interact with the electrons of atoms; their interaction with the core is negligible. The electromagnetic field of the incoming wave couples to the charge density associated to the spatially distributed electrons, causing them to oscillate, which in turn results in the emission of electromagnetic waves. The secondary waves formed superpose on the stimulating wave and interfere with each other, yielding an intensity pattern that is characteristic for the charge distribution and thus the atomic structure of the material.

### 4.5.1 Scattering of photons with isolated atoms

As discussed above, the outcome of a x-ray scattering experiment is essentially determined by the spatial distributions of the electrons. However, the fact that electrons are mostly tied to atomic cores justifies to replace the spatial distributions of the electrons  $\rho_{el}(r)$  by the positions of the atoms, given by *atomic density*  $\rho_{at}(r)$ . In order to do so the x-ray scattering potential of a single atom is needed. The latter can be obtained by considering each volume element of the electronic shell as the origin of a scattering event whose magnitude is weighted by the local charge density, and integrating all emanating waves over the electron distribution of the atom. The result is called the *atomic form factor*  $f_0$

$$f_0 = \int_{atom} \rho_{el}(\mathbf{r}) \exp(i\mathbf{Q}\mathbf{r}) d\mathbf{r} \quad (4.12)$$

which in case of a spherical distribution becomes [113]

$$f_0 = 4\pi \int_0^\infty \frac{\rho_{el}(r) \sin(Qr)r^2}{Qr} dr \quad (4.13)$$

The atomic form factor describes the scattering strength of an isolated atom. Equation 4.12 shows that the magnitude of  $f_0$  is determined by  $\rho_{el}$  and a function of  $\mathbf{Q}$ . This  $Q$ -dependence must be taken into consideration when evaluating x-ray diffraction data.

In fact, equation 4.12 is only an approximation in the sense that it only describes the coherent part of the scattered intensity. According to the NIST standard, the total (x-ray) atomic form factor  $f$  is “the resonant scattering amplitude of x-rays by charge (primarily electron) density [115]”. In fact, it is a complex number whose real and imaginary part sum up the distinct interaction mechanisms of photons with atoms.

$$f = Re(f) + iIm(f) = f_0 + f' + f_{NT} + if'' \quad (4.14)$$

The real component  $Re(f)$  is composed of the “normal” coherent scattering factor  $f_0$ , the “anomalous” scattering factor  $f'$ , and the small nuclear Thomson term  $f_{NT}$ . The imaginary component  $Im(f) = f''$  is directly related to the atomic photoabsorption cross-section  $\sigma_{PE}$ . Together  $f'$  and  $f''$  describe the anomalous dispersion and strongly depend the energy of the incident photons. The anomalous dispersion is a result of resonance effects of the incoming radiation and the electrons in the atoms. If the energy of the incoming wave is close to an absorption edge it stimulates the inner electrons, promoting an electronic transition from a lower energy level to an upper one. The real component  $f'$  is 180° out of phase of with the normally scattered radiation, and the imaginary component  $f''$  is 90° out of phase with the normally scattered radiation. Thus, anomalous dispersion results in a diminished intensity of the scattered radiation and can be rationalized as a consequence of the electronic transition that drains energy from the incoming beam [116].

### 4.5.2 The electron density description

Considering that  $V(r)$  in 4.3 for x-rays can be identified with the local electron density distribution makes clear that the amplitude of the total scattered wave  $\Psi_s$  is actually the Fourier transform  $\mathcal{F}$  of the electron density  $\rho_{el}(Q)$

$$\Psi_s(\vec{Q}) = \tilde{\rho}_{el}(Q) = \mathcal{F}(\rho_{el}(r)) = \int \rho_{el}(r) \exp(-i\vec{Q}\vec{r}) d\vec{r} \quad (4.15)$$

The intensity scattered into the solid angle  $d\Omega$  therefore can be written as

$$\frac{d\sigma_c}{d\Omega}(Q) \propto |\Psi_s(Q)|^2 = |\tilde{\rho}_{el}(Q)|^2 \quad (4.16)$$

Applying the convolution theorem for Fourier transformation to equation 4.16 reveals that the coherent part of the intensity scattered into the solid angle  $d\Omega$  corresponds to the Fourier transform of the *equal-time electron density-density correlation function*

$$C_{el}(r) = \langle \rho_{el}(r', t), \rho_{el}(r' + r, t) \rangle \quad (4.17)$$

where the angular brackets  $\langle \dots \rangle$  denote the ensemble average.

### 4.5.3 The atomic density description

Assuming that the total scattering potential of the sample can be written as a sum over the atomic form factors of the scatterers at the positions  $\mathbf{R}_i$ , i.e.  $V(\mathbf{r}) = \sum f_i \delta(\mathbf{r} - \mathbf{R}_i)$ , the transition from the electron density to the atomic density,  $\rho_{el}(r) \rightarrow \rho_{at} = N^{-1} \sum \delta(\mathbf{r} - \mathbf{R}_i)$  can be made. Here,  $\delta(\mathbf{r})$  denotes the *delta function* in three dimensions. The amplitude of the total scattered wave then becomes

$$\Psi_s(\mathbf{Q}) = \langle f \rangle^{-1} \sum f_i(\mathbf{R}_i) \exp(i\mathbf{Q}\mathbf{R}_i) \quad (4.18)$$

from what follows

$$\frac{d\sigma_c}{d\Omega}(\mathbf{Q}) = \frac{1}{N} \langle f \rangle^2 |\Psi_s(\mathbf{Q})|^2 = \frac{1}{N} \sum_{i,j} f_i f_j' \exp(i\mathbf{Q}(\mathbf{R}_j - \mathbf{R}_i)) \quad (4.19)$$

With the transition  $\rho_{el}(r) \rightarrow \rho_{at}$  the sample scattering amplitude  $\Psi(\mathbf{Q})$  in equation 4.18 can be recognized as the Fourier transform of the atomic positions  $\mathbf{R}_i$ . The fact that the scattered intensity is determined by the Fourier transform of the *equal-time atomic density-density correlation function*  $C_{at}(r)$  is an important insight. It shows that the outcome of a scattering experiment yields information on spatial density variations in the system. If it were possible to measure  $\Psi(\mathbf{Q})$  directly, real-space information on the structure could be immediately obtained by the inverse Fourier transformation of equation 4.18. However, detectors measure the scattered intensity not the amplitudes. Therefore the information on the angular distribution of the particles is lost; what survives is the information on the atomic separation [113]. As will be shown in the following the latter can be extracted from pair correlation functions, which are obtained by Fourier transforming the reciprocal-space intensity data back into real space data.

## 4.6 Corrections for the observed intensity

The total intensity measured during an experiment includes several effects that must be considered in order to derive information on the structure of the sample. The total intensity of the scattered wave  $I_t$  can be written as a sum of several contributions [113]:

$$I_T = I_C + I_{IC} + I_{MS} + I_{BG} \quad (4.20)$$

Here  $I_C$  is the coherent part,  $I_{IC}$  the incoherent part,  $I_{MS}$  is the multiple-scattering intensity, and  $I_{BG}$  is the background intensity. The information about the structure of the sample is contained in the coherent part of the scattered intensity,  $I_C$ . It is related to the coherent differential scattering cross section via

$$I_c = APC \frac{d\sigma_c}{d\Omega} \quad (4.21)$$

where  $A$  is the absorption factor, depending on the geometry of the sample and the nature of the scattering particle,  $P$  is the polarization factor, and  $C$  is a normalization factor needed to express  $\sigma_c/d\Omega$  in the units of intensity per atom [113]. The experimentally measured coherent part of the intensity  $I_c$  is thus modified by absorption and polarization. This must be taken into account when analyzing diffraction data (cf. chapter 5).

The aim of a scattering experiment is often to determine the total structure factor  $S(\mathbf{Q})$ , which is related to coherent part of the scattered intensity  $I_c$  via equation 4.23, and to transform it back into real space data. All other, non-negligible contributions to the measured intensity must be eliminated. This requires to apply several correction procedures and the raw intensity data  $I_{raw}$ . In the following the corrections performed to  $I_{raw}$  are named and described. The aim is to give a short overview of these effects rather than a complete mathematical and physical description. For a more detailed treatise the reader is referred to reference [113] and the references therein.

### Absorption correction

Some of the incoming radiation is attenuated by the sample. This needs to be considered for a proper data analysis. The mass-attenuation coefficient of a material can be calculated based on tabulated data for the different elements [113]. The linear absorption coefficient is obtained from multiplying it by the sample density. Alternatively, the sample attenuation can be measured experimentally. This can be accomplished by comparing the intensity of the beam in the absence of a sample,  $I_0$ , with the intensity  $I$  that is transmitted through a sample (cf. figure 4.2). The linear attenuation coefficient  $\mu$  is determined from the Beer-Lambert law,  $I = I_0 \exp(-\mu t)$ , and the sample thickness  $t$ . Modern analysis program like *PDFgetX2* [117] allow to calculate the theoretical attenuation coefficients based

on tabulated data. A comparison between the experimentally determined values and the theoretical values calculated using *PDFgetX2* is shown in figure 4.3. Obviously, the two methods yield nearly identical results.

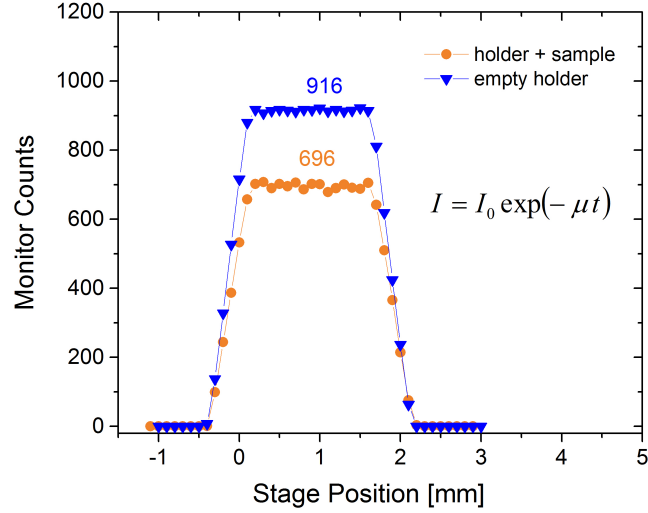


Figure 4.2: Experimental determination of the sample attenuation/absorption for the  $Pt_{60}Cu_{16}Co_2P_{22}$  bulk metallic glass.

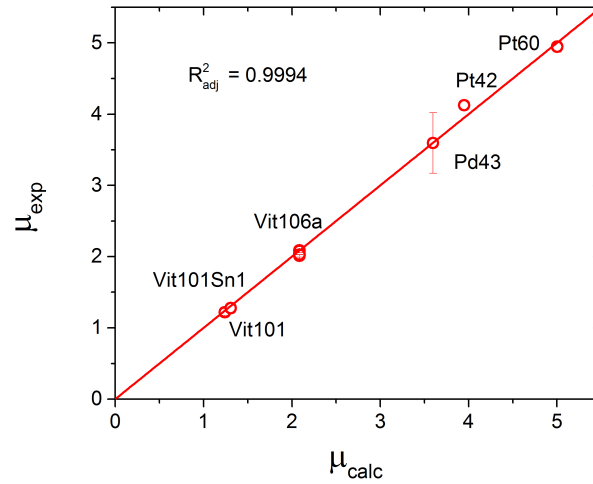


Figure 4.3: Calculated vs. experimental attenuation coefficients. The coefficients experimentally measured are compared to the theoretical attenuation coefficients calculated using the *PDFgetX2*-software [117].

## Background correction

In practice, the measured intensity does not only stem from the sample itself. The incoming and scattered intensity also interacts with experimental periphery of the sample, such as the experimental apparatus or the sample holder, making it necessary to quantify and eliminate these effects. This can be done in the following way. First, detector images of the experimental setup are taken in the absence of the sample itself. These patterns are considered to give the unscaled intensity of the background  $I_0^{BG}$ . Then, the transmittance of the incoming intensity through the sample is measured according to the procedure explained in the previous section in order to take into account that the scattered background intensity is modified due to the attenuation in the sample. This yields a scaling factor for the transmitted intensity which is applied to  $I_0^{BG}$  to determine the modified background intensity [113, 117] that is finally subtracted from the raw intensity.

## Polarization correction

As a consequence of the scattering process x-rays become polarized. This causes an angle dependence of the scattered intensity and hence needs to be considered. The *polarization correction factor*  $P$  is given by [118]

$$P = \frac{1 + A \cos^2(2\theta)}{1 + A} \quad (4.22)$$

where  $A$  is a factor depending on the degree of polarization of the incoming beam and  $2\theta$  is the scattering angle. In case that the beam is fully polarized perpendicular to the scattering plane - a situation met in modern storage rings such as the PETRA III at DESY -  $A = 0$  so that  $P = 1$ . In this case there is no need for a polarization correction. However, this is not always the case. If the beam is for example monochromatized through Bragg scattering on a crystal it becomes polarized and its polarization must be accounted.

## Inelastic coherent scattering

Inelastic scattering refers to any scattering process in which the kinetic energy of an incident particle or wave is not conserved. In case of photons there are various mechanisms that can lead to an exchange of energy between the incident beam and the sample. The typical x-ray energies used in diffraction or scattering experiments are in the range of a few to about 100 keV. In contrast, the energy range of most excitation processes, e.g. phonons is much lower reaching from  $meV$  to  $eV$  [113]. Accordingly, the resolution of the energy transfer associated with these processes would require energy resolutions of the order of  $10^{-6}$  [113]. This however is often far beyond the energy resolution of the detectors used

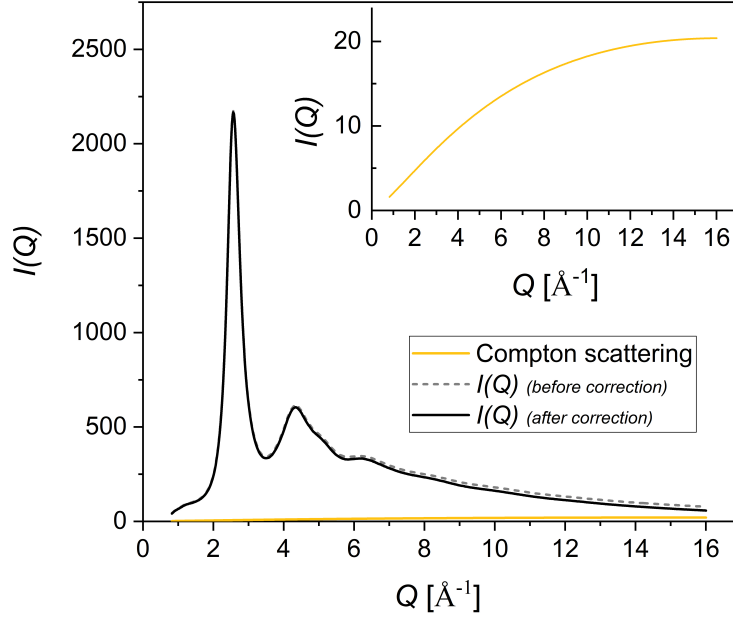


Figure 4.4: Compton Scattering for the  $Zr_{58.5}Cu_{15.6}Ni_{12.8}Al_{10.3}Nb_{2.8}$  (Vit.106a) bulk metallic glass forming liquid measured in the electrostatic levitation (ESL) setup.

during an x-ray scattering experiment. In this case the detector cannot discriminate between the coherent inelastic scattering, e.g. phonon scattering, and the “purely elastic” scattering, and the measured “elastic” intensity in fact includes the unresolved low-energy inelastic scattering [113].

### Compton Scattering

The interaction of photons with electrons can give rise to another type of intensity that imposes to the elastic coherent scattering. If a photon interacts with a weakly or unbound electron it can transfer some of its energy to the electron. In consequence the wavelength of the scattered photon increases. This scattering mechanism is referred to as *Compton scattering*. The Compton scattering is an inelastic, incoherent process, and contains information about the momentum distribution of the electrons. However, due to its incoherent character it does not bear information on the structure and hence needs to be eliminated for structural analysis. This can either be done by directly determining the Compton scattering experimentally, or by calculating its intensity, and subtracting it from the measured intensity. The ratio of the Compton scattering to the unmodified scattering becomes larger for lighter atoms, and increases with increasing beam energy. Its magnitude strongly varies with the scattering angle as shown in fig-

ure 4.4. At large  $Q$  the incoherent Compton scattering makes a non-negligible contribution to the overall intensity. This can cause a low signal-to-noise ratio (STNR) at higher angles, when the Compton scattering is subtracted from the total intensity. However, the high fluxes available at modern facilities together with the use of 2D array detectors normally yield high counting statistics even at large  $Q$ . Modern x-ray data analysis software enables to calculate and subtract the Compton scattering by relying on tabulated data from data bases such as the International Tables of Crystallography C [119]. For a more detailed treatise of the Compton scattering corrections the reader is referred to ref. [113] and the references given therein.

## 4.7 The total structure factor $S(Q)$

It is common to analyze the structure of liquids and gases in terms of their *structure factors* rather than of their intensities. The structure factor  $S(Q)$  is defined as [113]

$$S(Q) = \frac{I_c(Q)}{N \langle f(Q) \rangle^2} \quad (4.23)$$

and can be regarded as the normalized coherent intensity. In case that there are scatterers of different strengths, it is common to eliminate the so-called Laue monotonic diffuse scattering which stems from the imperfect cancellation of intensity at destructive interference conditions, given by  $\langle (f - \langle f \rangle)^2 / \langle f \rangle^2 \rangle$ , so that the structure factor becomes [113]

$$S(Q) = 1 + \frac{1}{N \langle f(Q) \rangle^2} \sum_{i \neq j} f_i^*(Q) f_j(Q) \exp(iQ \mathbf{r}_{ij}) \quad (4.24)$$

where  $\mathbf{r}_{ij}$  is the vector from the scatterer located at  $\mathbf{R}_i$  to the scatterer located at  $\mathbf{R}_j$ . For an isotropic material, e.g. a liquid, a glass, or a powder of crystals,  $\mathbf{r}_{ij}$  has equal probability in all directions so that  $S(Q)$  is given by [113]

$$S(Q) = 1 + \frac{1}{N \langle f(Q) \rangle^2} \sum_{i \neq j} f_i^*(Q) f_j(Q) \frac{\sin(Qr_{ij})}{Qr_{ij}} \quad (4.25)$$

referred to as the *Debye equation*.

## 4.8 From reciprocal space to real-space

The spatial distribution of the coherently scattered intensity  $I_c$  is determined by the Fourier transform of the (electron) density-density correlation function, which



describes density variations in the atomic configuration. Accordingly, Fourier-back-transformation of the intensity data ( $I_c$  or  $S(Q)$ ) enables to extract information on the real space structure. As will be shown it is useful to define the *reduced structure function*

$$F(Q) = Q[S(Q) - 1] \quad (4.26)$$

which in case of a homogeneous, isotropic material becomes [113]

$$F(Q) = \frac{1}{N \langle f(Q) \rangle^2} \sum_{i \neq j} f'_i(Q) f_j(Q) \frac{\sin(Qr_{ij})}{r_{ij}} \quad (4.27)$$

It can be shown [113] that the sine Fourier transformation of  $F(Q)$  directly yields the *radial distribution function* (RDF)  $R(r)$

$$\frac{R(r)}{r} = 2\pi^{-1} \int_0^\infty F(Q) \sin Qr dQ \quad (4.28)$$

which is related to the *pair distribution function* (PDF),  $g(r)$ , via

$$R(r) = 4\pi r^2 \rho_0 g(r) \quad (4.29)$$

The above equations are strictly speaking only valid if the entire  $Q$ -range  $[0; \infty]$  is considered. However, in practice the measured  $Q$ -range is limited. For example, when a 2D array detector is used, the high limit  $Q_{max}$  is determined by its size and its distance to the sample. The lower limit  $Q_{min}$  is often determined by the size of the beam stop that is needed to shield the detector from the high-intensity direct beam. In this case the Fourier transformation in equation 4.28 is performed over the finite range  $[Q_{min}; Q_{max}]$ , and the behavior at the limits  $Q \rightarrow 0$  and  $Q \rightarrow \infty$  is not included, so that a part of the information is lost. Considering the reciprocal nature of the  $Q$ -space, the information stored in the low- $Q$  limit corresponds to structural features whose size is of the order of nanometers. Information on this length scale can be obtained by small angle scattering (SAXS) where a large sample-to-detector distance is chosen to magnify the low- $Q$  what in turn sacrifices the high  $Q$ -range. The latter however is important to obtaining a high quality PDF since a too low  $Q_{max}$  value results in artifacts, i.e. so-called termination ripples with a wavelength  $\lambda \approx 2\pi/Q_{max}$ . Measuring the PDF in a single measurement thus demands to find a reasonable compromise between  $Q_{min}$  and  $Q_{max}$ .

Due to the truncation of the  $Q$ -range the Fourier transform no longer yields the RDF (equation 4.28) [113]. Instead, in case that all the small-angle scattering is below  $Q_{min}$ , the integration from  $Q_{min}$  to  $Q_{max}$  yields the *reduced pair distribution function*  $G(r)$  [113]

$$G(r) = 2\pi^{-1} \int_{Q_{min}}^{Q_{max}} F(Q) \sin Qr dQ \quad (4.30)$$

The function is related to the PDF via [113]

$$G(r) = 4\pi r \rho_0 [g(r) - 1] = 4\pi r [\rho(r) - \rho_0] \quad (4.31)$$

Which of the distribution functions is most suitable depends on the situation. Each of these functions has its own characteristics, advantages and disadvantages. The different correlation functions are briefly discussed in the following. For a comprehensive comparison of the different correlation functions used, the reader is referred to [120].

## 4.9 Pair Correlation functions

### 4.9.1 The radial distribution function

The radial distribution function is an intuitively easily conceivable function. Inserting equation 4.27 into equation 4.28 and performing the integration yields [113]

$$R(r) = \frac{1}{N \langle f \rangle^2} \sum_i \sum_j f_i^* f_j \delta(r - r_{ij}) \quad (4.32)$$

In case of a single species of scatterers the weighting factors  $w_{ij} = f_i^* f_j / \langle f \rangle^2$  cancel out.

$$R(r) = \frac{1}{N} \sum_i \sum_j \delta(r - r_{ij}) \quad (4.33)$$

Integration of  $R(r)$  from  $r_1$  to  $r_2$  yields

$$\int_{r_1}^{r_2} R(r) dr = \frac{1}{N} \int_{r_1}^{r_2} dr \sum_i \sum_{j \in S} = N_{12} \quad (4.34)$$

the average number  $N_{12}$  of atoms in between  $r_1$  and  $r_2$ . Note that  $i$  runs over all atoms in the system, while the summation over  $j$  is carried out only over atoms belonging to the shell defined by  $r_1$  and  $r_2$  around the atom  $i$ . Thus, the quantity  $R(r)dr$  directly gives the number of atoms in an annulus of thickness  $dr$  at distance  $r$  from another atom. This can be used to calculate the coordination number,  $N_C$ , if the integration is performed over a single coordination shell.

### 4.9.2 The pair density function

The *pair density function*  $\rho(r)$  yields the variation of the density at the distance  $r$  from a reference particle situated at the origin. Recalling that  $R(r)dr$  gives the average number of atoms in the annulus of thickness  $dr$  at  $r$ ,  $dn(r)$ , and that its volume is given by  $dV = 4\pi r^2 dr$ , the local number density is given by

$$\rho(r) = \frac{dn(r)}{dV(r)} = \frac{R(r)}{4\pi r^2} \quad (4.35)$$

An advantage of  $\rho(r)$  is that it emphasizes the short-range order. In a sample with perfect structural coherence, e.g a perfect crystal, the amplitude of oscillations in  $\rho(r)$  ceases with a functional dependence of  $r^{-1}$  [113]. However, as uncertainties in the data fall off like  $r^{-1}$  the accentuation of the short range order is rather cosmetic as the error bars scale with the amplitude of the signal [113].

### 4.9.3 The pair distribution function

The *pair distribution function* (PDF)  $g(r)$  is defined as the ratio between the local density  $\rho(r)$  at a distance  $r$  and the global average density  $\rho_0$ .

$$g(r) = \frac{\rho(r)}{\rho_0} \quad (4.36)$$

Just as  $\rho(r)$ , the PDF  $g(r)$  is a pair correlation function that measures the local density variations. It gives information on how much the local density deviates from the average density. Being normalized, the  $g(r)$  is a measure of the probability to find an atom at the distance  $r$  if another atom is situated at the origin.

### 4.9.4 The reduced pair distribution function

The reduced pair distribution function  $G(r)$  is the function that is directly obtained from Fourier transformation of the reciprocal space data when the transformation is carried out over a finite  $Q$ -range [113]. Due to the lower limit  $Q_{min}$  the information stemming from small angle scattering below  $Q_{min}$  is not included. Thus,

$$G(r) = R(r)/r - L(r) \quad (4.37)$$

where  $L(r)$  is the small angle scattering term corresponding to the Fourier transform of  $F(Q)$  in the  $Q$ -region below  $Q_{min}$  [113]. In case of an infinite system of uniform number density [113],  $L(r) = 4\pi r \rho_0$ , thus

$$G(r) = 4\pi r [\rho(r) - \rho_0] = 4\pi r \rho_0 [g(r) - 1] \quad (4.38)$$

One of the advantages of  $G(r)$  it that it is directly obtained from the diffraction data without the need to determine the number density  $\rho_0$ , required to calculate  $g(r)$  or  $\rho(r)$ . In case of metallic liquids the latter can be difficult as the melts are often reactive and prone to contamination by their environment, e.g. the atmosphere, crucible or sample holders. A nice and sophisticated approach to prevent this are levitation techniques, such as electrostatic levitation (ESL), enabling to study the melts in crucible free environments. Another advantage of  $G(r)$  is related to the fact that the random uncertainties in the data are constant in  $r$  [113]. This makes the comparison of the correlation function calculated from a model and the experimentally obtained correlation function easier as fluctuations

in these two have the same significance at all  $r$  [113]. Moreover, provided that the structure is a perfectly periodic infinite crystal and a perfect resolution measurement is performed oscillations in  $G(r)$  persist up to infinity with a constant peak-to-peak amplitude [113]. Although these conditions are never met in a real measurement, the amplitude of the oscillations in  $G(r)$  can be used to study the structural coherence of the sample [113]. The larger is the structural incoherence, the faster is the decay of the oscillations with increasing  $r$ , and vice versa.

## 4.10 Multi-component systems

In multicomponent systems one is often interested in the local structure around a particular species. For instance, one aims to explore details on the chemistry of the local coordination environment, i.e. on the probability that atoms of a species  $a$  are in direct neighborhood of a species  $b$ . This information is provided by so-called *partial pair distribution functions*  $g_{ij}$ . In analogy to equations 4.33, 4.35 and 4.36, the partials can be defined as [113]

$$g'_{a,b} = \frac{1}{4\pi N \rho_0 r^2} \sum_{i \in a} \sum_{j \in b} \delta(r - r_{ij}) \quad (4.39)$$

so that the total pair distribution function would be given by  $g(r) = \sum_a \sum_b g'_{a,b}(r)$ .

Accordingly, the total scattering from a multi-component system is the sum of all the contributions stemming from the individual partials, i.e. [113]

$$S(Q) = \sum_i \sum_j S'_{ij}(Q) \quad (4.40)$$

Although valid, these definitions are not the standard. Most commonly the so-called Faber-Ziman formalism is used [113]. In this formulation the total structure factor is decomposed into a weighted sum of its partials  $S_{ab}$

$$S(Q) = \sum_a \sum_b \frac{c_a c_b f_a(Q) f_b(Q)}{(\sum_a c_a f_a(Q))^2} S_{ab}(Q) = \sum_a \sum_b w_{ab} S_{ab} \quad (4.41)$$

where  $w_{ab}$  defined by equation 4.41 are weighting factor that take into account the concentration  $c_a$  and scattering strength  $f_a$  of the species  $a$  [113]. The factorization has the convenience that the partials tend to unity in the limit  $Q \rightarrow \infty$ , and  $S_{ab}$  are the structure factors that one would measure if the whole sample was made up of the pairs  $ab$ .

The Fourier transform of  $S_{ab}$  via equation 4.30 yields  $G_{ab}(r)$ , so that the total reduced pair distribution function  $G(r)$  can be written as [113]

$$G(r) = \sum_a \sum_b w_{ab} G_{ab}(r) \quad (4.42)$$

The total PDF then is given by

$$g(r) = \sum_a \sum_b w_{ab} g_{ab}(r) \quad (4.43)$$

where  $g_{ab}(r) = \sum_a \sum_b w_{ab}^{-1} g'_{ab}(r)$  with respect to equation 4.39 [113].

In case that  $f$  is a function of  $Q$ , the total PDF is not exactly the weighted sum of its partials, as the  $Q$ -dependence is “carried” into the Fourier transformation. Strictly speaking the transition from equation 4.41 to equation 4.42 and equation 4.43 is only valid if  $w_{ab}$  has negligible  $Q$ -dependence. This conditions is met for neutrons but not for x-rays. A frequently-used approach to solve this issue is the so called Morningstar-Warren approximation [121]. In this approximation the atomic form factor of a scatterer  $i$  is decomposed into the product

$$f_a(Q) = f_a(0) \frac{\sum c_a f_a(Q)}{\sum c_a f_a(0)} \quad (4.44)$$

with the further assumption that  $f_a(0) \cong Z_a$ . Thus, the atomic form factor of a scatterer  $a$  is approximated as the product of its atomic number  $Z_a$  and the  $Q$ -dependence of the average form factor. The validity of the Morningstar-Warren approximation is justified by its success to describe the PDFs of multicomponent systems [113].

## 4.11 Structural information provided by correlation functions

As detectors measure the intensity of the scattered radiation, not their amplitudes, a part of the information of the real space structure of a sample is lost. What remains is the information on the distributions of atomic separations summarized in the pair correlation functions described above. Insights on the orientational order can be only obtained by establishing structural models and comparing them to the experimental data (e.g. reference [57]), either in real or in reciprocal space (see e.g. [9, 51]).<sup>5</sup> Still, also the correlation functions alone bear useful information on the structure, as discussed in the following.

### The peak shape

The shape of a peak reveals information on the atomic probability distribution (APD) determined by the interatomic pair potential. In a perfect crystal at 0 K the histogram of atomic distances is a sum of delta functions. The PDF thus consists of very sharp peaks whose position corresponds to the individual atomic separations in conformity with the lattice structure. However, any atomic

---

<sup>5</sup>A detailed treatise on structural modeling can be found e.g. in [9] or in [113].

disorder in form of zero-point or thermal motion, or any displacement of the atoms away from their ideal lattice sites results a variation of atom-atom distances and thus leads to broadening of the peaks. In case of a crystalline solid in harmonic approximation, the atomic probability distribution is Gaussian and so the peaks in the PDF are to a high degree of accuracy also Gaussian [113]. On the other hand, for a non-symmetric APD the peaks in the PDF are skewed [113].

## Peak positions

In case of a symmetric atomic probability distribution (e.g. Gaussian), the position of the maximum of the  $n^{th}$ -peak corresponds to the average separation of atomic pairs in the  $n^{th}$  coordination shell. Obviously, in case of a skewed, i.e. non-symmetric, distribution, the average separation no longer given by the maximum of the peak, but by the centroid of the area. In practice the coordination shells often interpenetrate each other, making it difficult to properly set the boundaries. In principle this can be solved by decomposing the PDF into different peaks, by modelling the peaks with analytic functions.

In a multicomponent system the situation is even more complex. A peak in the total PDF is composed of several subpeaks corresponding to its partial PDFs. There are several methods that allow to determine the partials, e.g. EXAFS, anomalous x-ray scattering and isotopic substitution<sup>6</sup>. However, in practice the decomposition of the total PDF into its partials in systems having more than two species is often difficult. For a material composed of  $n$  different species, the total PDF, as well as the total structure factor  $S(Q)$ , consist of  $(n + 1)n/2$  different partials. For  $n = 5$  there are in total 15 partials that give information about the distribution and structure of the individual species. Moreover, the PDF of a multicomponent system is a (scattering strength-) weighted histogram of the atomic pair distances, and the transition from equation 4.32 to equation 4.33 is only valid for  $f_a^* f_b = \langle f \rangle^2$ . In all other cases the  $Q$ -dependence of the weighting factors  $w_{ab}$  (cf. equation 4.41) is carried into the Fourier transformation of  $S(Q)$  into  $G(r)$  and thus will affect the shape of the peaks. Obviously, the major contributions to the total PDF stem from the pairs with the highest values of  $c_a f_a c_b f_b$ . In bulk metallic glass formers this is often the case for the main constituent, i.e. the solvent species, of the alloy. Figure 4.5 shows the Faber-Ziman weighting factors of the  $Zr_{58.5}Cu_{15.6}Ni_{12.8}Al_{10.3}Nb_{2.8}$ . As visible the Zr-Zr pairs make the majority of the scattered signal.

## The peak area

For monatomic systems the area  $A$  under the RDF corresponds to the number of atoms within the integration limits (cf. equation 4.34). Applied to a single peak,

---

<sup>6</sup>Isotopic substitution is only applicable in case of neutrons as the difference in x-ray scattering length of the isotopes is too weak to yield a notable changes in the diffraction patterns.

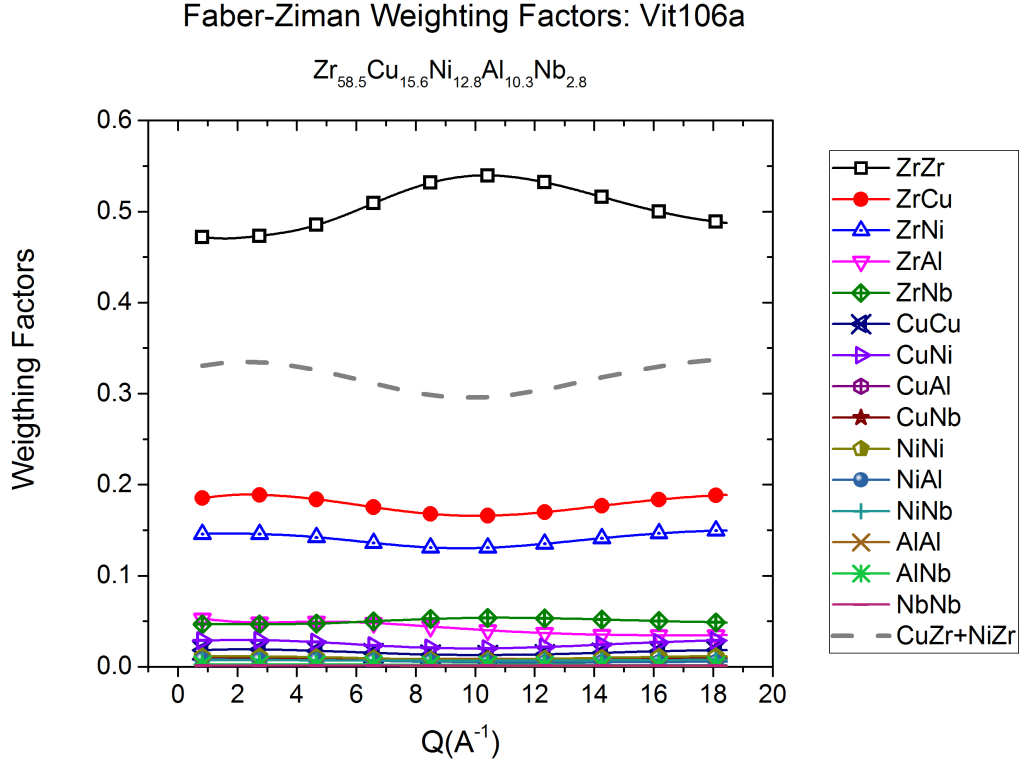


Figure 4.5: Faber-Ziman weighting factors of the Vit106a bulk metallic glass forming alloy. The Zr-Zr pairs contribute to about 50 % of the total structure factor. Together with the Zr-Cu and Zr-Ni pairs they make more than 80 % of the overall intensity. Including also the Zr-Al and Zr-Nb pairs, about 90 % of the intensity stems from correlations involving Zr atoms, while only about 10 % stems from other pairs.

$A$  gives the number of atoms inside a coordination shell. The number of nearest neighbors is given by the area underneath the first peak of the RDF, the number of the second nearest neighbors by the area underneath the second peaks, and so on. The accumulated number of atoms included in the sphere with a radius  $r'$  around a central atom is given by integrating  $R(r)$  from 0 to  $r'$ .

In case that the PDF can be decomposed into its partials, the peak area in the partials yields the partial coordination numbers. The partial coordination numbers contain information on the chemical ordering parameter. For example, in a binary system (A-B) the integration of  $g_{AB}$  over the first coordination shell yields the average probability that an atom of species  $A$  is surrounded by atoms of the species  $B$ . This allows the definition of order parameters that quantify the amount of chemical short-range order present in the systems, and are helpful to study (chemical) order-disorder transition.

# Chapter 5

## Materials, Methods and Experiments

### 5.1 X-ray Synchrotron Diffraction Studies

X-rays interact only weakly with matter. Moreover, the amorphous structure of glasses and liquids results in a much lower scattered intensity than in crystalline materials. Therefore, a large flux of the incident radiation is needed in order to obtain high quality data. This condition is met by synchrotron radiation. The high brilliance of latest generation synchrotron sources such as PETRA III at DESY yields a large flux of incident photons, resulting in high-quality data with a low signal-to-noise ratio, even for relatively short exposure times. Accordingly, fast measurements can be performed, much faster than in case of neutrons, enabling structural investigations under rapidly changing conditions such as continuous heating or cooling experiments. The latter is of particular importance when one is interested in metastable or out-of-equilibrium systems, as in case of the present work where the structural changes of supercooled liquids and glasses are investigated. Even faster acquisitions can be performed with free electron lasers.

#### 5.1.1 Synchrotron radiation

When a charged particle is accelerated it emits electromagnetic radiation. According to classical electrodynamics, a charge  $q$  that is accelerated by  $a$ , emits a wave whose energy flux density, characterized by its pointing vector  $\mathbf{S}$ , at large distances  $r$  is given by [116]

$$\mathbf{S} = \frac{1}{(4\pi)^2} \frac{q^2 \mathbf{a}^2 \sin^2(\theta)}{\epsilon_0 c^3} \frac{1}{r^2} \mathbf{r}' \quad (5.1)$$

where  $\mathbf{r}'$  is the direction pointing to the observer and  $\theta$  denotes the angle



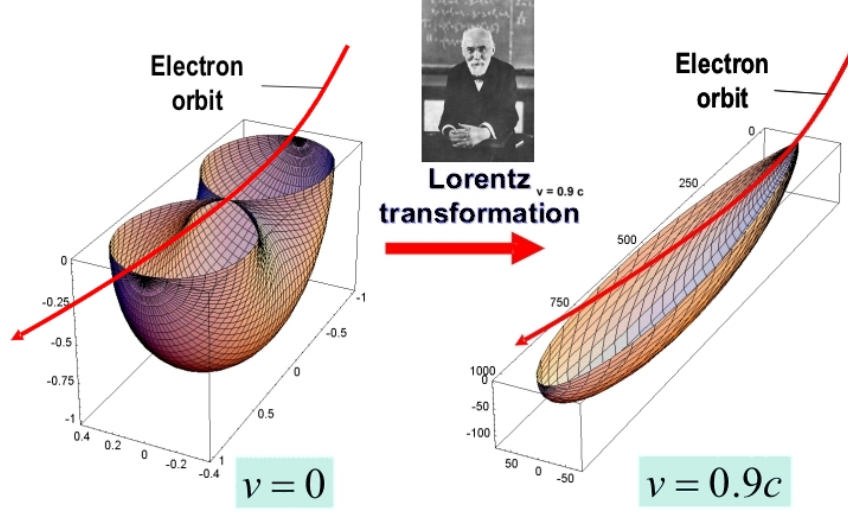


Figure 5.1: Sychrotron radiation cone: Relativistic effect on the spatial distribution of the emitted radiation. At zero relative velocity the spatial distribution of the emitted radiation is given by a doughnut-like pattern (left). With the transition to the relativistic regime (here: 90 % of the speed of light) a strong forward collimation of the emitted radiation occurs. The figure is taken from [122].

between the acceleration and the observer. Accordingly, the radiated power per solid angle is [116]

$$\frac{dP}{d\Omega} = \frac{q^2 a^2}{(4\pi)^2 \epsilon_0 c^3} \sin^2(\theta) \quad (5.2)$$

yielding a total emitted power per particle

$$P = \frac{1}{6\pi} \frac{q^2 \mathbf{a}^2}{\epsilon_0 c^3} \quad (5.3)$$

Equation 5.3 is the well-known *Lamor formulae* for a non-relativistic accelerated charge. Note that for a circular motion at angular frequency  $\omega$ ,  $\mathbf{a} = \omega^2 \mathbf{r}$ , with  $\mathbf{r}$  being the radius of the orbit. The Lamor formula shows that a larger acceleration, results in more power emitted by the particle. The above equations show that the emitted radiation has a doughnut-like spatial distribution (cf. figure 5.1). With the transition to the relativistic regime (Lorentz transformation) the spatial distribution of the emitted radiation changes, and, in case that the acceleration is perpendicular to the velocity, is given by [116]

$$\frac{dP}{d\Omega} = \frac{q^2 a^2}{(4\pi)^2 \epsilon_0 c^3} \frac{\sin^2(\theta)}{(1 - \beta \cos(\theta))^5} \quad (5.4)$$

where  $\beta$  is the charge velocity divided by the speed of light. The transition to the relativistic regime ( $\beta \rightarrow 1$ ) goes ahead with a strong deformation of the

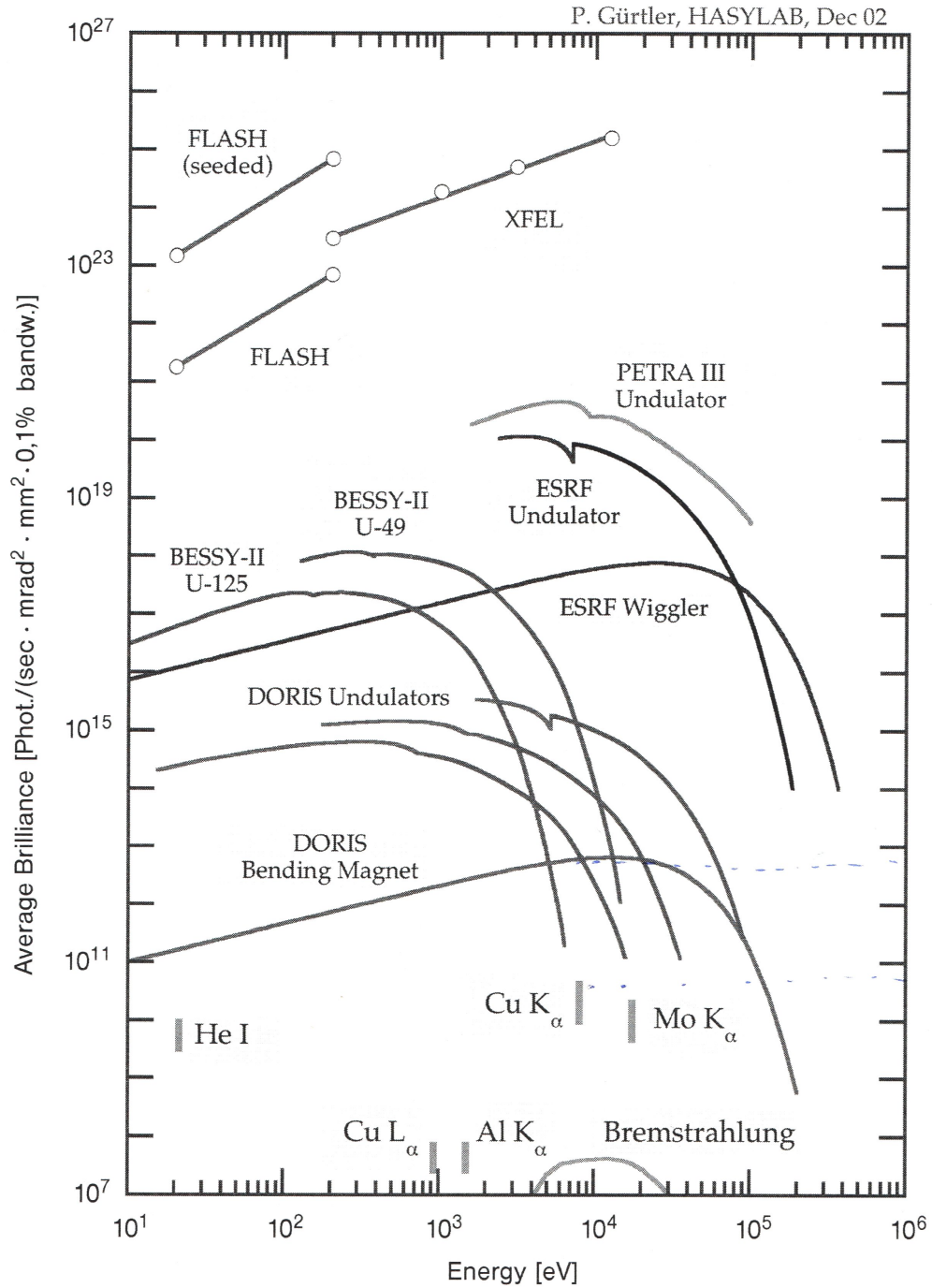


Figure 5.2: Comparison of the brilliance of different, x-ray sources. Compared to laboratory x-ray sources, synchrotron radiation has a five to ten order of magnitude higher brilliance, enabling much faster, spatially resolved measurements. With the use of wiggler and undulators a further increase in the brilliance can be obtained. Free electron lasers have the highest brilliance. The figure is taken from [116].

radiation pattern and results is a radiation cone that is strongly forward directed with respect to the velocity vector (cf. figure 5.1). Typical opening angles are in the range of a 0.1 - 1 mrad [116], so most of the emitted radiation is concentrated in a very narrow angular range. Due to the strong forward collimation and the circular motion, a stationary observer only sees a short radiation pulse every time a bunch of electrons passes by. Synchrotron radiation is thus a short-time pulsed radiation (cf. figure 5.3). The spectrum of wavelengths emitted spans several orders of magnitude ranging from infrared ( $10^{-4}$  m) down to hard x-ray radiation with wavelength as short as  $10^{-12}$  m [116]. This enables studies on larger objects such as cell structures down to objects having sizes of single atoms, opening a wide range of possible applications in almost all fields of applied and fundamental science: medicine, geology, biology, chemistry, crystallography, physics and materials. The wide applicability of synchrotron radiation relies on the following outstanding properties [116]: high intensities, small source sizes, strong collimation in forward direction, high degree of linear polarization in the orbit plane, elliptical or circular polarization above and below the orbit plane, well-defined pulsed time structure, and quantitatively known characteristics.

Its high quality properties makes synchrotron radiation a powerful tool for structural investigations of amorphous materials. In contrast to crystalline materials, where the scattered intensity concentrates among a few designated direction, the scattered intensity of an amorphous sample is diffuse. Accordingly, a high quality incident flux is needed to get high quality data with a satisfying signal-to-noise ratio. The former is given in terms of the *brilliance* defined as by the number of photons emitted per time interval, per opening angle, and per 0.1 % spectral bandwidth, divided by the source size [116]. A comparison of the brilliance of different x-ray sources is shown in figure 5.2. With the use of wigglers and undulators the brilliance can be further increased by several orders of magnitudes as discussed in more detail in the following section. Note the brilliance of synchrotron radiation is about five to ten orders of magnitude higher than for conventional laboratory x-ray tubes, enabling obtain higher quality data in shorter times combined with a better energy and spatial resolution.

### 5.1.2 Synchrotron Sources - Storage Rings, Wiggler, and Undulators

The first experimental observation of synchrotron radiation was made in 1947 at General Electrics during the acceleration of electrons [123]. Initially considered as an disturbing byproduct of particle accelerators affecting the machine performance, the growing demand of high intensity, high-quality radiation resulted in a growing number of facilities over the last decades, exclusively dedicated to the generation of synchrotron radiation [116]. At present, there are about 60 facilities (including free electron lasers) worldwide [124] serving researcher from all fields

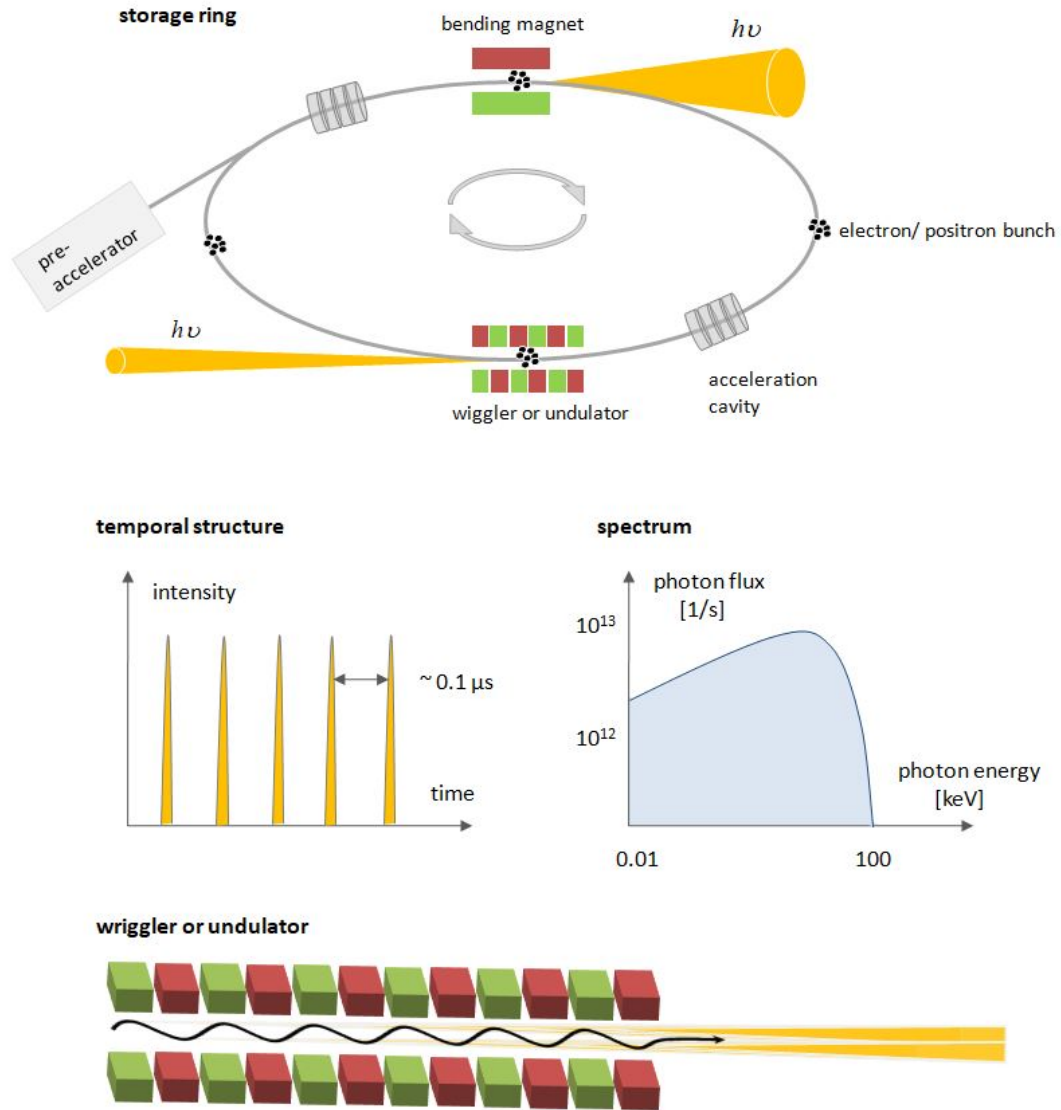


Figure 5.3: Schematic illustration of a storage ring. Charge bunches are pre-accelerated and forced onto an orbit by bending magnets. As a consequence of their acceleration they emit radiation which in the relativistic regime is strongly collimated in forward direction. Synchrotron radiation is a high-brilliance, pulsed radiation including a wide spectrum of energies. With the use of wigglers and undulators placed along the orbit the brilliance can be further improved.

of science. Most of the facilities dedicated to produce synchrotron radiation are *storage rings* (cf. figure 5.3). A typical storage ring is composed of accelerating cavities, bending magnets as well as special magnetic insertion devices, i.e. wigglers and undulators. The functional principle of a storage ring can be describe as follows. Bunches of electrons or positrons are traveling at a closed orbit at constant velocity at almost the speed of light (99.99 %). When they pass bending magnets or special magnetic insertion devices, i.e. wigglers and undulators, they are forced to follow a precisely defined trajectory, and due to the acceleration that the particles experience along this path they emit synchrotron radiation. The emitted radiation can be further amplified by Wrigglers and undulators. Wrigglers and undulators are special magnetic multipole devices with alternating magnetic fields that force the charges on usually sinusoidal trajectories. The radiation emitted in each half-cycle sums up, yielding a strong increase of the emitted intensity (cf. figure 5.3). The discrimination is made based on the *the wiggler parameter*

$$K := \alpha\gamma = \frac{eB_0\lambda_0}{2\pi m_e c} \quad (5.5)$$

giving the ratio of the deflection angle  $\alpha$  of the particles in the  $B$ -field with respect to the opening cone of the emitted radiation determined by  $1/\gamma$ , where  $\lambda_0$  is the period of the magnetic field and  $B_0$  the peak value [116]. For wigglers  $K > 1$  while for undulators  $K \leq 1$ . In undulators and wigglers the  $N$  magnetic periods can be considered as  $2N$  bending magnets with a bending radius determined by the strength of the alternating magnetic field. In case of wigglers the deflection of the electrons is large and the radiation cones do not interfere. Thus, the total emitted intensity scales with the number of magnetic periods  $I \propto N$ . In case of undulators, the geometry of the magnetic field is designed in a way that the emitted radiation can interfere constructively. The intensity of an undulator is therefore proportional to  $N^2$ . For a more detailed description of wigglers and undulators the reader is referred to [116] and references listed therein.

### 5.1.3 Experimental Conduct

#### In-situ x-ray diffraction studies on levitated molten droplets

Materials used in this study were prepared by arc-melting elements with purities ranging from 99.95 to 99.999 at.% in a high-purity argon Ti-gettered atmosphere. Small pieces were remelted in an arc melter to produce spherical samples with a mass of  $\approx 40 - 100$  mg and a diameter of about 2 - 3 mm suitable for electrostatic levitation and x-ray diffraction.

In-situ synchrotron x-ray scattering experiments were performed at the German Synchrotron (DESY) in Hamburg at the PETRAIII high intensity beamline P07. The measurements were performed in collaboration with the Institute for

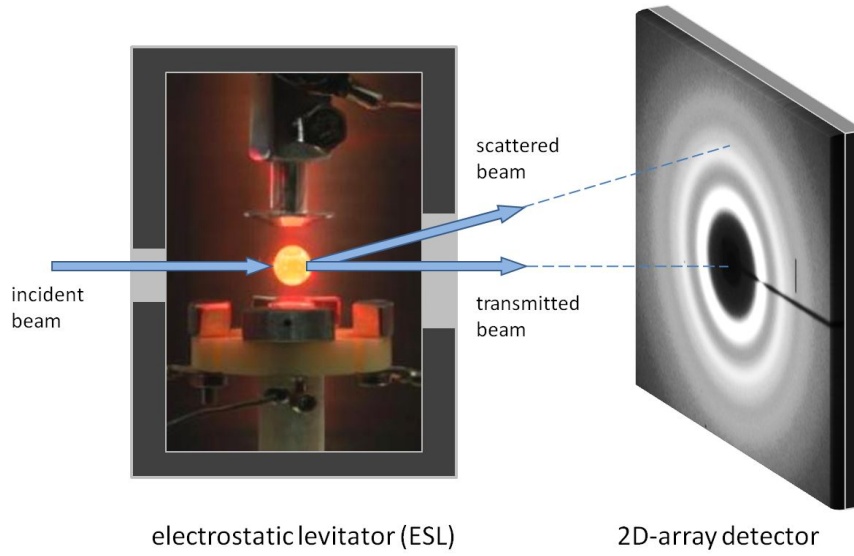


Figure 5.4: Experimental setup used for the high temperature structural analysis of metallic glass forming melts. Droplets of the alloy are levitated in an electrostatic levitator place upstream the synchrotron beam. The scattered intensity is measured using a 2D-array detector place downstream. The transmitted beam is captured by a beam-stop. The  $Q$ -range captured is determined can be adjusted by the sample-to-detector distance. The lower limit  $Q_{min}$  is defined by shading of the beam stop.

Material in Space from the DLR in Cologne. The x-ray diffraction experiments were carried out in transmission using a Perkin Elmer XRD1621 CsI bonded amorphous silicon detector (2048 x 2048 pixels,  $200 \mu\text{m}^2$  pixel size). The beam size was chosen as  $0.8 \times 0.8 \text{ mm}^2$ . The energy of the radiation was 100 keV corresponding to a wavelength of 0.124 angstrom. For continuous heating and cooling experiments, data with a temporal resolution of 0.5 s or 1 s were acquired. The temperature profiles were correlated to the diffraction patterns using the onsets of crystallization and melting determined from thermal analysis (DSC and DTA).

Measurements were performed using a custom-built electrostatic levitator (ESL) to provide a contact-less sample environment (see [125] for detailed design and parameters of ESL). In the ESL, the spherical samples are levitated against gravitational force by a vertical electrostatic field (cf figure 5.4) under high vacuum conditions ( $\approx 10^{-7}$  mbar). Electrostatic levitation requires sufficient positive charging of the sample which can be generated through capacitive, photoelectric or thermionic charging. At low temperatures, where thermionic charging is absent, a UV lamp creates surface charge by the photoelectric effect. Once the sample is heated, thermionic emission generates charging of the sample (Richardson's law). The position of the sample is measured and actively con-

trolled using two orthogonally arranged defocused lasers that cast the shadow of the sample onto position sensitive photodetectors. Together with two additional pairs of electrodes which control the lateral displacement of the molten droplet, the droplet is stabilized in the center between the vertical electrodes (see figure 5.4). The levitated sample is heated using two infrared Nd:YAG lasers ( $\lambda = 808\text{ nm}$ ). The temperature of the sample is measured using two pyrometers at two different positions at the sample with an estimated error of about 10 K. A temperature profile can be programmed and is controlled by adjusting the laser power. Under high vacuum conditions the maximum cooling rate that can be achieved is determined by purely radiative cooling of the droplet. According to the Stefan-Boltzmann law the cooling rate  $dT/dt$  for purely radiative cooling is determined by

$$mc_p dT/dt = 4\pi r^2 \sigma_{SB} \epsilon (T^4 - T_0^4) \quad (5.6)$$

where  $c_p$  is the specific heat capacity,  $r$  denotes the radius of the droplet,  $\sigma_{SB} = 5.670510^{-8} \text{ W/m}^2 \text{ K}^4$  is the Stefan-Boltzmann constant,  $\epsilon$  is the total hemispherical emissivity, and  $T_0$  is the temperature of the sample environment. Using the calibrated pyrometer signal the temperature of the samples can be monitored, and the specific heat capacity over emissivity,  $c_p/\epsilon$ , can be calculated from the cooling rates  $dT/dt$ , relying on equation 5.6.

### In-situ x-ray diffraction studies of glasses and supercooled liquids near the glass transition

The  $\text{Au}_{49}\text{Cu}_{26.9}\text{Si}_{16.3}\text{Ag}_{5.5}\text{Pd}_{2.3}$  (Au49) alloy was prepared by inductively heating the pure elements in  $\text{Al}_2\text{O}_3$  crucibles inside a high-purity argon atmosphere. Amorphous samples were produced by tilt-casting the melt into water-cooled copper molds. In case of  $\text{Pt}_{42.5}\text{Cu}_{27}\text{Ni}_{9.5}\text{P}_{21}$  (Pt42) and  $\text{Pt}_{60}\text{Cu}_{16}\text{Co}_{2}\text{P}_{22}$  (Pt60) the raw elements were molten inductively in a silica tube. Subsequently the master alloy was subjected to a fluxing procedure to minimize contamination. The fluxing procedure was performed in the molten state using dehydrated  $\text{B}_2\text{O}_3$ . Amorphous samples were produced by tilt-casting the melt into water-cooled copper molds.  $\text{Zr}_{58.5}\text{Cu}_{15.6}\text{Ni}_{12.8}\text{Al}_{10.3}\text{Nb}_{2.8}$  (Vitreloy106a or Vit106a),  $\text{Cu}_{47-x}\text{Ti}_{34}\text{Zr}_{11}\text{Ni}_8\text{Sn}_x$  (Vit101Snx) with  $x = 1, 2, 3, 4$  prepared by arc-melting elements with purities ranging from 99.9 to 99.999 at-% in a high-purity argon Ti-gettered atmosphere. The master alloys were re-melted in an arc-melting furnace and suction cast into water-cooled copper molds to create amorphous plates. Amorphous samples of the  $\text{Zr}_{44}\text{Ti}_{11}\text{Cu}_{10}\text{Ni}_{10}\text{Be}_{25}$  (Vitreloy1b or Vit1b) and  $\text{Zr}_{52.5}\text{Cu}_{17.9}\text{Ni}_{14.6}\text{Al}_{10}\text{Ti}_5$  (Vitreloy105 or Vit105) alloys were supplied by Liquidmetal Technologies. Samples for the synchrotron experiments were prepared by cutting thin discs or beams (thickness  $\approx 200\text{ }\mu\text{m}$ ) from amorphous rods or plates. In case of Au49, the samples were stored in a freezer at  $-18^\circ\text{C}$  prior to the measurements to avoid possible relaxation at ambient temperatures.

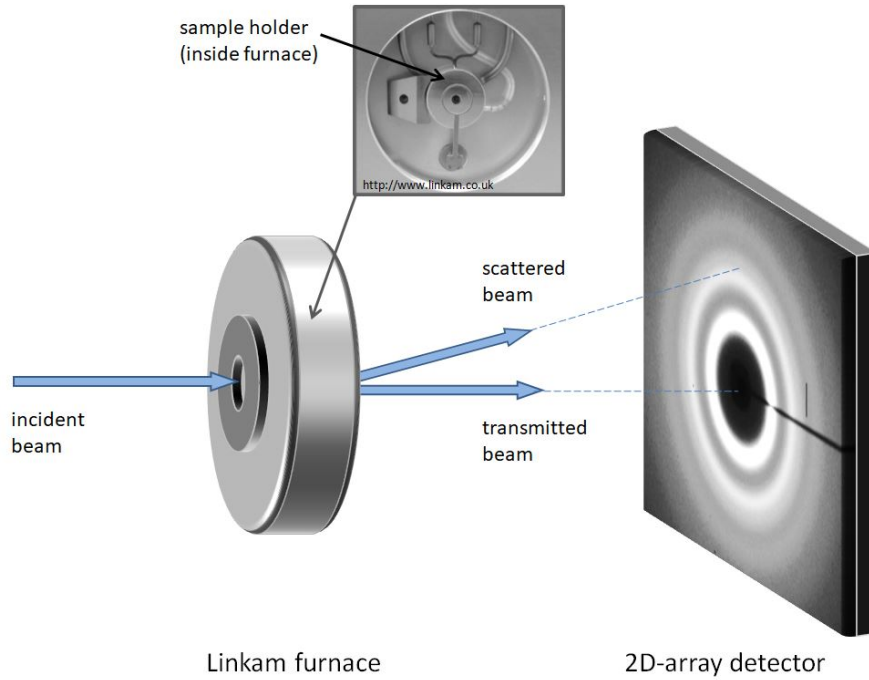


Figure 5.5: Experimental setup for synchrotron diffraction studies performed close to the glass transition. The samples are mounted in the Linkam furnace placed upstream. The Linkam furnace enables to measure the samples up to 600 °C under high purity inert gas atmospheres.

In-situ synchrotron x-ray scattering experiments were performed at the HASYLAB/DESY, Hamburg, with the PETRA III high intensity beamline P02.1. The x-ray diffraction experiments were carried out in transmission mode using a Perkin Elmer XRD1621 CsI-bonded amorphous silicon detector (2048 x 2048 pixels, 200  $\mu\text{m}^2$  pixel size). The beam size was 0.8 x 0.8 mm<sup>2</sup> with a wavelength of 0.207 Å (59.83 keV). The as-cast amorphous samples (except *Vit.1b* annealed) were heated from glass into the supercooled liquid region in-situ at a rate between 20 and 60 K/min under a flow of high-purity argon in a Linkam THMS 600 furnace.

#### 5.1.4 Details on Data Treatment

Analysis of the diffraction data is performed using the Fit2D data analysis software [126]. The exact position and orientation of between the sample and the detector, i.e. sample-to-detector-distance (SDD), the rotation angle of the tilting plane (RATP), the angle of detector tilt (ADT), as well as the beam center in  $x$  and  $y$  direction,  $(x_c, y_c)$  are determined by calibration using crystalline calibra-



tion standards (*Si* or *CeO<sub>2</sub>* powder samples) placed in the furnace at the position of the samples. The calibration substances are exposed and detector images are taken, the position of the diffraction rings is analyzed using Fit2D and compared to tabulated data, yielding precise values for SDD, RATP, ADT,  $x_c$ ,  $y_c$ . The sample absorption is measured for each sample at room temperature by moving the sample horizontally into, and out of the x-ray beam with a detector. The attenuation coefficients of the alloys are determined from the ratio between the transmitted intensity  $I$  (monitor counts) to the initial intensity (monitor counts) using the relation  $\mu t = -\ln(I/I_0)$  and assumed too remain constant upon heating. Dark images of the detectors are taken and subtracted from the measured detector images. The 2D detector images of the samples are azimuthally integrated using Fit2D, yielding the intensity raw data  $I(Q)_{raw}$ . A mask file is used in order to eliminate features originating from the surroundings (e.g. the beam stop) or dead pixels.

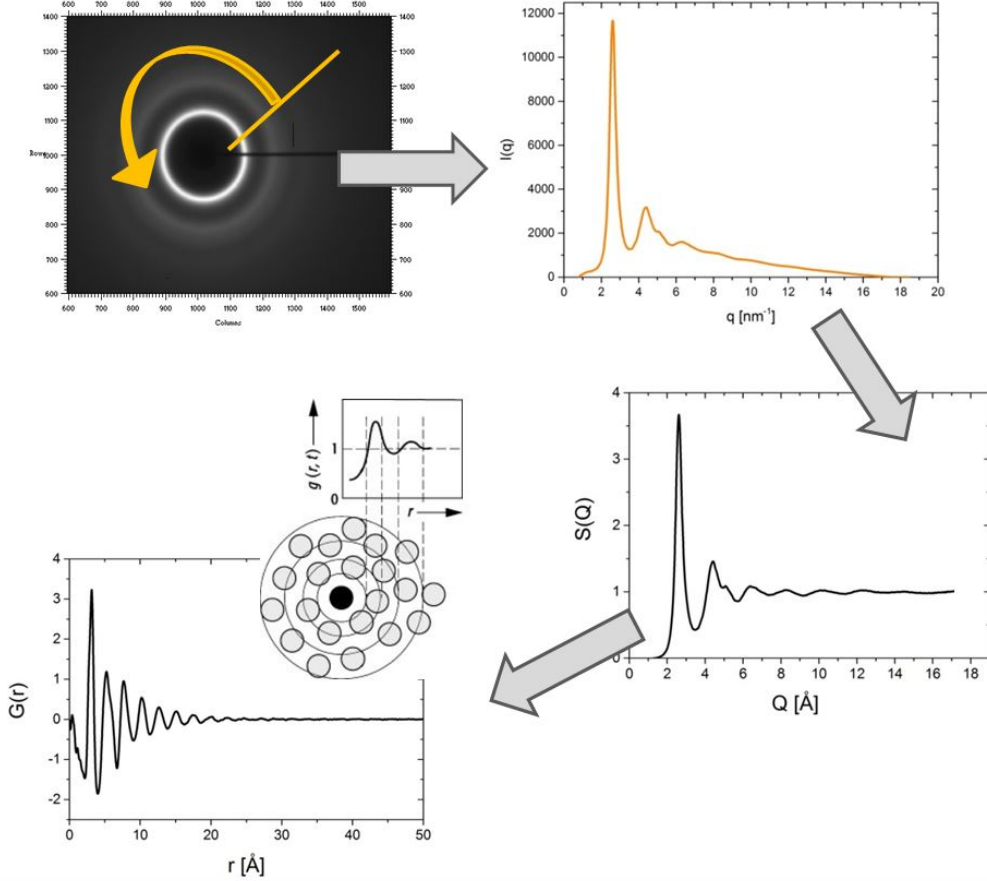


Figure 5.6: Steps involved in the data analysis: Integration of detector images to obtain  $I(Q)$  (*Fit2D*), calculation of  $S(Q)$ , and transformation to real space  $G(r)$  (*PDFgetX2*). Details on each step can be found in the main text.

Data analysis of the integrated raw intensity  $I(Q)_{raw}$  is performed using the *PDFgetX2* software [117]. After appropriate background subtraction taking into account absorption effects, the  $I(Q)$  data are corrected in terms of sample self-absorption, multiple scattering, Compton scattering, fluorescence, energy dependence of the detector, as well as Compton scattering, and the total structure factor  $S(Q)$  is calculated according to equation 4.24. The parameters for fluorescence and energy dependence of the detector are obtained by an optimization algorithm of the *PDFgetX2* software. The algorithm optimizes  $G(r)$  in the low- $r$  range below the onset of the first coordination shell in terms of minimizing the oscillations to obtain an as straight as possible linear decay behavior of  $G(r)$  with a slope of  $-4\pi\rho_0r$ . The reduced pair distribution function  $G(r)$  is obtained by ad hoc integration of the  $S(Q)$  data. As a result of this optimization  $S(Q)$  oscillates and decays well around 1, and  $S(Q) - 1 \rightarrow 0$  for large  $Q$  as demanded. The  $Q$ -range used for Fourier transformation is properly chosen based on the quality of the  $Q$  data. While theoretically the highest possible  $Q_{max}$  value gives the best resolution, practically a poor data quality (low-signal to noise ratio) at high  $Q$  can be detrimental. For the measurements performed in the Linkam furnace a  $Q_{max}$  in between 10 and 14  $\text{\AA}^{-1}$  is found to be the most reasonable choice. For the measurements performed in ESL a  $Q_{max}$  of 16  $\text{\AA}^{-1}$  is found to be appropriate. The peak positions of  $G(r)$  and  $g(r)$  are determined by cubic-spline interpolation using *OriginPro*. It is found that this procedure generates qualitatively equivalent results to fitting the peaks with Bi-Gaussian functions [127]. The maxima of the peaks is determined from the interpolated data using a scripted peak search procedure in *OriginPro*.

## 5.2 Thermophysical analysis

Different thermophysical measurements were performed in order to connect the structural data obtained from diffraction measurements with the thermal and volumetric behavior of the studied systems in the crystalline, glassy and liquid state. This section gives an overview of the measuring techniques and principles used: calorimetry (DTA and DSC), thermomechanical analysis (TMA), and dilatometry.

### 5.2.1 Calorimetry

Changes in the state of a physical system, e.g. chemical reactions or phase transformations, are associated with a heat exchange between the system and its environment. The aim of a calorimetric measurement is to measure the heat exchange  $\Delta Q$  as a function of temperature  $T$  or time  $t$ , and to derive information on the underlying processes. The quantity connecting  $\Delta Q$  with  $T$  is the “specific heat capacity”

$$c_p = m^{-1} \frac{\Delta Q}{\Delta T} \quad (5.7)$$

where  $m$  is the mass of the sample. The specific heat capacity is a material specific property that measures how much energy is needed to heat a unity mass of the sample about 1 unity in temperature. At constant pressure, the heat transferred is equal to the change in enthalpy of the system,

$$\dot{Q} = \frac{\partial Q}{\partial t} = \left( \frac{\partial H}{\partial t} \right)_p = \frac{d}{dt} \int m c_p dT \quad (5.8)$$

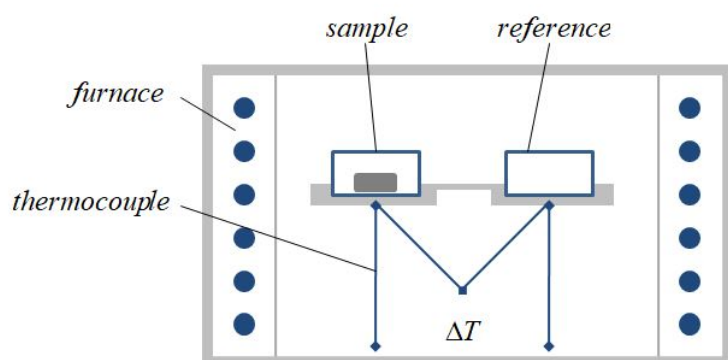
and  $c_p$  can be determined by measuring the heat flow  $\dot{Q}$  into or out of a sample that is subjected to changes in temperature. Its evolution is closely linked to the structural evolution in the samples (cf. section 2.8), and can be set in relation with the dynamics, considering its relation to the excess or configurational entropy (cf. equation 2.12 and section 3.5.3).

$$dS = \frac{dQ}{T} = \frac{(dH)_p}{T} = \frac{m c_p dT}{T} \quad (5.9)$$

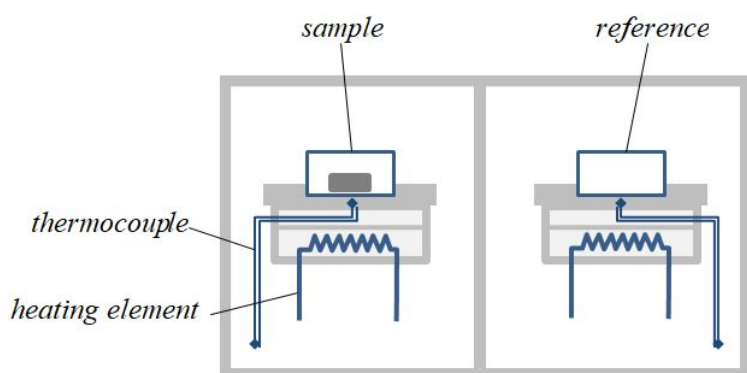
## Differential scanning calorimetry

Differential scanning calorimetry refers to a calorimetric measurement in which the change of heat flow rate difference between a sample and a reference is measured, while the sample and reference are subjected to a controlled temperature program. Differential scanning calorimeters (DSCs) are commonly classified into two categories, depending on their operating principle: heat-flux DSCs and power compensated DSCs. The characteristic principle of both types is that the heat flux difference between the sample and a reference becomes non-zero when a thermal event such as a phase transition or reaction takes place. A schematic representation of the two types is shown in figure 5.7.

In *heat-flux DSC* the sample and reference are placed in the same environment (furnace). A defined exchange of heat with the environment takes place via a well-defined heat conduction path with a given thermal resistance [128]. The sample and reference are subjected to a programmed temperature profile, and the difference in temperature  $\Delta T = T_S - T_R$  is recorded using thermocouples or resistance thermometers (see figure 5.7). When the furnace is heated, heat flows into the sample and reference via the conduction path. Often the reference is chosen as empty crucible. Due to the different thermal reaction of the sample and the reference, a temperature difference  $\Delta T \neq 0$  arises, which is proportional to the difference between the heat flow rate to the sample and the heat flow rate to the reference [128], i.e.  $\phi_S - \phi_R \propto \Delta T$ . As the thermocouples actually yield a voltage difference  $\Delta U$ , not a temperature, a calibration must be performed. This



**Heat flux DSC**



**Power-compensated DSC**

Figure 5.7: Differential scanning calorimetry: heat flux vs. power compensated. In a heat flux DSC the sample and reference holder are placed in the same furnace, and the difference in heat flow is measured based on the temperature difference measured between the two. In a power compensated DSC the sample and furnace are placed in separate furnaces. The difference in heat flow is measured based on the compensation heating power supplied by the heating elements that is required to hold the sample and reference at the same temperature.

is done by melting pure substances and comparing the measured values, e.g. the onset melting temperature and the enthalpy of fusion, against literature data.

In *power-compensated DSC* the sample and reference are situated in two identical, thermally decoupled furnaces (see figure 5.7) equipped with controlled heating elements (thermal resistors) that are directly placed below the sample or reference. This makes it possible to compensate the temperature differences arising from a reaction or transformation in the sample. The temperature difference  $\Delta T$  determined from the thermocouples serves as the input of a second control circuit that compensates the difference in the heat flow between the sample and reference using a proportional control  $\Delta P \propto \Delta T$  by increasing or decreasing additional heating power to the sample furnace [128]. The heat released or consumed by a reaction in the sample is thus proportional to the time integration over the compensation heating power [128].

It can be shown [128] that under steady-state conditions the difference in the heat flow rate between the sample (S) and reference (R) is given by

$$\Delta\phi_{SR} = \phi_S - \phi_R = c_S \frac{dT_S}{dt} - c_R \frac{dT_R}{dt} = (c_S - c_R) dT/dt \quad (5.10)$$

Equation 5.10 shows that the difference in heat flow rates measured,  $\Delta\phi_{SR}$ , is essentially the difference in the heat capacity between the sample and reference,  $c_S - c_R$ , amplified by the heating rate  $dT/dt$ . Accordingly,  $c_S$  can be determined by measuring the sample against a calibration substance whose heat capacity  $c_{ref}$  as a function of temperature is known. To eliminate all influences stemming from potential asymmetries of the DSC a zeroline is determined in a separate measurement under the same conditions using empty crucibles. Accordingly, a three step method is applied: (I) the zeroline (empty scan) is performed, (II) the calibration substance is measured against an empty crucible, (III) the sample is measured against an empty crucible. The heat capacity of the sample can then be obtained from equation 5.10 by comparing the measured heat flow rates

$$c_s = \frac{\phi_S - \phi_0}{\phi_{ref} - \phi_0} \frac{m_{ref}}{m_S c_{ref}} \quad (5.11)$$

In case of amorphous materials such as metallic glasses often one is interested in the thermodynamic excess properties with respect to the glassy or crystalline phase. Instead of the previously described method, constant heating-rate measurements of metallic glasses are usually performed in a two-step method. First the amorphous material is heated at a constant heating rate. Around the glass transition temperature  $T_g$  the glassy sample starts to “unfreezes” and the structural units regain their atomic mobility. The system restores its equilibrium and transforms into a supercooled liquid. As the liquid has a higher heat capacity than the glass, the heat flow necessary to keep the sample at the imposed heating rate increases. Accordingly, the transition from the glass to the undercooled

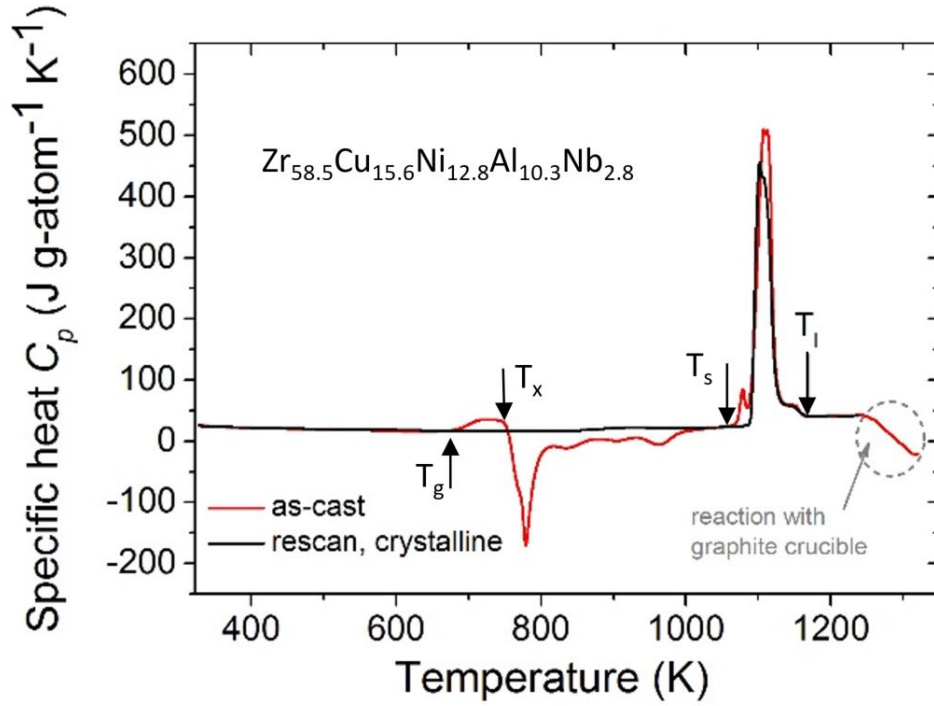


Figure 5.8: Typical example of a DTA analysis performed on the Vit106a bulk metallic glass forming alloy. The red curves corresponds to the first scan of the initially amorphous samples. Upon heating the glassy sample unfreezes and undergoes a glass transition, manifesting as an endothermic step-like increase in the heat capacity at  $T_g$ . At higher temperatures the supercooled liquid starts to crystallize at  $T_x$ , resulting in multiple exothermic events (crystallization peaks). At the solidus temperature  $T_s$  the systems starts to melt (endothermic peaks). Above the liquidus temperature  $T_l$  the system is fully molten. The black curve corresponds to an initially fully crystalline sample. Here, neither a glass transition nor indications for a phase transition are visible, except the melting at higher temperature.

liquid manifests as an endothermic sigmoidal-like event (cf. figure 5.8). With increasing temperature the atomic mobility in the supercooled liquid increases, and liquid crystallizes at the onset of crystallization  $T_x$ . As the enthalpy of the crystal is lower than that of the liquid, a pronounced exothermic event (peaks) occurs. Further heating results in a full transformation of the amorphous sample into a crystalline sample. The crystalline sample is cooled, and the same measurement is repeated on an initially crystalline sample. Finally the two data sets are subtracted. The advantage of this procedure is that there is no need to do a zeroline scan, as the potential asymmetries of the DSC are already canceled out. The heat flow obtained after subtraction is directly proportional to the excess heat capacity of the glass and liquid over the crystalline state. This method has become a standard in the glass community and hence is used for the continuous DSC scans performed in the present study.

## 5.2.2 Thermomechanical analysis

Thermomechanical analysis (TMA) is performed using a Netzsch thermomechanical analyzer TMA 402. Two types of measurements are performed: three-point beam bending relaxation experiments and dilatometry. In TMA experiments the sample is placed on a sample holder with known thermal expansion behavior. In the present case fused silica is used due to its small thermal expansion. The sample holder and sample are placed into a furnace, and the time- and temperature dependent geometrical response of the sample is measured using a linear variable differential transformer (LVDT). The temperature of the sample  $T(t)$  is measured using a thermocouple that is placed in close vicinity to the sample.

### Dilatometry

Dilatometry is performed to determine the thermal expansion of the alloys in the glassy in the supercooled liquid state near the glass transition temperature. Small beams and cylinders are cut from fully amorphous cast plates and rods. The length of the samples is about 10 mm, and the diameters of the samples are in between 2 to 5 mm depending on the alloy and their respective glass forming abilities. The samples are grinded to assure plan parallel end surfaces. The probe is carefully adjusted to the height of the sample, and a minimum load is applied to assure stable contact of the probe onto the sample surface. Using the known spring constant of the setup  $k = 11.6 \text{ Nm}^{-1}$ , the force applied to the sample is estimated as 0.0002 - 0.0003 N. The length change of the sample as a function of temperature  $l(T)$  is measured using the LVDT, and the linear thermal expansion  $\alpha$  is determined

$$l(T) = l_0 + \Delta l(T) = l_0 + \frac{\partial l}{\partial T} \Delta T = l_0 (1 + \alpha \Delta T) \quad (5.12)$$

As-cast and pretreated samples are used for the study. The pretreated samples are heated into the supercooled liquid, cooled back to room temperature with a cooling rate  $q$ , and afterwards heated with the same rate  $h = q$ .

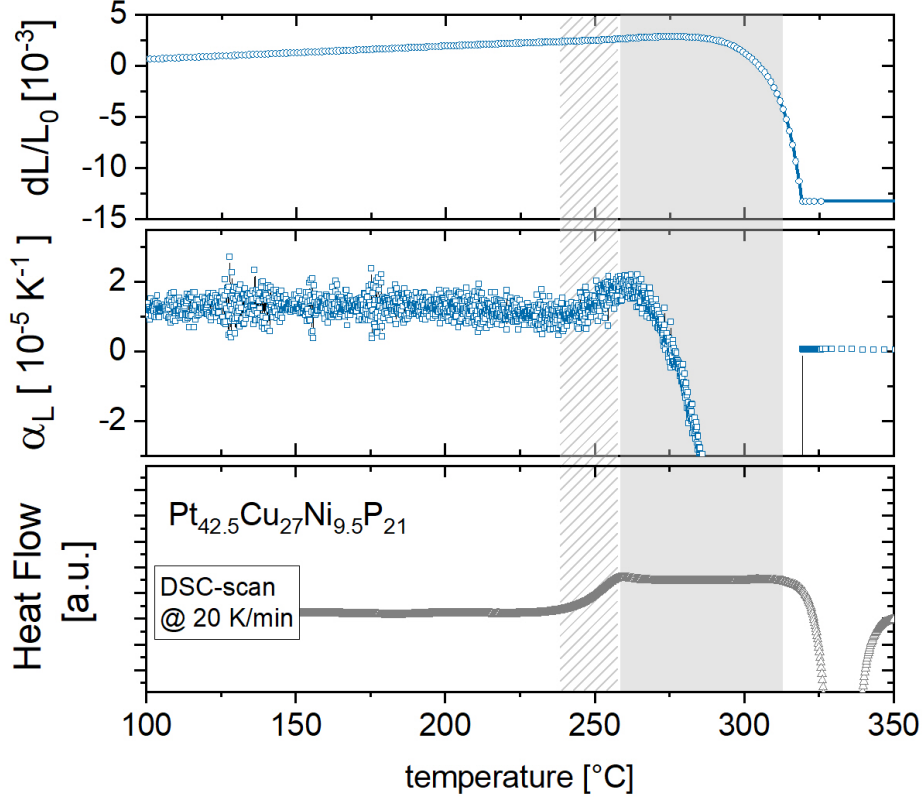


Figure 5.9: Typical result of dilatometry measurement performed in a TMA. The upper subfigure shows the measured relative increase in the sample length,  $dL/L_0$ . The derived linear thermal expansion coefficient  $\alpha_L$  is shown in the center. The lower subfigure shows a DSC-scan of the corresponding alloy (here  $Pt_{42.5}Cu_{27}Ni_{9.5}P_{21}$ ) performed with the same heating rate. During the glass transition range (line-shaded region) the thermal expansion coefficient increases as expected. The structural unfreezing leads to a pronounced softening of the sample, reflected by a pronounced downwards bending of  $dL/L_0$  and  $\alpha_L$  in the supercooled liquid region (grey-shaded area), preventing a proper determination of the thermal expansion coefficient there.

### Three point beam bending relaxation studies

To determine the equilibrium viscosities of the alloys near the glass transition temperature, three-point beam bending relaxation experiments are performed. Two types of measurements are conducted: (I) constant heating rate experiments,



and (II) isothermal relaxation studies. For each measurement type small beams of the alloys are cut from fully amorphous cast plates, and grinded prior to the measurements. The samples are placed on the sample holder and subjected to a programmed heating cycle. The deflection of the beams  $z(t)$  is measured using a linear variable differential transformer (LVDT). The rate of deflection  $\dot{z}(t)$ <sup>1</sup> is converted into viscosity data  $\eta$  according to the Hagy equation [129]:

$$\eta = \frac{gL^3}{144I} \left( M + \frac{\rho AL}{1.6} \right) \frac{1}{\dot{z}(t)} \quad (5.13)$$

where  $g$  is the gravitational acceleration constant ( $m/s^2$ ),  $L$  is the length of the beam within the supports,  $I$  is the second area moment of inertia with respect to the neutral fiber<sup>2</sup>,  $\rho$  is the density ( $g/cm^3$ ), and  $A$  is the cross section area of the beams. In the constant heating rate experiments are conducted in a sample-temperature controlled mode (STC), while in the isothermal heating experiments the furnace-temperature controlled mode is chosen in order to avoid temperature overshoots.

During the constant heating rate experiments the sample continuously softens with increasing temperatures, leading to an increasing deflection rate with increasing temperature (cf. figure 5.9). With the transition to the supercooled liquid state the deflection rate increases, indicating a more pronounced temperature dependence of the viscosity in the supercooled liquid state (cf. figure 5.10). At around 730 K the sample crystallizes, resulting in a strong increase in the measured viscosity.

During the isothermal measurements the viscosities are observed to relax slowly from an initial glassy state  $\eta_{glass}$  to a plateau value. The equilibrium viscosities  $\eta_{eq}$  are extracted from the viscosity-time plots by fitting the viscosity data with a stretched exponential Kohlrausch-Williams-Watts (KWW) equation 3.7. By fitting the  $\eta_{eq}$  data with the VFT equation, the liquid fragility parameters  $D^*$  and  $T_0$  can be determined. Alternatively, the fragility index  $m$  can be determined according to equation 3.9. The two can be converted via  $D^* = 590/(m - 16)$ . A typical example of the results obtained by this analysis is shown in figure 5.10 for the  $Cu_{45}Ti_{37}Zr_{11}Ni_8Sn_2$  (Vit101Sn2) bulk metallic glass. A comprehensive overview of this methods including the fundamental steps to derive the Hagy equation can be found for example in [98].

### 5.2.3 Volume measurements in ESL

Volume measurements are performed in collaboration at the German Aerospace Research Center (DLR), and the data are provided. The measurements are car-

---

<sup>1</sup>Note that  $z$  is counted positive in negative  $z$ -axis, as the beam bends downwards due to its self-weight and the loading applied.

<sup>2</sup>For a rectangular beam:  $I = 1/12BH^3$ , where  $B$  is the beam width, and  $H$  is the height of the beam.

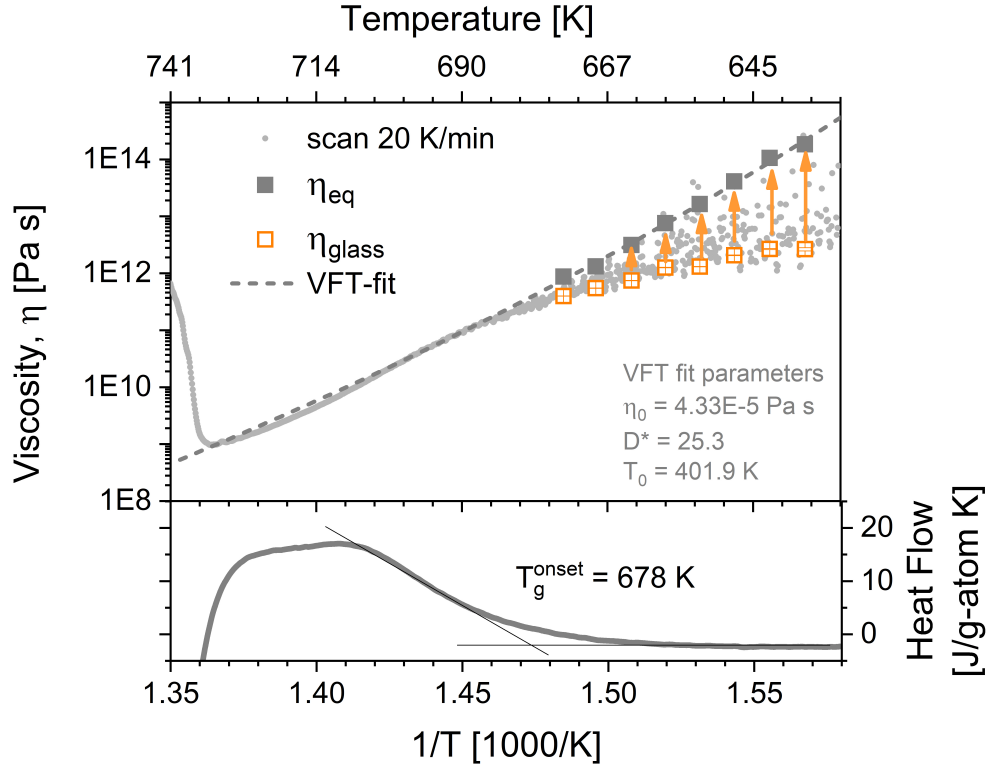


Figure 5.10: Typical result of the determination of the low temperature fragility using the three-point beam bending relaxation method. The light grey points correspond to the constant heating rate experiment. The single data points are the results obtained during the isothermal relaxation measurements. The dashed lines corresponds to the VFT-fit through the equilibrium viscosity data. The open orange squares are the initial viscosity values in the glassy state. Arrows indicate the relaxation pathways during isothermal annealing. The lower panel shows the heat flow measured in constant heating rate DSC scan plotted versus  $1000/T$ .

ried out on the levitated droplets in the ESL by recording back-lit sample images during continuous cooling and heating using a high speed camera with 200 frames per second. The volume of the sample was calculated according to the area of the shadow assuming a rotational symmetry and calibrated with standard spheres with known volumes. For each data point, 20 images were collected within 0.1 s. During this period, the sample temperature is assumed to be constant. For a more detailed description the reader is referred to [130].

## Chapter 6

# On the Thermal Dilatation of Metallic Glasses and Liquids

### 6.1 Bragg's Law and the Ehrenfest Relation

There has been a long debate about the structural origin of the principal diffraction peak (*PDP*) in multicomponent atomic liquids and glasses. In particular the question on what information can be drawn from changes in its shape, height and position was subject of intense earlier research activities [93, 131–137]. The occurrence of a marked, diffuse diffraction ring at low scattering angles close to the unscattered, incident beam (cf. figure 2.1), suggests a dominant interatomic spacing to be present in the amorphous structure. Accordingly, the position of the maximum of the *PDP* is often taken as a measure of the mean interatomic spacing, and therefore should be related to the density. In this chapter following the main findings of these earlier works are taken up, elaborated, and put in the context of the current studies. Starting with a treatise of the crystalline materials on the basis of Bragg's law, the Ehrenfest relation, providing a link between the position of the *PDP* and the volume in amorphous materials is introduced. The thermal expansion of a variety of multicomponent bulk metallic glass formers is determined and the validity of the Ehrenfest relation is tested in the glassy and liquid state.

#### 6.1.1 Crystalline materials

In crystalline materials, the positions of the individual diffraction peaks can be associated to distinct distances of crystallographic planes in the highly ordered lattice structure. The quantitative relation between the distance of crystallographic planes  $hkl$ ,  $d_{hkl}$ , and the positions of peaks in a diffraction pattern,

occurring at a scattering angle  $\theta$ , is given by *Bragg's law*:

$$d_{hkl} = \frac{n\lambda}{2\sin(\theta)} \quad (6.1)$$

where  $n$  is a positive integer, and  $\lambda$  corresponds to the wavelength of radiation used to probe the sample. Some fundamental insights can be gained from Bragg's law. For a given wavelength, a larger interatomic spacing  $d_{hkl}$  between the atoms belonging to the crystallographic planes  $hkl$  corresponds to a smaller scattering angle  $\theta$  and vice versa. This inverse relation between the distances in real space  $d_{hkl}$  and the positions of the peaks with respect to the unscattered incident beams, defined by the scattering angle  $\theta$ , is called the *reciprocity of spaces*. Physically it results from the fact that a diffraction experiment can be viewed as a Fourier transformation of the real space structure into the reciprocal space. In case of a crystalline lattice structure with the basis  $\{\mathbf{a}_i\}$ , the experimentally observed diffraction pattern yields a reciprocal lattice with the basis  $\{\mathbf{b}_j\}$  where  $\mathbf{a}_i \cdot \mathbf{b}_j = 2\pi\delta_{ij}$ . Obviously, a larger magnitude  $|\mathbf{a}|$  corresponds to a smaller magnitude of  $|\mathbf{b}|$  and vice versa. With the help of Bragg's law (equation 6.1) the individual peaks in a diffraction pattern of a crystalline substance can be identified with specific interplanar spacings in the lattice structure. As shown by Simmons and Balluffi [138], the local thermal expansion of the lattice structure, i.e.  $\Delta a/a$ , deduced by the temperature-induced shift of the peak positions, not necessarily equals the macroscopic length changes measured via dilatometry  $\Delta l/l$  (cf. figure 6.1). This is due to the fact that localized structural defects can change the macroscopic average density without markedly affecting the mean interatomic distances. The formation of thermal vacancies at higher temperatures leads to an increase in the global volume, but, except for small relaxation effects around the defects, does not change the mean interatomic spacing. At lower temperatures the difference in the local and global expansion is negligible, but at  $T > 0.75T_m$  the effect becomes measurable [138]. However, in crystalline materials the differences between  $\Delta a/a$  and  $\Delta l/l$  are small. Below  $T_m$  the differences are less than 0.1 % [138] and very precise measuring techniques and data are required to detect them.

### 6.1.2 Amorphous materials

For isotropic materials such as amorphous materials the scattered intensity is given by the Debye equation (equation 4.25). However, the Debye equation is of limited use to determine the mean interatomic spacing  $d$  as it requires the knowledge about all atomic positions. In order to derive an expression that links  $d$  to the observed features of diffraction pattern of amorphous substances, Ehrenfest proposed that the intensity scattered from an amorphous material can be approximated by applying the Debye equation to the case of a diatomic gas where the coherent scattering between the molecules is neglected [133]. In case

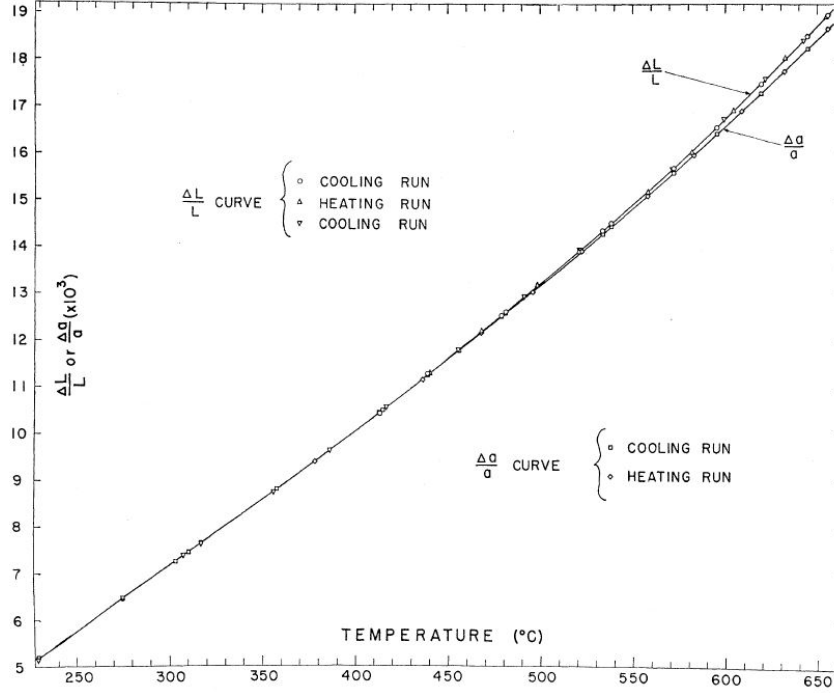


Figure 6.1: Experimental results of Simmons and Balluffi obtained for high purity aluminum (99.995%). The global dilatation, i.e. the length expansion  $\Delta l/l$ , and the average local dilatation, i.e. the expansion of the lattice parameter are plotted against the temperature. The two curves start to diverge at around  $0.75T_m$ . This is attributed to the thermal-induced formation of lattice-vacancy-type defects. The figure is taken from [138].

of identical atoms this leads to

$$I(Q) = 2f^2 \left( 1 + \frac{Qd}{\sin(Qd)} \right) \quad (6.2)$$

where  $d$  is the distance between the two atoms [133]. Given that  $f$  does not depend on  $Q$ , the first maximum of the scattered intensity then should occur at a scattering vector [132]

$$Q_1 = 1.23 \frac{2\pi}{d} \quad (6.3)$$

It can be expected that, provided that there is a single dominant interatomic spacing  $d$ , a similar type of equation holds generally for the case of condensed matter [133, 139]

$$Q_1 = K \frac{2\pi}{d} \quad (6.4)$$

where  $K$  is a constant that depends on the particular arrangement of the atoms. Equation 6.4 is referred to as “Ehrenfest relation”. Although the direct calculation of  $d$  requires  $K$  which in turn can only be determined with the complete

information of all atomic positions, the Ehrenfest relation should still yield valuable information in situations where one is only interested in normalized changes of  $d$  with respect to a reference value  $d_0$ , as by taking the ratio  $d/d_0$ , the constant  $K$  can be eliminated. This idea has been tested and applied to the case of amorphous metals by Yavari et al. and others [132, 133, 135, 136, 140].

## 6.2 Thermal Expansion of Metallic Glasses

Upon heating metals usually increase their volumes. In the solid state the applied thermal energy is mainly stored in vibrational motions of the particle. The magnitude of the deviations from the equilibrium position is determined by the strength of the bonds between the particles, which in turn is given by the atomic interaction potential. Stronger bonds lead to lower vibrational amplitudes and vice versa. As the strength of the bonds is related to the melting point of a substance, the thermal expansion in the solid state, indicating the stretching of bonds, should scale inversely with the melting point  $\alpha \propto T_m^{-1}$  which indeed is observed for metallic elements. On closer examination, it turns out that the magnitude of the thermal expansion is determined by the asymmetry of the interatomic pair potential  $U(r)$ . In general the repulsive part of  $U(r)$  is steeper than the attractive part, so that for a given displacement  $r - r_0$  from the equilibrium position  $r_0$ , a particle experiences a higher restoring force when entering the repulsive part of  $U(r)$ , i.e. for  $r - r_0 < 0$ , than when entering the attractive part, i.e. for  $r - r_0 > 0$ . Vibrating particles thus experiences a net shift towards larger distances, whose magnitude increases with increasing temperatures. Mathematically the asymmetry of a function  $f(x)$  corresponds to the change in the curvature, i.e. the second derivative  $\partial^2 f / \partial x^2$ . Accordingly, the thermal expansion behavior is determined by the third derivative of the interatomic pair potential  $U(r)$  with respect to distance  $r$ , i.e.  $\partial^3 U(r) / \partial r^3$ .

The thermal expansion of a substance is quantified by its thermal expansion coefficients. The thermal expansion coefficients are defined macroscopically and depend on the state of matter. Normally the thermal expansion of liquids is more pronounced than for solids, which can be viewed as a consequence of a thermal-induced increase of the concentration of local structural defects (free volume) on the atomic scale (cf. chapter 3). It is common to distinguish the linear thermal expansion coefficient  $\alpha_l$  from the volume expansion coefficient  $\alpha_V$ . For homogeneous, isotropic materials is equal in all directions, so that in first approximation

$$\alpha_V = \frac{1}{V} \frac{\partial V}{\partial T} = 3 \frac{1}{L} \frac{\partial L}{\partial T} = 3\alpha_L \quad (6.5)$$

Provided that the macroscopic volume  $V$  is proportional to the mean atomic volume  $v \propto d^3$ , and given that  $d$  is inverse proportional to  $Q_1$  as implied by the Ehrenfest relation (equation 6.4), it can be expected [132]

$$\frac{V(T)}{V(T_{ref})} = 1 + \alpha_V (T - T_{ref}) = \left( \frac{Q_1(T_{ref})}{Q_1(T)} \right)^3 \quad (6.6)$$

where  $T_{ref}$  is a chosen reference temperature. Equation (6.6) provides a link between the thermal expansion  $\alpha_V$  of amorphous materials and the thermal-induced shifts of their principal diffraction peak  $Q_1$ . It states that a more pronounced shift towards lower  $Q$  corresponds to a larger thermal expansion, and vice-versa.

However, several studies report that the exponent relating  $v$  and  $Q_1$  is not 3, but takes non-integer values less than 3 [9, 134, 141]. Comparing the atomic volume  $v$ , derived from macroscopic density data of a variety of metallic glasses at ambient temperature, with the position of their principal diffraction peaks,  $Q_1$ , Ma et al. [134] found that the data can be best described by

$$v \propto Q_1^{-\xi} \quad (6.7)$$

when the exponent has a non-integer value  $\xi = 2.31$ . Taking into account that the exponent  $\xi$  represents the dimensionality, the non-integer value of  $\xi$  was interpreted as evidence that metallic glasses are composed of a fractal cluster network structure with fractal dimension  $n = 2.3$ . This value is comparable to fractal dimensions of silica particle aggregates ( $n = 2.27 - 2.65$ ), colloidal gold particles ( $n = 2.05$ ), as well as the fractal dimension of quasicrystals ( $n = 2.72$ ), which exhibit quasiperiodic long-range order and are characterized by a hierarchy of atomic clusters [134]. Similar studies on the scaling behavior of  $v$  and  $Q_1$  in metallic glasses are reported by Cheng et al. in reference [9]. Taking data from literature and plotting  $\log(Q_1)$  vs.  $\log(v)$  Cheng et al. found that an exponent of 2.96 yields the best description for the selected alloys. On the other hand, their data obtained from MD simulations of CuZr-based metallic glasses were found to be best fitted with an exponent 2.66. Figure 6.2 summarizes all data points reported in these previous studies. Obviously, when plotted on a logarithmic scale, the best description of all data points is obtained for exponents  $\xi \neq 3$  (cf. right figure 6.2). In the present case, the best fit through all data points is achieved for  $\xi = 2.52$  ( $R^2 = 0.977$ ). For comparison also the fit assuming  $\xi = 2.31$  (as suggested by Ma et al.), as well as the fit assuming  $\xi = 3$  (in accordance with the Ehrenfest relation) are shown. However, as pointed out earlier for the case of the data of Ma et al. [93], plotting the data as  $Q_1$  versus  $v^{-1/3}$  on a linear scale reveals that essentially the same fit quality can be obtained by assuming  $\xi = 3$ , challenging the conception of a fractal structure in metallic glasses (cf. left figure 6.2). Further evidence supporting a non-integer value of  $\xi$  is reported by Zeng et al. [141]. Using a diamond anvil cell they studied the pressure dependence of the shift of the principal diffraction peak as a function of the density of three bulk metallic glass formers and found that “the density of MG varies with the 5/2 power of  $Q_1$ , instead of the expected cubic relationship” [141].

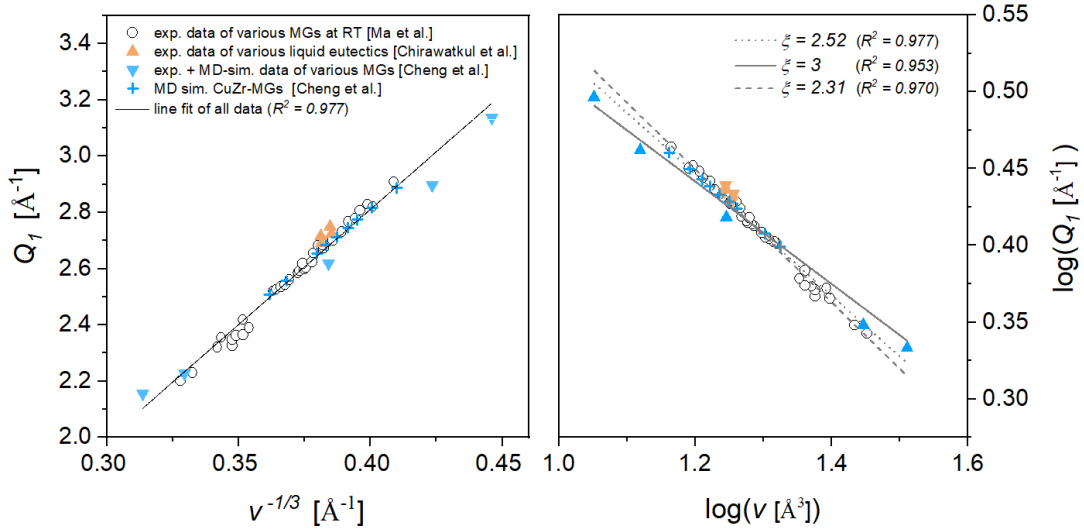


Figure 6.2: Position of the principal diffraction peak  $Q_1$  vs. atomic volume  $v$  in metallic glasses and eutectic liquids from literature. Right: Plotting  $\log(Q_1)$  vs.  $\log(v)$  the data are best described assuming a straight line with a slope  $-2.52$ . Note that the negative of the slope corresponds to the exponent  $\xi$  in equation 6.7. For comparison also the fits assuming a slope  $-2.31$  (as suggested by Ma et al. [134]) and  $-3$  (as implied by the Ehrenfest relation) are shown. Left: On the other hand, if  $Q_1$  is plotted vs  $v^{-1/3}$  on a linear scale as implied by the Ehrenfest a similar fit quality is obtained.

Recently, the question of whether metallic glasses are composed of a fractal structure was taken up by Ding et al.[142]. Using large-scale MD simulations a comprehensive study on 12 distinct MG samples (1 monatomic, 9 binary, 2 ternary alloys), spanning a wide range of compositions and cooling rates, was performed [142]. Based on a classical fractal analysis based on the mass distribution  $M(r)$ , which is expected to follow  $M(r) \propto r^{D_f}$ , with  $M(r)$  being the number of atoms within a volume defined by the radius  $r$ , and  $D_f$  being the fractal dimension, it is found that both, the mass distribution for atomic packing as well as cluster packing, scale with an exponent  $D_f = 3$ , questioning the fractal nature of metallic glasses. Ding et al. also investigated the (hydrostatic) pressure-induced scaling between  $v$  and  $Q_1$  by calculating the X-ray structure factors of their MD-glasses and observed that depending on the specific alloy chosen the power-law exponent varies between 2.8 and 3.6, challenging the conception of a universal scaling exponent [142].

The findings of these previous studies are obtained either from compositional variations of different MGs at a single temperature (room temperature) or by



following (hydrostatic) pressure-induced changes of  $v$  and  $Q_1$ . All together it appears that there is no clear consensus on the question if the position of the principal peak can be used to mirror changes in the macroscopic volume, if there is a universal scaling exponent relating  $v$  and  $Q_1$ , and if so, what is its value. On the other hand, the Ehrenfest relation (equation 6.4) is often assumed to be valid in metallic glasses and liquids and has been successfully applied to study free volume changes [132] or strain distributions [133, 143]. In the following a comprehensive study on the temperature-induced changes of  $v$  and  $Q_1$  including various bulk metallic glasses is performed. Extending the relation of Ma et al. 6.7 to the thermal volume expansion coefficient it follows

$$\alpha_V^{DIL} := \frac{1}{v} dv/dT = -\xi \frac{1}{Q_1} dQ_1/dT =: \alpha_V^{XRD} \quad (6.8)$$

The above equation provides a link between the volumetric macroscopic thermal expansion as measured from dilatometry and the thermal expansion deduced from the shift of the principal diffraction peak  $Q_1$ . Comparing the dilatometric thermal expansion coefficient,  $\alpha_V^{DIL}$ , with the thermal dilatation predicted from the temperature-induced shift of the principal diffraction peak,  $\alpha_V^{XRD}$ , the exponent  $\xi$  can be derived, enabling to test the validity of the Ehrenfest relation.

A typical example for the results obtained in this study is exemplarily shown in figure 6.3 for the  $Pt_{60}Cu_{20}Co_2P_{22}$  bulk metallic glass. The upper subfigure shows the inverse of the principal diffraction peak measured during heating normalized to its value at 50 °C, i.e.  $Q_1(50^\circ\text{C})/Q_1(T)$ . The center subfigure shows the linear thermal expansion measured in classical dilatometry, which can be converted into the volume expansion coefficient based on equation 6.5. The lowest subfigure shows the DSC trace as obtained for heating a glassy sample at a rate of 20 K/min. In the glassy state an almost linear behavior is observed for  $Q_1(50^\circ\text{C})/Q_1(T)$  and  $\Delta L/L_0$ . As liquids have a larger thermal expansion than glasses, an increase in the slope of the  $\Delta L/L_0$ -curve is expected once the glass transition is reached (line-shaded region). In contrast the  $\Delta L/L_0$ -curve rather becomes shallower when approaching the glass transition, and finally bends downwards in the supercooled liquid region (grey-shaded region). These observations can be explained as follows: In the glassy state the material essentially behaves like a solid. At low temperatures no structural relaxation take place and the thermal energy is stored mainly in vibrational motion. Due to the asymmetry of the atomic pair potentials the mean separation of atoms increases and the system expands, leading to an increase in  $L/L_0$  and a decrease in  $Q_1$ . At higher temperatures relaxation effects in the glass occur, as the system is in a out-of-equilibrium liquid state. The closer the system is to the glass transition temperature, the lower is its structural relaxation time with respect to the timescale of the experiment. At sufficiently high temperatures sub- $T_g$  relaxation processes take place, during which the excess (free) volume and enthalpy are released. Accordingly, the thermal expansion measured corresponds to the sum of the two competing

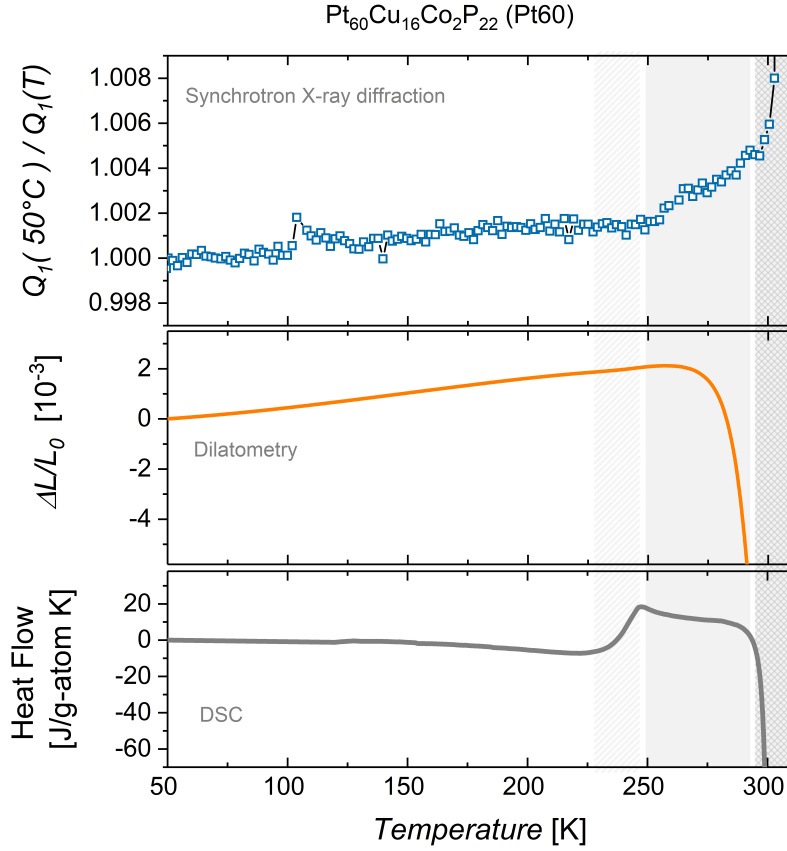


Figure 6.3: Upper panel: Synchrotron x-ray diffraction data - Evolution of the position of the principal diffraction peak during heating normalized to its value at 50 °C. Center panel: Linear thermal expansion of the sample as measured by dilatometry. Lowest panel: Standard DSC trace of for the same thermal protocol as used for the synchrotron and dilatometry measurements.

contributions: vibrational expansion and densification caused by relaxation effects, i.e.  $\Delta L = \Delta L_{vib} - \Delta L_{relax}$  with  $\Delta L_{vib} > 0$  and  $\Delta L_{relax} < 0$ . For this reason the thermal expansion coefficients are determined from the low temperature data in the glassy state only, where no indication for structural relaxation is found, neither in the structural data, nor in the diffraction data, nor in the DSC scans. During the glass transition the systems restores its ergodicity and finally reaches its metastable equilibrium, i.e. the supercooled liquid regime. With the transition from the glass to the liquid pronounced softening occurs. In the present case of the  $\text{Pt}_{60}\text{Cu}_{20}\text{Co}_2\text{P}_{22}$  bulk metallic glass forming liquid the viscosity changes about 4 - 5 orders of magnitude from the onset of the glass transition to the onset of crystallization. As a consequence the sample deforms even under the very small loadings applied. This leads to a strong downwards bending in the  $\Delta L/L_0$ -curve (cf. grey-shaded region in figure 6.3), preventing a proper deter-

mination of the thermal expansion coefficient in the supercooled liquid from the dilatometric data.

Figure 6.4 summarizes of the results obtained in this study along with additional data from literature. The diagonal dashed-line is a straight line through origin, indicating equality of the  $\alpha_V^{DIL}$  and  $\alpha_V^{XRD}$ . Two cases  $\xi = 3$ , in agreement with the Ehrenfest relation, and  $\xi = 2.3$ , as suggested by the analysis of Ma et al. are considered. For  $\xi = 3$  a good agreement is observed, except for the data of Mattern et al. [135]. In general the thermal expansion values derived from the diffraction data show a slight tendency to underestimate the macroscopic thermal expansion. Obviously, the assumption of a smaller exponent only worsens the correlation as shown here for the case  $\xi = 2.3$ . The present findings thus support that in the glassy state the macroscopic volume changes indeed scale with  $Q_1^{-3}$  as implied the Ehrenfest relation.

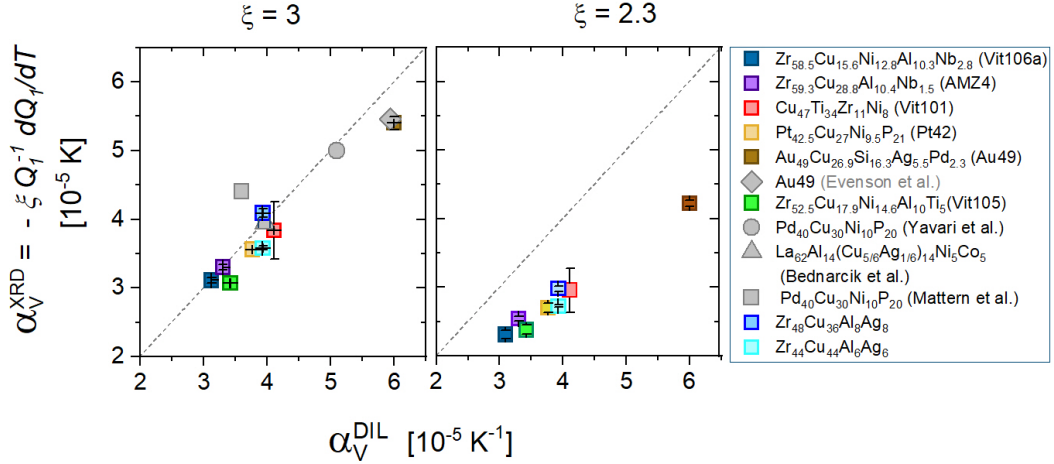


Figure 6.4: Thermal expansion: diffraction vs. volume measurements. Thermal expansion coefficients derived from synchrotron x-ray diffraction analysis,  $\alpha_V^{XRD} = -\xi Q_1 dQ_1/dT$ , plotted versus the volumetric thermal expansion coefficient derived from dilatometry,  $\alpha_V^{DIL}$  for the two exponents  $\xi = 3$  (Ehrenfest relation) and  $\xi = 2.3$  (fractal approach) as proposed by Ma et al. [134]. The dashed line is a straight line through the origin with a slope equal to one.

### 6.3 Thermal Expansion in the Liquid state

Knowing that in the glassy state the global thermal expansion is reflected by the thermal-induced shift of the principal diffraction peak,  $Q_1$ , assuming a scaling exponent  $\xi = 3$  in equation 6.7 as implied by the Ehrenfest relation, it may be

asked if the same relation also holds for the liquid state. A comprehensive study on the validity of the Ehrenfest equation in metallic liquids has been performed earlier by Gangopadhyay et al. [137]. Combining electrostatic levitation and synchrotron diffraction they determined the first peak position of  $S(Q)$ ,  $Q_1$ , and atomic volumes  $v$  of over 30 metallic alloys. Plotting  $Q_1$  versus  $v$  at a temperature  $2T_g$ , Gangopadhyay et al. found that the data can be best described assuming a functional dependence  $v \propto Q_1^{-2.28 \pm 0.11}$  as shown in figure 6.5. This value, within the error, is almost equal to the value  $-2.31$  derived by Ma et al. for metallic glass forming alloys in the glassy state [134], suggesting that a universal exponent  $\xi = 2.3$  is applicable to amorphous state in general. On the other hand, as pointed out earlier, the data of Ma et al. as well as other data of metallic glasses at room temperature can be equally well described by assuming an exponent  $\xi = 3$  (cf. figure 6.2), questioning the conception of a fractal cluster structure with a non-integer value of  $\xi \neq 3$  in the glassy state.

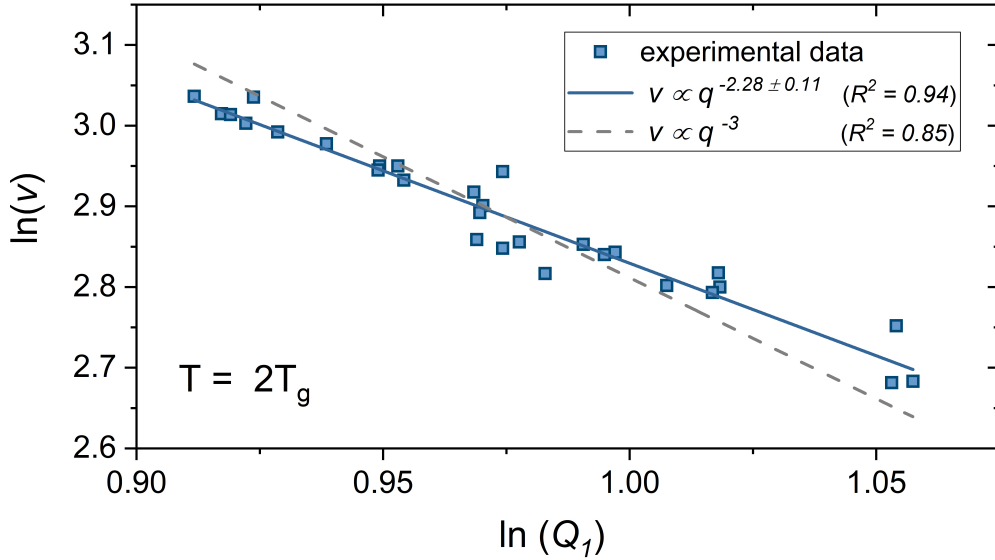


Figure 6.5: Atomic volume of various glass forming liquids at  $T_g$  plotted against the position of the PDP,  $q_1$ . The two straight lines show the fitting results obtained for keeping  $\xi$  as a free parameter (solid red line), and for assuming  $\xi = 3$  (dashed black line). The data is taken and replotted from reference [137].

In reference [137] the authors state that within the temperature range from  $T_g$  to  $2.5T_g$  the exponent  $\xi$  is found to show no pronounced temperature dependence. Given that there exists a universal scaling exponent between  $v$  and  $Q_1$ , it thus should be possible to relate the thermal expansion, derived from the diffraction data,  $\alpha_V^{XRD}$ , to the volumetric thermal expansion,  $\alpha_V^{DIL}$ , by relying on equation 6.8. According to the data of Gangopadhyay et al. obtained at  $T = 2T_g$  the value of the scaling exponent should be  $\xi \approx 2.3$  (cf. figure 6.5). However, neither

the data reported by the authors in reference [137] nor the data obtained in the current study, derived from volume measurements and synchrotron diffraction studies in the ESL, support the existence of a universal scaling exponent. This is shown in figure 6.6 for the cases  $\xi = 3$  and  $\xi = 2.3$ . Although there appears to be a general trend of increasing  $\alpha_V^{XRD}$  with increasing  $\alpha_V^{DIL}$  the data show a large scattering around the diagonal, indicating that neither of the two exponents is able to give a satisfying description of the dilatation data of all metallic liquids. It turns out that also assuming other values of  $\xi$  cannot give a satisfying correlation between  $\alpha_V^{XRD}$  and  $\alpha_V^{DIL}$ . A one-to-one correspondence of  $\alpha_V^{XRD}$  and  $\alpha_V^{DIL}$  can only be obtained if different exponents are assumed for the different alloys. Nevertheless,  $\xi = 2.3$  yields an improved description compared to  $\xi = 3$ , as seen by comparing the root-mean-square deviation,  $RMSD = \sum (\alpha^{DIL} - \alpha^{XRD})^2$ . For  $\xi = 3$ ,  $RMSD = 1.87 \cdot 10^{-5}$ , while  $\xi = 2.3$  yields  $RMSD = 1.58 \cdot 10^{-5}$ .

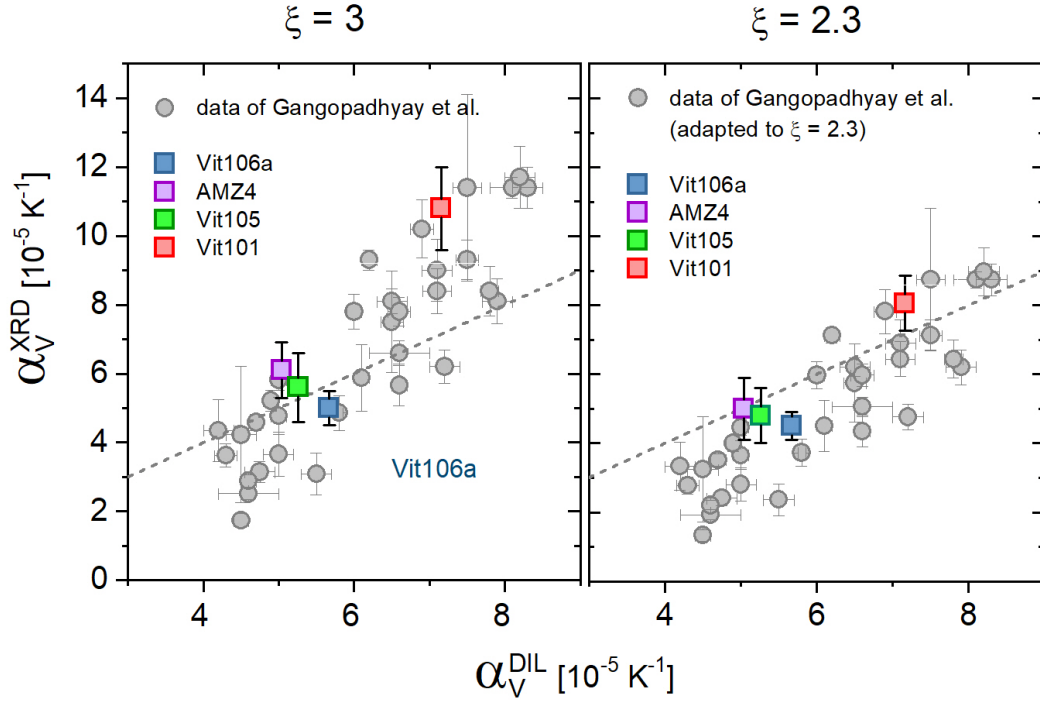


Figure 6.6: The thermal expansion determined from diffraction data,  $\alpha_V^{XRD}$ , in comparison to the thermal expansion determined from volumetric measurements,  $\alpha_V^{DIL}$ , performed in ESL for a large variety of metallic alloys in the liquid state.

The above findings indicate that the Ehrenfest relation, which appears to be valid in the glassy state, no longer applies for multicomponent alloys in the liquid state. A possible explanation for the origin of this observation is discussed in the following. The Ehrenfest relation in its original form (equation 6.3) is derived for monatomic systems, and its generalization to the case of condensed

matter assumes a single predominant interatomic spacing. In contrast, in multicomponent liquids the structure factor  $S(Q)$  is a superposition of several partial structure factors which are directly related to the partial pair distribution functions belonging to individual atomic pairs. Furthermore, the contribution of the individual partials to the total structure factor that is measured during a diffraction experiments depends on the weighting factor of the partial, which in turn is determined by the concentration and scattering strength of the elements belonging to the atomic pair associated with the partial. In contrast to the glassy state where the structure, apart from relaxation effects, essentially remains frozen, the structure of liquids changes markedly upon heating and cooling. This causes pronounced changes in the shape, heights and positions of the individual partial structure factors, whose magnitudes can strongly differ for different pairs. As a consequence the shift of the position of the maximum of the total structure factor  $S(Q)$  not necessarily mirrors the average increase of atomic distances, but rather is determined by the shifts of those partials that build up the maximum of the principal diffraction peak. In addition, different liquids vary in terms of their resistance against temperature-induced structural changes. More fragile liquids undergo more pronounced structural changes than stronger liquids, as reflected by changes in their entropy. Thus, a universal scaling exponent for multicomponent liquids might rather be surprising than to be expected.

The fact that pronounced structural changes can lead to discrepancies between  $\alpha_V^{XRD}$  and  $\alpha_V^{DIL}$  can also be understood in terms of the original formulation of the Ehrenfest relation (equation 6.4). In equation 6.4 the constant  $K$  depends on the particular atomic configuration. Its value therefore changes if pronounced structural rearrangements take place. The temperature dependence of  $K$  is carried into the thermal expansion coefficient via

$$\frac{1}{V} \frac{dV}{dT} = -\xi \frac{1}{Q_1} \frac{dQ_1}{dT} + \frac{1}{K} \frac{dK}{dT} \quad (6.9)$$

as can be easily seen by setting  $V \propto Q_1^{-\xi} = (2\pi Kd)^{-\xi}$  and applying the definition of the thermal expansion coefficient. Obviously, in any case where  $dK/dT \neq 0$  the thermal volume expansion deviates from the thermal expansion derived from the shift of  $Q_1$ . In the glassy state the structure apart from increasing vibrations remains self-similar. Thus, at temperatures far below  $T_g$  where relaxation effects are negligible,  $dK/dT \approx 0$ . On the other hand, in the liquid state the atomic configuration is strongly temperature dependent, so that it can be expected  $dK/dT \neq 0$ . As mentioned above, the magnitude of structural changes varies significantly among different metallic liquids. More fragile liquids show a much higher structural sensitivity with respect to temperature than strong liquids. Hence, thermal-induced change in  $K$  in general should be more pronounced in fragile than in stronger liquids. In any case, the different magnitude of  $dK/dT$  finds expression in the above equation 6.9, providing a possible explanation why

the macroscopic thermal expansion cannot be deduced from the shift of  $Q_1$  assuming a universal scaling exponent  $\xi$  (cf. figure 6.6). Indeed, a closer inspection of left panel of figure 6.6 suggests that in particular alloys with larger  $\alpha_{XRD}$  tend to show a larger deviation to  $\alpha_{DIL}$  when assuming  $\xi = 3$ . Later on in this chapter it will be shown that a larger value of  $\alpha_{XRD}$  correlates with a larger kinetic fragility  $m$ . In this context, the present findings suggests that more fragile liquids show a tendency for larger differences between  $\alpha_{XRD}$  and  $\alpha_{DIL}$ , supporting the conception that the origin of this discrepancy is linked to the magnitude of pronounced thermal-induced structural changes in the liquid state. In principle the term  $K^{-1}dK/dT$  can be derived from equation 6.4 by demanding  $\alpha_{XRD}! = \alpha_{DIL}$ . It would be interesting to test whether the derived values for  $K^{-1}dK/dT$  indeed correlate with the fragility  $m$  of these alloys.

## 6.4 Length-scale Dependence of the Thermal Expansion in Glasses and Liquids

The global thermal expansion,  $\Delta L/L$ , of crystalline materials does not necessarily mirror the local expansion on the atomic length scale, i.e. the separation of nearest neighbors given by the change in the lattice parameter  $\Delta a/a$  [138]. As shown by Simmons and Balluffi [138] this is due to the occurrence of thermal-induced structural defects which increase the global volume without markedly affecting the separation of nearest neighbors in the lattice structure.<sup>1</sup> The experiments of Simmons and Balluffi further show that the difference between  $\Delta L/L$  and  $\Delta a/a$  is negligible at lower temperatures but becomes more pronounced with increasing temperature (cf. figure 6.1).

Although in the liquid phase the long-range periodicity of the structure is broken, the structure is not fully random. Chemical and topological-driven effects result in the formation of short- or medium-range ordering. In fact, the structure of metallic liquids can be considered as an assemblage of a multitude of different atomic cluster species (cf. section 2.5). In (bulk) metallic glass forming liquids differences in atomic size and chemical affinity between the constituents favor solute-centered clusters [57, 62] that are characterized by a higher (thermal) stability [144] and a prolonged lifetime [9] as compared to the average cluster structure. With increasing temperature the amount of topological and chemical disorder increases. The increase in disorder normally goes along with an decrease of the local packing density and thus might be viewed as an increase in the concentration of (local volume) defects as compared to a more ordered structure at lower temperatures. Since there are no “principal building rules” how to set up the structure - as it is the case for crystalline materials in order to conserve the

---

<sup>1</sup>In fact, relaxation effects around the defects (vacancies) result in a small, localized decrease of the atomic distances around the defects compared to a perfect, defect-free lattice structure.

long-range periodicity of the lattice structure - the local dilatation in liquids in principle may vary at the different length scales, depending on where the defects are introduced. The “non-rigidity” of the liquid structure principally allows a non-uniform distribution of the defects (local volume changes) throughout the coordination shells.

A possible scenario for a locally inhomogeneous distribution of thermal-induced “defects” is schematically shown in figure 6.7 for the case of a binary system. The binary alloy can be considered as assemblage of solute-centered clusters (dashed rings) which are “glued” by the solvent atoms  $A$ . By heating the system from  $T_1$  to  $T_2$  the structure expands. This can occur in different ways: In the homogeneous scenario the thermal-induced excess volume is redistributed (more or less) uniformly among all atoms, irrespective of whether they belong to a solute-centered cluster or not. The solute-centered clusters as well as the “gluing” atoms in between increase their distances to their neighbors. Obviously this scenario would apply for systems in which the strength of bonds of the pairs  $A - A$ , given by the interatomic pair potential, is similar to the strength of the bonds of the pairs  $A - B$ . In the inhomogeneous scenario the thermal-induced excess volume is mainly redistributed among the “gluing” atoms, while the solute-centered clusters show a much less pronounced dilatation. This should be the case if the interatomic pair potential between  $A - B$ -pairs is much stronger than for  $A - A$ -pairs. Evidently, the difference in the redistribution of excess volume should be also reflected in the atomic pair distribution functions.<sup>2</sup> Similar considerations of course can be applied to multicomponent alloys and other structural units, e.g. larger cluster structures, whose sizes extend beyond a single coordination shell.

To gain insights about the thermal-induced redistribution of atomic distances in the glassy and liquid state, the position and height of the individual peaks in the distribution functions of various metallic glass forming alloys are analyzed as a function of temperature. The real-space data,  $G(r)$ , obtained from Fourier transformation of the total structure factor,  $S(Q)$ , are interpolated using cubic splines to obtain a better resolution, and the position and height of the maxima of the peaks are extracted and plotted as a function of temperature. In this approach it is assumed that the maxima of the peaks are a suitable measure of the position of the individual coordination shells. This hypothesis was tested on

---

<sup>2</sup>In the two scenarios depicted the maximum of the first coordination shell is mainly determined by the distance of the  $A$ -atoms belonging to shell of the solute centered clusters. This fact can be rationalized as follows: (I) In (bulk) metallic glass forming liquids the solvent atoms are the main constituents and usually have the highest weighting factors (cf. section 4.10). Therefore their partials normally determine the position of the peak. (II) In the depicted case the number of  $A$ -atoms belonging to the solute-centered clusters is larger than the number of “gluing”  $A$ -atoms. Also, due to the architecture of the dense-packed solute-centered cluster, their distances are sharper-defined as compared to the distances of the “gluing” atoms, whose distance to their neighbors is smeared. The first peak in the  $A - A$ -partial should therefore be mainly determined by them. Summarizing, the shell atoms should essentially determine the peak position corresponding to the first coordination shell.



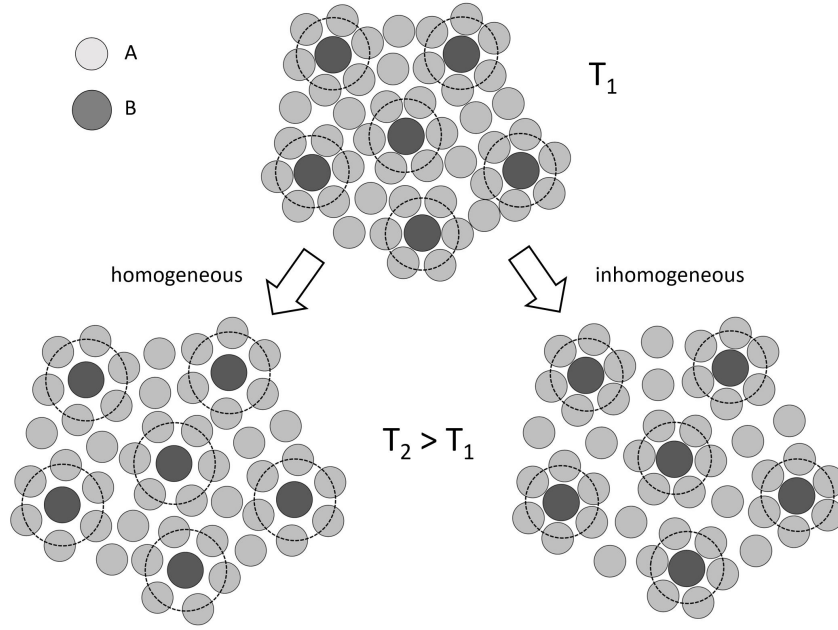


Figure 6.7: Schematic to illustrate possible origins of the length-scale dependence of thermal expansion in metallic liquids and glasses.

a variety of glass forming alloys, and it was found that this procedure generates qualitatively equivalent results to fitting the peaks with Bi-Gaussian functions [127].

A typical example of the results obtained in this study is shown in figure 6.8 for the case of the Vit1b bulk metallic glass forming alloy. In the upper panel, the peak positions of  $G(r)$ ,  $r_i$ , normalized to their values at 50 °C,  $r_{i,0}$ , are plotted as a function of temperature during heating a glassy sample in a furnace while analyzing its structural changes using x-ray synchrotron radiation. The lower panel shows a standard DSC scan taken at the same heating rate. For reason of comprehensibility the different regimes are indicated by shadowing. The structural analysis of the Vit1b bulk metallic glass forming alloy shows that the temperature-induced shift of the individual peak positions  $r_i$  varies among the different coordination shells (cf. figure 6.8). Further it can be seen that the peak shift behavior varies in the different temperature regimes, i.e. the glass (white area), the glass transition (line-shaded area), the supercooled liquid (grey-shaded area), and during crystallization (diamond-shaded area). When entering the glass transition regime the temperature dependence of the peaks shift increases. In the present case, the negative trend of the first peak becomes more negative, while all other peak show a more pronounced positive shift, in line with the conception that structural changes become more pronounced when the system unfreezes. In addition, it appears that in the glassy state the peaks of the first and second

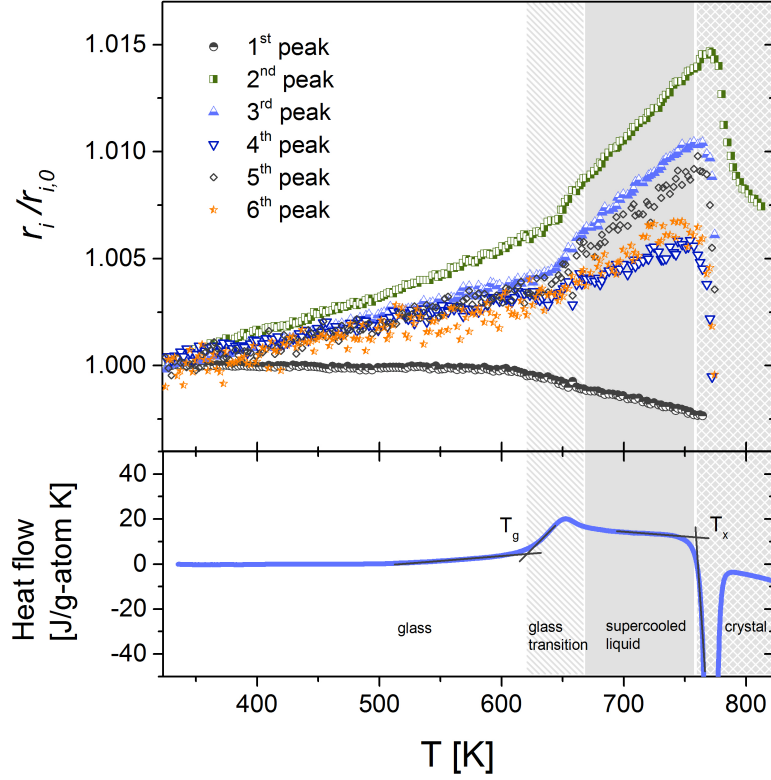


Figure 6.8: Upper panel: Shift of the peaks of  $g(r)$  in the Vit1b bulk metallic glass former in the different regimes. For clarity the individual temperature regimes are highlighted: glass transition (line-shaded), supercooled liquid (grey-shaded), crystallization (diamond-shaded).

coordination shell ( $r_1$  and  $r_2$ ), indicative for structural changes on the length scale of short-range order show a different thermal behavior compared to the peaks belonging to the higher coordination shells ( $r_3, r_4, r_5, r_6$ ), which rather show a more or less uniform behavior in the glassy state, implying a uniform dilatation on the length scale associated with medium- or extended-range ordering. On the other hand, by passing the glass transition regime the curves of  $r_3, r_4, r_5$ , and  $r_6$  start to branch, suggesting a non-uniform expansion at all length scales in the supercooled liquid regime.

To test whether the previous observations are common for metallic glass formers in general, the study is extended to other metallic glass forming alloys. The corresponding results of study are summarized in figure 6.9 for the glassy state and in figure 6.10 for the supercooled liquid state.

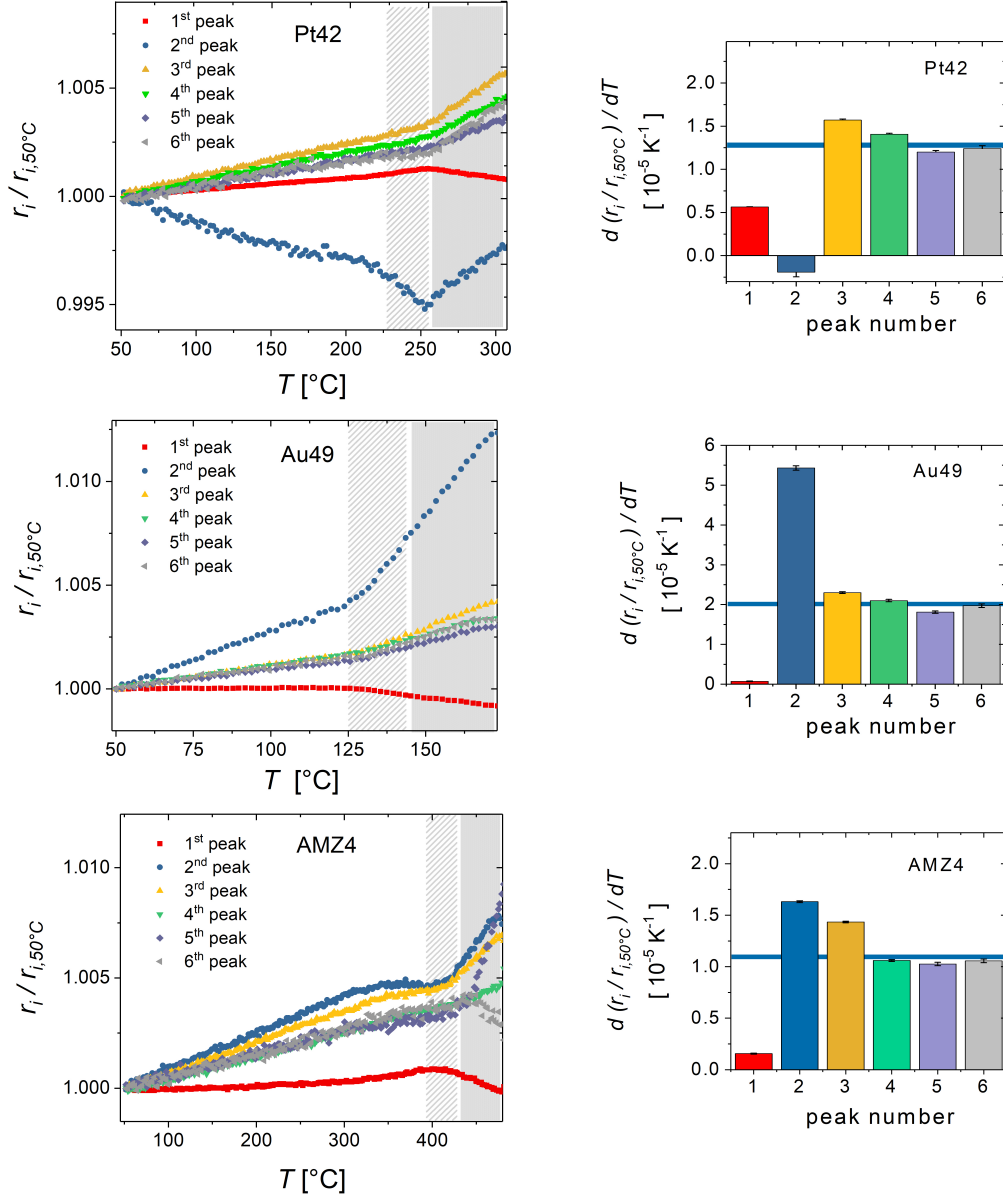


Figure 6.9: Left panel: Shift of the peak positions in  $g(r)$  for three bulk metallic forming alloys in the glass and supercooled liquid. The glass transition regime, ranging from the onset of the glass transition  $T_g^{\text{on}}$  to the end of the glass transition  $T_g^{\text{end}}$  is indicated by the line-shaded area, while the supercooled liquid regime, ranging from  $T_g^{\text{end}}$  to the onset of crystallization  $T_x$  corresponds to the grey-shaded area. Lower panel: Constant heating DSC trace of the alloy obtained for the same thermal protocol. Right panel: The local thermal dilatation in the glassy state as derived from the shift of the individual peaks in comparison to the macroscopic thermal expansion coefficient determined from dilatometry (horizontal blue lines).

## The glassy regime

In the glassy state at temperature well below  $T_g$  atoms are more or less frozen at their positions and no marked structural changes are expected to take place except for thermal vibrations of the atoms around their “equilibrium” positions, in accordance with the observation that the molar heat capacity of glasses,  $c_p$ , is usually close to  $3R$ . One might expect that the thermal-induced dilatation occurs more or less uniformly among the coordination shells. Given that  $r_i$  is indicative for the dilatation of the  $i^{th}$  coordination shell, the slopes of the curves  $d(\Delta r_i/r_{i,50C})/dT$  then should be nearly constant for all  $i$ . In contrast figure 6.8 and figure 6.9 reveal that this generally only applies to higher coordination shells ( $i \geq 4$ ), while the peak positions of the lower coordination shells ( $i \leq 3$ ) show a diverse behavior. This is illustrated by the diagrams on the right site of figure 6.9 in which the slopes  $d(\Delta r_i/r_{i,50C})/dT$  deduced from linear fitting of  $\Delta r_i/r_{i,50C}$  are shown. A comparison with the dilatometric data reveals that the thermal-induced expansion coefficients  $d(\Delta r_i/r_{i,50C})/dT$  beyond the third coordination shell, i.e. for  $i \geq 4$  essentially mirrors the macroscopically measured thermal dilatation (blue lines). A similar observation was already made for a binary Zr-Cu metallic glass in an earlier study performed by Mattern et al. [135]. These findings imply that, irrespective of the alloy, the thermal-induced shift of the coordination shells corresponding to atomic correlations on length scales beyond roughly 1 nm mirrors the macroscopic global expansion of the glass. On the other hand, the observation that the peaks  $r_1$ ,  $r_2$ ,  $r_3$  show a diverse thermal expansion which deviates from the macroscopic thermal expansion implies pronounced local atomic rearrangements on these length scales. The present findings thus support the conception of structural changes on the length scale of short-range order in addition to the effect of volume expansion and thermal oscillations as a consequence of the structural heterogeneity in the glass, in accordance to earlier observations made for a binary Cu-Zr glass [145].

## The supercooled liquid regime

With the transition into the supercooled liquid regime the structural units regain their mobility and no longer are frozen. The system restores its ergodicity and samples all configurations in the energy landscape that are thermally available. When passing the glass transition regime (line-shaded area), and entering the supercooled liquid region (diamond-shaded area), the curves in figure 6.9 branch, and the temperature dependence of the peak positions becomes more pronounced, as indicated by the increase in the steepness slopes of the curves, in agreement to what has been already observed for the Vit1b alloy (cf. figure 6.8). This suggest that the transition from the glassy to the liquid state goes ahead with an unfreezing of the structure on all length scales including short-, medium- and

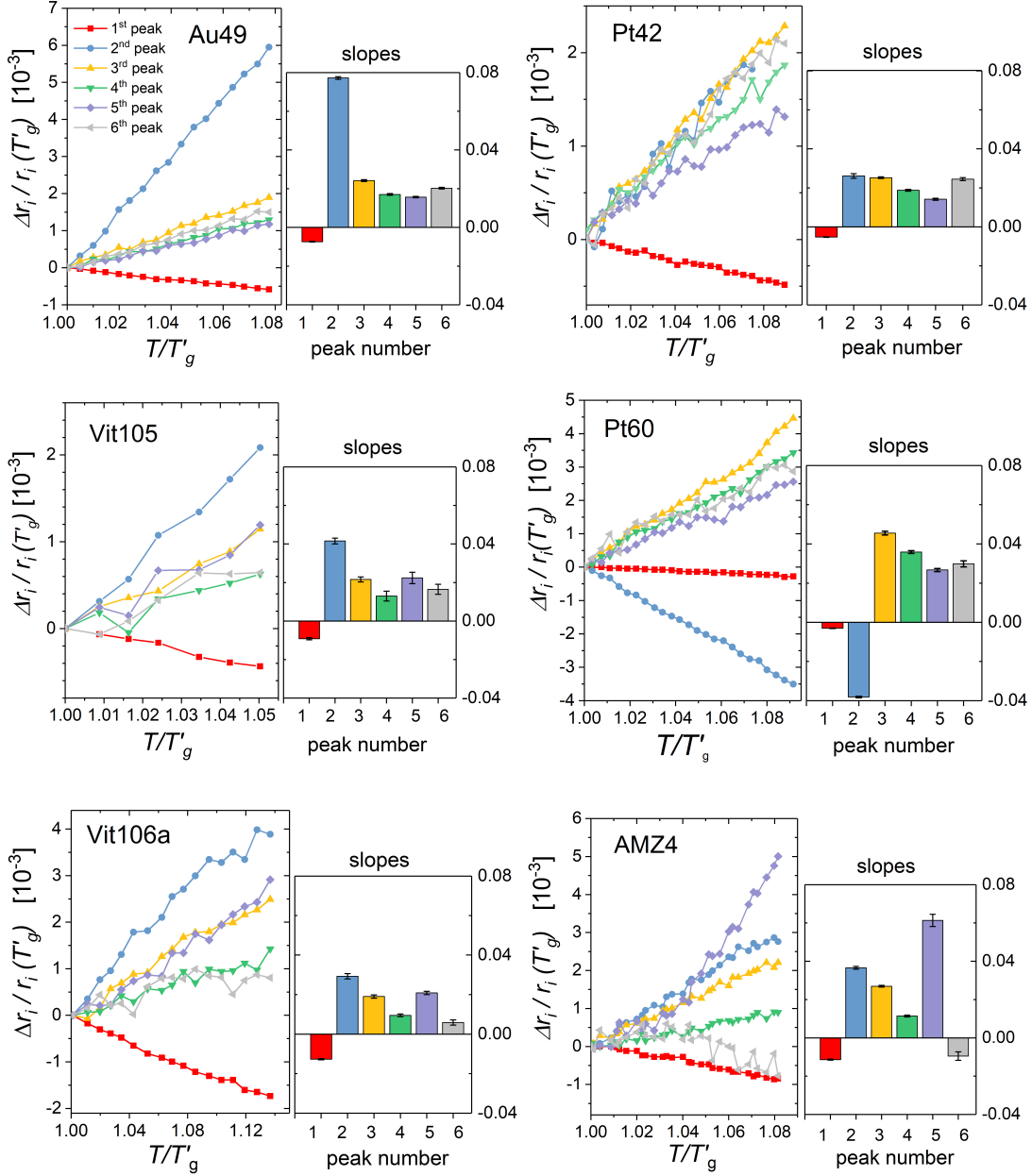


Figure 6.10: Large panels: Thermal-induced shift of the individual peak positions of the pair distribution function  $g(r)$  in the supercooled liquid of six bulk metallic glass forming alloys. Small panels: Slopes of the curves  $d(\Delta r_i(T)/r_i(T'_g))/d(T/T'_g)$ . Note that due to the normalization to  $T'_g$ , the values cannot directly be interpreted as the thermal expansion coefficient of the individual coordination shells.

extended-range ordering.<sup>3</sup>

In figure 6.10 the thermal shift of the peak positions of six bulk metallic glass forming systems in the supercooled liquid regime, normalized to their values at  $T'_g$ ,  $\Delta r_i/r_i(T'_g)$  is plotted versus a  $T'_g$ -scaled temperature. Note that  $T'_g$  denotes the end of the glass transition region, corresponding to the temperature where the system has fully equilibrated and restores its thermodynamic and dynamic properties of the metastable supercooled liquid state.

Provided that the shift of the peak mirrors the thermal-induced changes in the positions of the coordination shells, the observed diverse behavior implies a length-scale variant dilatation. The results summarized in figure 6.10 suggest that the thermal dilatation not only varies within a single system, but also that different systems show marked differences in their local thermal dilatation. This can be conceived by a comparison of the small panels which summarizes the slopes of the curves,  $d(\Delta r_i/r_i(T'_g))/d(T/T'_g)$ , obtained by linear fitting. Obviously, no clear pattern can be observed, except for the fact that in all alloys the first peak positions shows a (maybe unexpected) negative shift with temperature. At first glance this might be surprising as metallic liquids, in absence of any phase transition, normally show an increase in volume with temperature. However, the apparent negative expansion of the first coordination shell is a common observation made for metallic liquids and has been debated recently [146, 147]. For example, Lou et al. assign it to a decrease in coordination number which is attributed to the formation of more densely packed atomic clusters at higher temperatures [147]. An alternative explanation was given by Ding et al. who showed that a negative shift in  $r_1$  can also arise from a thermal-induced redistribution of atomic positions relative to the inherent liquid structure, implying that the “apparent negative expansion” in fact results from the asymmetry of the interatomic pair potentials at constant coordination number [146]. The six bulk metallic glass forming liquids shown in figure 6.10 span a wide range of fragility. Later in this thesis an attempt is made to find commonalities in the structural evolution among the different systems and to relate them to their fragilities.

## 6.5 Summary

Summarizing it can be stated that the current study supports that the classical Ehrenfest relation assuming  $v \propto Q_1^{-3}$  holds in the glassy state, but breaks down in the liquid state. Although there is a trend that a more pronounced thermal-induced shift of  $Q_1$  corresponds to a larger thermal dilatation, neither the assumption of an exponent  $\xi = 3$  (Ehrenfest) nor the (better) assumption of a  $\xi = 2.3$  (broken dimensionality, fractal structure) yield an accurate description of

---

<sup>3</sup>Note that in the glassy state the peaks belonging the 4<sup>th</sup>, 5<sup>th</sup>, and 6<sup>th</sup> coordination shell ( $r_4, r_5, r_6$ ) showed a uniform thermal expansion that mirrors the global thermal expansion as derived from dilatometry.

the thermal expansion data of various metallic liquids. A possible explanation is provided based on pronounced structural re-configurations that come along with a diverse shift behavior of the partial structure factors. In terms of the original formulation of the Ehrenfest relation 6.4 this can be rationalized by a marked temperature dependence of the constant  $K$ , that depends on the specific distribution of all atomic distances and thus should be affected by temperature-induced structural changes. Moreover, a comparison of the dilatometric thermal expansion data with the local thermal expansion data derived from the thermal-induced shifts of the peak positions in the pair distribution function  $G(r)$  indicates that (I) although the overall structure is essentially frozen in the glassy state, in addition to volume expansion, pronounced thermal-induced atomic redistributions take place on length scales corresponding to short-range ordering, (II) in the (supercooled) liquid state thermal-induced structural changes occur on all length scales comprising short- and medium- or extended ordering, (III) in the glassy state, the local thermal expansion derived from the shift of peaks beyond the third coordination shell, corresponding the length scales beyond one nanometer, mirrors the global thermal expansion derived from dilatometry.

## Chapter 7

# On the transformation of information between the reciprocal and real space

To get an understanding on the relation between  $Q_1$  and the total pair distribution function (PDF) it is useful to study the “transport” of information from reciprocal space ( $Q$ -space) into real space ( $r$ -space). As the two are related via Fourier transformation, the  $Q$ -space information can be viewed as the spectrum of density variation in  $r$ -space. Obviously, the majority of the  $r$ -space information stems from the first peaks in the  $Q$ -space, as the peak intensity decreases with increasing  $Q$ .<sup>1</sup> This is exemplarily shown in figure 7.1 for the  $Zr_{58.5}Cu_{15.6}Ni_{12.8}Al_{10.3}Nb_{2.8}$  (Vitreyloy106a) bulk metallic glass-forming liquid at around 300 K above its liquidus temperature  $T_l$ . The decomposition of the  $Q$ -space data clearly shows that, quantitatively, the majority of the information is “carried” into  $r$ -space by the low- $Q$ -data ( $Q < 5.7 \text{ \AA}$ ), while only a minor (but not necessarily unimportant) part of information is “stored” in the large- $Q$  data, i.e.  $Q > 5.7 \text{ \AA}$ . Nevertheless, it should be emphasized that a precise analysis of the PDF requires high quality diffraction data at all  $Q$ -ranges.

Often structural analysis of amorphous systems in  $Q$ -space is performed on the basis of features of the principal diffraction peak in  $I(Q)$  or  $S(Q)$ . To get a better understanding on the real-space information that is stored in the principal diffraction peak (PDP), a Fourier analysis of the PDP of  $S(Q)$  is performed, and it is found: (I) The Fourier transform of only the “positive deviation” of the PDP, i.e.  $S(Q) > 1$  yields a reasonable description of the atomic correlations at length scales corresponding to medium- or extended range ordering, while it gives a rather poor description of the short-range ordering (cf. blue lines in figure 7.2). (II) The wavelength of the density variations, corresponding to the average

---

<sup>1</sup>Note the  $Q$ -space function that is transformed is  $F(Q) = [Q(S(Q) - 1)]$ , not the structure factor  $S(Q)$  or the intensity  $I(Q)$ . However, normally the major peaks in  $S(Q)$  or  $I(Q)$  coincide with the major peaks in  $F(Q)$ .



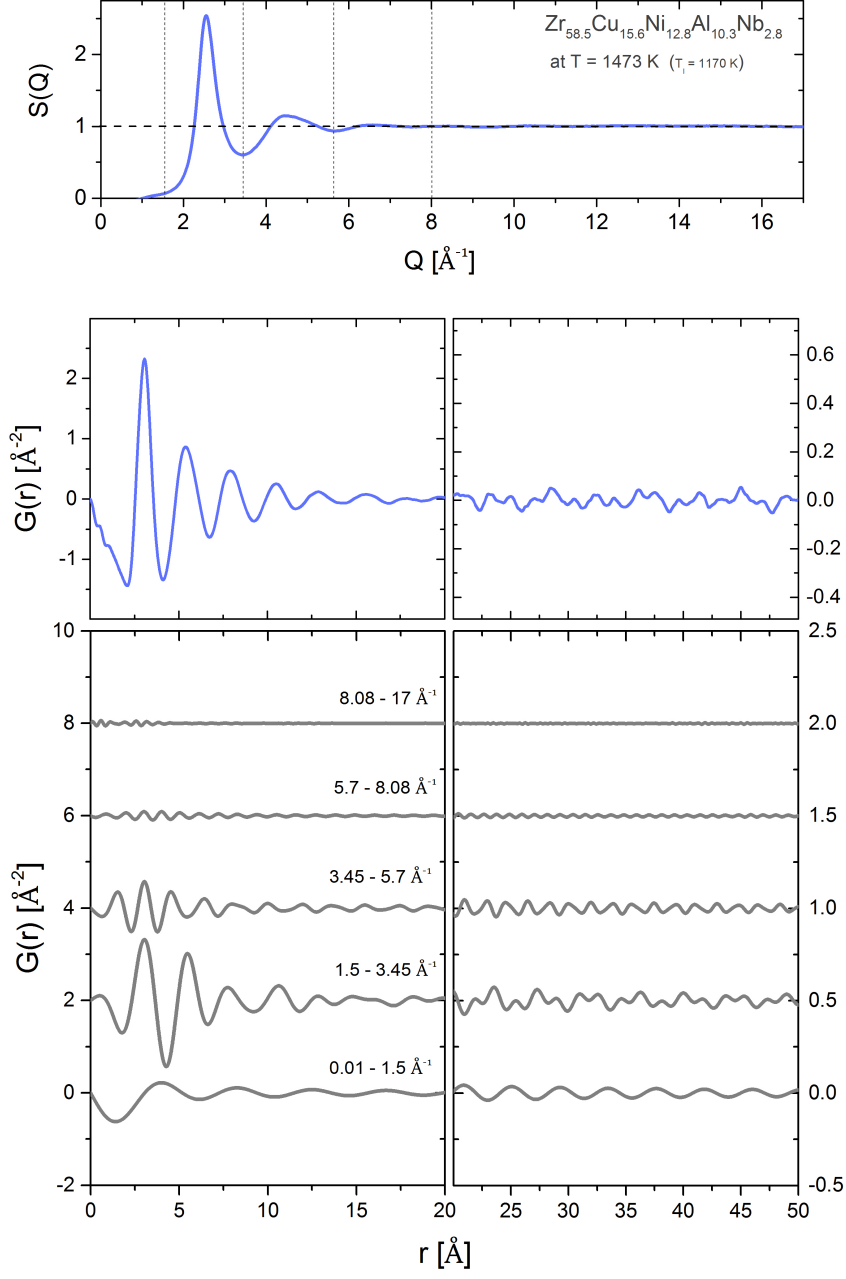


Figure 7.1: Fourier transforms of selected parts of the structure factor  $S(Q)$  of the  $Zr_{56.5}Cu_{15.6}Ni_{12.8}Al_{10.3}Nb_{2.8}$  (Vitreloy106a) bulk metallic glass-forming liquid at around 300 K above its liquidus temperature  $T_l$ .

spacing of the coordination shells, is “stored” in the position of the maximum of  $S(Q)$  (cf. orange lines in figure 7.2).

Although sometimes used as a measure of the degree of order present in a system, the peak height of the principal diffraction peak  $S(Q_1)$  is of limited use to extract information on the overall course of the PDF. Nevertheless, an increase in  $S(Q_1)$  normally reflects an increase in order in the system, as can be conceived by what follows. At higher temperatures the principal peak broadens and loses intensity, as shown in figure 7.3 for the Vit106a bulk metallic glass former at 1473 K and 300 K. This goes ahead with smaller peaks and a more pronounced decay behavior of  $G(r)$  at medium- and extended-range length scales (cf. large panels in figure 7.3), which is well-described by the Fourier transform of the “positive deviation” of  $S(Q)$ , i.e.  $S(Q) > 1$ , as mentioned above. Later on in this theses it will be shown that the evolution of the FWHM of the principal peak of  $S(Q)$  scales with the magnitude of the decay behavior, determined by the correlation length that can be extracted from a Ornstein-Zernike analysis of the long-range density oscillations.

Summarizing, it can be stated that the (I) the majority of information on the real space structure stems from the scattered intensity corresponding to the first two peaks in the structure factor, (II) the position of the principal diffraction peak is a signature of the average spacing of coordination shells in the glass and in the liquid, (III) the long-range decay of intensity variations in the structure is reasonably well-described by the “positive” part of the principal diffraction peak ( $S(Q) > 1$ ), (IV) during heating the PSD broadens and loses intensity corresponding to a more pronounced decay of long-range density variations, in agreement with a decrease of structural coherence with increasing temperature.

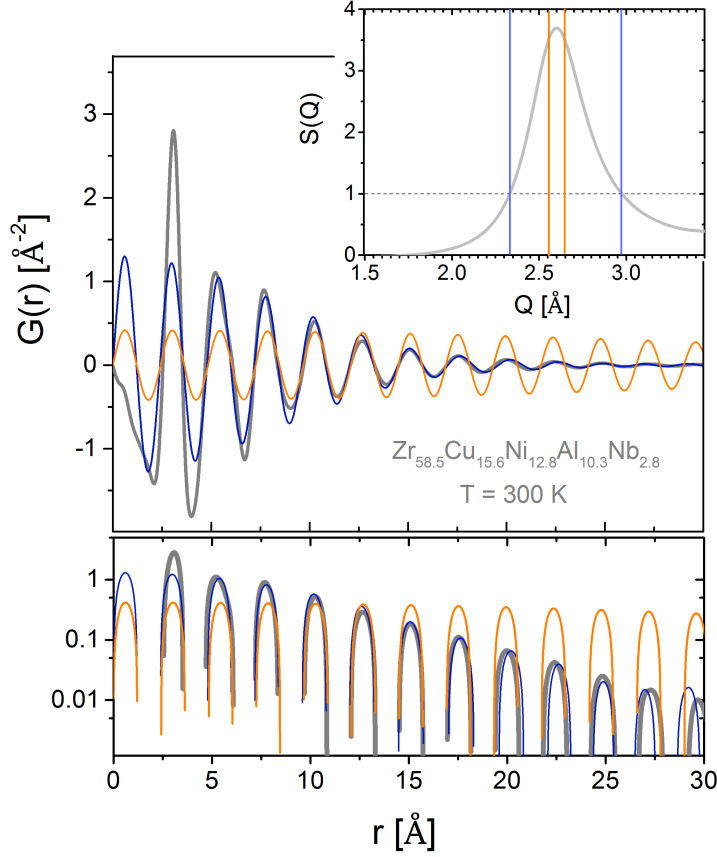


Figure 7.2: Structural information “carried” by the principal diffraction peak. Fourier transformation of only the “positive” part of the first peak of  $S(Q)$ , i.e.  $S(Q) > 1$  in between the two dotted, blue line in the inset figures, yields a reasonable description of atomic correlation at medium- or extended length scales, while only a poor description of short range ordering is obtained (blue lines). The maximum of the first peak “carries” the wavelength of density variations (orange lines). This becomes clearly visible in a logarithmic plot (lower panel).

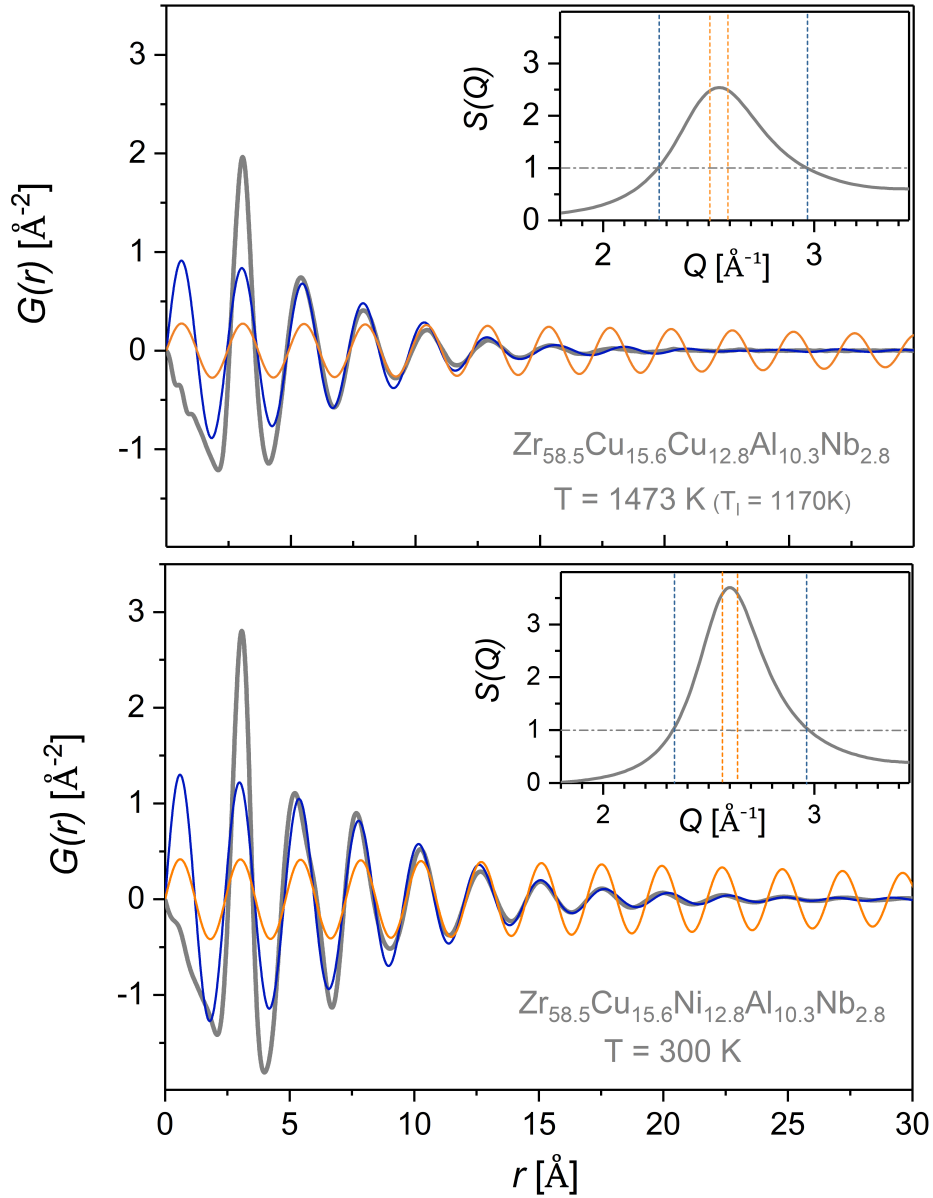


Figure 7.3: Effect of temperature on the principal diffraction peak  $S(Q)$  and its corresponding real-space data. At lower temperatures the principal peak of  $S(Q)$  sharpens and gains intensity. This corresponds to a less pronounced decay of the PDF. Irrespective of the temperature the Fourier transform of only the positive part of the principal peak (blue lines) adequately recaptures the decay behavior at medium- or extended-range length scales.

## Chapter 8

# Structure-Fragility Relations in Reciprocal Space

In this section an attempt is made to find correlations between the kinetic fragility and thermal-induced structural changes in bulk metallic glass forming liquids. The structural analysis is carried out in the reciprocal space, which, in contrast to the real space data that yield a direct picture of the atomic pair correlations present in the system, is directly accessible from diffraction experiments without invoking a mathematical transformation (Fourier transformation).

### 8.1 Empirical correlations between fragility and the first sharp diffraction peak

Changes in the external conditions of a physical system (e.g. temperature, volume, or pressure) cause changes in its structure, which in turn are reflected in the features of the diffraction patterns. The first sharp diffraction peak is the most outstanding feature of the diffraction pattern of an amorphous material. As the principal peak it carries a major part of the structural information. It is for this reason that its characteristics such as position, height and shape (e.g. its width) are often used to quantify structural changes. As discussed in chapter 7 its position corresponds to the wavelength of oscillations in the pair distribution function and hence gives the periodicity of the structure in real space, i.e. the periodicity of the coordination shells. Its height and width are related to the amount of disorder in the structure. For a given system, the peak becomes smaller and broadens with increasing temperature, reflecting a more pronounced smearing of atomic correlations in the systems. Later on in chapter 11 it will be shown on basis of an Orstein-Zernike analysis that its full width at half maximum (FWHM) is directly correlated to the correlation length of the long-range decay of density fluctuations in the real space structure. The structural analysis presented here in this chapter are performed using synchrotron radiation.

Glassy samples are heated in a furnace under high purity Argon atmosphere at a constant heating rate and diffraction patterns are recorded using a 2D-array detector. For further details on the experimental conduct the reader is referred to chapter 5. The present approach enables to investigate the structural changes in the glass and in the supercooled liquid near the glass transition up to the point where the amorphous structure transforms into the thermodynamically favored crystalline structure, defined by the onset temperature of crystallization,  $T_x$ , at the given heating rate.

To find a link between the fragility and structural changes, the thermal-induced shift of the first peak position in the intensity patterns,  $Q_1$ , of 8 bulk metallic glass forming alloys covering a wide range of fragility is investigated. It is found that either the intensity data  $I(Q)$  or the structure factor data  $S(Q)$  can be used without a notable loss of accuracy, in particular if one is interested only in relative changes of the peak positions due to changes in temperature.

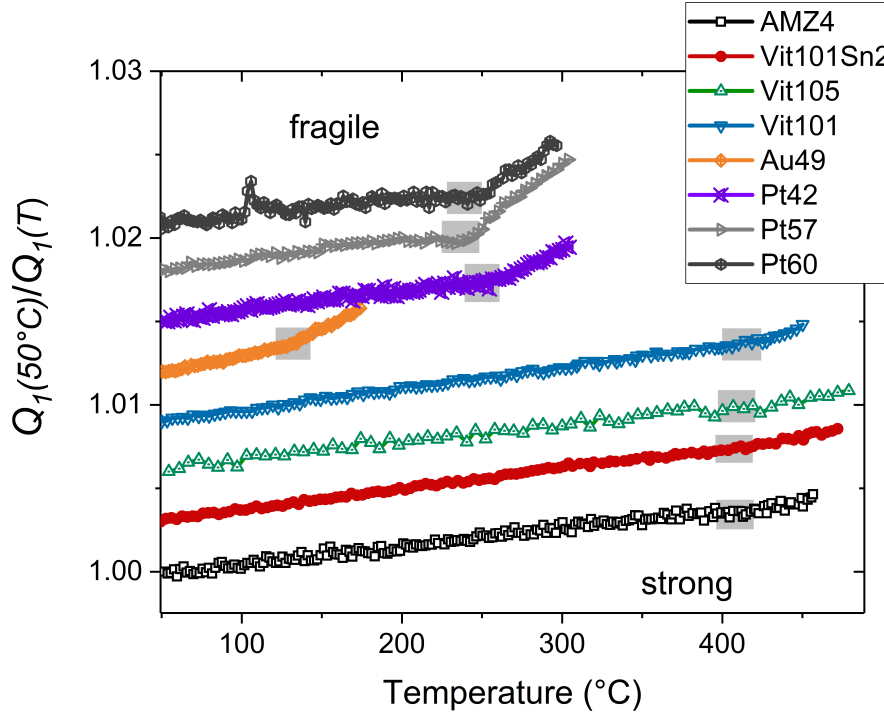


Figure 8.1: Thermal-induced relative shift of the position of the principal diffraction peak plotted as  $Q_1(T_{ref})/Q_1(T)$  during heating from room temperature to the onset of crystallization for 8 different bulk metallic glass forming alloys. The shaded areas define the glass transition regime of the alloys. The fragility of the liquid increases from the bottom to the top. Obviously, more fragile bulk metallic glass formers are characterized by a stronger temperature dependence of  $Q_1$  in the supercooled liquid than stronger bulk metallic glass formers.

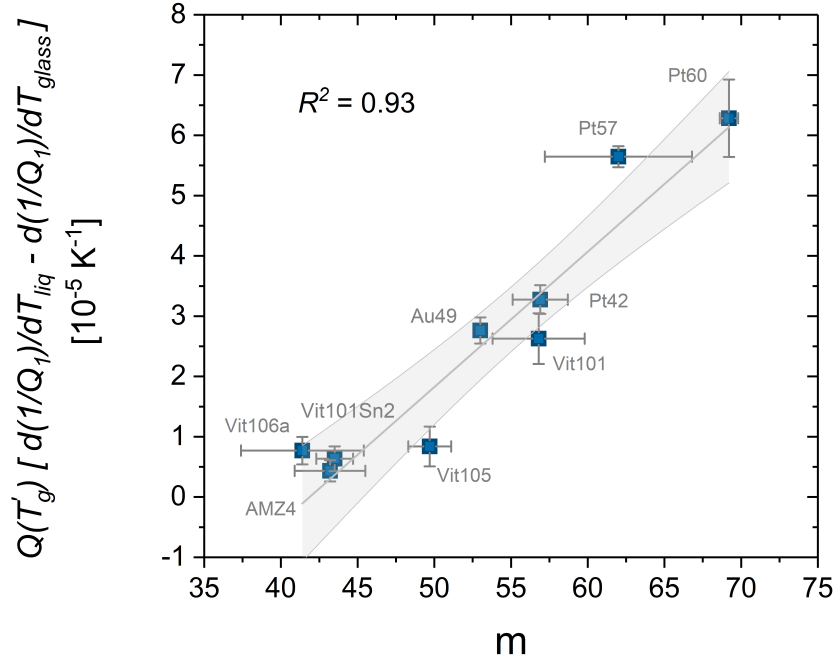


Figure 8.2: The thermal-induced shift of the principal diffraction peak relative to its value at  $T'_g$ ,  $Q_1(T'_g) \left[ (d(1/Q_1)/dT)_{liq} - (d(1/Q_1)/dT)_{glass} \right]$  for a variety of bulk metallic glass forming alloys plotted against the fragility index  $m$ . The errors bars indicate the standard deviation.

Figure 8.1 shows the thermal-induced shift of  $Q_1$  of 8 bulk metallic glass forming alloys, plotted as  $Q_1(T_{ref})/Q_1(T)$  with  $T_{ref} = 50^\circ C$ . The shaded areas indicate the glass transition regime of the individual alloys which are determined from DSC-analysis performed at same heating rate. For reason of clarity the curves are shifted along the y-axis and the data during crystallization and in the crystalline state is discarded. During heating the glassy samples  $Q_1$  decreases, i.e.  $Q_1(T_{ref})/Q_1(T)$  increases, in conformity with the conception that the structure expands due to the increasing kinetic energy of the particles. When heated through the glass transition range (shaded area), the thermal shift of  $Q_1$  becomes more pronounced indicating a higher sensitivity of the structure with respect to changes in temperature. Apparently, the increase of the thermal-induced shift in  $Q_1$  that occurs during the transition from the glassy to the supercooled liquid state is more pronounced for system with a larger kinetic fragility. Note that the kinetic fragility of the systems increases from the bottom to the top.

Kinetically, strong systems such as *AMZ4* or *Vit101Sn2* display almost no increase in their temperature dependence of  $Q_1$ , while kinetically more fragile systems such as the Pt-based alloys exhibit a marked increase in the slope of  $Q_1$

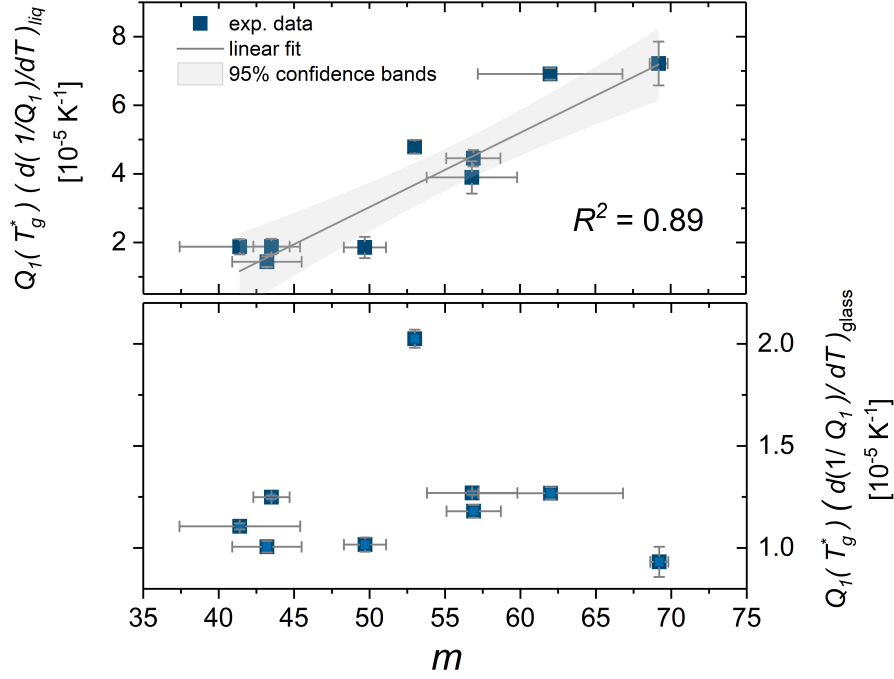


Figure 8.3: The thermal-induced shift of the principal diffraction peak relative to its value at  $T'_g$  for the liquid,  $Q_1(T'_g) (d(1/Q_1)/dT)_{liq}$  (upper panel), and for the glass  $Q_1(T'_g) (d(1/Q_1)/dT)_{glass}$  (lower panel), plotted against the fragility index  $m$ . The error bars indicate the standard deviation.

when passing through the glass transition. This suggests that fragility is linked to the relative increase in the temperature dependence of the thermal-induced shift in  $Q_1$  between the glassy and the liquid state. Indeed it is found that the kinetic fragility steepness index  $m$ , which measures the temperature dependence of the dynamics close to the glass transition, correlates well ( $R^2 = 0.93$ ) with the difference in the temperature dependence of the shift of  $Q_1$  between the liquid and the glassy state. This is shown in figure 8.2 where the difference of the slopes between the liquid and glass normalized to their values at  $T_g$ , i.e.  $Q_1(T'_g) [(d(1/Q_1)/dT)_{liq} - (d(1/Q_1)/dT)_{glass}]$ , determined from linear fitting in each temperature range, are plotted versus the kinetic fragility  $m$ . The fragility index  $m$  is a property of the liquid state and thus it might be expected that the good correlation found mainly stems from the liquid state. This is shown in figure 8.3 where the two contributions,  $Q_1(T'_g) (d(1/Q_1)/dT)_{liq}$  and  $Q_1(T'_g) (d(1/Q_1)/dT)_{glass}$ , are plotted individually against  $m$ . It is obvious that  $Q_1(T'_g) (d(1/Q_1)/dT)_{liq}$  shows a clear correlation with respect to  $m$ , while  $Q_1(T'_g) (d(1/Q_1)/dT)_{glass}$  essentially remains constant over the entire range of  $m$ , except for a single exception corresponding to *Au49* which is known to show unusual aging or relaxation phenomena in its glassy state [84, 90].



## 8.2 Connection to the free volume model

According to the free volume model more fragile liquids are characterized by a more pronounced temperature increase in the excess or free volume. Equation 3.10 establishes a connection between the increase in excess free volume given by the difference in the thermal expansion coefficients of the liquid and glassy states and the temperature dependence of the dynamics. These considerations tempt to transform the  $Q_1$ -behavior in each state into volume data, in order to challenge the data in terms of the free volume model. Note that a direct determination of  $\alpha$  in the supercooled liquid region via conventional dilatometry is precluded due to the pronounced softening that occurs during the measurement when the sample enters the glass transition and deforms plastically - already under the very low forces ( $mN$ ) exerted by the tactile sensor. This is in particular the case for the more fragile glass formers, where the softening, manifesting as a downwards bending of the  $\Delta L/L_0$ , occurs already immediately at the onset of the glass transition, leading to an underestimation of  $\alpha_{liq}$  or an apparent negative thermal expansion even under the lowest possible forces applied (0.05 mN) (cf. figure 6.3).

In chapter 6 it was shown that the Ehrenfest relation holds for the glassy state, meaning that  $Q_1^{-3}$  scales with the increase in the volume of the system. On the other hand the Ehrenfest relation seems to break down in the liquid state, and a clear functional dependence between the shift of  $Q_1$  and the volume  $V$  is less evident. Still, it appears that a better description of the experimental data in the liquid state can be given by assuming a non-integer value for the exponent  $\xi = 2.3$ , relating  $v$  and  $Q_1$  via equation 6.7. Using equation 6.8 the shift of  $Q_1$  can be transformed into a thermal coefficient  $\alpha_V^{XRD}$ . Assuming  $\xi = 3$  for the glass and  $\xi = 2.3$  for the liquid state and plotting the difference of the obtained thermal expansion coefficients between the liquid and the glass,  $\Delta\alpha_{l-g}$ , versus the kinetic fragility steepness index,  $m$ , yields figure 8.4. As anticipated, more fragile systems are characterized by a larger difference of the thermal expansion coefficients derived from the shift of  $Q_1$ , in agreement with the conception that a more pronounced increase in volume with temperature should go along with a higher temperature sensitivity of the dynamics.

Due to the universal connection between  $D^*$  and  $m$  proposed by Bohmer et al. [148], the  $\Delta\alpha_{l-g}$  data can be equally well plotted as a function of  $D^*$  as shown in figure 8.4. The orange squares are obtained by transforming the  $m$  values of figure 8.4 into  $D^*$  using the relation between  $D^*$  which is tested against experimental data derived from fitting of viscosity data in the inset. In both cases it appears that  $\Delta\alpha_{l-g}$  asymptotically approaches the zero-line (dashed line in figure 8.4 with decreasing fragility  $m$ , so that for the strongest liquids  $\alpha_l \approx \alpha_g$ . Since there is no reason to assume that  $\Delta\alpha_l < \Delta\alpha_g$ , this suggests an upper bound for  $D^*$  in metallic glass forming alloys. Indeed, the maximum  $D^*$  value found for a metallic glass forming liquid is  $D^* = 35$  [98], corresponding to  $m \approx 33$ . This is markedly larger than the absolute minimum value  $m = 16$  indicative for a simple

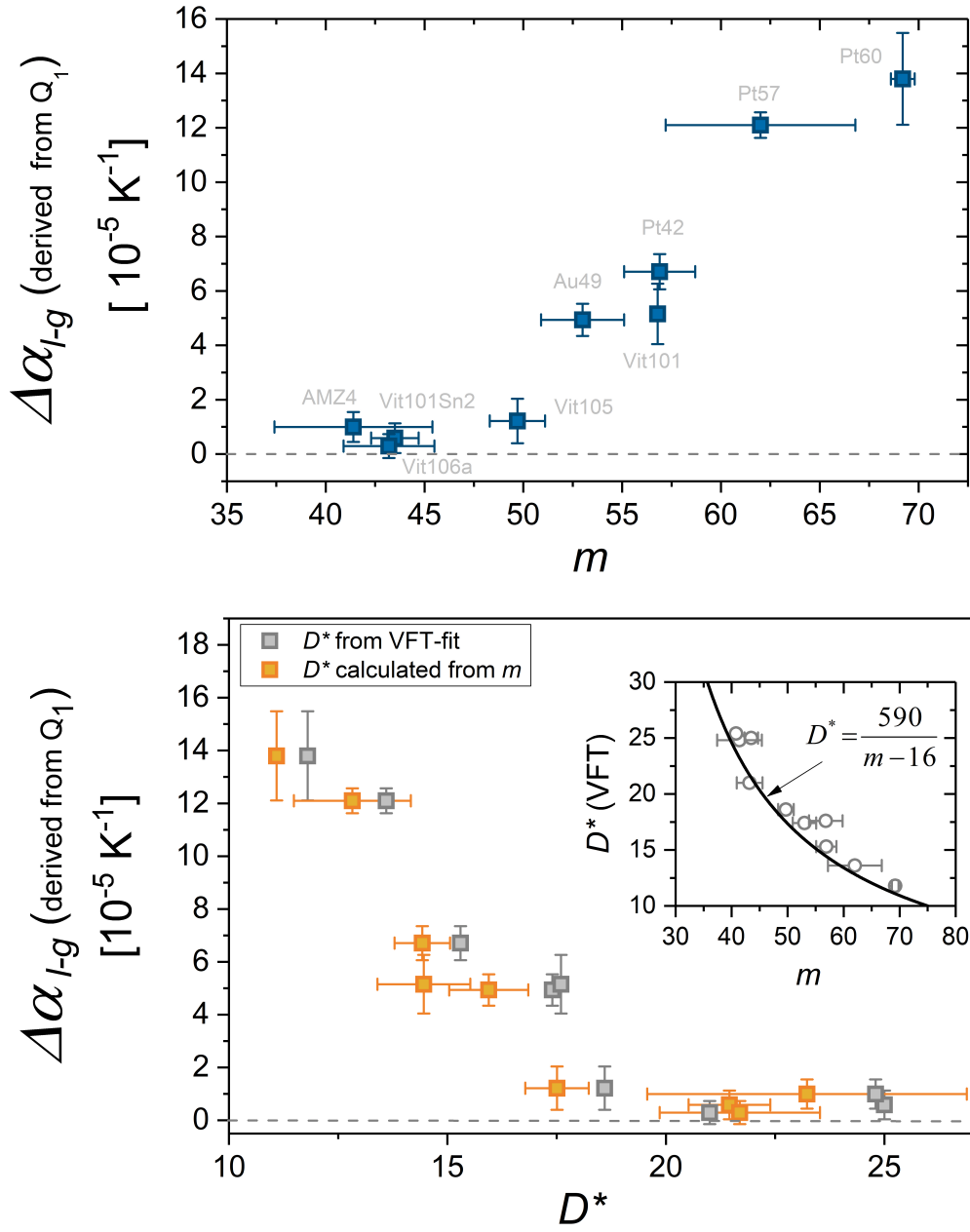


Figure 8.4: Upper panel: Difference in thermal expansion coefficient between the liquid and glass,  $\Delta\alpha_{l-g}$  as derived from the thermal shift of the maximum in the principal diffraction peak,  $Q_1$ , plotted versus the kinetic fragility indices  $m$  (upper panel) and  $D^*$  (lower panel). Inset in the lower panel: Inset: Experimental data tested against the relation between  $D^*$  and  $m$ , proposed by Boehmer et al. [148].

exponential, Arrhenius-like dynamic behavior.

### 8.3 Summary

The present study performed on the reciprocal space diffraction data of various bulk metallic glass formers indicates that fragility correlates with the thermal-induced shift of the inverse position of the principal diffraction peak. A more pronounced difference between the shift in supercooled liquid and glassy state generally correlates with a higher kinetic fragility. This originates mainly from the diverse shift behavior in the liquid state, while no clear correlation between the shift and the fragility is found for the glassy state. Relying on the observations made in chapter 6, the peak shifts are transferred into volume expansions and discussed in terms of the free volume model. The corresponding data support the conception that more fragile glass formers are characterized by a more pronounced formation of excess (free) volume in the liquid, while the strongest glass formers are characterized by a rather marginal formation of free volume in the supercooled liquid regime. This implies that, in contrast to fragile liquids that show a marked densification upon undercooling before they freeze into a glass, the strongest bulk metallic glass forming liquids reach high-density packed states already at temperatures well above the glass transition temperature.

## Chapter 9

# Structure-Fragility Correlations in Real Space

The studies performed and reported in this chapter intend to find common characteristics of structural changes in bulk metallic glass forming liquids that can be linked to their fragility. In particular, the following questions are addressed.

1. Are there common structural features that correlate with fragility?
2. Do they occur on particular length scales?
3. Is it possible to define a structural metric that serves as an indicator for the fragility?
4. How to interpret these correlations physically?

To answer these questions, the structure of a variety of bulk metallic glass forming alloys, covering a wide range of fragility, is investigated in the deeply undercooled liquid state close to  $T_g$  using synchrotron x-ray diffraction at the P07 beamline at the German Synchrotron DESY. The measured diffraction data are integrated, the integrated raw intensities  $I_{raw}(Q)$  are corrected to obtain the total structure factor  $S(Q)$ , and transformed into real-space data  $G(r)$  according to the procedure described in chapter 5. The structural data are set in relation to available equilibrium viscosity data that are obtained from three point beam bending relaxation studies. As the kinetic fragility is a measure of dynamics in the liquid state, the analysis is limited from the end of the glass transition,  $T'_g$ , where the system has fully equilibrated, until the onset of crystallization  $T_x$ .

The main challenge in relating the fragility of liquids to their structure lies in identifying suitable structural parameters from structural metrics available via the distribution functions. Close to the glass transition, fragility is normally quantified via the so-called *steepness index*  $m$  (equation 9.1) which graphically corresponds to the slope of the viscosity curve at  $T/T_g = 1$  in the Angell-plot (cf. figure 3.7). This suggests to analyze the structural metrics in a similar way in order to reveal possible structure-fragility correlations.

## 9.1 The peak position approach

As a first step the temperature-induced shift of the peak positions of  $G(r)$ ,  $r_i$  is investigated. Although intuitively less amenable in terms of its physical interpretation  $G(r)$  is used instead of  $g(r)$  as it is the quantity that is directly obtained from Fourier transformation and does not require knowledge of the temperature dependence of the number density  $\rho$ . As the peak positions in the two distributions are not necessarily equal, an estimation of the error was made by a comparison of the peak maxima in  $G(r)$  and  $g(r)$ , and it was found that either of the two functions gives qualitatively equivalent results, justifying an interpretation in terms of  $g(r)$ .

To analyze whether there is a generic connection between the fragility and thermal-induced peak shifts, the normalized shift of positions  $\Delta r_i/r_i(T'_g)$  of variety of supercooled bulk metallic glass formers liquids is plotted against a  $T'_g$ -scaled inverse temperature ordinate,  $T'_g/T$ . It is noticed that, on distinct length scales, the  $\Delta r_i/r_i(T'_g)$  data of the glass forming liquids follows a trend comparable to their viscosity behavior. Most notably, the thermal-induced shifts of the first and fourth peak,  $r_1$  and  $r_4$ , follow trends that apparently correlate with the viscosity behavior, suggesting a particular role of these length scales with respect to fragility. This is shown in figure 9.1. Systems with a more fragile kinetic behavior (higher  $m$ ) tend to show a smaller thermal-induced shift of in the first peak position  $\Delta r_1/r_1(T'_g)$ , while the negative of the thermal-induced shifts of the fourth peak positions,  $-\Delta r_4/r_4(T'_g)$ , tend to directly mimic the fragility of the alloys. To quantify these observations, structural fragility parameters are defined and compared to the kinetic fragility index  $m$ . Following the definition of the fragility steepness index  $m$  the structural fragility parameters are defined as

$$m_{str}^{r_i} = \frac{\partial \Delta r_i/r_i(T'_g)}{\partial T'_g/T} \Big|_{T=T'_g} \quad (9.1)$$

Note that  $m_{str}^{r_i}$  geometrically corresponds to the slope of the curves in figure 9.1 at  $T'_g/T = 1$ , just as the fragility index  $m$  corresponds to the slope of the dynamics in the Angell-plot. With the help of this definition quantitative correlations between the structural changes in the liquid state and the kinetic fragility can be established as shown in the lower panels of figure 9.1. Note that in case of the first peak the inverse of  $m_{str}^{r_1}$  is plotted in order to account that a larger shift in  $r_1$  appears to correlate with a smaller fragility  $m$ . Linear regression analysis between  $m_{str}^{r_i}$  with  $i = 1, 4$  and  $m$ , in both cases, yields  $R^2 = 0.88$ .

The two correlations obtained are surprisingly similar. Indeed linear regression analysis between the inverse of  $m_{str}^{r_1}$  and  $m_{str}^{r_4}$  yields  $R^2 = 0.957$ , suggesting a strong coupling between the thermal induced structural changes on the length scales of nearest neighbors and atomic pair correlations on the length scale of 1 nm. It is emphasized here that the latter is of the order of the expected length scale of medium-range ordering in bulk metallic glasses, i.e. 0.7 to 1 nm [57].

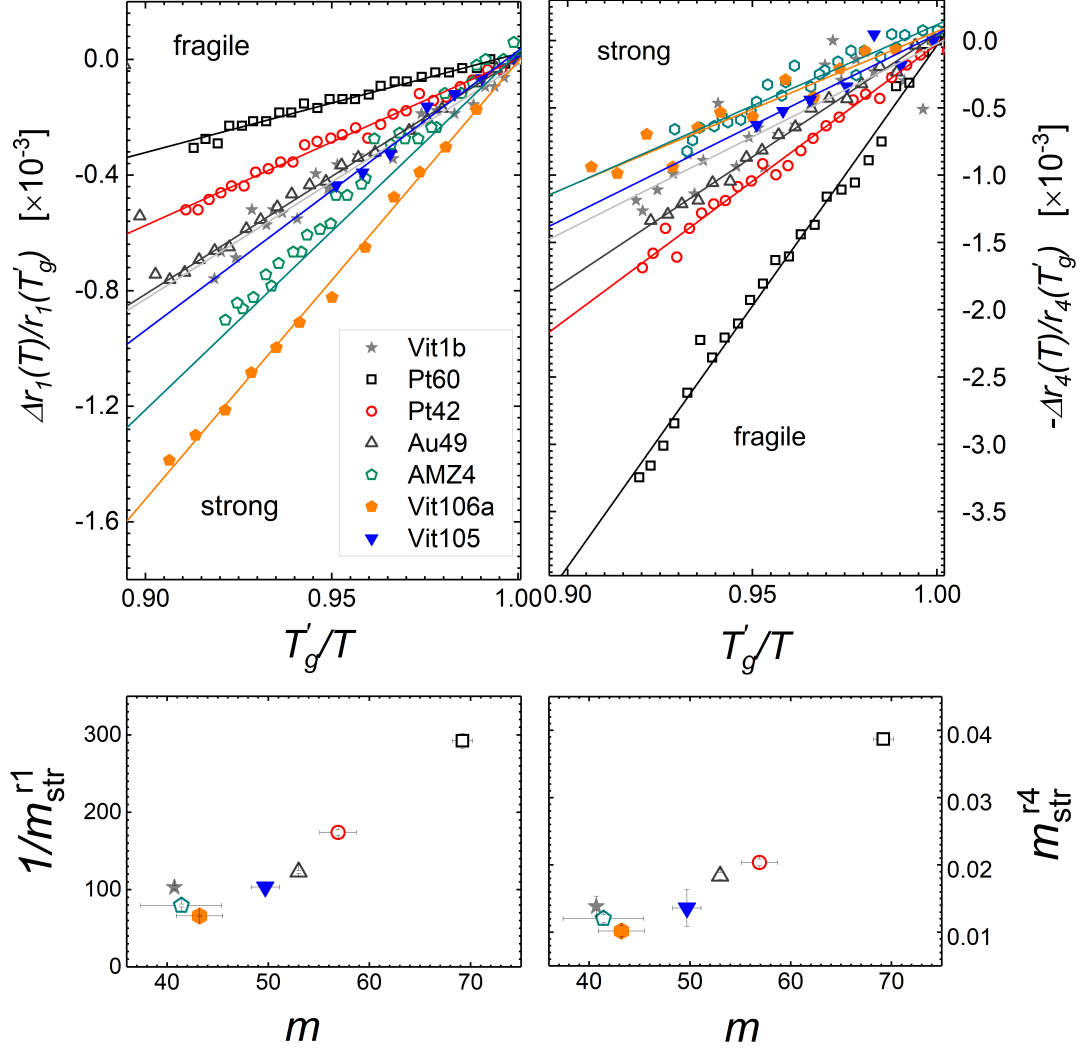


Figure 9.1: Empirical correlation between the temperature induced shift of peak positions in  $g(r)$  and the fragility  $m$ . The upper panels show the thermal-induced shift of the first and fourth peak maxima of  $G(r)$  plotted versus  $T_g'/T$  in accordance with the definition of the steepness index  $m$ . The lower panels show the empirical correlations obtained if the slope of the curves in the upper panels is plotted versus the fragility  $m$ .

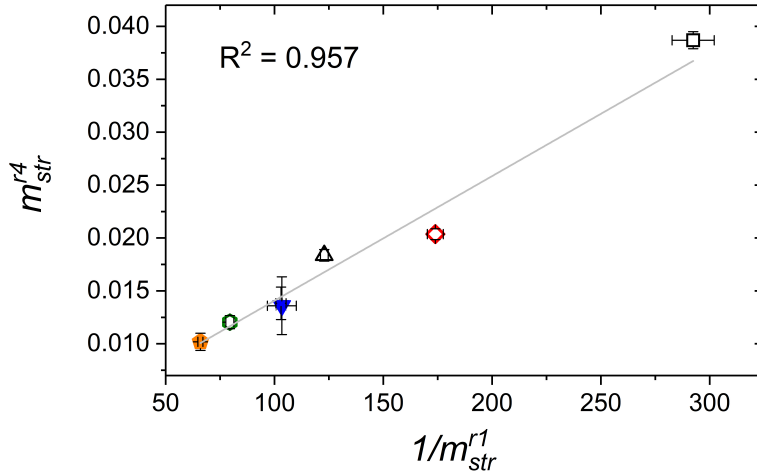


Figure 9.2: Correlation between the two structural fragility parameters  $m_{str}^{r_1}$  and  $m_{str}^{r_4}$ .

## 9.2 The local dilatation approach

It is an old conception that changes in dynamics are linked to changes in the local volume that is accessible to the structural units (molecules, particles, etc.) composing a system. The Doolittle equation and free volume models treated in chapter 3 are different approaches to quantify this idea. In case of the Doolittle equation 3.10 the atomic mobility is linked to the average molar volume while no assumptions are made on the spatial density variations in the structure. On the other hand, the free volume models assume a non-uniform spatial distribution of volume throughout the system. Here, the amorphous structure is considered to be composed of cells formed by nearest neighbor cages whose local volume defines the local mobility. Regions of lower local density are considered to be sources of increased atomic mobility (liquid-like) while regions of higher local density are considered as less mobile (solid-like). In a fully random system, e.g. an ideal gas-like structure, the volume (or density) is distributed equally in space and does not fluctuate among different length scales, therefore  $g(r) = 1$  for  $r > r_c$ , where  $r_c$  refers to the minimum separation possible between two atoms. In contrast, liquids do show ordering tendencies that result in local density variations. In general, ordering is more pronounced on shorter length scales and ceases on larger distances. The distribution functions defined in chapter 3 expose how much the density varies along the different length scales.

The peak analysis performed in the previous section shows that the thermal-induced peak shift can vary strongly among the coordination shells. Furthermore, it appears that fragility correlates with thermal-induced peak shifts at certain length scales, while at others it does not. These conceptions and observations

stimulate to relate fragility to the thermal-induced local volume changes. Assuming in first approximation that  $r_i$  represents the average distance of the  $i^{th}$  coordination shell, the volume included in the volume sphere up to  $r_i$  at temperature  $T$ ,  $V_i(T)$  is

$$V_i(T) = 4/3\pi r_i(T)^3 \quad (9.2)$$

Changes in  $V_i(T)$  due to changes in temperature can then be regarded as the thermally-induced “volume dilatation” on the length scale  $r \leq r_i$ . Naturally, this volume description applied to the first and fourth coordination shell,  $V_1$  and  $V_4$ , leads to essentially identical correlations with fragility as those reported in figure 9.1 and thus are not shown here again. The correlation of  $V_1$  with  $m$  means that the fragility scales inversely with the negative volume expansion of the first coordination shell. The apparent negative expansion of the first coordination shell has been interpreted as a change in coordination number [147] or as an evidence for a thermal-induced asymmetric redistribution of atoms towards the repulsive part of the pair potential [146]. Accordingly, the observed correlation between  $V_1$  and  $m$  suggest that a softer repulsion coincides with a stronger kinetic behavior - an idea that is supported by observations made in colloidal systems and recently has been transferred to supercooled metallic liquids [149, 150]. The correlation between  $V_4$  and  $m$  might be more surprising. Obviously,  $V_4$  corresponds to the extension of medium-range ordering in metallic glasses that is expected from structural models like the efficient cluster packing (ECP), which assumes that the structure of glasses (and therefore also deeply undercooled liquids) is composed of solute-centered clusters that are arranged in efficient cluster-packing schemes like for example fcc, hcp, or icosadecral [57]. Due to mismatch strains the cluster super-structure is expected to break down at roughly 1 nm in agreement with the length scale of  $V_4$ . The solute-centered clusters themselves only contribute to the first two peaks in  $G(r)$ . Assuming that the viscous slowdown is related to the formation of (efficiently-packed) cluster networks or superstructures, it might therefore be expected that fragility in the supercooled liquid should be linked to the thermal-induced dilatation at a length scale somewhere in between the second and fourth coordination shell (also cf. section 6.4 and figure 6.7).

To test this hypothesis, the volume spheres  $V_i$  are sectioned into spherical volume shells. The volume in between the  $i^{th}$  and  $j^{th}$  coordination shell is given by

$$V_{ij} = V_i - V_j = 4/3\pi(r_i^3 - r_j^3) \quad (9.3)$$

with  $j = 1, 2, 3$  and  $i = j + 1$ . Accordingly, the volume dilatation, normalized at  $T'_g$ ,  $\epsilon_{ij}$  would be given by

$$\epsilon_{ij} = \frac{V_{ij}(T) - V_{ij}(T'_g)}{V_{ij}(T'_g)} = \frac{\Delta V_{ij}(T)}{V_{ij}(T'_g)} \quad (9.4)$$

These definitions now allow to investigate the spatial distribution of the thermally induced volume changes in each volume shell, which in turn should enable



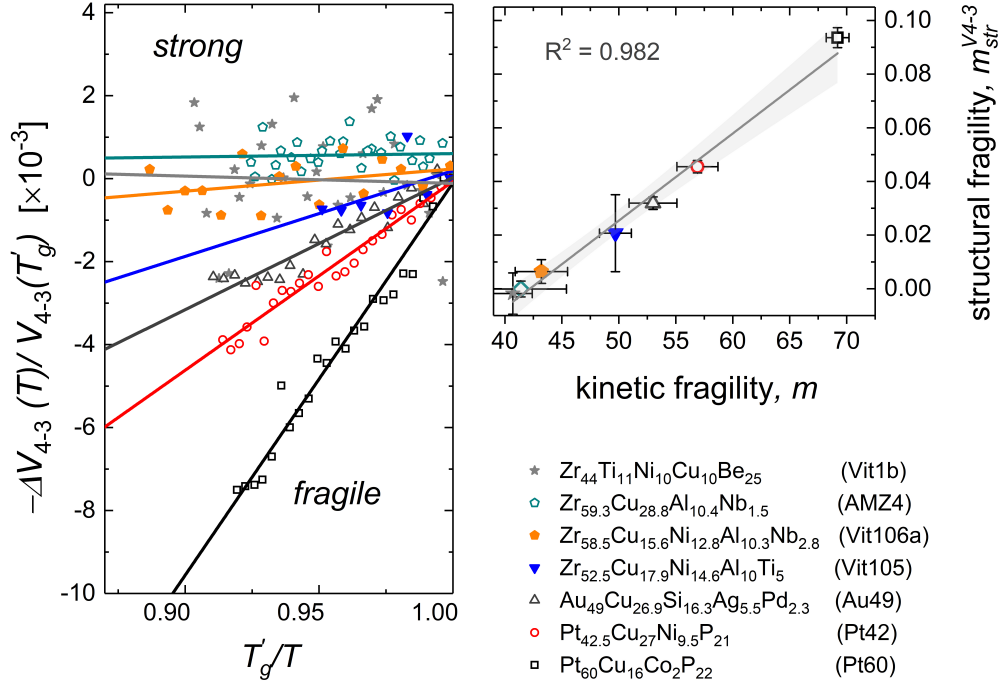


Figure 9.3: Correlation between the local dilation on a length scale between 0.7 and 1 Å,  $-\Delta V_{4-3}/V_{4-3}(T'_g)$ , and the temperature dependence of the viscosity near the glass transition, i.e. the fragility  $m$ . More fragile liquids show a more pronounced dilation, while almost no dilatation is found for the strongest metallic glass formers (left panel). Plotting the slope of the curves against the fragility index  $m$  yields a strong linear correlation ( $R^2 = 0.982$ ).

to more precisely identify the length scale of the structural changes that are connected to fragility. Calculating the thermal-induced dilatation in the shells, it is observed that  $\epsilon_{ij}$  varies among the different volume shells, implying a heterogeneous distribution of the thermal-induced volume. Comparing the local dilatation of the shells among all alloy systems studied, it is found that only  $\epsilon_{43}$  correlates with the kinetic fragility index  $m$ , whereas all other  $\epsilon_{ij}$  for  $j = 1, 2, 3$  and  $i = j + 1$  do not. This is shown in figure 9.3 where the local dilatation  $\epsilon_{43}$  is plotted versus the  $T'_g$ -scaled inverse of temperature, in analogy to the Angell-plot. It is easily recognized that the magnitude of changes in  $\epsilon_{43}$  follows the trend of the dynamics (fragility). Kinetically stronger system, having a shallower slope around  $T_g$  in the Angell-plot, exhibit smaller changes in  $\epsilon_{43}$ , while more fragile systems, characterized by a steeper slope, show more pronounced changes in  $\epsilon_{34}$ . To quantify this observation, it is useful to introduce another structural fragility parameter

defined in analogy to the steepness index  $m$

$$m_{str}^{43} = - \frac{\partial \left( \Delta V_{43}(T) / V_{43}(T'_g) \right)}{\partial \left( T'_g / T \right)} \Big|_{T=T'_g} \quad (9.5)$$

Note that  $m_{str}^{43}$  geometrically corresponds to the slope of the curves in figure 9.3, just as  $m$  corresponds to the slope of the viscosity (or relaxation) times in the Angell-plot. Plotting the structural fragility parameter  $m_{str}^{43}$  versus the kinetic fragility  $m$  yields a linear correlation with a  $R^2$  of 0.982 implying a link between the thermal-induced dilatation on a length scale in between 0.7 to 1 nm, i.e. the length scale expected for the extension of medium-range ordering in liquids and glasses as hypothesized from the efficient cluster packing (ECP) model [57], and the thermal-induced changes in viscosity. As mentioned earlier .

### 9.3 Summary

Summarizing, the above findings imply a connection between the dynamic behavior and thermal induced structural changes on particular length scales. It appears that more fragile liquids are characterized by more pronounced peak shift on the length scale of approximately 1 nm, i.e. the length scale expected for the extension of medium-range ordering in bulk metallic glasses [57], coupled with less pronounced structural changes in the first coordination shell, or more precisely a less pronounced negative shift in the first peak position. The latter observation might be related to the compressibility or the softness of the repulsive part of the interaction potential. Provided that a more negative shift of  $r_1$  indeed results from a softer repulsion, the current observation implies that “softer pair potentials make stronger liquids”- a relation found for colloidal systems and recently transferred to metallic system [149, 150].

The present analysis of the local dilatation, calculated from the thermal shift of the peak positions, suggest that fragility is linked to the local expansion on a length-scale of about 0.7 to 1 nm. Considering that this is the length scale expected from the efficient cluster packing model for the extension of medium-range ordering due to the formation of supercluster structures, the present findings support the conception that the viscous slowdown, experienced by liquids when cooled towards the glass transition, is connected to an aggregation or network formation of energetically preferred, locally favored structures, as observed in recent computational studies [59, 66, 68, 151]. Recognizing that energetically preferred structures, e.g. efficiently packed clusters should have a higher stability against thermal dilatation, the scenario of an inhomogeneous redistribution of volume among the clusters aggregates might be a possible explanation of the observed correlation. In more fragile metallic glass formers the larger volume expansion leads to a more pronounced disintegration of the cluster

aggregates which in turn results in more rapid viscosity decrease upon heating. On the other hand, in stronger metallic glass formers the less pronounced thermal dilatation goes along with a less pronounced disruption of the cluster structure explaining their lower sensitivity of the dynamics (viscosity) with respect to temperature changes in the supercooled liquid regime.

# Chapter 10

## On liquid-liquid phase transitions in bulk metallic glass forming liquids

Reyling on previous observations made on a similar glass forming alloy [152], the present chapter aims to find of structural evidences for a liquid-liquid phase transition in the  $Zr_{58.5}Cu_{15.6}Ni_{12.8}Al_{10.3}Nb_{2.8}$  based bulk metallic glass forming alloy. To this end, high energy synchrotron x-ray diffraction studies combined with electrostatic levitation was performed at DESY Petra III beamline P07. This study was performed in collaboration with the Institute for Materials Physics in Space at the German Aerospace Center (DLR). The results of this work and parts of this chapter are published in [153]. Here the main findings are reproduced along with some complementary work.

### 10.1 Liquid-liquid transitions

Within the last decades increasing evidence for polymorphous phase transitions in the liquid state, referred to as liquid-liquid transitions (LLTs) has been reported experimentally [154–156] as well as computationally [35, 157–159]. These findings include the liquid [155, 159, 160] as well as its frozen-in glassy state [161] and span a wide range of chemical species including, e.g., water [162, 163] aqueous solutions [164],  $Y_2O_3 - Al_2O_3$  [154],  $SiO_2$  [159],  $BeF_2$  [165], triphenyl phosphite [144, 166], Si, P [155, 160], Ge [156], and recently multi-component bulk metallic glass (BMG) forming systems (Ce-Al [161], Zr-Cu-Ti-Ni-Be [152]).

Aside from the fundamental question of whether a system that is characterized by permanently rearranging configurations can exist in distinct modifications (liquid phases) that are equal in composition but differ in local structure and thermodynamic properties [167], LLTs are also of interest due to their implications on the system's dynamics. In particular, LLTs have been proposed to explain exper-

imentally observed anomalous changes in liquid dynamics, a phenomenon known as fragile-strong transition (FST) [107, 108, 152, 159, 168]. Apart from their relevance to fundamental aspects of physics, FSTs recently have been recognized for their technological importance, e.g., in phase-change memory applications [127, 169].

### 10.1.1 Phenomenology of LLTs

The sensitivity of liquid dynamics with respect to temperature changes is quantified by the concept of *fragility* [94]. Liquids that follow a near exponential temperature dependence (Arrhenius behavior) are classified as *strong*, while liquids that deviate from Arrhenius behavior are defined as *fragile*. Often, experimental data are best described by the empirical Vogel-Fulcher-Tamman (VFT) equation  $f = f_0 \exp\left(\frac{D^*T_0}{T-T_0}\right)$  where  $D^*$  and  $T_0$  are system-specific parameters,  $f$  denotes a dynamical variable (e.g. diffusivity, viscosity or relaxation time),  $f_0$  is the lower limit for  $T \rightarrow \infty$ ,  $T_0$  is the temperature where  $f$  would approach infinity in the limit  $T \rightarrow T_0$ , and  $D^*$  is the so-called fragility parameter. Strong liquids are characterized by larger values of  $D^*$  and  $T_g/T_0$ , fragile liquids exhibit lower  $D^*$  and  $T_g/T_0$  where  $T_g$  denotes the glass transition temperature. In this description a FST manifests in changes in  $D^*$  and  $T_g/T_0$ .

A connection between the dynamics and thermodynamics can be established via the Adam-Gibbs-relation [64]  $f = f_0 \exp(B/TS_c)$  where  $B$  is an effective activation energy barrier usually obtained from fitting of experimental data [102]. In this model the fundamental quantity that drives the evolution of the dynamics is the configurational entropy,  $S_c$ , which is a measure of the number of configurational states that the system can access in its potential energy landscape [106]. Though the theoretical basis of the Adam-Gibbs entropy model [64] has been questioned [103] its general applicability to describe the viscous slowdown is corroborated by the strong empirical correlation that is found between the fragility and the evolution of excess entropy of the liquid over the crystalline phase,  $S_{ex}$ , in a large number of glass-forming systems [65, 104]. Expecting that the structural changes occurring during a LLT manifest themselves in the thermodynamics via a change in  $S_c$ , the Adam-Gibbs equation provides a link to the resulting changes in the liquid's dynamics.

The fact that the configurational and excess entropy are linked to fragility also means that changes in the excess specific heat capacity of the liquid over the glass,  $\Delta c_p^{ex} = c_p(liquid) - c_p(crystal)$  are directly related to changes in the viscous behavior. In principle two scenarios can be conceived to explain the experimentally observed changes in the fragility between two temperature regimes of the same system. Each scenario can be related to the nature of the underlying phase transition. The first scenario is a continuous transition. In this case, the underlying structural changes occur progressively over a relatively large tem-

perature range. The fragility as well as the thermodynamics associated with it, i.e. the entropy and heat capacity, change gradually. In the second scenario the changes occur rather abrupt. The dynamic crossover as well as the changes of its thermodynamic counterparts are confined to a narrow temperature range. Such a behavior is obviously observed in case of a first order transition, for which a non-diverging, step-like discontinuity in the response functions can be expected.

A broader view on the phenomenology of LLTs is proposed by Angell in its “big picture” of glass forming liquids [107]. In this picture fragile liquids differs from strong liquids by occupying different flanks of an underlying order-disorder transition. Whether a liquid exhibits is strong or fragile depends on the relative position of the observation temperature <sup>1</sup> with respect to the critical temperature  $T_c$  of the order-disorder transition <sup>2</sup>. According to this model, any liquid is supposed to be fragile at high enough temperatures and its (excess) heat capacity is expected to decreases with increasing temperature. On the other hand, at low enough temperatures any liquid will become strong and its (excess) heat capacity is assumed to increase.<sup>3</sup> Based on these considerations, any liquid will ultimately undergo a fragile-to-strong transition during cooling, where the transition from a less ordered fragile to a more ordered strong liquid phase manifests as a maximum (peak) in the heat capacity (cf. figure 3.16).

For liquids, in which the transition temperature,  $T_c$ , is located far above the liquidus, the experimentally accessible observation window only captures the low temperature flank of the order-disorder transition. The (smeared)  $c_p$ - peak of the transition lies (far) above the melting point, and  $c_p$  is expected to decreases with decreasing temperature. This leads to a gradual change of the (excess) entropy upon cooling and small heat capacity jump at the glass transitions. Such a behavior is typically observed in the archetypical strong, single component network glass formers ( $SiO_2$ ,  $GeO_2$ ,  $BeF_2$ ). On the other hand, in very fragile molecular glass formers such as 1 – *butene* or *toluene* the transition can occur at temperatures so low temperatures that it can be obscured by the laboratory glass transition ( $T_c < T_g$ ). These liquids therefore appear as fragile down to  $T_g$  and show a fast decrease of entropy due to the pronounced increase in  $c_p$  upon cooling towards  $T_c$ . Obviously, in this case, the detection of the LLT is complicated by the intervention of the laboratory glass transition. The transition and its corresponding manifestation in the thermodynamics and dynamics can only be observed by shifting the fictive temperature below  $T_c$ . This can either be achieved by choosing very slow cooling rates, increasing the propensity of the liquid to crystallize, or by long term annealing below the laboratory  $T_g$  [84]. Bulk metallic glass forming alloy are usually intermediate strong glass formers, i.e. their fragilities lie in between the two cases discussed above. In this case the

---

<sup>1</sup>This is the temperature where the experiment is carried out.

<sup>2</sup>As the heat capacity peaks are smeared-out often, it is convenient to define the critical temperature as the temperature of the peak maximum.

<sup>3</sup>At least it shows a less pronounced temperature dependence than in the fragile state.

transition is assumed to be located in between  $T_g$  and  $T_l$ .<sup>4</sup> As this is also the temperature regime where the crystallization rate takes its maximum, this often complicates experimental investigations of the dynamic behavior in this region or even prevents the detection of the transition. However, these liquids, having a more fragile behavior above or near  $T_l$ , should show a stronger behavior near  $T_g$ . Given that a liquid in the absence of any transition can be described by unique fragility (e.g. by the fragility parameter  $D^*$ ) over the entire temperature range, a discrepancy in the between the high and low temperature fragility can be regarded as indirect evidence for a LLT between  $T_m$  and  $T_g$ . Indeed, the viscosity data of a number of bulk metallic glass forming liquids can only be reasonably well fitted if different fragilities are assumed at high and low temperatures [98, 152, 170], implying that these alloys undergo a LLT in the metastable regime between  $T_g$  and  $T_l$ .

From an energetic landscape perspective, liquid-liquid transitions correspond to a transition among two mega-basins of the potential energy landscape which differ in terms of their topology [107]. The different ruggedness leads to a different temperature dependence of the activation energy for diffusive or collective motion (viscous flow) upon cooling, explaining the change in fragility when the system moves from one basin to another. This may require to mount an energetic ridge separating the two mega-basins, which in principle can cause metastability until the undercooled phase reaches the spinodal.

### 10.1.2 Critical points, the Widom line, and Jagla Potentials

The previously discussed phenomenology of liquid-liquid (phase) transitions and their associated anomalies in the dynamics and thermodynamics are considered to arise from liquid-liquid critical points (LLCP) in the phase diagram [109]. In particular there appears to exist a correlation between the crossover of dynamics from a kinetically more fragile to stronger behavior and the loci of the response functions which emanate from a LLCP [109, 112].

Schematics of phase diagrams including critical regions and liquid-liquid critical points are shown in figure 10.1. The coexistence line displays the equilibrium line of two phases, and when it is crossed, a (first-order) phase transition occurs (path  $\beta$ ). In case that the system persists in a metastable state (e.g. supersaturation, undercooling, overheating, etc.) the transition is “postponed” to the spinodal, where the transition now no longer requires nucleation of the precipitating equilibrium phase but can form spontaneously via local energy fluctuations. Given that the two phases differ in terms of their structure and viscous behaviour, the (first-order) liquid-liquid phase transition obviously result in a

---

<sup>4</sup>In some cases a transition can be also located in the temperature regime close below  $T_g$ , see e.g. [84].

fragile-to-strong transition.

A dynamic crossover can also be expected when a system crosses its Widom line [109]. The Widom line can be regarded as the extension of the coexistence line into the “one-phase region” [109, 112] at which all maxima of the response functions tend to concur as the critical point is approached [109, 112]. The appearance of the maxima in the thermodynamic response functions, e.g. the heat capacity  $c_p$  or the isothermal compressibility  $\kappa_T$ , now strongly depends on the relative position of the system with respect to its critical point in the phase diagram. Below the critical pressure, isobaric cooling results in a first order transition characterized by a discontinuous, but finite change in the response functions (path  $\beta$ ).<sup>5</sup> On the other hand, if the liquid is cooled above the critical pressure  $P_c$ , the thermodynamic state functions change in a continuous manner when the liquid transform from the high temperature phase into the low temperature phase (path  $\alpha$ ). Here, the response functions have maxima that tend to smear-out with larger the distances  $P - P_c$  to the critical point similar to the case of the liquid-gas transition (upper right panel in figure 10.1) as shown in the inset of figure 10.2 for the heat capacity of the noble gas Argon at various pressures at and above the critical point.

This behavior is reproduced in simulations based on the spherically-symmetric “two-scale” Jagla ramp potential [109, 112] which models the atomic pair interaction in terms of a hard core diameter  $r = a$ , a soft core diameter  $r = b$ , and a long-range cut-off  $c$  (see figure 10.3). For an appropriate choice of the parameter set  $\{a, b, c\}$  crystallization can be avoided, and the Jagla model is able to reproduce polymorphism in the amorphous phases (liquid and glass) - a phenomenon referred to as *polyamorphism* [112]. The lower panels in figure 10.3 show the appearance of the isobaric heat capacity  $c_p$  and compressibility  $\kappa_T$  at varying distances to the critical pressure ( $P_c = 0.243$ ), obtained from simulations made Xu et al. [112]. The larger is  $P - P_c$ , the more the peaks of  $c_p$  and  $\kappa_T$  are smeared. Note that for  $P < P_c$  the system is still above its spinodal and thus no discontinuities are observed in the present case due to metastability.

The phase diagram depicted in figure 10.1 requires the existence of two different equilibrium liquid phases that differ in structure, thermodynamics and dynamics. Ordering tendencies in liquids have basically two, not necessarily independent, origins: chemical affinities and topological constraints. In multi-component systems chemical affinities favor either mixing or demixing of the constituents. At lower temperatures enthalpic gains exceed the natural striving towards higher entropic states, so that ordered structures become energetically more favorable. Often, but not necessarily always, the lower enthalpy states are characterized by higher order and lower volumes (higher packing densities), so that the system compacts during cooling. This should be in particular true system in which non-directional bonding prevails, e.g. metals. In other more-

---

<sup>5</sup>Note that in some cases, e.g. water (figure 10.1c) the situation is inverse.



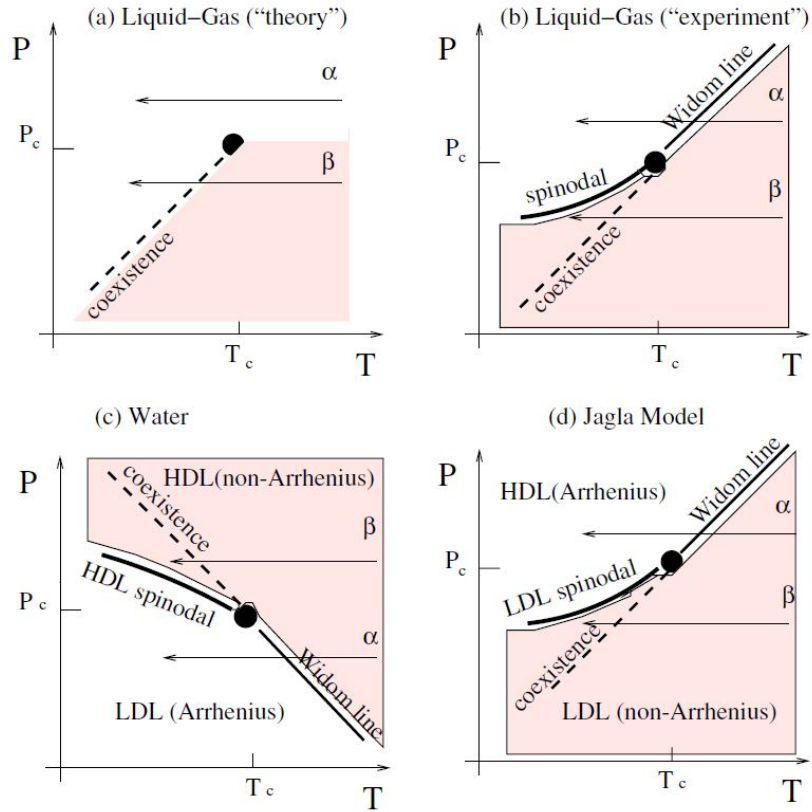


Figure 10.1: Schematic representation of phase diagrams including critical points. a) Classical liquid-gas theory. b) Liquid-gas phase diagram in experiments. c) Phase diagram for water d) Phase diagram of the Jagla model. In case of water and for the Jagla model a liquid-liquid critical point (LLCP) is expected. The stability range of the two liquid phases is defined by the coexistence line, the Widom line, and the spinodals. A liquid-liquid transition is expected when the system crosses the coexistence line (first order transition) or the Widom line (continuous transition). Due to metastability the transition can be postponed to the spinodals. The figure is taken from [112].

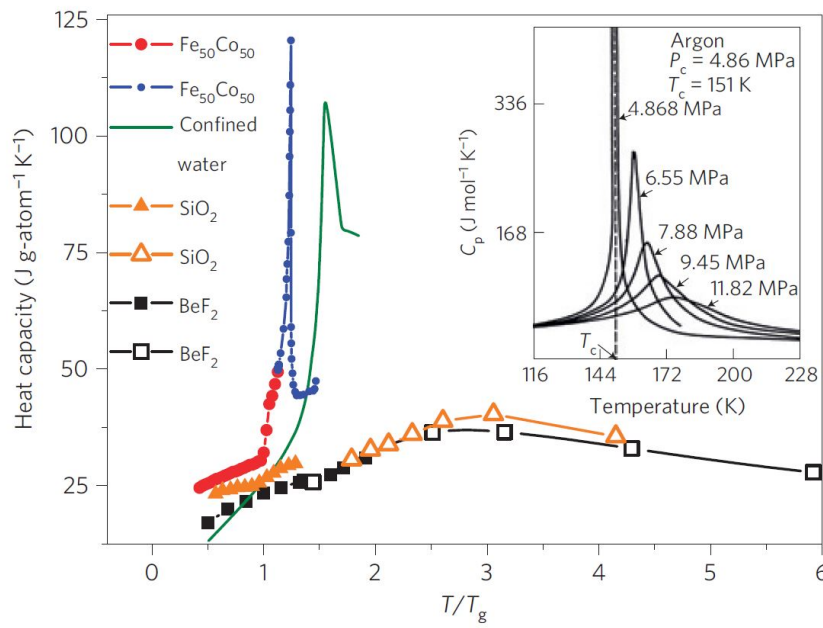


Figure 10.2: Heat capacity of various glass forming systems. The inset shows how the appearance of the heat capacity maximum changes when the isobaric cooling is performed with increasing distances to the critical pressure. The figure is taken from [171].

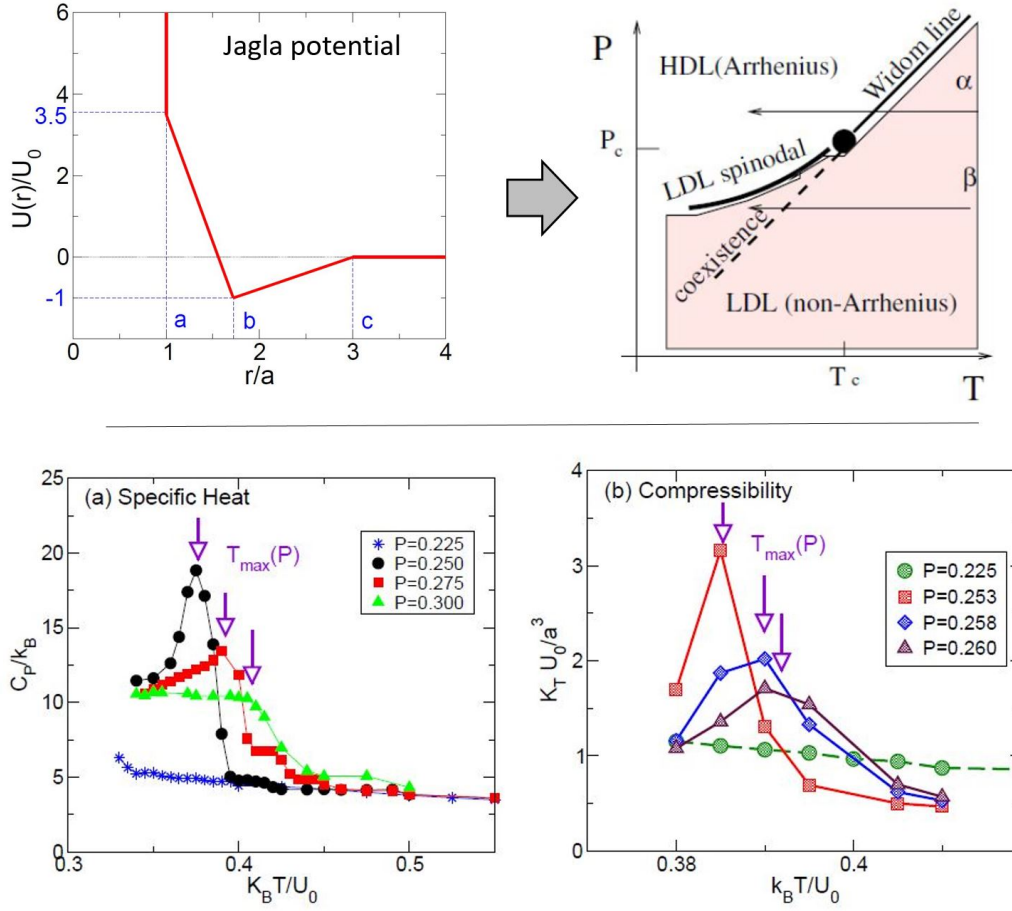


Figure 10.3: The two scale Jagla ramp potential according to [112] (upper left figure) along with its predicted phase diagram (upper right figure). The atomic interaction is approximated by a hard-core diameter  $a$ , a soft core diameter  $b$ , and a long range cut-off  $c$ , which defines the range of the attractive part. The lower figures show the evolution of the heat capacity  $c_p$  and the isothermal compressibility  $\kappa_T$  when the system is cooled along different paths in the phase diagram. Obviously, the peak of the response functions smear with increasing distance to the critical point, similar to the observations made for the noble gas Argon around its liquid-gas critical point (cf. figure 10.2). The figures are taken from [112].

directionally bonded system the lowest energy states do not necessarily coincide with the most-densely packed states, so that a more ordered phase not necessarily has a higher density. For example, in case of water the high density liquid (HDL) is promoted at higher pressures and temperatures. However, more frequently the high temperature phase corresponds to the low density liquid phase (LDL). The latter can be anticipated for metallic liquids and glasses. Accordingly, for metallic glass forming liquids it may be expected that a LLT during cooling occurs as a transition from a more disordered, lower density liquid at higher temperatures to a more ordered, higher density liquid at lower temperatures. However, in this context it needs to be emphasized that for bulk metallic glass forming liquids, which already reach a very high packing density in their high temperature liquid state, the density changes accompanying a LLT should be rather small.

## 10.2 On fragile-to-strong transitions in Zr-based bulk metallic glass forming liquids

The transition from one liquid phase to another is usually accompanied by distinctive change in the dynamics, e.g. viscosity, diffusion, or relaxation time [109, 112]. In case of a polymorphic transition, the two liquid phases have identical compositions but can differ in structure, density and/or entropy. Thus, given that a LLT takes place signatures in the structure, the heat capacity, and in the dynamics can be expected.

### 10.2.1 Previous work and motivation

In a variety of bulk metallic glass forming systems it is observed that the liquid at high temperature liquid close to its melting point shows a different temperature dependence of its dynamics (fragility) than in the supercooled liquid regime in vicinity to glass transition temperature. While at high temperatures, the temperature dependence of the viscosity, determined from Couette-viscometry, can be well described by a VFT-fragility parameter around  $D^* \approx 10$ , the low temperature viscosity data, obtained from three-point beam bending relaxation studies, yield  $D^* \approx 20$ , indicating a kinetically much stronger (more Arrhenius-like) behavior [98, 172]. This is shown in figure 10.4 for the case of Zr-based and Cu-Ti-based bulk metallic glass formers. Given that the a single  $D^*$  value is appropriate to describe the fragility of a liquid over the entire temperature range, this suggest a dynamic crossover in the temperature region between  $T_g$  and  $T_m$ , in line with the behavior expected from the big picture of glass forming liquids [107, 108] for intermediate strong glass-formers.

A similar observation was made earlier for the *Vit1* bulk metallic glass forming alloy [170]. In this case, the dynamic crossover is further supported by a dynamic hysteresis that is experimentally found in undercooling experiments around the

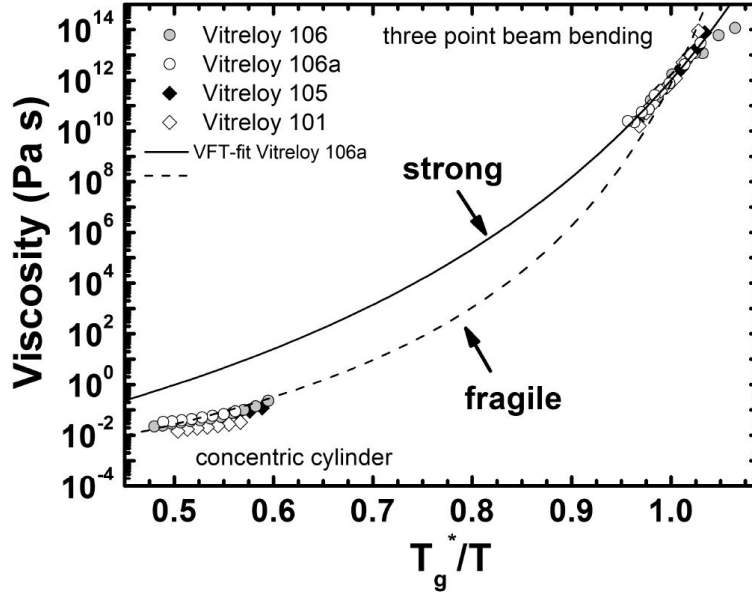


Figure 10.4: Differences in fragility between the low and high temperature liquids in Zr-based bulk metallic glass forming liquids. The figure is taken from [98].

melting point [170] (cf. figure 10.5). Inspired by this, Wei et al. performed synchrotron x-ray diffraction studies and heat capacity measurements on *Vit1* in the liquid state [152]. During undercooling an unexpected shift in the principal diffraction peak (PDP) was observed that coincides with an exothermic heat release, as indicated by the occurrence of a peak in the specific heat capacity [152]. Moreover, a reversed peak shift in the PDP was observed upon heating, coinciding with an endothermic heat capacity peak above the liquidus. Based on fact that the transition temperatures of the structural and thermodynamic anomalies coincide with the temperature range of the dynamic transition observed by Way et al. [170], it was concluded that the latter is the dynamic signature of an underlying LLT in the liquid state. Since the changes in the structure, dynamics and heat capacity show a hysteresis behavior upon cooling and heating, Wei et al. conjectured that the LLT must be of first-order [152].

### 10.2.2 ESL-synchrotron studies on the Vitreloy106a bulk metallic glass forming liquid

Considering the previous findings by Wei et al. [152], the discrepancy in the fragility of the low and high temperature viscosity data of the Vitreloy106a bulk metallic glass forming alloy, shown in figure 10.4 along with some other candidates, suggests a LLT in between  $T_g$  and  $T_l$ . To detect and explore a possible

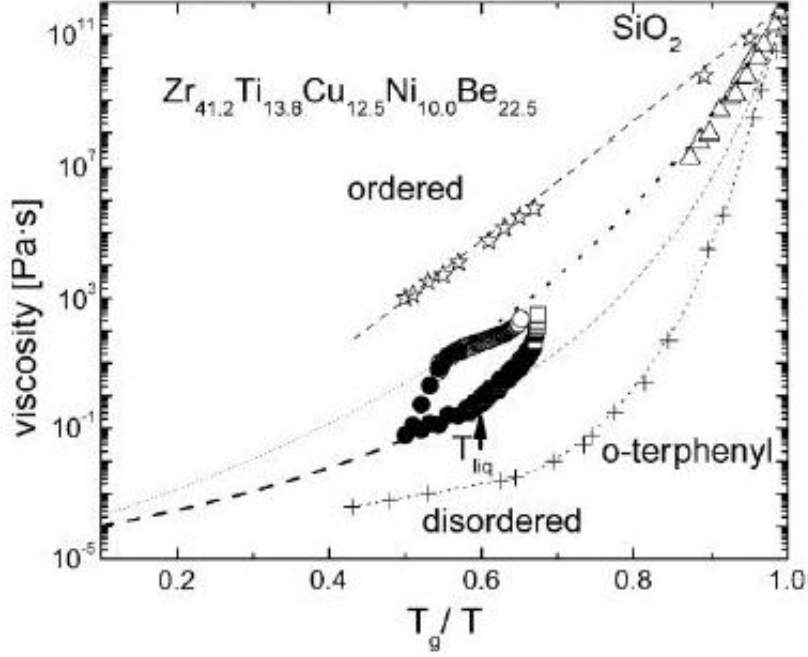


Figure 10.5: Viscosity hysteresis in the Vitreloy1 bulk metallic glass forming liquid. Upon initial heating, the viscosity shows a strong behavior (open circles) that matches the extrapolation of the low temperature viscosity data obtained from TMA measurements around the glass transition (open triangles). At 1125 K a two-orders of magnitude drop of the viscosity transition is observed (black circles at  $T_g/T = 0.55$ ). During subsequent cooling the viscosity remains low and shows a less pronounced temperature dependence as indicative for a more fragile liquid. At around 100 K below the liquidus ( $T_l$ ) an unexpected large increase in viscosity towards the high viscosity obtained during heating is measured (open squares). This is interpreted as an evidence for a fragile-strong transition from a more disordered high-temperature liquid state to a more ordered low-temperature liquid state. The figure is taken from [172].

LLT in this alloy, in-situ high energy synchrotron x-ray diffraction (HESXRD) on electrostatic levitated (ESL) droplets is performed. One advantage of this alloy is that it possesses a relatively low critical cooling rate for glass formation (1.75 K/s) [173], rendering it ideal for structural investigations over a wide temperature range from above the liquidus,  $T_l$ , down to the glass transition temperature,  $T_g$ . Synchrotron x-ray diffraction is chosen as it enables fast time-resolved structural studies on the atomic scale suitable to study metallic melts under cooling rates that are appropriate to avoid crystallization. Due to the absence of container walls that may act as preferential nucleation sites, the ESL technique allows access to the deeply undercooled liquid state [125]. For a detailed description of

the experimental setup and data analysis the reader is referred to chapter 5 and the references therein.

### Temperature profile and volume changes during cooling

The fastest cooling rate in the high vacuum ESL chamber is obtained by radiative cooling. The temperature-time profile obtained of the levitated molten droplet during free cooling is shown in figure 10.6. Within the temperature range from 1473 K to 673 K no recalescence due to bulk crystallization of the sample is observed. Note that 673 K is the lower detection limit of the pyrometer used within this study.

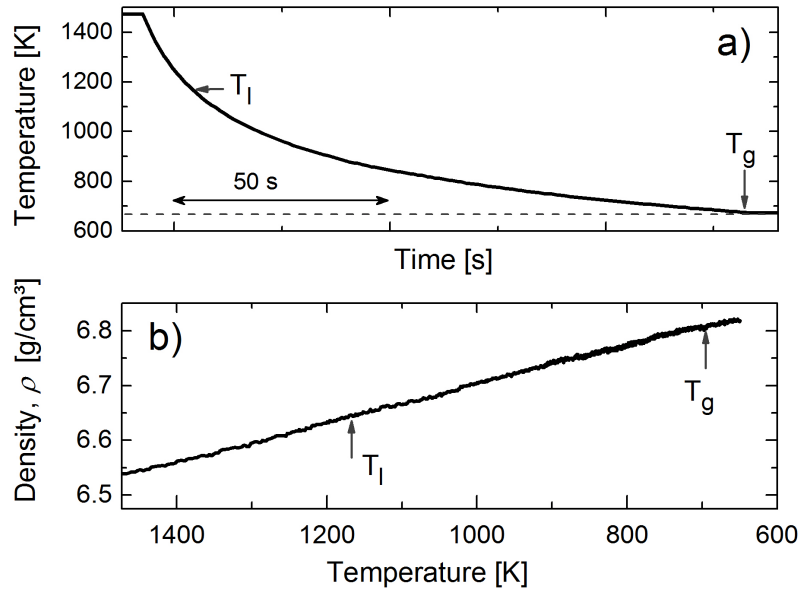


Figure 10.6: a) Temperature-time profile of a levitated liquid droplet during free radiative cooling in the ESL from above the liquidus temperature,  $T_l$ , down to the glass transition temperature,  $T_g$ . The dashed line corresponds to the lower detection of the pyrometer used. b) Density vs. temperature plot of a levitated droplet cooled under the same conditions as in a).

Figure 1b shows a density versus temperature plot obtained from a separate volume measurement in the ESL under similar experimental conditions. During undercooling towards the glass transition,  $T_g$ , the density increases continuously without any evidence of a sudden change that would indicate crystallization.

### Structural analysis in reciprocal space

The evolution of the total structure factor  $S(Q)$  during cooling into the glass is shown in figure 10.7. At all temperatures,  $S(Q)$  reveals the typical appear-

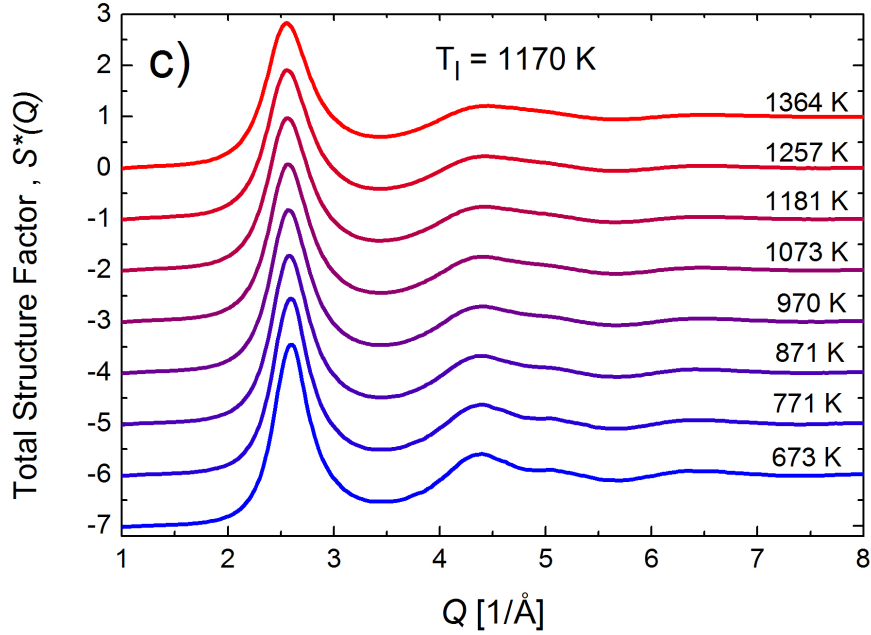


Figure 10.7: Evolution of the static total structure factor  $S(Q)$  during undercooling the levitated molten droplet into the glassy state for the temperature profile shown above.

ance of an amorphous structure lacking long-range order. During undercooling, the maxima of  $S(Q)$  sharpen and gain in intensity, reflecting a less pronounced thermally-induced smearing of atomic correlations. However, the patterns do not show any evidence for crystallization. No Bragg peaks are visible in the entire temperature and  $Q$ -range of the investigation. Moreover, a careful inspection of the measured 2D-detector patterns reveals no indications of the formation of crystallites.

To reveal a possible phase transition in the liquid state, the changes in the total static structure factor  $S(Q)$  with temperature are analyzed [152, 175]. In figure 10.8 the position of the first maximum in  $S(Q)$ ,  $Q_{1max}$ , is plotted during heating at 100 K/min from an initially glassy sample and subsequent free cooling from the equilibrium liquid at 1473 K. For clarity the data of the crystallized material (gap in heating data) is not displayed. During heating,  $Q_{1max}$  decreases as expected for an increase of interatomic distances with decreasing density [132]. At around 770 K, the sample crystallizes in agreement with differential thermal analysis. Above the melting point,  $T_m$ ,  $Q_{1max}$  once again decreases with increasing temperature. However, a linear extrapolation of the low temperature supercooled liquid data ( $T < 800$  K) does not match the high temperature data ( $T > T_m$ ). Upon subsequent cooling,  $Q_{1max}$  first follows the heating data until a sudden increase occurs in the deeply undercooled liquid between 900 K and



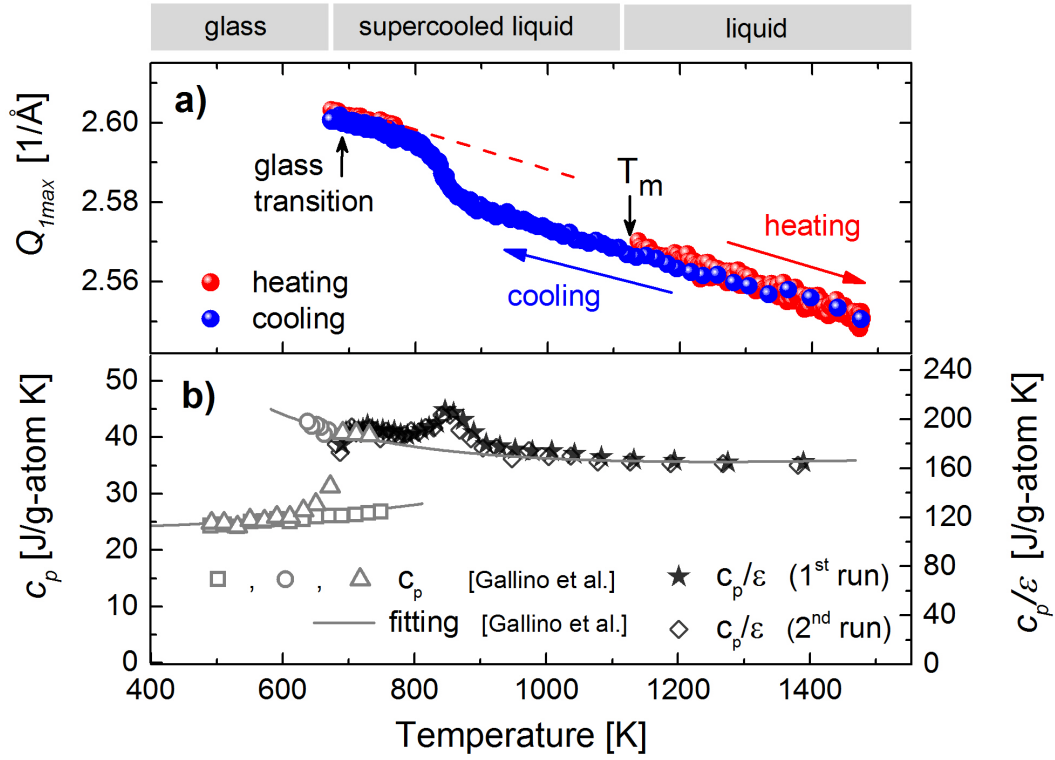


Figure 10.8: a) Position of the first maximum of  $S(Q)$ ,  $Q_{1max}$ , during heating of an initially glassy sample and subsequent cooling down to the glassy state. b) Ratio of specific heat capacity to total hemispherical emissivity,  $c_p/\epsilon$  calculated from the temperature profile measured in ESL, during cooling to the glassy state in comparison with the measured calorimetric  $c_p$ -data of Gallino et al. [174].

800 K. As a result, the values of  $Q_{1max}$  match those obtained during previous heating.

A qualitatively similar observation is made for the full width at half maximum (FWHM) of the principal peak of  $S(Q)$ ,  $\gamma$ , as shown in figure 10.9 for the case of cooling. Again a finite, unexpected change is observed. As will be shown later this indicates an increase in the correlation length  $\xi$ .

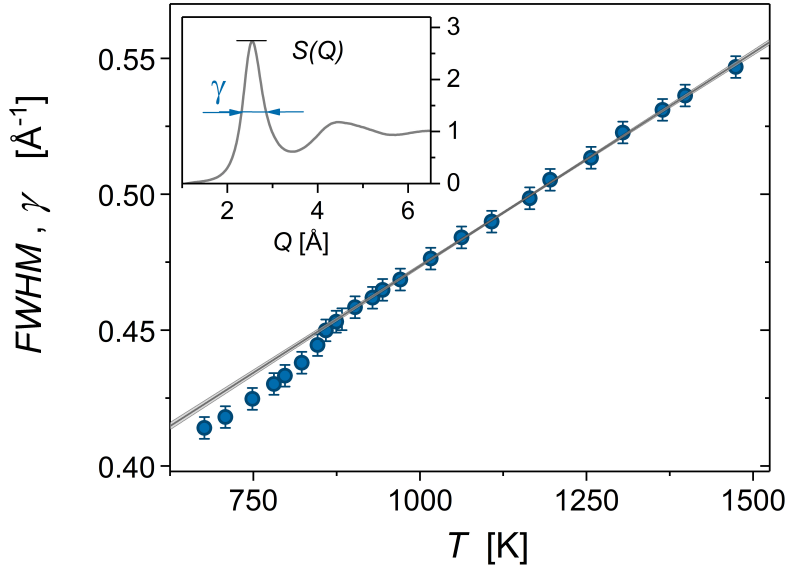


Figure 10.9: Evolution of the FWHM of principal peak of  $S(Q)$ ,  $\gamma$ , during cooling. The gray lines is an linear extrapolation of the high temperature data. The shaded area corresponds to the 95 %-confidence interval.

To further exclude that the shift of  $Q_{1max}$  results from the formation of crystallites, the changes in the diffraction intensity  $\Delta I_{LLT}(Q)$  are compared with the changes associated with the initial stage of crystallization  $\Delta I_{cryst}(Q)$ . Both are found to be substantially different (see figure 3) corroborating that the observed behavior of  $S(Q)$  is the signature of a structural transition within the deeply undercooled liquid state and does not correspond to the onset of crystallization of the melt.

### Thermodynamic signature of the LLT

The aforementioned findings imply a thermodynamic signature associated with a reorganization of the atomic structure. Using the Stefan-Boltzmann law (equation 5.6),  $c_p/\epsilon$  is calculated from the temperature-time profiles during cooling (figure 10.6). The corresponding results are shown in figure 10.8 in comparison to literature data obtained from calorimetric measurements [174]. In contrast to the expected course, predicted from fitting of the  $c_p$ -data close to  $T_g$  [174], the

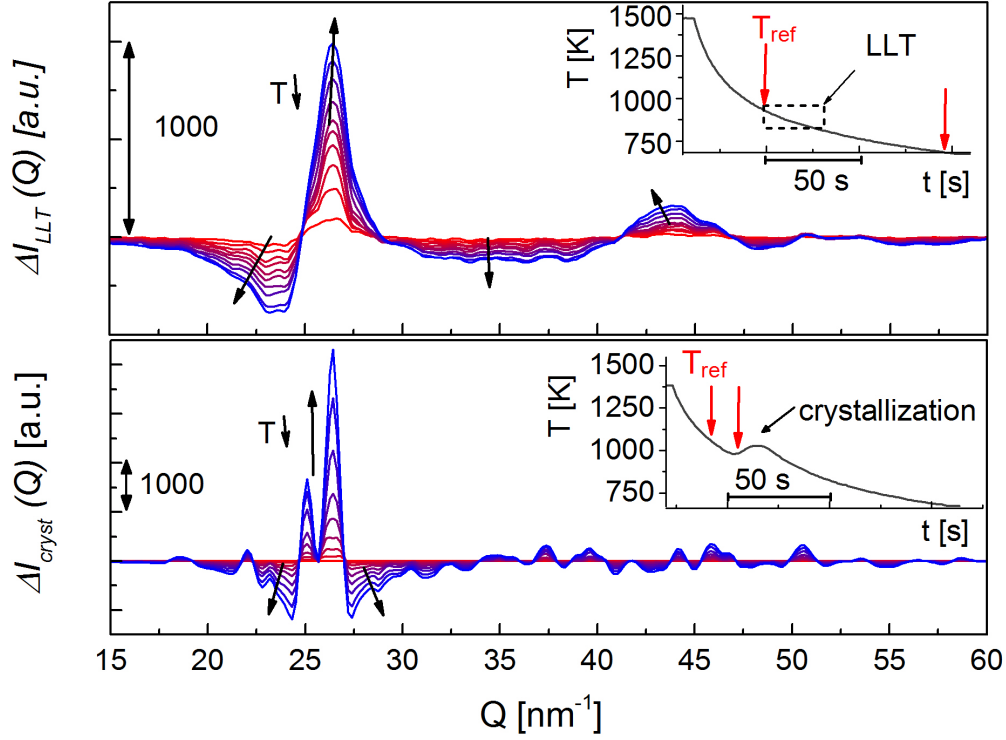


Figure 10.10: Changes in diffraction patterns  $I(Q)$  associated with the LLT,  $\Delta I_{LLT}(Q)$ , (upper part) and with the initial stage of crystallization  $\Delta I_{cryst}(Q)$  (lower part). Changes are determined with respect to a reference temperature  $T_{ref}$  to amplify the changes associated with each process. Insets show the corresponding temperature-time profiles of the sample. The reference temperatures and the temperature range used for the comparison are indicated by arrows in the inset.

measured  $c_p/\epsilon$  passes through a maximum coinciding with the observed anomaly in  $S(Q)$  and is therefore regarded as the thermal signature associated with the transition in the deeply undercooled liquid. Taking  $\epsilon = 0.22$  for temperatures around  $T_g$ , as deduced from the comparison of  $c_p/\epsilon$  with the calorimetric  $c_p$  in figure 10.8, the additional heat release obtained from integration of the peak is estimated as  $\approx 0.5 \text{ kJ/g} - \text{atom}$ , corresponding to a decrease in entropy of  $\approx 0.6 \text{ J/g} - \text{atomK}$ , i.e.  $\approx 7\%$  of the entropy of fusion [174], in good agreement with the values measured earlier for a LLT in another bulk metallic glass former [152]. This is consistent with an increase in order during the transition, i.e., a transition from a less ordered high temperature (HTL) to a more ordered low temperature liquid phase (LTL). The appearance of peak-like anomalies in  $c_p/\epsilon$  and volumetric thermal expansion coefficient  $\alpha$  for the current alloy has been reported earlier [176]. Lacking diffraction data, those observations were attributed to crystallization [176], which is not supported by the current structural analysis.

The large scattering observed in the present analysis of the volume expansion  $\alpha$  does not allow one to draw conclusions about an anomaly as observed in reference [176] (see 10.11). However, the continuous linear change of density with temperature indicates that there is no significant change in density or  $\alpha$  associated with LLT.

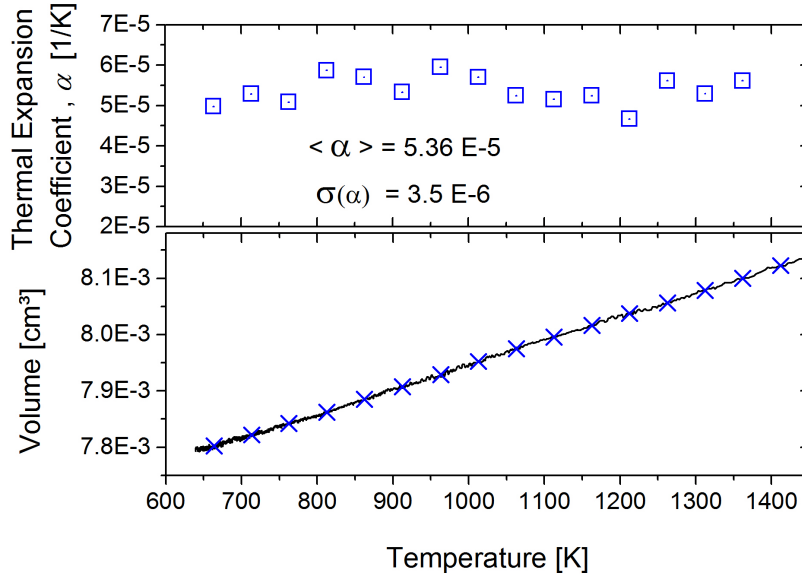


Figure 10.11: Thermal expansion coefficient  $\alpha$  (upper figure) calculated from the volume versus temperature profile (lower figure) during cooling the equilibrium liquid above the liquidus down to the glass. For completeness, the average value and standard deviation are given. Due to scattering, the directly measured volume profile in the lower figure (serrated solid line) is processed using *OriginPro9.1*. Data reduction by grouping is performed yielding a reduced number of equidistant data points (crosses in lower figure). Appropriate grouping locally averages the measured data profile and improves the statistics, without sacrificing its course. The reduced data is used to calculate the course of  $\alpha$ .

In the former study [152] a hysteresis was found for the  $c_p$  peak and the structural data. Besides the  $c_p$  anomaly found in the supercooled liquid during cooling, in heating another  $c_p$  anomaly was observed slightly above the liquidus. In the present alloy neither the structural data nor the  $c_p$  data showed any anomalies in the equilibrium liquid above  $T_l$  (cf. figure 5.8), implying that the crystal directly melts into to fragile high-temperature liquid.

### Real space data analysis

To gain deeper insight into the structural changes in real space,  $S(Q)$  is Fourier transformed and the evolution of the total radial distribution function  $G(r)$  is an-

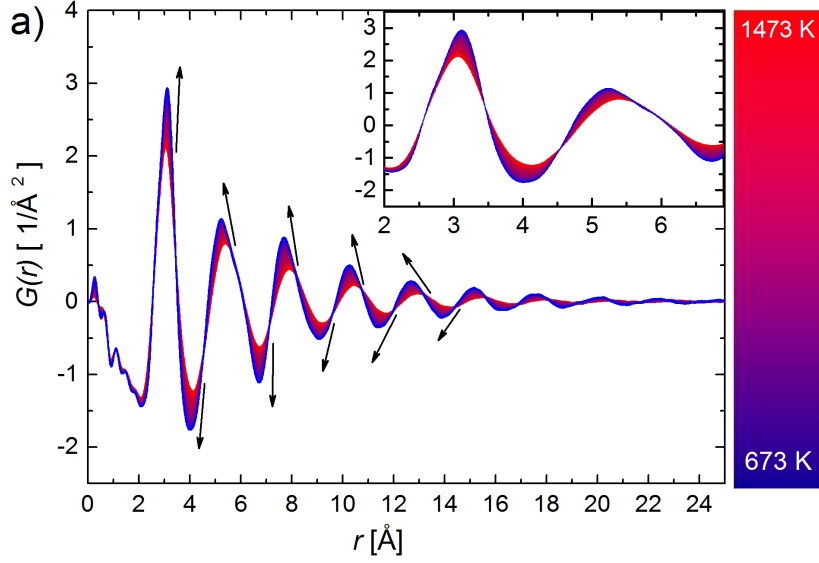


Figure 10.12: Evolution of  $G(r)$  during undercooling the levitated droplet from above the melting point down into the glass. The inset shows a close up view of the first two peak positions. Arrows indicate the evolution of peak maxima and minima with decreasing temperatures.

alyzed. It is noted that the total structure factor of a five component alloy is the sum of 15 partial structure factors, which prevents a detailed structural analysis. Nevertheless, it will be shown that the  $G(r)$  data are in accordance with a structural transition as indicated by the evolution of thermodynamics and structure in reciprocal space. Furthermore, the calculated  $G(r)$  can be used to connect the structural changes to the dynamics, relying on the empirical correlation between the local volume dilation and fragility established earlier.

Figure 10.12 shows the evolution of  $G(r)$  during cooling from 1473 K, i.e. about 300 K above the liquidus, down to 673 K. Arrows indicate the shift of maxima and minima with decreasing temperature. A close up view of the first two peaks corresponding to interatomic correlations at the length scale of SRO is shown in the inset. With lower temperatures, the peaks at all length scales sharpen and gain in intensity, reflecting higher interatomic correlations resulting from the increasing spatial confinement and less pronounced thermal vibrations of the atoms.

Figure 10.13 shows the evolution of the first five peak positions,  $r_i$ , and peak intensities  $G(r_i)$  normalized to their value at 673 K upon cooling from the equilibrium liquid down to the glass. Several anomalies, involving the length scale of SRO and MRO, can be detected. For instance,  $r_1$  shows an unexpected change in slope,  $r_4$  and  $r_5$  display step-like decreases, while  $G(r_4)$  and  $G(r_5)$  exhibit



abrupt increases upon undercooling. The anomalies in real space data coincide exactly with the shift of  $Q_{1max}$  and the  $c_p/\epsilon$  peak as illustrated by the shaded region, implying a direct connection. As already discussed earlier the anomalous, negative expansion of  $r_1$  is a common observation in metallic melts whose origin has been debated recently [137, 146, 147]. Figure 10.13 further supports the picture of a diverse structural evolution at different length scales, which in turn might explain the absence of a pronounced density change during the LLT - an observation made already earlier in another bulk metallic glass forming melt [152]. This might be connected to the metallic bonding character, which energetically does not prefer considerably less-efficiently packed structures as compared to systems that are dominated by directional bonding. It thus appears that, in multi-component metallic systems, the transition from one densely packed liquid phase to another is driven by chemical ordering tendencies resulting from the large negative heat of mixing among the constituents, rather than topological ordering towards lower the specific volume states.

### Structural changes in SRO

The above findings imply that the LLT involves structural changes on the length scales corresponding to SRO (cf., e.g.,  $r_1$ ) as well as MRO (cf., e.g.,  $r_4$  and  $r_5$ ). Theoretical [39, 50, 177], numerical and experimental findings indicate that energetically-preferred, more efficiently packed atomic clusters (EPCs) exemplarily but not necessarily icosahedra- are locally favored structures associated with SRO in metallic liquids [50, 51, 63, 67]. Moreover, molecular dynamics studies suggests that EPCs can aggregate, building up larger (e.g. network-like) structural units, which, in turn, have been related to the viscous slowdown during undercooling [59, 66, 68, 151, 178]. According to the efficient cluster packing model of Miracle [57], the present alloy can be classified as a  $\langle 12, 10, 8 \rangle_{fcc}$  structure. Based on this, the primary ( $\alpha$ )-solute centered clusters should be composed of a central *Cu*-atom surrounded by 12 *Zr*-atoms, and the locally-favored structure should be a solute-centered icosahedron. In this case the ratio of the next-but-one-nearest to the next-nearest *Zr*-atoms would be given by the golden ratio  $\phi = 1.618$ .<sup>6</sup> Considering that the main contribution ( $\approx 50\%$ ) of the scattered coherent intensity stems from *Zr* – *Zr* pairs, the majority of the real space information stems from *Zr* – *Zr* pairs. Note that all pairs involving *Zr* atoms make about 92 % of the measured coherent intensity. Thus, the real space data is mainly determined by the distribution of *Zr* atoms, and it might be asked if the evolution of  $G(r)$  on the length scale of SRO is in accordance with the predicted

---

<sup>6</sup>In a regular icosahedron consisting of 13 atoms of the same species, the atoms in the shell surrounding the central atom do not touch each other, but touch the central atom. If distance between two shell-atoms is  $a$ , the distance between a shell atom and the central atom is  $\approx 0.951a$ . For shell-atoms the next but one nearest neighbor on the cluster shell has a distance  $\phi a$ , where  $\phi$  is the golden ratio.

icosahedral ordering.

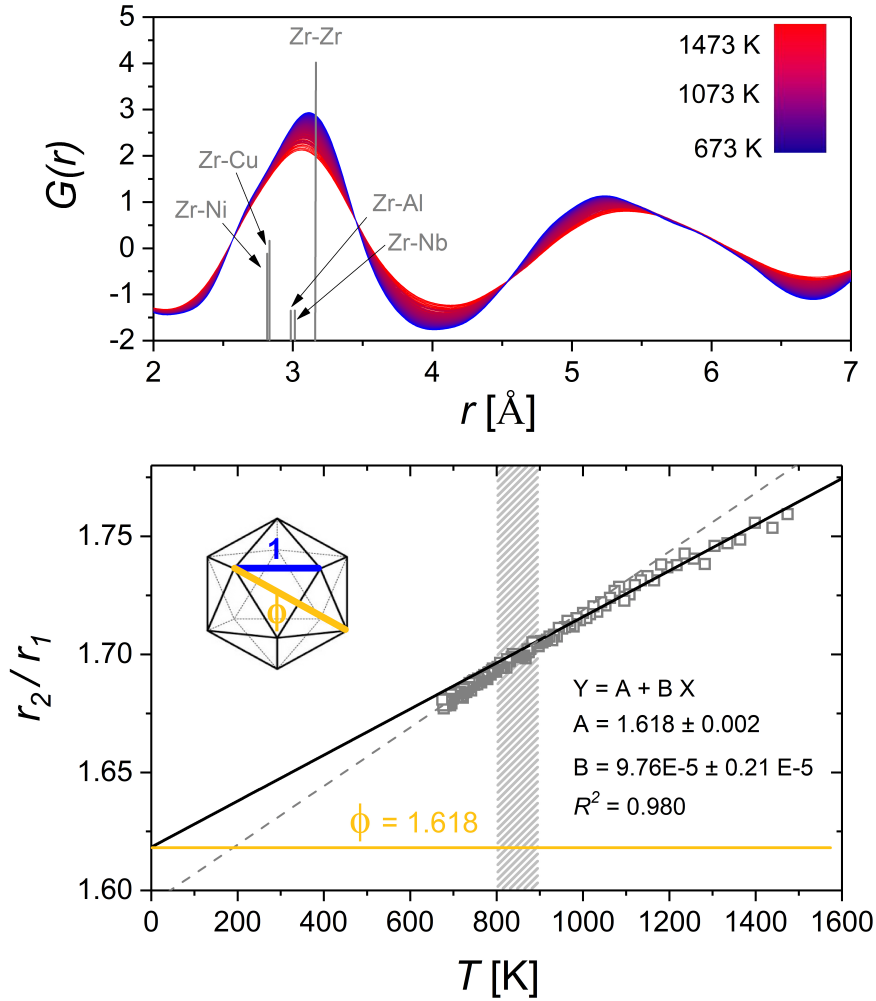


Figure 10.14: Analysis of structural changes on the length scale associated with short-range ordering. The upper panel shows the evolution of the first two peaks of  $G(r)$  upon cooling together with the separation of all atomic pairs including  $Zr$  atoms, estimated from the radii of the elements. The height of the bars scales with the Faber-Ziman weighting factors. The lower panel shows the evolution of the second-to-first peak position ratio  $r_2/r_1$ . The black solid line is the extrapolation of the high temperature data ( $T > 900$  K) obtained from fitting assuming a linear temperature-dependence. The dashed line is the extrapolation from the low temperature data  $T < 800$  K. The shaded area corresponds to the temperature range where the  $c_p$ -peak and the anomalies in the structural data are detected. The horizontal orange line defines the golden ratio  $\phi$ , corresponding the ratio of the next-but-one-nearest to next-nearest neighbor separation of shell atoms in an ideal icosahedron.



First, it can be noticed that the maximum of the first peak of  $G(r)$  is situated close the  $r$ -values expected for pair distances including  $Zr$ , assuming the following atomic radii for the elements [58]:  $Zr=316$  pm,  $Cu=126$  pm,  $Ni=126$  pm,  $Al=141$  pm,  $Nb=143$  pm. This can be seen in the upper part of figure 10.14 where the distance of the  $Zr$ -pairs is plotted versus  $G(r)$ . The height of the bars scales with the average of their Faber-Ziman weighting factors in the  $Q$ -range used for Fourier transformation (cf. figure 4.5). Second, it can be seen that the ratio  $r_2/r_1$  continuously decreases almost linearly with decreasing temperature and shows a small downward bend when the system enters the region where the anomalies in the structure and  $c_p$  data are found (shaded area). If the evolution of the high temperature data ( $T > 900$  K) is extrapolated to lower temperatures assuming a linear temperature dependence,  $r_2/r_1$  progressively approaches the golden ratio  $\phi$ , and at 0 K finally matches  $\phi$ . This might be seen as an experimental indication that the structural evolution in the high temperature liquid is characterized by a striving towards energetically favored structural motifs in which the ratio of the next-but-one nearest to next-nearest neighbors is given by the golden ratio, e.g. icosahedral solute-centered clusters.

### Structural changes in MRO and implications to the dynamics

Due to their lower degeneracy of states [50], the formation of locally favored structures (EPCs or their agglomerates) is accompanied by an increase in order. Thermodynamically, an increasing ordering tendency upon cooling manifests as a rise in  $c_p$  as  $T_g$  is approached [50, 66]. Although the direct observation of a dynamic crossover via conventional viscometry in the present alloy is precluded by crystallization, in the following, it is demonstrated that the observed structural changes imply a FST, giving an explanation for the difference in fragility observed between the high and low temperature viscosities. To validate that the atomic-scale structural changes are in agreement with a FST, the empirical correlation discussed in chapter 9 which links fragility to the evolution of atomic correlations on length scales of about 1 nm is used (MRO) (cf. figure 9.3). Alternatively, a correlation that links the high temperature viscosity of metallic melts to the evolution of the height of the first peak in  $S(Q)$  was proposed recently [179]. However, based on its derivation, this relation is unable to explain the experimentally observed diversity of the fragility of metallic liquids at lower temperatures near  $T_g$  and, hence, is not used in the present study. Instead the correlation established in chapter 9 that links the fragility  $m$  to a structural metric defined as  $\delta = \frac{V_{43}(T)}{V_{43}(T'_g)} = \frac{V_{43}(T) - V_{43}(T'_g)}{V_{43}(T'_g)}$ , which as a first approximation might be interpreted as the temperature-induced structural dilatation on a length scale of about 3 to 4 atomic diameters ( $\approx 1$  nm) is applied. The variable  $V_{43}$  denotes the volume enclosed between the 3<sup>rd</sup> and 4<sup>th</sup> peak position of  $G(r)$ ,  $r_3$  and  $r_4$ , and  $T'_g$  is the temperature where the systems structurally has entered its super-cooled liquid state when heated through the glass transition. Considering that

cluster-based structural models for metallic glasses estimate the extent of locally dense-packed cluster aggregates to be of the order of 1 nm [57] and taking into account that the expansion of MRO through an aggregation or network formation of EPCs is thought to be related to the viscous slowdown [59, 68, 151, 178], it is justifiable to assume that fragility is inherently linked to structural changes on this length scale. In particular, it is found that a larger  $\delta$  corresponds to a more fragile behavior, and vice versa (cf. 9.3).

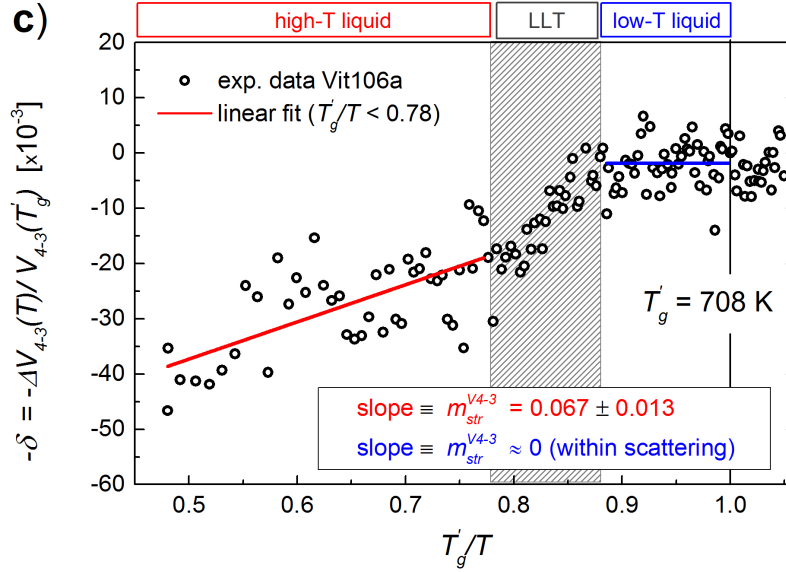


Figure 10.15: Volume changes,  $\Delta V_{43}$ , with respect to its value at  $T'_g$ ,  $\delta$ , plotted versus  $T'_g/T$  during undercooling a levitated, molten droplet from a temperature far above melting point down to the glass transition. The solid line corresponds to the linear fit. Note that its slope  $m_{str(V43)} = 0.067$  can be transferred into the kinetic fragility  $m = 65$  (cf. figure 9.3).

In accordance to chapter 9,  $\delta$  is calculated from the temperature dependence of  $r_3$  and  $r_4$  and its negative value is plotted on a  $T'_g$ -scaled inverse temperature plot in figure 10.15. It is evident that the high temperature liquid (HTL) and the low temperature liquid (LTL) vary significantly in terms of  $\delta$ . In the HTL,  $\delta$  noticeably decreases upon cooling, as expected for a more fragile liquid (cf. 9.3). In contrast, below the LLT,  $\delta$  remains almost constant, fluctuating around zero, as is characteristic for kinetically stronger behavior (cf. 9.3). Making use of the linear correlation depicted in 9.3, the slope of  $\delta$  in figure 10.15,  $m_{str(V43)}$ , of the HTL is converted into  $m$  and  $D^*$  values. This yields a change from  $D^*(LTL)_{exp} = 21$  for the LTL [172] to  $D^*(HTL) = 12$  for the HTL which is close to the value obtained from VFT fitting of the high temperature viscosity data obtained from Couette-viscometry  $D^*(HTL)_{exp} = 10$  [172]. The analysis of the structural data

thus predicts a FST associated with the LLT in the deeply undercooled liquid at  $T/T_g \approx 1.2$ .

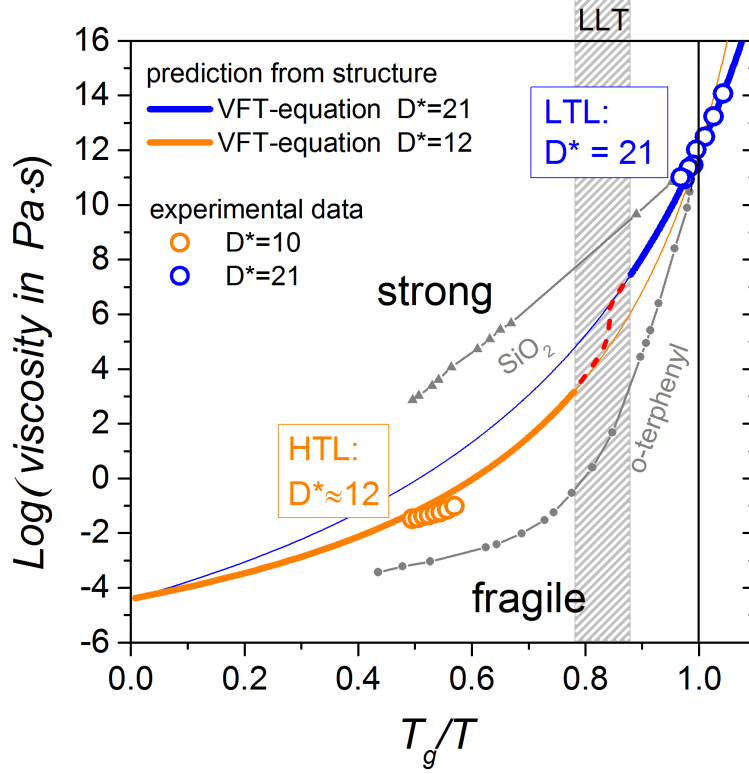


Figure 10.16:  $T_g$ -scaled Arrhenius plot (Angell-plot) of the viscosity behavior derived from the structural data according to the empirical correlation found in this study (solid lines). The predicted trend adequately reproduces the experimentally observed viscous behavior (empty circles). The dashed line connecting the viscosity data of the HTL with the LTL is the hypothesized course during the LLT. For comparison the data for  $SiO_2$  and o-terphenyl taken from reference [180] are included.

A graphical representation of the structure-predicted viscosity behavior in comparison to the experimental data is shown in figure 10.16. The course of viscosity is determined from the structural data by inserting the derived  $D^*$  values into VFT equation. The high temperature limit  $T \rightarrow \infty$ , corresponding to the pre-exponential factor  $\eta_0$  in the VFT-equation, is calculated as  $\eta_0 = (N_A h)/V_m$  where  $h$  is Planck's constant,  $N_A$  is Avogadro's number and  $V_m$  is the molar volume, based on Eyring's considerations on the lower bound for viscosity [95]. Figure 10.16 demonstrates that the structure-predicted viscosity behavior adequately describes the experimental data. Furthermore, a two order of magnitude change in viscosity is suggested as illustrated by the hypothesized course of viscos-

ity during the LLT (dashed line in figure 10.16), in agreement with the magnitude of the viscosity change during the viscosity hysteresis in the *Vit1b* bulk metallic glass forming alloy found by Way et al. using Couette-viscometry [170].

### 10.3 Summary

In conclusion, the present study provides structural and thermodynamic evidences for a LLT in the deeply undercooled liquid state at  $T/T_g \approx 1.2$  in which a less ordered high temperature phase transforms to a more ordered low temperature phase. The analysis of the real space data shows that the LLT incorporates changes in the short- and medium range order. Relying on a previously established, empirical correlation between structural changes and fragility, it is demonstrated that the changes in MRO correlations on the length scale of about 1 nm predict a fragile-strong-transition scenario that is accompanied by a 2 order of magnitude change in viscosity, which can adequately describe the experimentally observed changes in the viscous behavior. The present findings substantiate the idea that MRO correlations are inherently linked to the viscous behavior which is in line with recent MD simulations that relate the viscous slowdown of metallic liquids upon undercooling to the expansion of MRO by an aggregation or network formation of energetically-preferred atomic clusters. Moreover, the findings presented corroborate the conception that strong liquids differ from fragile liquids by occupying different flanks of an underlying order-disorder transition as postulated in the “big picture” of glass forming liquids [107, 108].

# Chapter 11

## Ornstein Zernike Analysis of bulk metallic glass formers

In Chapter 10 strong evidences for a liquid-liquid transition (LLT) in the deeply undercooled liquid state of the Vit106a BMG forming alloy are reported. It is shown there that the LLT features structural signatures in the reciprocal as well as the real space data. In reciprocal space, the LLT manifests as an unexpected shift of the position of the structure factor maximum, while in real space several abrupt changes in the peak positions of  $G(r)$  are observed. Furthermore, it is shown that the evolution thermal-induced dilatation on the length scale of about 0.7 nm to 1 nm can be used as a structural metric that is able to reproduce the experimentally observed changes in the dynamic behavior, i.e. a transition from a more fragile, less-ordered high temperature phase to a more ordered, kinetically stronger low temperature phase, suggesting a connection between the evolution of medium-range atomic correlations and fragility. In this section a more comprehensive study on the long-range decay behavior of the correlation function is performed on the basis of an Ornstein-Zernike analysis of the decay of density fluctuations. The characteristic decay parameters are determined based on experimental data obtained from synchrotron diffraction studies and discussed in terms of their implications on the dynamics.

### 11.1 Decay of density fluctuations according to Ornstein and Zernike

The most characteristic feature of the amorphous structure compared to the crystalline structure is the asymptotic decay of the atomic correlations. The decay behavior is characteristic for the structural coherence, and can be used to determine the degree of disorder present in a system [113]. For a perfectly periodic infinite crystal, oscillations in  $G(r)$  persist up to infinity with a constant peak-peak amplitude, provided that a perfect resolution measurement is performed

[113]. On the other hand any structural incoherence will result in a faster the decay of the long-range correlations. Liquids are characterized by large structural disorder; their peaks in  $G(r)$  asymptotically decay to zero with increasing  $r$  (cf. for example figure 10.13), reflecting the limited structural coherence due to the lack of long-range order. Based on solutions of the Ornstein-Zernike equation the decay behavior of long range correlations can be modeled and characteristic parameter such as the correlation length can be extracted.

### 11.1.1 The classical Ornstein Zernike approach

Density variations in liquid and glasses directly result from the interaction between the particles. In case of rigid-ion pair models, the interaction potential is composed of three terms: a short-range repulsive part, a Coulomb term, and a dispersion term that depends on the polarisability of the ions [93]. It can be shown that if the dispersion terms are absent, irrespective of whether the Coulomb term is present or absent, a pole analysis of reciprocal space solutions of the Ornstein-Zernike equations leads, in the case of a high particle density, to an asymptotic decay of the total pair-distribution function of the form [93]

$$h(r) = \frac{A}{r} \exp\left(-\frac{r}{\xi}\right) \sin(kr - \theta) \quad (11.1)$$

where  $h(r) = g(r) - 1$  is the *total correlation function*. Equation 11.1 is a special case for the correlation function of a 3-dimensional system at high density. A more universal description in the framework of classical theories predicts the critical behavior of the correlation function to follow the form [181]

$$g(r) \propto r^{-(D-2+\eta)} \exp\left(-\frac{r}{\xi(T)}\right) \quad (11.2)$$

where  $D$  is the dimensionality of the system,  $\xi$  is the correlation length, and  $\eta$  is a parameter that is used to quantify the deviation from the Ornstein-Zernike behavior. For a three-dimensional system equality of the two equations, apart from the sinusoidal term, requires  $\eta = 0$ . Any system obeying equation 11.2 with  $\eta = 0$  is said to follow an *Ornstein-Zernike-behavior* [181].

### 11.1.2 The cluster approach

An alternative approach to explain the decay behavior of density fluctuations in metallic glasses has been proposed by Ma et al. [134]. In this approach, the medium- or extended-range ordering is interpreted in terms of a self-similar packing of atomic clusters which results in the formation a fractal network with a dimension  $D_f$  [93, 134]. For a such a fractal network of quasi-equivalent clusters, the number of clusters within a radius  $r$  around a given cluster,  $N(r)$ , is

expected to follow a power-law distribution  $N(r) \propto r^{D_f}$ , where  $D_f$  denotes the dimensionality of the fractal structure [134]. This yields a cluster correlation function of the form  $C(r) = g_{Cluster}(r) - 1 \propto A/(r^{D-D_f})$  with  $A$  being a constant [134]. According to this cluster model, the decay behavior of metallic glasses is modeled as

$$C(r) = \frac{A}{r^{D-D_f}} \exp(-r/\xi) \sin(kr + \theta) \quad (11.3)$$

where the exponential cut-off term is used to account for the finite cluster size and cluster entanglement effects, while the sinusoidal function is introduced to model the oscillations observed in experiments [134]. Note that the classical Ornstein-Zernike relation (equation 11.1) for 3D space is recovered from the fractal approach if  $D - D_f = 1$ . Accordingly, in a 3-D cluster structure that is in accordance with an Ornstein Zernike behavior, the cluster number follows  $N(r) \propto r^2$ .

### 11.1.3 Comparison of the two models - Ornstein-Zernike vs. the cluster approach

The wavelength of the oscillations in  $g(r)$  is essentially given by the position of the principal diffraction peak, suggesting to set  $k = Q_1$  (cf. chapter 7). On the other hand the magnitude of pre-factor in equation 11.2 and 11.3 is determined by the dimensionality  $D$  of the system, which in turn again is linked to  $Q_1$  (cf. chapter 6). Investigating the density and diffraction data of several bulk metallic glasses at room temperature, Ma et al. found that the experimental volume and diffraction data, can be best described by assuming a relation  $v \propto Q_1^{-\xi}$  with an exponent of 2.31, taking this as evidence for a fractal cluster structure [134] in the glassy state. Consequently, the decay of  $g(r)$  was modeled assuming  $D - D_f = 0.69$ . It was noted by the authors [134]: “It is remarkable that equation 11.3 [...] can account so well for the experimental  $[g(r) - 1]$  for  $r \geq 6.5A$ .” while “On the other hand, equation 11.3 failed to describe  $[g(r) - 1]$  for  $r \leq 6.5A$ ”, leading them to conclude that “fractal behavior is only observed in the medium-range length scale.” However, it was later argued by Salmon and Zeitler that the data of Ma et al. can be equivalently well described by assuming an exponent 3 [93], questioning the fractal approach proposed. The latter is in accordance with the observation that the Ehrenfest relation holds in the glassy state, which is supported by the analysis presented in chapter 6. In study performed by Chirawatkul et al. [182] it was found that the classical (non-fractal) Ornstein-Zernike approach 11.1 yields an accurate description of the decay behavior of several binary eutectic and near-eutectic alloys in the liquid state. Based on that, Salmon and Zeitler [93] anticipated that the same can be expected for the glassy materials studied by Ma et al. [134], leading them to conclude that “The fractal approach for describing extended-range ordering in liquid and glassy metals is not, therefore, convincing [93]”. However, a fractional non-cubic power

law dependence between  $Q_1$  and  $v$  in metallic glasses was later on again observed by Zeng et al. [141]. Using a diamond anvil cell Zeng et al. studied the pressure dependence of the shift of the principal diffraction peak of three bulk metallic glass formers and found that “the density of MG (metallic glasses) varies with the 5/2 power of  $q_1$ , instead of the expected cubic relationship [141]”. Recently, Ding et al. performed another comprehensive study on the fractal structure in metallic glasses [142]. Using computer simulation and experimental data it was found that the mass distribution, i.e. the number of structural units within a given radius  $r$ , scales like  $M(r) \propto r^{D_f}$ , with  $D_f = 3$  irrespective if atoms or clusters are considered, questioning a fractal structure in metallic glasses. By simulating the structure factor of their MD liquids at various pressures they also tested the previously mentioned universality between the volume  $v$  and the position of the principal diffraction peak  $Q_1$ , and found that “for all MGs studied at various hydrostatic pressure values, [...] the power  $D$  is observed to span values ranging between 2.8 and 3.6.[142]”, questioning a universal (non-integer) value of  $D$  in the relation  $V \propto (1/Q_1)^D$ . By studying the pressure-induced shift of the first peak positions in the partial pair distribution functions of a binary  $Cu_{46}Zr_{54}$  metallic glass as a function of volume they further observed that each partial seems to have its own value  $D$ , which does not necessarily coincide with the value derived from the total pair distribution function [142]. This is considered to arise from the intrinsic inhomogeneous deformation of metallic glasses, as different bond types display different compressibilities [142]. Ding et al. also studied the shift of the positions of higher coordination shells and stated “For each MG,  $D$  is observed to increase, decrease, or fluctuate with increasing peak positions, showing a general trend of convergence toward 3 at larger  $r$ .”[142].

Summarizing these previous studies, there appears to be no clear consensus on the exact value of the exponent  $\xi$  linking  $v$  and  $Q_1$ , nor if there even is a universal value at all, and hence on the validity of the classical Ornstein-Zernike approach (in the form of relation 11.1) to describe multicomponent metallic liquids or glasses. On the one hand, the structure of binary near-eutectic alloys in the liquid state can be suitably described by the classical OZ equation 11.1 [182]. On the other hand, the fractal approach of Ma et al. [134] (equation 11.3) apparently yields a reasonable description of the glassy state. A systematic analysis of the long-range density variations in the amorphous state over a wide range of temperatures, ranging from the equilibrium liquid down to the glassy state, has not been performed to the best of the authors knowledge, but might provide deeper insights into the evolution of medium- or extended-range translational structural ordering during undercooling. Provided that the structural coherence in a sample affects its viscous behavior, it might be asked if thermal-induced changes in correlation length  $\xi$  are related to the temperature-dependence of the viscosity. Furthermore, the evolution of the correlation length may give additional insights in the nature of possible transitions in the liquid state.



## 11.2 Ornstein Zernike analysis of a Zr-Cu-Ni-Al-Nb BMG former in the liquid state

There has been intense and long debates on the nature of LLTs in metallic glass forming systems but their distinct type (continuous, discontinuous) or order (e.g. first, second,  $\lambda$ ) remains unclear. Simulations performed on Jagla-liquids indicate that LLTs are linked to the existence of liquid-liquid critical points in the  $p, T$ -phase diagram. A first order transition, characterized by a divergence of the response functions, is expected to occur if the liquid is cooled over its coexistence line below the LLC, while a smeared out order-disorder transition, characterized by smeared peaks in the response functions, takes place when the liquid crosses its Widom-line above the LLC [35, 107] (cf. chapter 10). For each scenario the correlation length should show a characteristic behavior in the critical region, and hence a deeper understanding of the nature of LLTs might be obtained by studying the evolution of order parameters or the correlation length.

Using the classical Ornstein-Zernike relation (equation 11.1) a comprehensive analysis of decay behavior of density variations in the  $Zr_{58.5}Cu_{15.6}Ni_{12.8}Al_{10.3}Nb_{2.3}$  (Vit106a) bulk metallic glass forming alloy is performed. Electrostatic levitation combined with synchrotron X-ray diffraction is chosen, as it enables access to structural data comprising the entire temperature range from above the liquidus ( $T_l$ ) down to the glass transition ( $T_g$ ). This is possible due to the relatively low critical cooling rate of less than 2 K/min [173] which in the absence of crucible walls, which may act as heterogeneous nucleation sites, prevents crystallization, even when the melt is cooled by radiation only. As shown in chapter 10, this alloy shows several indications for a LLT in the deeply undercooled liquid state slightly above the glass transition temperature ( $T/T_g = 1.2$ ). Structural analysis implies that the LLT involves changes at short- and medium-range length-scales. Furthermore, the structural changes occurring on a length scale of approximately 0.7 nm to 1 nm, when compared with other bulk metallic glass forming liquids, predict a dynamic crossover in accordance with experimental viscosity data. Following the line of thought that the viscous slowdown is linked to an extension of medium-range order by an aggregation or network formation of energetically-preferred atomic clusters, changes in the long-range decay behavior of the PDF might be expected, when the fragile high temperature liquid is cooled and transforms into a stronger liquid at lower temperature. Notably it can be expected that the LLT leads to an increase in the correlation length.

### Transformation of $G(r)$ into $g(r)$

To analyze the evolution of the decay behavior of  $g(r)$  the number density as a function of temperature  $\rho_0(T)$  is needed. However, the Fourier transform of the structure factor  $S(Q)$  over a limited  $Q$ -range yields  $G(r)$  not  $g(r)$ . In principal  $\rho_0$  is “hidden” in the low  $r$ -range behavior of  $G(r)$ , but numerous errors and

effects resulting from experimental limitations give rise to ripples in the low  $r$ -region, deteriorating a proper determination of  $\rho_0$  in many cases. Although in the present case the number density derived from the low-range behavior of  $G(r)$  is in adequate agreement with the number density derived from direct volume measurements in the ESL (cf. figure 11.1),  $g(r)$  is calculated using the direct density data obtained from volume measurements in the electrostatic levitator.

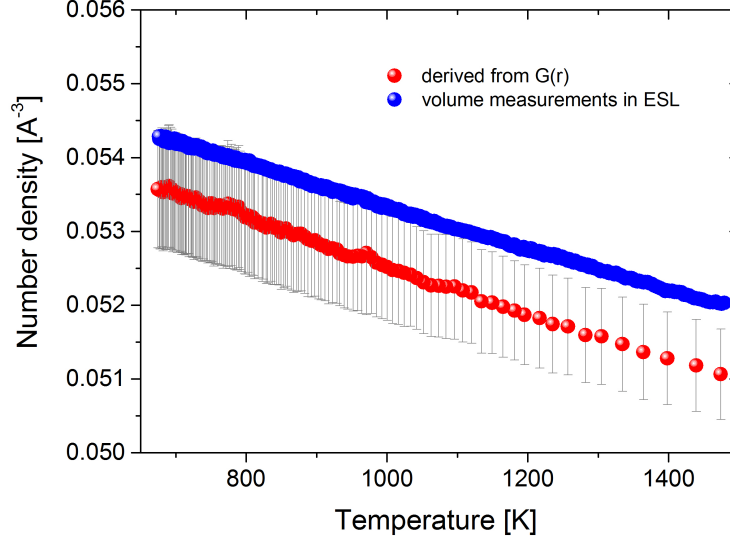


Figure 11.1: Number density derived from diffraction data versus the number density derived from volume measurements in the ESL. The error bars correspond to the standard deviation obtained from fitting of the low- $r$   $G(r)$  data.

### Choice of the dimensionality $D_f$

The decay of density oscillation in a system composed of a fractal cluster network in principal can be analyzed using equation 11.3. However, a direct determination of  $D - D_f$  by fitting is complicated by mutual dependencies between the fit parameters  $A$ ,  $D - D_f$ , and  $\xi$ . For a given value of  $A$  the two parameters  $D - D_f$  and  $\xi$  have opposite effects on  $g(r)$ . The larger is  $D - D_f$ , the faster is the decrease of the prefactor  $A/(D - D_f)$ , while a smaller  $\xi$  leads to a less pronounced exponential decay. This difficulty was noted already by Ma et al. [134] who therefore set  $D - D_f = 0.69$  according to their own analysis of the relation between  $Q_1$  and  $v_m$ . On the other hand, the analysis on the validity of the Ehrenfest relation performed in chapter 6 suggests to take  $D - D_f = 1$  for the glassy state, and a non-integer value  $D - D_f \neq 1$  for the liquid state. The latter however is challenged by the observation of Chiratawul et al. who found that

the experimental structural data of several eutectic or near eutectic alloys in the equilibrium liquid can be well described assuming a classical Ornstein-Zernike behavior [182].

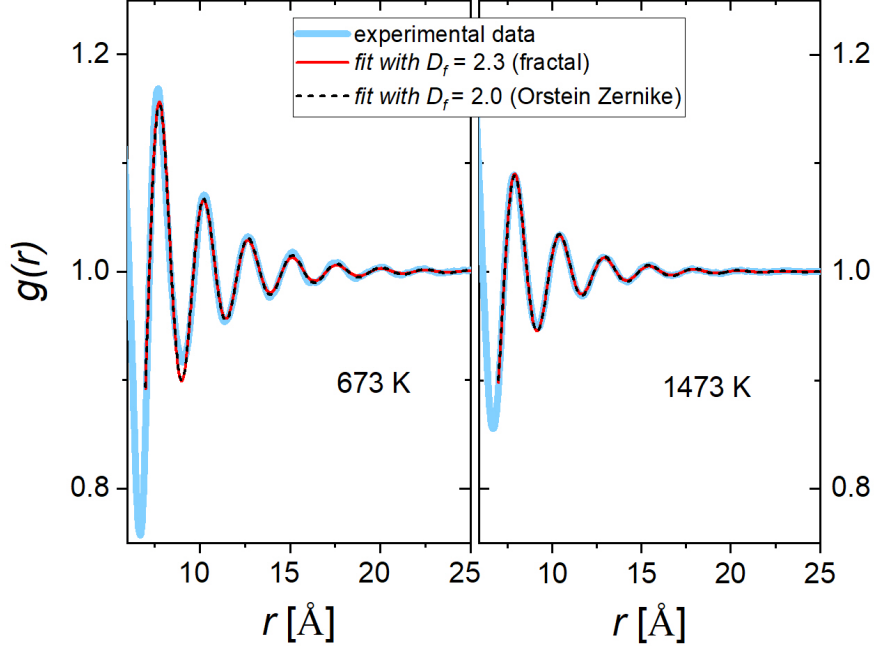


Figure 11.2: Description of the long range decay of density variations in the *Vit106a* BMG former in the equilibrium liquid (1473 K) and around the glass transition temperature (673 K) obtained by assuming a classical Ornstein Zernike behavior ( $D_f = 2.0$ ), and a fractal cluster structure ( $D_f = 2.31$ ).

Within the current study the observation is made that  $g(r)$  in the liquid state can be equally well fitted assuming either  $D_f = 2$  or  $D_f = 2.31$  without any loss of accuracy or qualitative statements on the temperature dependence of the other fit parameters. This is shown in figure 11.2 for the structural data of the *Vit106a* bulk metallic glass forming alloy in the equilibrium liquid at 1473 K, and around the glass transition 673 K. Virtually no difference can be observed for the quality of the fits irrespective of the choice of  $D_f$ . It is striking that the description of the experimental data worsens at lower temperatures, in particular for the lower coordination shells. This observation will be taken up later again. All together the present finding along with the previous findings of Chiratawul et al. and Ma et al. suggest that the quality of fitting is not markedly affected by the value of  $D - D_f$ , presumably as the mutual dependency between the fit parameters allows to balance the particular choice of  $D - D_f$ . For this reason an analysis of the

evolution of  $D - D_f$  is disregarded, and it is assumed that a classical Ornstein-Zernike behavior can be applied to the entire temperature range of the amorphous structure, i.e. in the liquid as well as the glassy state. Nonetheless, it would be interesting to see how  $D_f$  evolves during cooling from a high temperature liquid state down into the glass, as this might reveal the formation of an aggregated cluster structure upon undercooling towards the glass transition.

### Initialization of fit parameters ( $A$ , $\xi$ , $k$ , $\theta$ )

In a first step, the fitting is performed at 1473 K keeping all four variables ( $A$ ,  $\xi$ ,  $k$ ,  $\theta$ ) as free fitting parameters. As the Ornstein-Zernike approach is only valid to describe the decay of long-range oscillations, short-range ordering needs to be excluded. Different integration limits are investigated in the present study.

In general, all fits excluding the low  $r$  regions corresponding to short-range ordering, i.e. the first and second coordination shell, give acceptable descriptions of the long-range decay behavior. Nonetheless, if only the first two coordination shells are excluded, the fits, showing a very good fit quality ( $R^2 > 0.995$ ) in the high temperature liquid, struggle to capture the low- $r$  peaks of the low temperature data (cf. figure 11.3). For instance, at 798 K the position, the height, and the skewness of the 3<sup>rd</sup> coordination shell are not well reproduced leading to an  $R^2 = 0.979$ . If the lower integration limit is chosen beyond the 3<sup>rd</sup> coordination shell, an improved fit quality is found even at lower temperatures ( $R^2 = 0.995$ ). This suggests that peculiarities of the local structure, becoming more marked at lower temperatures, extend to larger length scales. At higher temperatures, the peculiarities of the atomic cluster structure are confined to the length-scale of short range order and hence only contribute to the first peaks of  $g(r)$ . On the other hand, in the supercooled liquid state at 789 K the structural peculiarities persist up to a length scale of about 1 nm while they “average out” at larger length scales and follow the decay behavior predicted by the Ornstein Zernike relation. In this regard, the failure of the Ornstein-Zernike to describe the lower coordination shells may be taken as indication for an extension of alloy specific medium-range ordering tendencies which obviously are not captured by the generality of the Ornstein-Zernike relation. In this context it is noted that this length scale agrees well with length scale expected for the extension of medium-range ordering due to the formation of specific cluster-aggregates within the efficient cluster packing model [57]. In chapter 9 and 10 it is shown that structural changes on this length scale show a strong correlation with fragility.

### Validation of the four parameter fit

As mentioned above, the fitting parameters  $A$  and  $\xi$  show mutual dependency and have opposite effects on the decay behavior. For all other parameters fixed, a larger  $A$  yields a lower  $\xi$ , and vice versa. Thus, performing the fits by keeping

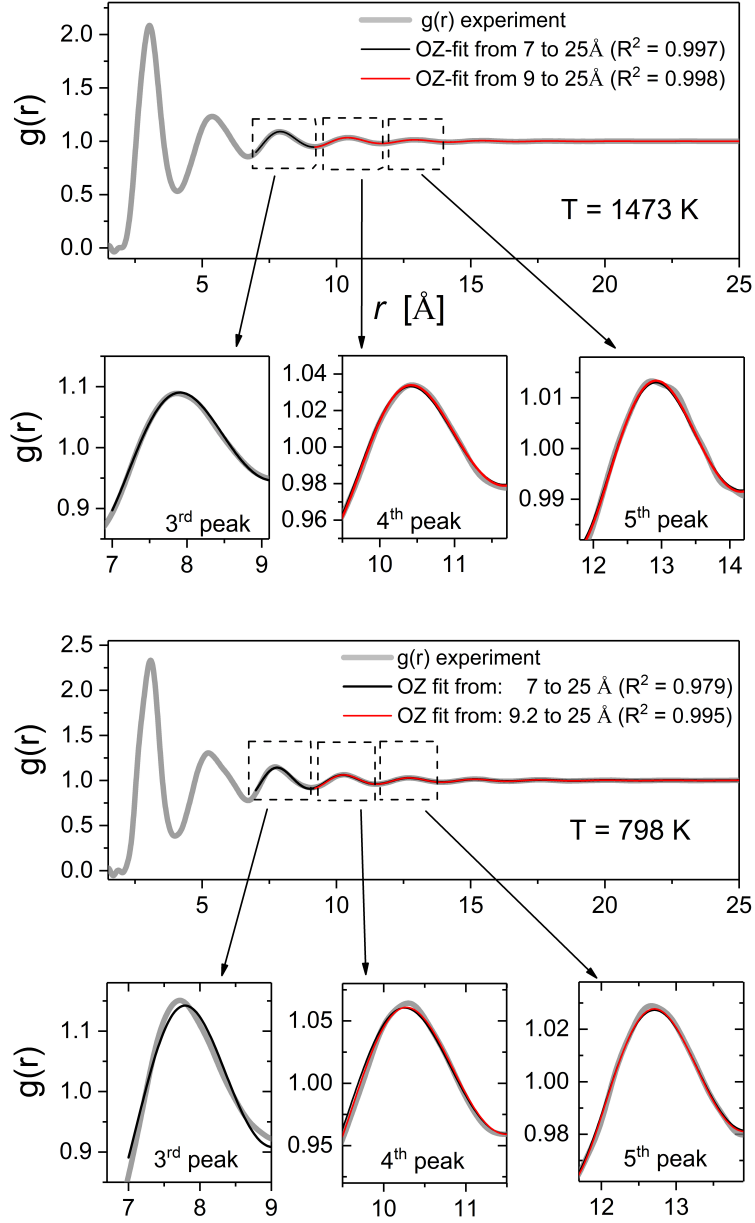


Figure 11.3: Influence of the chosen integration limits on the quality of the Ornstein-Zernike fits. At high temperatures in the equilibrium liquid above the liquidus, the fit quality is not markedly affected by whether the lower integration limit is chosen at the 3<sup>rd</sup> or the 4<sup>th</sup> coordination shell. At lower temperatures the fits progressively struggle to describe the shape of atomic correlations below the 4<sup>th</sup> coordination shell, suggesting that structural peculiarities extend to this length scale when the system is cooled and local order increases.

all parameters as free variables minimizes the sum of squares of the residuals, but a-priori does not ensure that the method yields well-founded  $\xi$  values. It is therefore necessary to challenge the values obtained. A closer inspection of equation 11.1 reveals that the maxima of  $\ln|r(g(r) - 1)|$  should obey a linear relation of the form  $y_0 + mr$  with respect to  $r$ , whose slope  $m$  is related to the correlation length  $\xi$  via  $m = -\xi^{-1}$ . This enables to extract values for  $\xi$  without invoking  $A$ . The corresponding analysis is shown in figure 11.4 for the  $g(r)$  at 1473 K. Using this method it is found  $\xi = 3.56 \pm 0.05$  Å, in good agreement with the value obtained from the four parameter fit of  $g(r)$ , i.e.  $\xi = 3.48 \pm 0.02$  Å as shown below. The two values are in good agreement with the values reported by Ma et al. who derived  $\xi = 4$  Å for a similar bulk metallic glass forming glass at room temperature [134].

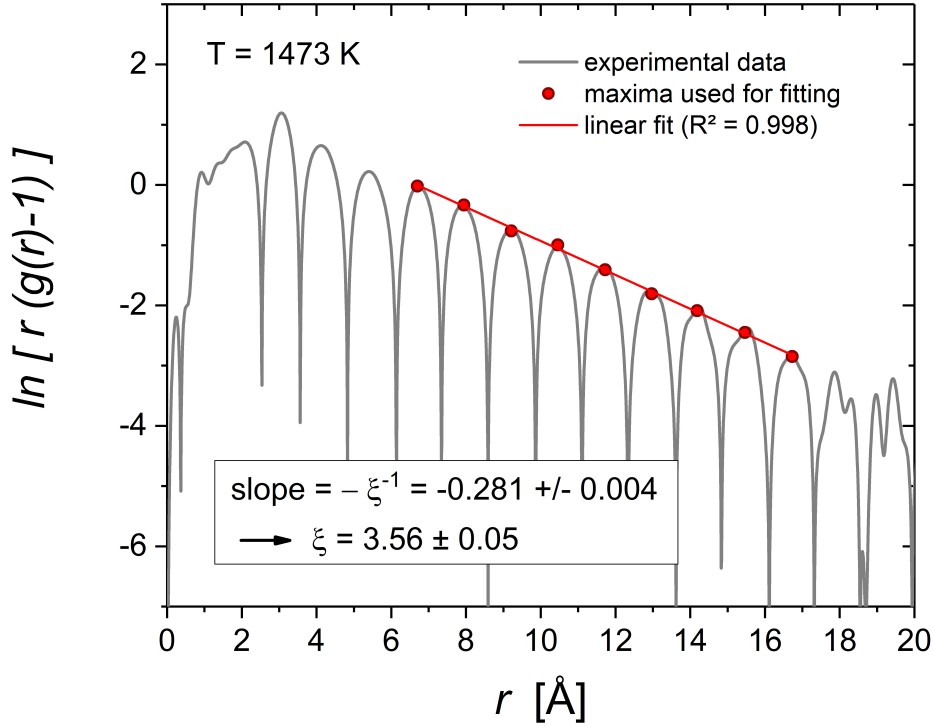


Figure 11.4: Logarithmic plot of the absolute value of  $r[g(r) - 1]$ . The negative inverse of the slope of the straight line through the maxima yields the correlation length  $\xi$ . This method allows to extract the value of  $\xi$  without making an assumption on the amplitude  $A$ .

## Extension to all other temperatures

Based on the good agreement of  $\xi$  obtained from the parameter initialization and the value  $\xi$  determined graphically, the parameter  $A$  is set constant to  $A = 7.1$ , and fitting at all lower temperatures is performed with the remaining three parameters  $k$ ,  $\xi$ , and  $\theta$ . Above the liquidus (shaded line in figure 11.5) all fits have  $R^2 > 0.995$ . With decreasing temperature the fit quality worsens as already mentioned earlier. Whether this can be improved by an adjustment of the dimensionality  $D_f$  remains to be explored. However, even at the lowest temperature studied (673 K), an acceptable fit quality is obtained ( $R^2 = 0.988$ ) by assuming  $D - D_f = 1$ .

Above the region where the LLT takes place all fit parameters show a continuous behavior. The phase shift  $\theta$  slightly decreases upon cooling, while  $\xi$  and  $k$  increase as expected for a contracting structure that increases in order. During the temperature range where the LLT takes place, indicated by the shaded areas in figure 11.5, the parameters deviate from their initial trends and the parameters  $k$  and  $\xi$  show an unexpected increase, while  $\theta$  shows a small decrease. This supports that the LLT involves notable changes in the length scale associated with extended- or medium-range ordering, corroborating the observations made in chapter 10.

## Discussion and interpretation of $k$

The values and the evolution of the fit parameter  $k$  strongly remind on the course of  $Q_1$  (cf. figure 10.8). In equation 11.1 and equation 11.3 the parameter  $k$  plays the part of a wave vector, that defines the wavelength of density oscillations. In chapter 7 it is shown that the Fourier transform of the “positive” part of the principal peak of the structure factor ( $S(Q) > 1$ ) alone already yields a reasonable description of the decay of the extended range oscillations in  $g(r)$ .

Furthermore, it is shown that the Fourier transform of the maximum of  $S(Q)$  essentially yields a harmonic wave whose wavelength mirrors the wavelength of the oscillations in  $g(r)$ , implying a direct link between  $k$  and  $Q_1$ . Later it will be shown that this connection directly follows from the classical Ornstein-Zernike approach that predicts the structure factor to be a Lorentzian centered at  $Q = 0$  [181]. As demonstrated there, a shift of the Lorentzian about a vector  $Q_1$  yields in an additional term  $\exp(iQ_1 r)$  in the correlation function, suggesting to set  $k = Q_1$  in equation 11.1. A direct comparison of  $k$  and  $Q_1$ , determined from  $S(Q)$ , reveals that the two indeed show a strong linear correlation ( $R^2 = 0.992$ ) and differ in magnitude by only 1 % to 2 % over a temperature range of about 800 K (cf. inset figure 11.6).

The results shown in figure 11.5 are obtained by keeping  $k$  a free fit parameter, while on the other hand the above considerations suggest to set  $k = Q_1$ . In order to test the sensitivity of  $\xi$  depending on whether  $k$  is kept as a free parameter

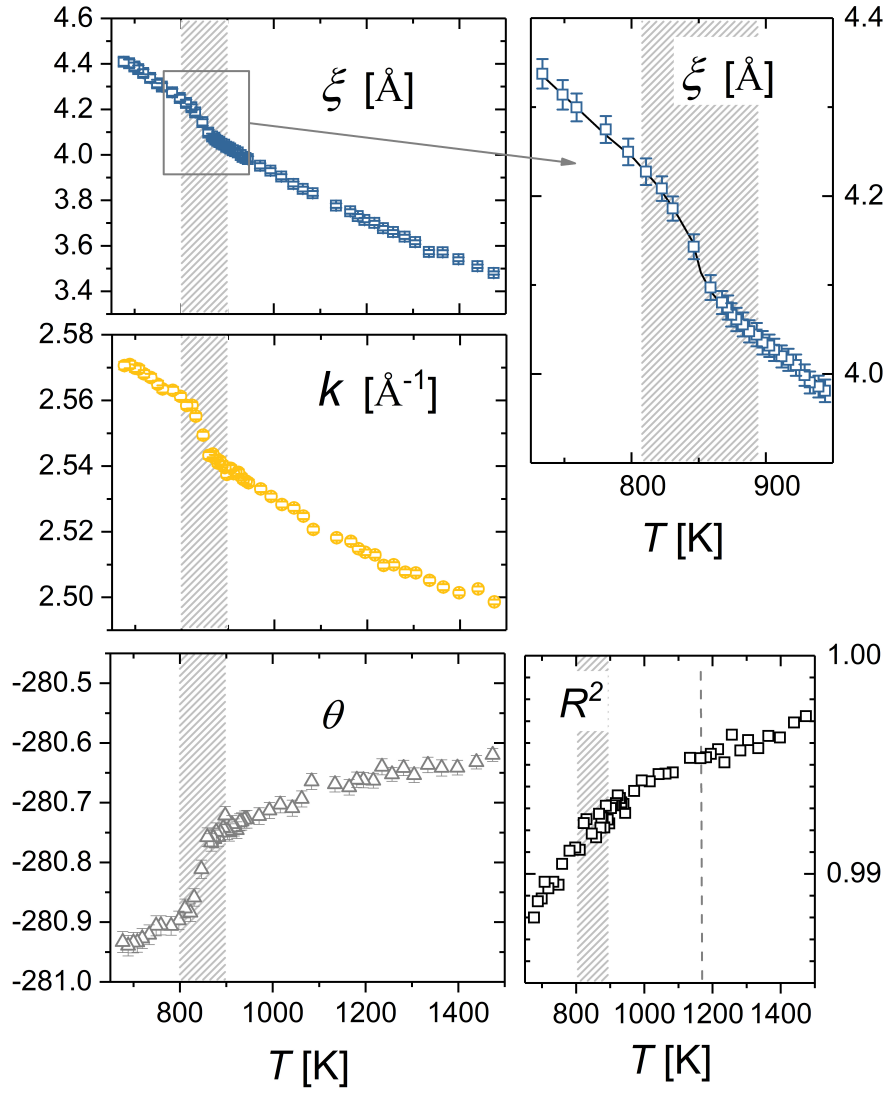


Figure 11.5: Fit results obtained by the three-parameter ( $k$ ,  $\theta$ ,  $\xi$ ) Orstein-Zernike analysis. The shaded area corresponds to the temperature region where a liquid-liquid phase transition is expected. The dashed line indicates the liquidus of the alloy.



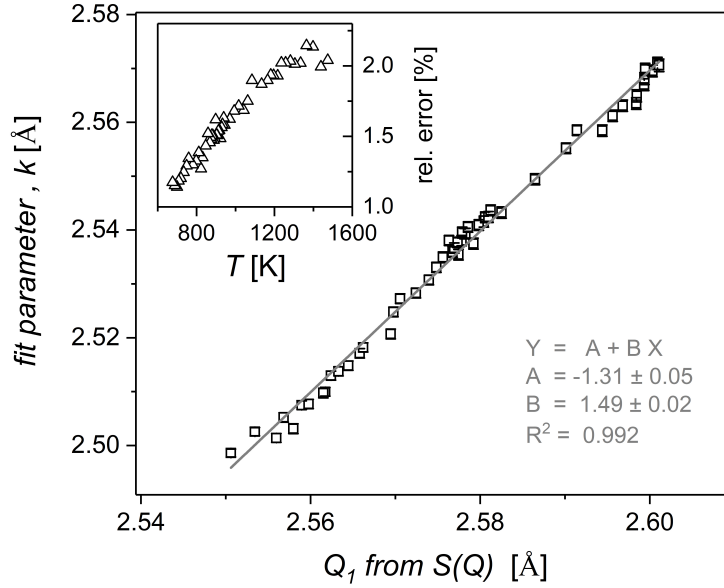


Figure 11.6: The fit parameter  $k$  plotted vs. the position of the principal diffraction peak of  $S(Q)$ ,  $Q_1$ . The two quantities show a strong linear correlation and differ only in between 1 % and 2 % over the entire temperature range of  $\approx 800$  K as shown in the inset.

or identified with  $Q_1$ , the Orstein-Zernike fits were repeated by manually setting  $k = Q_1$ . The results are shown in figure 11.7 in comparison to the values obtained for free fitting. The two values obtained for  $\xi$  are virtually identical, and fall on a straight line through the origin with a slope of unity.

### Discussion and interpretation of $\xi$

The decay exponent  $\xi$  in the Orstein-Zernike relations can be considered as the structural correlation length. It measures the magnitude of the decay of atomic pair correlations on medium- and extended-range and needs to be discriminated from the dynamic correlation length which describes the extension of dynamic heterogeneities (cf. figure 2.29). An increase in  $\xi$  with decreasing temperature reflects an extension of atomic correlations upon cooling, while at the same time the liquid viscosity increases. Following the line of thought that an increased structural coherence should go along with a dynamic slowdown, a link between the evolution of  $\xi$  and  $\eta$  may be expected.

In the high temperature liquid above the anticipated LLT (gray-shaded region in figure 11.7) the correlation length steadily increases with decreasing temperature, implying an increase of structural coherence during cooling. In the tem-

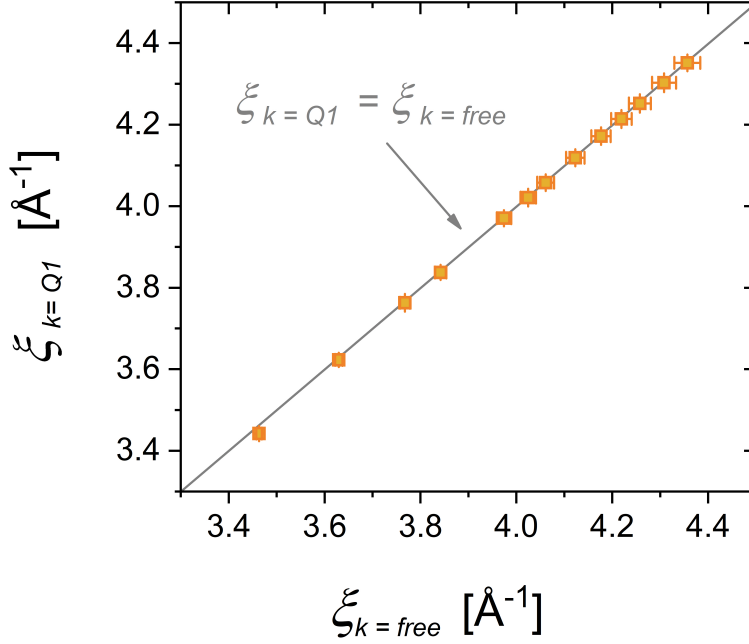


Figure 11.7: Irrespective of whether  $k$  is kept as a free fit parameter or identified with  $Q_1$  from  $S(Q)$ , nearly identical values for  $\xi$  are obtained. When plotted against each other the data points fall on a straight line through origin with a slope of unity (grey line).

perature regime associated with the LLT an additional increase in  $\xi$  is observed indicating that the low temperature phase is characterized by larger correlation length. This is corroborated by the top view of the real space data (contour plot of  $G(r)$ ) in shown in figure 11.8. Note that the gray scale represents the amplitudes of the oscillations in  $G(r)$ . At around 850 K atomic correlations at larger  $r$  become more pronounced in accordance with an increase in the correlation length during the LLT. Taking into account that an increase in the correlation length  $\xi$  should go along with a decrease in the fluidity, the present finding are in agreement with an additional viscosity increase during LLT, in accordance with the hypothesized course of the viscosity shown in figure 10.16.

The present observation of a finite increase in  $\xi$  in the temperature region where the structural and thermodynamic anomalies are detected suggests that the LLT is a first order phase transition, rather than a continuous transition. In this case each liquid phase could become metastable, and a hysteresis behavior of the transition can be expected, similar to what has been observed for the *Vit1* bulk metallic glass forming alloy [152, 170]. This could be tested by additional experiments which study the temperature dependence of the structural and thermodynamic signatures of the LLT at different cooling rates. However, a finite

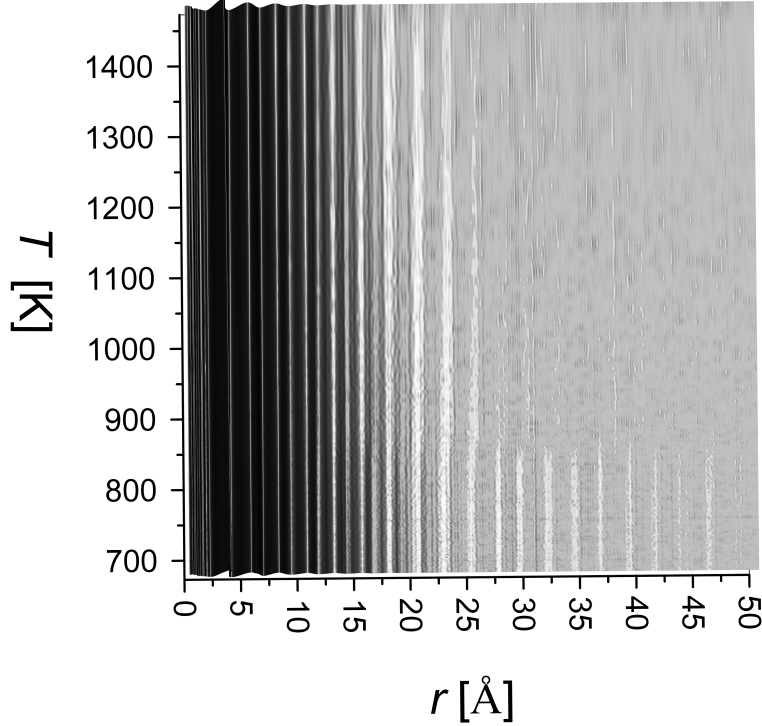


Figure 11.8: Extension of atomic correlations of the Vit106a BMG forming alloy during undercooling.

increase of the correlation length  $\xi$  as observed in figure 11.5 may also be expected for a smeared-out order-disorder transition as discussed in more detail in chapter 12. A final statement on the underlying nature of the LLT based on the evolution of  $\xi$  thus cannot be given. However, the results presented in chapter 12 suggest that the LLT is a smeared order-disorder transition above a liquid-liquid critical point in the phase diagram in which a more fragile, more disordered liquid transforms into a kinetically stronger, more ordered phase when the system crosses its Widom line.

### Extraction of the correlation length from the structure factor

The classical Ornstein-Zernike approximation predicts the scattered intensity to have a Lorentz-peak at  $Q = 0$  whose full width at half maximum (FWHM) is given by the inverse of  $\xi$  [181]

$$S_{OZ}(Q) \approx -K \frac{1}{\xi^{-2} + Q^2} \quad (11.4)$$

with  $K$  being a constant. A transformation of equation 11.4 into real-space predicts an exponential decay according to equation 11.2 which, for the case  $D = 3$  and  $\eta = 0$ , differs from equation 11.1 only by the sinusoidal term.

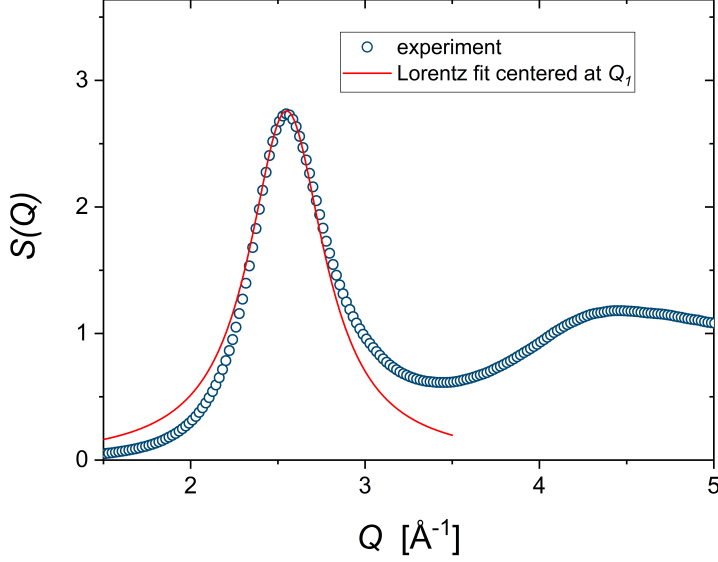


Figure 11.9: Lorentz fit of principal peak of  $S(Q)$  at 1473 K.

Obviously, the maximum of the structure factor is not at  $Q_1 = 0$  but shifted about  $Q_1$ , suggesting to write

$$S_{OZ}(Q - Q_1) \approx -K \frac{1}{\xi^{-2} + (Q - Q_1)^2} \quad (11.5)$$

According to the rules for Fourier transformation a shift in  $k$ -space about  $\Delta k$  yields an additional factor  $\exp(i\Delta k r)$  in real space. For the real part of the Fourier transform of  $S_{OZ}(Q - Q_1)$  one therefore obtains

$$\text{Re}\{\mathcal{F}[S_{OZ}(Q - Q_1)]\} \propto r^{-1} \exp(-r/\xi) \cos(Q_1 r) \quad (11.6)$$

which apart from a phase shift  $\pi/2$  is exactly equation 11.1.

In a real experiment the principal diffraction peak is only to a limited degree a Lorentzian. For the experimental obtained structure factor of the *Vit106a* at 1473 K the Lorentz-fit at low  $Q$  overestimates the experimental data, while at high  $Q$  the situation is inverse (cf. figure 11.9). Often a better description can be obtained by assuming a pseudo-Voigt function [136]. Irrespective of that, the above considerations suggest a direct connection between the width of the principal diffraction peak and  $\xi$ .

Plotting  $\xi$  obtained from the Ornstein-Zernike analysis against the inverse of the full width at half maximum (FWHM),  $\gamma^{-1}$ , determined directly from the

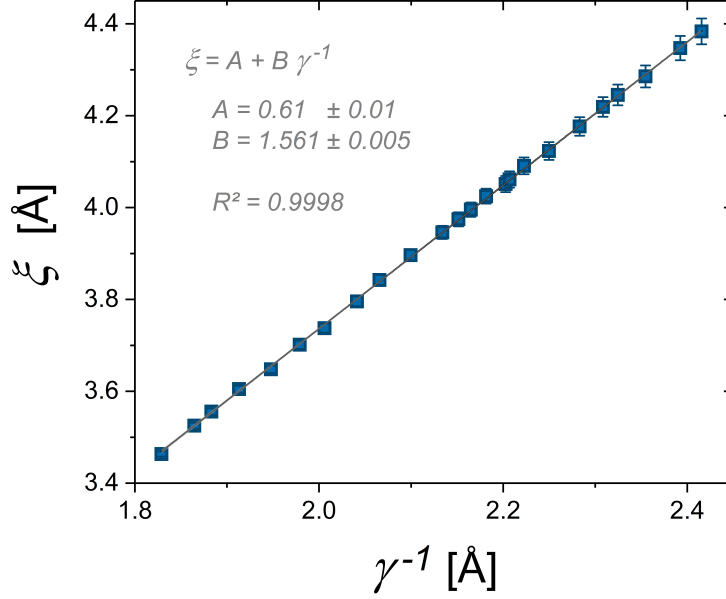


Figure 11.10: The correlation length  $\xi$ , extracted from the Ornstein-Zernike analysis of the real space data  $g(r)$ , plotted versus the inverse of the full width at half maximum (FWHM),  $\gamma^{-1}$ , determined manually from the  $S(Q)$  data, without a fit procedure presuming an analytical description of the peak.

experimental  $S(Q)$  data, without a fit procedure presuming an analytical description of the peak, a strong linear relation is obtained (cf. figure 11.10). This is remarkable considering that the system is a multicomponent liquid which undergoes drastic structural changes over a large temperature range including a liquid-liquid transition.

### **G(r) vs. g(r)**

The fact that the number density as a function of temperature,  $\rho$ , is needed to transform  $G(r)$  into  $g(r)$  tempts to perform the Ornstein-Zernike analysis on  $G(r)$ . This however can have influence on the results as oscillations in  $G(r)$  are magnified by a factor  $4\pi\rho r$  compared to  $g(r)$ . Adapted to  $G(r)$  the Ornstein-Zernike equation becomes

$$G(r) = A^* \exp(-r/\xi) \sin(kr - \theta) \quad (11.7)$$

where  $A^*$  is a temperature dependent prefactor that is related to  $\rho$  and  $A$  via  $A^*(T) = 4\pi A \rho(T)$ .

In order to quantify the errors made by using  $G(r)$  instead of  $g(r)$ , the OZA is repeated on  $G(r)$ . In contrast to the analysis performed earlier on  $g(r)$  the

amplitude is kept as a free fit parameter in order to account for its temperature dependence. The results of the OZA performed on  $G(r)$  are summarized in figure 11.11. A comparison with figure 11.5 reveals that the two approaches yield very similar results. Again, a good fit quality ( $R^2 > 0.992$ ) is achieved over the entire temperature range. All parameters show a clear change of their initial trends between 800 K and 900 K, in accordance with a structural transition.

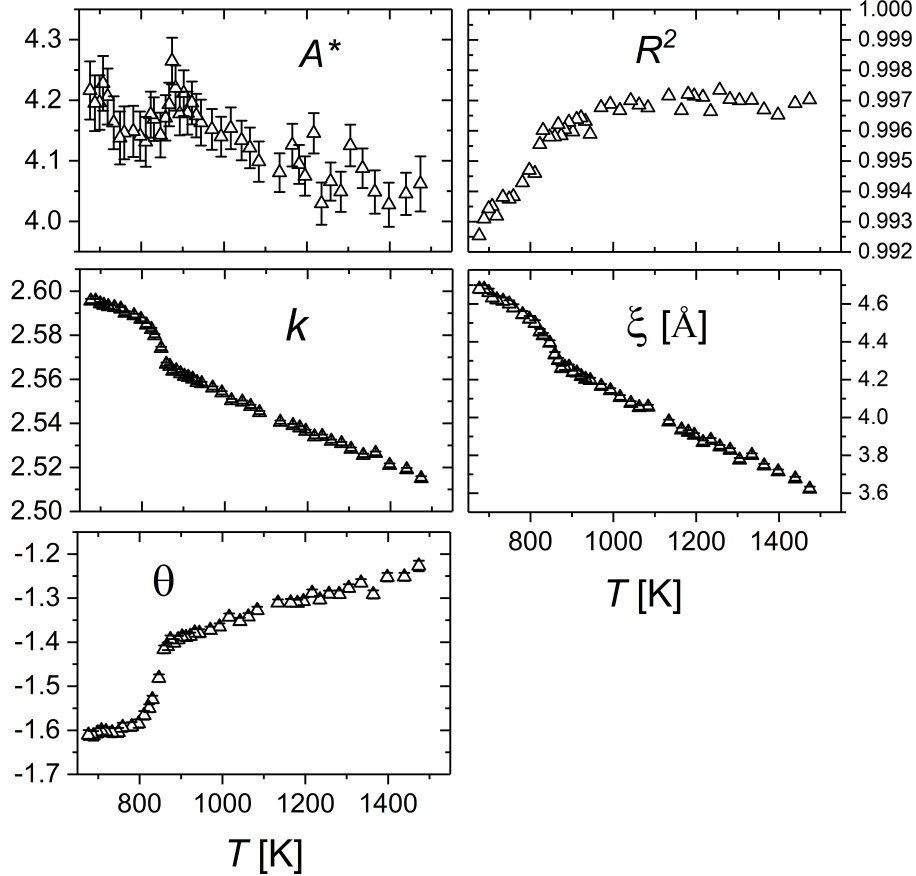


Figure 11.11: Results of the Ornstein-Zernike analysis performed on  $G(r)$  of the  $Zr_{58.5}Cu_{15.6}Ni_{12.8}Al_{10.3}Nb_{2.8}$  in the liquid phase. In contrast to the fit procedure applied to the case of  $g(r)$ , the amplitude  $A^*$  is kept as a free parameter in order to account its temperature dependence. The latter stems from the temperature dependence of the number density  $\rho$  as explained in the text.

Quantitatively, there is a tendency for slightly higher values of  $k$  and  $\xi$ , however, the changes are relatively small. For  $k$  the relative difference in the values obtained by the two approaches is less than 1%, while for  $\xi$  the relative difference is in between 3 - 6%. The temperature dependence of  $\xi$  determined by linear fitting of the data above 900 K is  $d\xi/dT = 10.8 \pm 0.2 E - 4$ , which is about

10 % larger than the temperature dependence of  $\xi$  determined from the analysis based on  $g(r)$ , i.e.  $d\xi/dT = 9.6 \pm 0.1E - 4$ . Again, an almost perfect linear correlation is found between  $k$  and  $Q_1$  ( $R^2 = 0.996$ ). The amplitude  $A^*$  shows a negative temperature dependence as expected for a decreasing density upon heating. Its value at 1473 K is about 58 % of the value for  $A$ . This is close to the ratio  $A^*/A \approx 66$  % as expected for  $\rho \approx 0.0525$ . When fitted in the temperature range above 900 K assuming a linear relation,  $dA^*/dT = -2.3 \pm 0.2E - 4$ . On the other hand, inserting  $A = 7.1$ , i.e. the value obtained from fitting of  $g(r)$  and  $d\rho/dT = 0.3E - 5A^{-3}K^{-1}$ , obtained from linear fitting of the density data shown in figure 11.1, yields  $dA^*/dT = 4\pi A d\rho/dT = 2.8E - 4$ . Thus the temperature dependence of the fitting parameter  $A^*$  can mainly be attributed to the temperature dependence of  $\rho$ . This is remarkable considering that  $A^*$  is directly obtained from the fit without making any assumption on its temperature dependence. For high quality data with low scattering this in principle allows to estimate  $\rho(T)$  from  $A^*(T)$ . Concluding it can be stated that the present findings indicate that the OZA can be performed either on  $g(r)$  or  $G(r)$  with reasonable errors that predominantly arise from the uncertainty in the number density.

### 11.3 Ornstein Zernike Analysis of the glass transition

In the previous section an Ornstein-Zernike analysis of a levitated droplet of a Zr-based bulk metallic glass former in the liquid state was performed during cooling from above the melting point down to the onset of the glass transition. Due to the detection limit of the pyrometer the analysis of the evolution of the long-range decay behavior throughout the glass transition could not been performed on the data set obtained in the electrostatic levitator. In this section the Ornstein-Zernike analysis (OZA) is extended to the glassy state and the glass transition using the structural data obtained from heating experiments of glassy samples in a Linkam furnace. For details on the experimental conduct the reader is referred to chapter 5.

An exact analysis of the long-range decay behavior in the Ornstein-Zernike description 11.1 requires knowledge of  $g(r)$ . However, the sine-Fourier transforms of  $F(Q)$  over a limited  $Q$ -range yields  $G(r) = 4\pi\rho[g(r) - 1]$ . In the glassy state  $\rho(T)$  can easily be obtained from dilatometry. However, in the (supercooled) liquid state the situation is more challenging due to the structural softening of the samples when the system approaches the glass transition (cf. figure 6.3). This makes a determination of the volume or thermal expansion not reliable. For this reason the OZA in this chapter is performed using  $G(r)$  instead of  $g(r)$ . However, as shown in the previous chapter the analysis based on  $G(r)$  yields qualitatively similar results with deviations in the fit parameters of the order of 10 %.

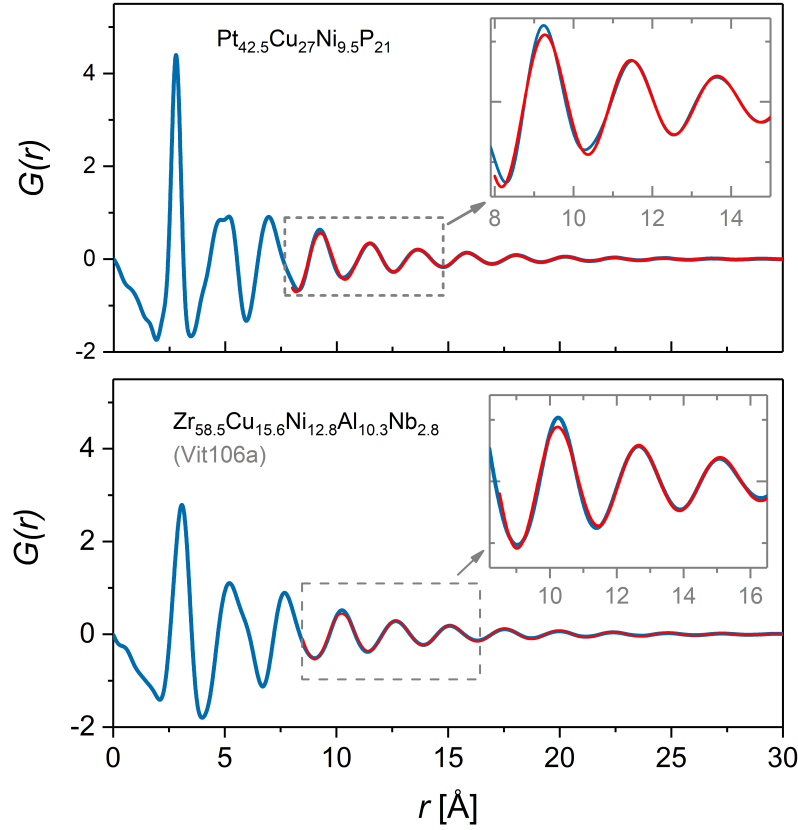


Figure 11.12: Ornstein Zernike Fits of the  $G(r)$  data of two different bulk metallic glasses at 50 °C. The insets give a close up view of the 4<sup>th</sup>, 5<sup>th</sup>, and 6<sup>th</sup> coordination shell. As visible, the OZ fits struggle to fit the experimentally determined  $G(r)$ -data at the 4<sup>th</sup> coordination shell but yield a good description beyond.

In general a good fit quality is achieved when applying equation 11.7 to the  $G(r)$  data in the glass, during the glass transition, and in the supercooled liquid state. This is exemplarily shown in figure 11.12 for the structural data of two bulk metallic glasses at 50 °C. A closer inspection shows that the fits capture the course of the higher oscillations very well, but struggle to describe the lowest  $r$ -region corresponding to the lower coordination shells (cf. insets). In general, the fit quality increases with increasing temperature (cf. figure 11.13). Notably, a stronger increase in the fit quality is observed when the system enters the supercooled liquid state. This results from the fact that in particular the lowest  $r$ -data corresponding to the lower coordination shells are better recaptured by the fits. Note that a similar observation is made for the high temperature ESL data (cf. figure 11.3). It thus appears that the Ornstein-Zernike description successively loses its ability to describe the atomic correlations at the lower co-



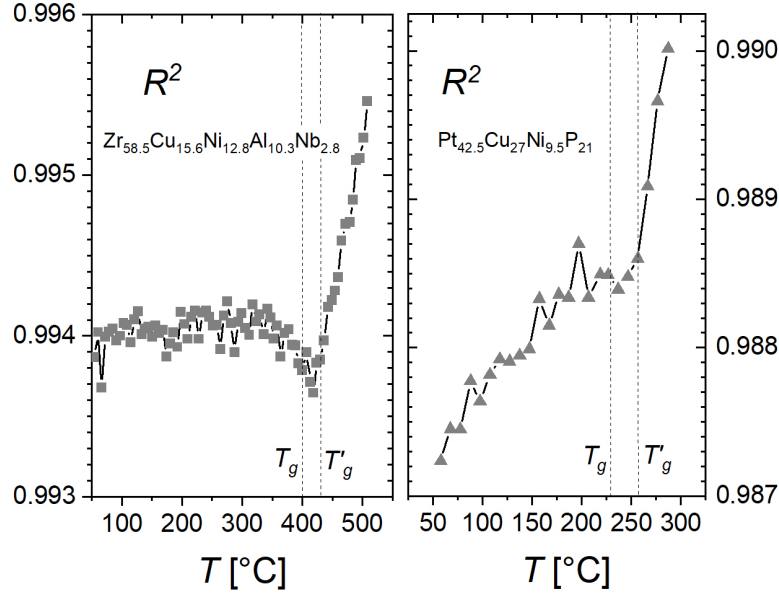


Figure 11.13: Evolution of the fit quality of the Ornstein-Zernike analysis. With the transition to the supercooled liquid state a marked increase in the fit quality can be observed. The onset of the glass transition is marked by  $T_g$ , the end of the glass transition where the system has fully equilibrated is marked with  $T'_g$ .

ordination shells (below the fourth) when the system is cooled towards the glass transition, suggesting that peculiarities of the cluster structure extend to larger length-scales but average out beyond. In the deeply undercooled liquid the structural peculiarities extend up to  $\approx 1$  nm, which agrees well with the length scale expected for the extension of a efficiently-packed solute-centered cluster structure [57]. Accordingly, it may be speculated that the loss of accuracy of the Ornstein-Zernike description for the lower coordination shells is related to the formation of a system-specific cluster structure whose extension increases during cooling towards the glass transition.

### 11.3.1 Evolution of the correlation length during the glass transition

The evolution of the correlation length during heating the two glassy alloys into the supercooled liquid until crystallization sets in is shown in figure 11.14. During heating the correlation length  $\xi$  in the glass decrease slightly, in accordance with the conception that an increase in thermal energy induces vibrational disorder that leads to a more pronounced decay of long-ranged atomic correlations. When approaching the glass transition the negative trend of  $\xi$  turns into a positive trend.

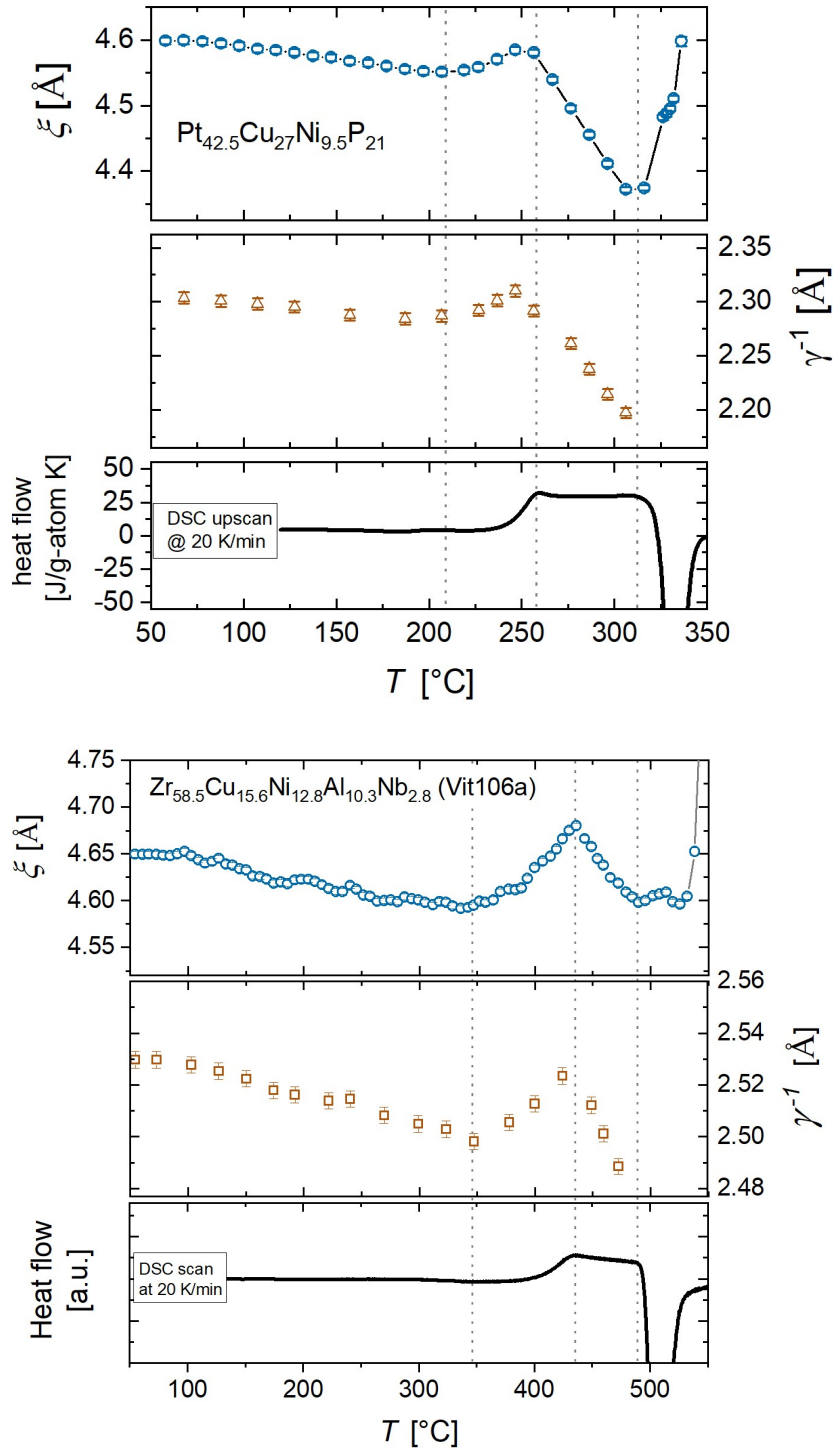


Figure 11.14: Evolution of the correlation length  $\xi$  and the FWHM of the principal peak of  $S(Q)$ ,  $\gamma$ , in the *Pt42* and *Vit106a* BMG forming alloys during heating from the glassy state into the supercooled liquid region.

For each of the two alloys this occurs at roughly  $0.9T_g$ . The increase in  $\xi$  continues until the end of the glass transition, where the system restores its metastable equilibrium in the liquid phase. A further increase in temperature leads to a pronounced decrease of  $\xi$  in the supercooled liquid region until crystallization takes place, where  $\xi$  dramatically increases as expected for a system in which long-range order is formed.

Given that the decay of long-range density oscillations is linked to the viscous behavior, one might expect that the a more pronounced decay of  $\xi$  in the supercooled liquid correlates with the kinetic fragility. A more fragile liquid then should exhibit a “faster” decay of  $\xi$  with increasing temperature, and vice versa. Comparing the temperature dependence of  $\xi$  in the supercooled liquid in the two alloys, indeed, it is observed that the more fragile Pt-based bulk metallic exhibits. Indeed it is observed that the temperature-dependence of  $\xi$  in the more fragile Pt-based alloy ( $d\xi/dT = 4.24E - 3 \pm 3E - 5 \text{ ÅK}^{-1}$ ) is more pronounced than in the stronger Zr-based alloy ( $d\xi/dT = 1.77E - 3 \pm 8E - 5 \text{ ÅK}^{-1}$ ). This also holds if the relative change with respect to the value at the end of glass transition  $T'_g$  is considered, Pt-based:  $(\xi^{-1}(T'_g)d\xi/dT = 9.27E - 4 \pm 7E - 6 \text{ K}^{-1})$ , Zr-based:  $(\xi^{-1}(T'_g)d\xi/dT = 3.81E - 4 \pm 1.7E - 5 \text{ K}^{-1})$ . Whether this is a generic correlation among bulk metallic glass forming alloys in general remains to be explored.

A strong (linear) correlation between the correlation length, extracted from the OZA of the real space data  $g(r)$ , and the inverse of the FWHM of  $S(Q)$ ,  $\gamma^{-1}$  is observed for the  $Zr_{58.5}Cu_{15.6}Ni_{12.8}Al_{10.3}Nb_{2.8}$  BMG forming alloy in the liquid state (cf. figure 11.14). Here, the OZA is performed on systems that undergo a transition from the glass into the supercooled liquid state. It might therefore be asked if the strong coupling between  $\xi$  and  $\gamma^{-1}$  also persist in the glassy state and/or throughout the glass transition. A comparison between the upper and the center panels of figure 11.14 reveals that  $\gamma^{-1}$  mirrors the course of  $\xi$ . A closer investigation shows that  $\xi$  and  $\gamma^{-1}$  obey a functional dependence of a linear form  $\xi = A + B\gamma^{-1}$  in the glass as well as in the supercooled liquid state with different values of the fit parameters  $A$  and  $B$ . In general, the correlation is stronger for the supercooled liquid than for the glass. The corresponding results are shown in figure 11.15.

The fact that  $\xi$  and  $\gamma^{-1}$  show a peak (maximum) at the end of the glass transition is an interest observation. In particular the question arises what is responsible for the increase in the two quantities when the system approaches the glass transition and transforms from the glass (frozen out-of equilibrium state) into a metastable equilibrium liquid state. Conceiving the glass a structurally rigid system, one would expect that, in the absence of any thermal atomic motion, neither  $\xi$  nor  $\gamma^{-1}$  show a decreasing trend with temperature but remain constant. On the other hand, above 0 K, atoms perform thermal-induced vibrations around their lattice sites, resulting in vibrational structural disorder that increases with increasing temperature. The corresponding loss of structural co-

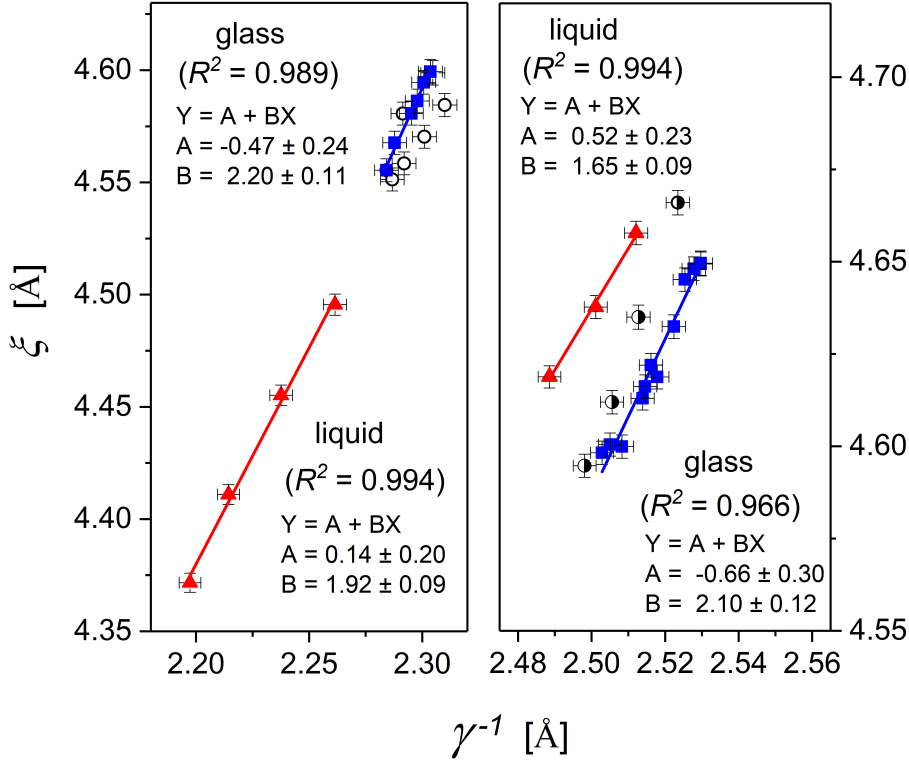


Figure 11.15: Linear regression analysis between  $\xi$  and  $\gamma^{-1}$  in the glass (blue squares), during glass transition (circles) and in the supercooled liquid (red triangles) for the *Pt42* bulk metallic glass (left figure) and the *Vit106a* bulk metallic (right figure).

herence should result in decay of density oscillations, which may explain the initially decreasing trend in  $\xi$  and  $\gamma^{-1}$  during heating in the glass. With the transition to the supercooled liquid regime, the structural units have restored their mobility, and structural rearrangements can occur. Measurements of the heat capacity or entropy show that pronounced structural disordering (configurational and vibrational) takes place in the supercooled liquid region. As  $c_p/T$  of the liquid is larger than for the glass, the temperature-induced formation of structural disorder in the liquid state is much more pronounced than in the glass, and hence the larger should be the loss of structural coherence with increasing temperature. This might explain why  $\xi$  shows a larger, negative temperature dependence in the liquid than in the glassy state. Still, the question remains why  $\xi$  at some temperature below the glass transition starts to deviate from its negative trend, turns into a positive trend, and reaches a maximum until it finally starts to decrease again as expected.

### 11.3.2 The complete picture

Knowing that the OZA analysis performed on  $G(r)$  gives quantitatively similar results compared to the analysis based on  $g(r)$ , the data of the *Vit106a* alloy determined in the glassy state and through the glass transition can be combined with the data obtained from the OZA of the liquid state data obtained in the ESL measurement, yielding the entire evolution of the correlation length  $\xi$  from room temperature up to 1473 K, i.e. 300 K above the liquidus (cf. figure 11.16).

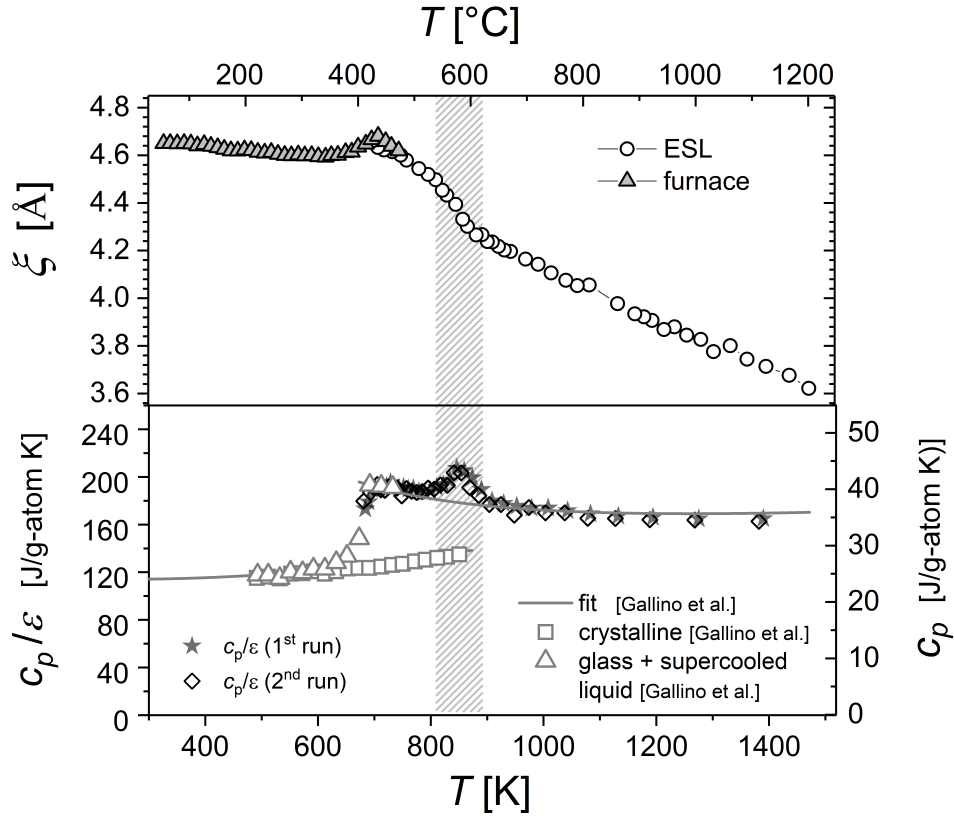


Figure 11.16: Evolution of the correlation length in the Vit106a alloy from ambient temperature to 1473 K. The graph combines the data obtained from the OZA in the glass, and throughout the glass transition, with the data in liquid state obtained from the OZA of the levitated droplet. Note the good match of the two data sets. The glass transition takes place around 670 K to 700 K. The liquidus temperature is 1170 K.

## 11.4 Summary

Summarizing it can be stated that the Ornstein-Zernike equation 11.1 provides a very good description of the long-range decay of density fluctuations in the liquid

as well as the glassy state. In general the fit quality is better for the liquid than for the glassy state and worsens with decreasing temperature. This results mainly from a progressively reduced ability to describe the structure of the lower (third and fourth) coordination shells when the system is cooled. The OZ-analysis can be performed either on  $g(r)$  or in an adapted version on  $G(r)$  with similar qualitative findings. However, for an accurate description the temperature dependence of the number density must be taken into account. In general the correlation length in the liquid extracted from the Ornstein-Zernike analysis shows a decreasing trend with temperature. As a consequence of the LLT in the Vit106a alloy a small, but marked, additional increase in the correlation length is observed in accordance with an additional increase in viscosity. Furthermore, the correlation length is found to show a strong linear correlation with the inverse of the FWHM. This holds for the glassy and the liquid state, although the correlation appears to be stronger for the liquid state. The temperature dependence of the  $\xi$  in the supercooled is found to be much stronger pronounced than in the glassy state, reflecting a more pronounced decay of long-range density oscillations, as expected for a more pronounced formation of structural disorder. During the glass transition the correlation length shows a peak (maximum) reminding of a lambda transition. While the decreasing trend of  $\xi$  in the low temperature regime in the glass and in the supercooled liquid might be understood in terms of an increasing thermal-induced structural disorder, the origin of the re-increase of  $\xi$  observed around  $0.9T_g$  remains to be explored. The temperature dependence of  $\xi$  in the supercooled liquid in the more fragile Pt-based glass former is more pronounced than in the stronger Zr-based glass former, suggesting that the decay of long-range density oscillations is linked to the temperature dependence (fragility) of the viscosity. Whether this correlation is universal among bulk metallic glass formers remains to be explored in future studies.

# Chapter 12

## Structural order parameter analysis of a bulk metallic glass forming liquid

### 12.1 Structural order parameters - Translational and bond-orientational ordering

The formation of structure in liquids is determined by the competition between thermal-disordering and interatomic forces that tend to create order. The latter is determined by the interatomic pair potentials. Tweaking the potentials in terms of their magnitude and shapes can reveal valuable information on what are the prerequisites for the formation of a certain phase, how stable are these phases with respect to other competing phases, and if they will transform into another phase. In this context, order parameters play an important role as they enable to quantify and trace the underlying structural changes. Over the last years, a number of research activities has focused on the question of what are the basic requirements for an interatomic potential to be in accordance with a liquid-liquid transition (see e.g. [111, 112, 183]). These studies show that already simple spherically-symmetric potentials with a “core-softened” short-range interaction can generate density and diffusion anomalies, and are in conformity with the scenario two coexisting equilibrium liquid phases in the phase diagram [183]. For two scale-ramp potentials, such as the Jagla-ramp potential, it is found that the structural anomaly region in the order parameter map<sup>1</sup> contains the diffusion anomaly region, which in turn contains the density anomaly region [183]. This indicates that anomalous changes in the dynamics (e.g. diffusion) are coupled to

---

<sup>1</sup>In an order map, the state points of the system are plotted onto the order parameter plane, i.e. the  $t$ - $Q$  plane for various temperatures or pressures. Order maps thus give information on where a certain state of matter (phase) is stable as a function of the order parameters. For a more detailed treatise of order maps, the reader is referred to references [183, 184].

anomalies in the structure and density.

In general, structural order can be divided into translational and orientational order [163]. The evolution of these two ordering tendencies can be quantified by two, not necessarily independent, order parameters, i.e. the translational structural order parameter (TSOP),  $t$ , and the bond-orientational order parameter (BOOP),  $Q_{lm}$  [112, 163, 183]. The translation order parameter  $t$  quantifies the tendency of particle pairs to adapt preferential separations [183], while the bond orientational order parameter  $Q_{lm}$  is a quantitative description of the bond orientation (symmetry) around a center atom [9], and therefore enables to measure how close the orientation of the nearest neighbor environment obeys a distinct structural arrangement, e.g. tetrahedra, icosahedra. Following Steinhardt et al. [185] the bond orientational order parameter  $Q_{lm}$  is defined as

$$Q_{lm}(\mathbf{r}) = Y_{lm}(\theta(\mathbf{r}), \phi(\mathbf{r})) \quad (12.1)$$

where  $Y_{lm}$  are spherical harmonics, and  $\theta(\mathbf{r})$  and  $\phi(\mathbf{r})$  are the polar angles of the bond measured against a reference coordinate system. A graphical illustration of some selected spherical harmonics is shown in figure 12.1. Usually only the average is considered  $\bar{Q}_{lm} = \langle Q_{lm}(\mathbf{r}) \rangle$ , where the average is taken over some suitable sets of bonds, e.g. all nearest neighbors [185]. In cubic systems the first nonzero averages (other than  $Q_{00}$ ) occur for  $l = 4$ , in icosahedral-oriented systems for  $l = 6$ . As the  $Q_{lm}$  for a given  $l$  can be scrambled by changing to a rotated coordinate system, it is helpful to consider the rotational invariant combinations, such as the second order invariant [185]

$$Q_l = \left( \frac{4\pi}{2l+1} \sum_{m=-l}^l |\bar{Q}_{lm}|^2 \right)^{1/2} \quad (12.2)$$

or even higher order invariants, e.g. the third order invariants  $\bar{W}_l$ . For the definition of the latter and the details on their calculation the reader is referred to reference [185].

With the help of the above definitions it is possible to trace the evolution of specific packing schemes, such as bcc, icosahedral, fcc, or hcp clusters in a sample. Each cluster species leaves a typical footprint (histogram of the invariants) as shown in figure 12.2. For example an icosahedral-like packing corresponds to non-zeros  $Q_6$ ,  $W_6$ ,  $Q_{10}$ ,  $W_{10}$ , while fcc-like packing corresponds to a non-zeros  $Q_4$ ,  $W_4$ ,  $Q_8$ ,  $W_8$  [185]. Accordingly, an increase in  $Q_6$ ,  $W_6$ ,  $Q_{10}$ , and  $W_{10}$  at the expense of  $Q_4$ ,  $W_4$ ,  $Q_8$ , and  $W_8$  implies a structural reconfiguration towards icosahedral ordering. This can be used to investigate relaxation effects or the effect of the cooling rate on the formation of orientational order in liquids and glasses [185]. However, as pointed out by Steinhardt et al. [185] “all evidence of bond-orientational order, of course, would be lost in a directionally-averaged “powder” x-ray diffraction pattern.”<sup>2</sup> The information that survives a diffraction

---

<sup>2</sup>Evidently, the same applies to isotropic liquids or glasses.



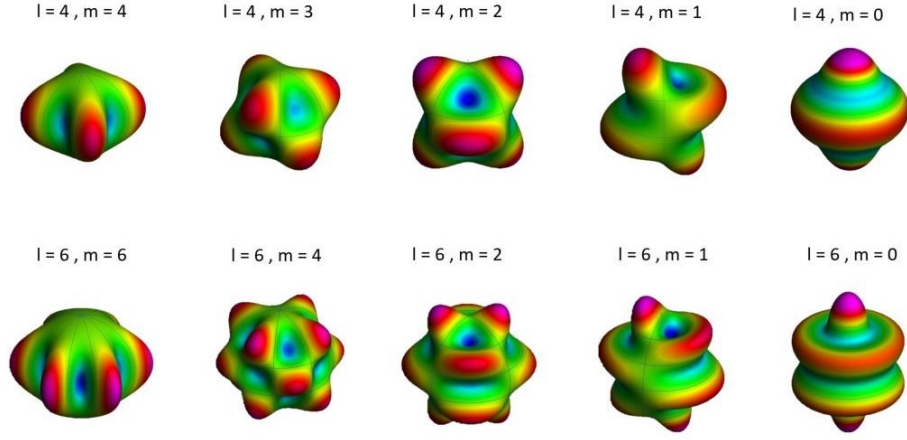


Figure 12.1: Illustration of selected spherical harmonics  $Y_{lm}$ . The figures are created using the online tool: [icgem.gfz – potsdam.de/vis3d/tutorial](http://icgem.gfz-potsdam.de/vis3d/tutorial).

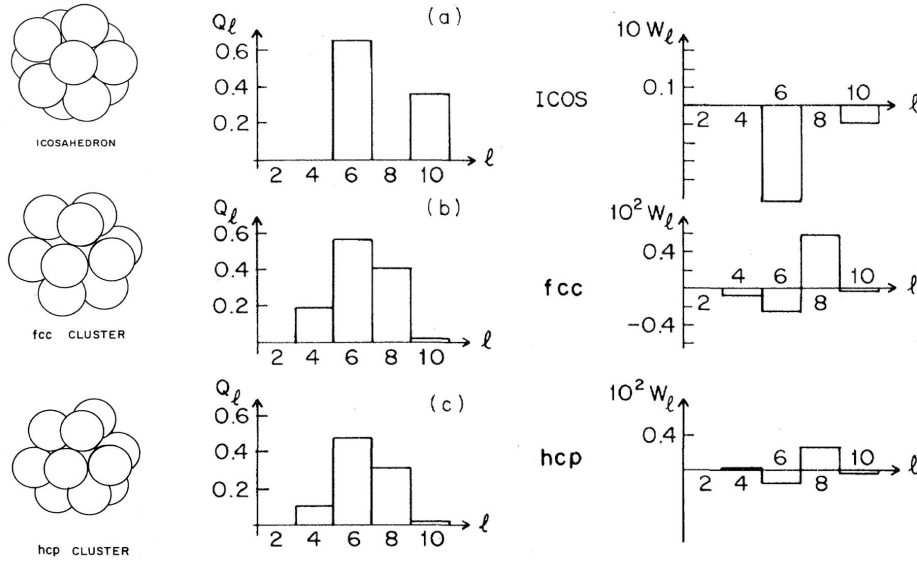


Figure 12.2: Histograms of quadratic  $Q_i$  and third-order invariants  $W_i$  for 13-atom cluster species: a) icosahedral, b) fcc, c) hcp. Each cluster species leaves a typical footprint. By tracing the invariants, the evolution of bond orientational order can be studied. For example, an increase in  $Q_6$ ,  $W_6$ ,  $Q_{10}$ , and  $W_{10}$  at the expense of  $Q_4$ ,  $W_4$ ,  $Q_8$ , and  $W_8$  implies a structural reconfiguration towards icosahedral ordering. The figure is taken from [185].

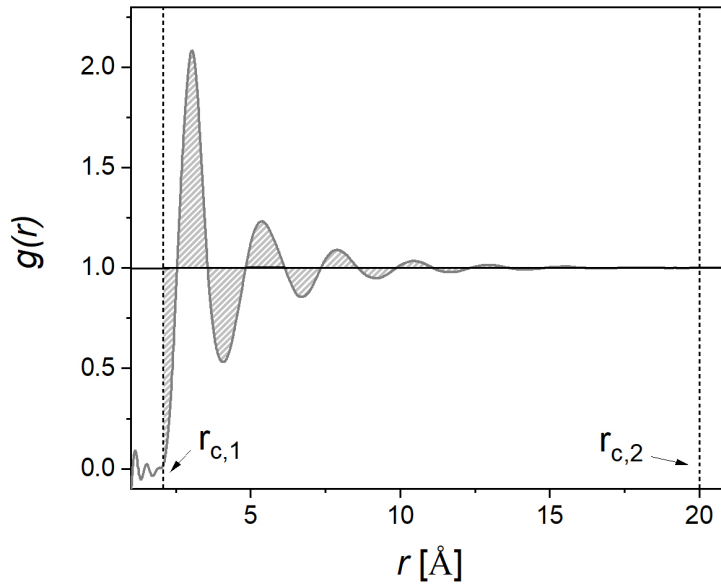


Figure 12.3: Graphical illustration of the translational structural order parameter (*TSOP*). The *TSOP* is a measure of the magnitude of density fluctuations with respect to a perfectly random structure. For a perfectly random system such as an ideal gas  $g(r) = 1$  for all  $r > r_{c,1}$ , where  $r_{c,1}$  is the lower cut-off corresponding to the minimum distance between the two atoms. The larger is the area enclosed between  $g(r)$  and  $g(r) = 1$ , the larger is the translational structural order present in the system, and the larger is the *TSOP*. A higher cut-off  $r_{c,2}$  is set to exclude the scattering in the high  $r$  regime of  $g(r)$ , here exemplarily set to 20 Å.

experiment is the distribution of atomic distances, given by the pair distribution functions. Accordingly, the experimental data obtained in the present work cannot be evaluated in terms of the bond-orientational order, but only in terms of the translational order.

The *translational structural order parameter (TSOP)*  $t$  can be defined as [112, 163, 183] :

$$t = \int_0^{r_c} |g(s) - 1| ds \quad (12.3)$$

where  $s = r\rho^{1/3}$  is the radial distance scaled by the mean particle distance,  $\rho$  is the density, and  $r_c$  is a cutoff that can be set to a suitable value, e.g. to one-half of the simulation box size [183]. For a completely uncorrelated system,  $g(r) = 1$ , and therefore  $t = 0^3$ . On the other hand, for systems with pronounced translational ordering  $t > 0$ , and,  $t$  grows with increasing translational order, i.e. when the oscillations in  $g(r)$  increase and extend.

## 12.2 Evolution of structural order parameters during a liquid-liquid phase transition - insights from simulations

Just as the response functions, structural order parameters show distinct changes during a phase transition. This has been used by Xu et al. [112] to investigate the behavior of Jagla-liquids during cooling at different pressures above and below the liquid-liquid critical point (LLCP) in their phase diagram (cf. figure 12.4). Figure 12.5 shows the evolution of the two order parameters  $t$  and  $Q_6$  during cooling the simulated Jagla-liquid above the LLCP when traversing the Widom line ( $\alpha$ -path in figure 12.4). Clearly, marked changes in  $t$  and  $Q_6$  can be observed when the Widom line is crossed ( $kT/U_0 \approx 0.4$ ). These changes clearly indicate a structural transition in the liquid state and go along with marked anomalies in the specific heat  $c_p$  and the isothermal compressibility  $\kappa_T$  as shown in figure 12.6. The closer the system is to its critical point ( $P_c = 0.234$ ) the more pronounced, i.e. the less smeared, are the changes in  $t$ ,  $Q_6$ , and in  $c_p$ ,  $\kappa_T$ . An corresponding analysis of the diffusivity shows that the transition between the two liquid phases is accompanied by a change in the dynamics, more precisely a transition from a more fragile behavior in the low density liquid (LDL) towards a stronger dynamics behavior in the high density liquid (HDL) (cf. figure 12.4).

---

<sup>3</sup>A value  $t = 0$  requires that the lower integration limit is defined as the minimum particle separation  $r_{min}$  as  $g(r) = 0$  for  $r < r_{min}$ .

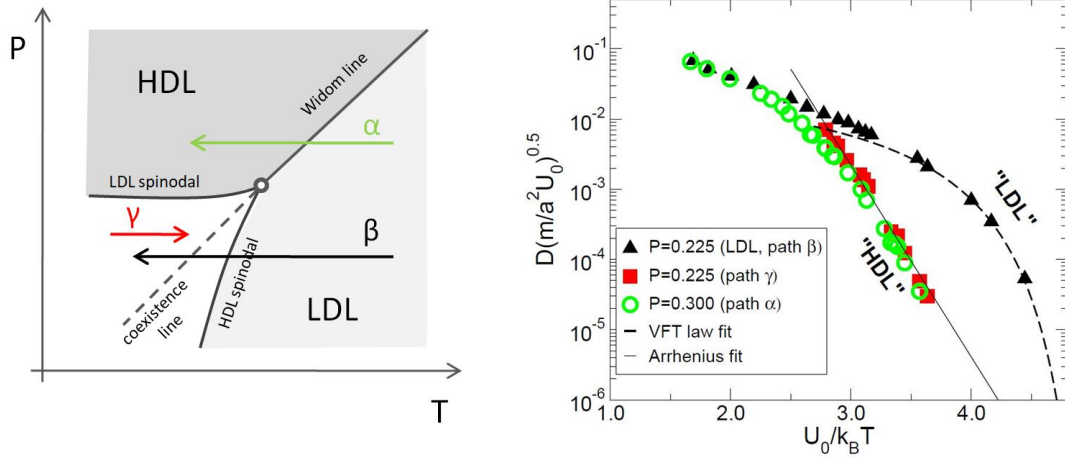


Figure 12.4: Dynamic behavior for a Jagla liquid around its critical point. The right figure shows the evolution of the diffusivity along the different pathes in the P-T-phase diagram. When the low density liquid (LDL) is cooled below the liquid-liquid critical point, LLCT, (open circle in the center of the left figure) a fragile (VFT) behavior is observed. On the other hand, when the system is cooled above the LLCT over its Widom line, the diffusivity shows a stronger (more Arrhenius-like) behavior at lower temperatures, indicating a fragile-strong transition when the liquid traverses the Widom line. The left figure is reproduced, and the right figure is taken from [112].

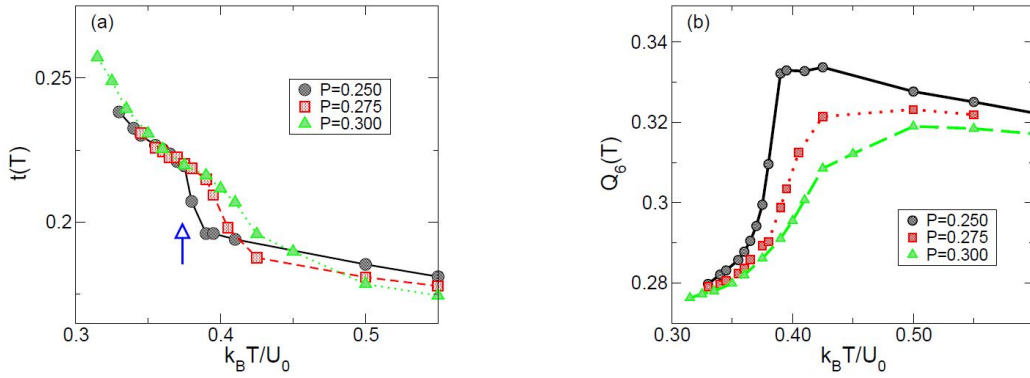


Figure 12.5: Evolution of structural order parameters during the LLT in a Jagla liquid. Marked changes in the structural order parameters  $t$  and  $Q$  are observed when the system crosses the Widom line. With increasing distance to the critical pressure ( $P_c = 0.234$ ) the changes in  $t$  and  $Q$  smear out progressively. The figure is taken from [112].

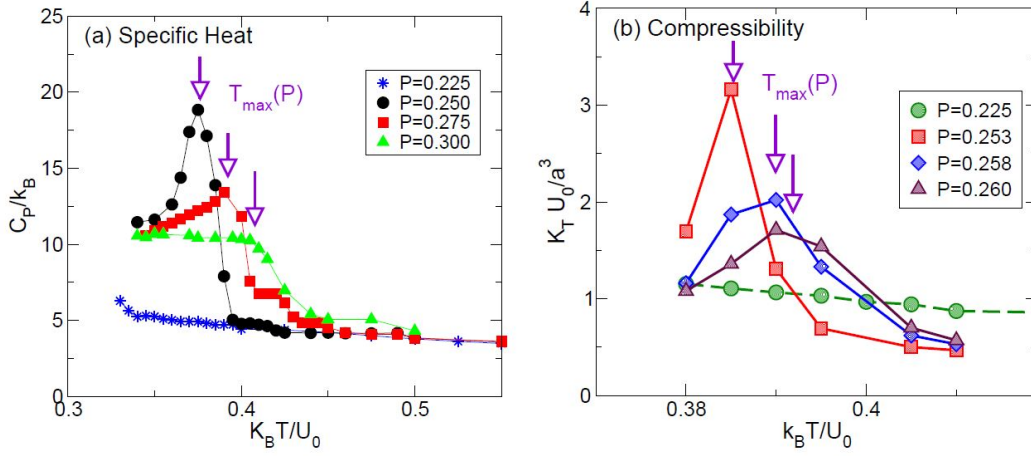


Figure 12.6: Evolution of the specific heat  $c_p$  and the isothermal compressibility  $\kappa_T$  when the system crosses the Widom line. Similar to the structural order parameters the peaks (anomalies) become smeared with higher distance to the critical pressure ( $P_c = 0.234$ ). Note that below the liquid-liquid critical point, the response functions do not expose any indication for a (first order) transition as they retain metastability until their spinodal limits. The figure is taken from [112].

### 12.3 Translational Structural Order Parameter Analysis for the LLT in Vitreloy106a

In the following a translational structural order parameter analysis is performed on the Vit106a bulk metallic glass forming alloy during cooling from above the liquidus down to the glass transition. The results are compared to the numerical findings obtained by Xu et al. for Jagla liquids and discussed in terms of their implications to the dynamic behavior [112].

Using equation 12.3 the translational structural order parameter (TSOP) is calculated from the real space structural data of the Vit106a BMG forming liquid. The total TSOP,  $t_{total}$ , is obtained by integrating  $g(r)$  over the entire physically plausible  $r$ -range, i.e. from  $2 \text{ \AA}$ , corresponding to the onset of the first coordination shell, to the upper limit of  $30 \text{ \AA}$ , where the oscillations essentially have died out and only scattering in the data is predominant. Mathematically, the TSOP corresponds to the area enclosed between  $g(r)$  and  $g(r) = 1$ ; physically, it measures the degree of density variations with respect to a fully random system, i.e. an ideal gas-like liquid (cf. figure 12.3).

As expected  $t_{total}$  increases with decreasing temperature indicating an increase in translational order during cooling. Within the temperature range of the LLT (shaded region) a small hump can be noticed, indicating an additional increase

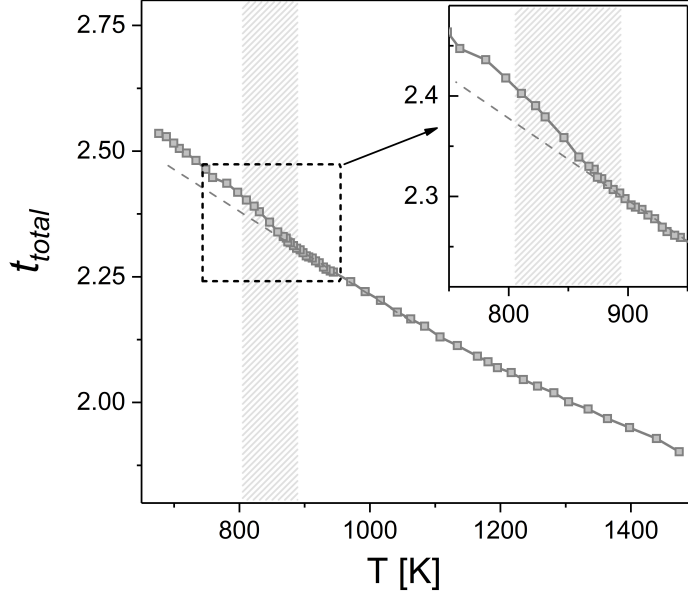


Figure 12.7: Evolution of the translational structural order parameters  $t_{total}$  in the undercooled liquid of the *Vit106a* bulk metallic glass forming alloy. The large panel show the course over the entire temperature range. The inset shows a magnified view of the temperature region associated to the LLT (shaded area). The dashed lines indicate the course expected for a extrapolation of the high temperature data in the absence of the LLT. An additional increase of  $t_{total}$  can be noticed in the shaded area indicating an increase of translational structural order as a consequence of the LLT.

in order in agreement with the exothermal heat release corresponding to the  $c_p$  peak observed in figure 10.8. The total change of  $t_{total}$  over the entire temperature range from 1473 K to 673 K is about 0.63. The change in  $t_{total}$  from the liquidus temperature  $T_l = 1170$  K to the onset of glass transition (673 K) is about 0.45, while the additional change<sup>4</sup> in the temperature region associated with the LLT is about 0.045, making about 10 % of the change in the entire undercooled liquid region. This magnitude is of the order of the relative changes in enthalpy or excess entropy associated to the LLT with respect to the overall changes in the supercooled liquid region that is found to be about 7 %. The exothermic heat release and the changes in the order parameters can be associated with a decrease in the configurational entropy which according to the Adam-Gibbs theory implies an additional increase in the structural relaxation time or viscosity, and a

<sup>4</sup>Note that the term “additional change” corresponds to the surplus with respect to the initial behavior, which graphically corresponds to the difference between the actual values of the TSOPs and the dashed lines in figure 12.7.

transition to a stronger dynamic behavior which is in line with the experimental viscosity data (see figure 10.16).

In summary, the present order parameter analysis indicates that translational structural order increases when the system is cooled towards the glass transition. The additional increase of the TSOP during the LLT is in accordance with the results obtained by simulations on Jagla liquids that traverse the Widom line in the  $p - T$ -phase diagram. The relative magnitude of this increase is of the same order of the relative change in excess entropy associated with the thermal signature of the LLT, i.e. the  $c_p$ -peak found in the deeply undercooled liquid regime.

## 12.4 Length-scale dependence of translational structural ordering: SRO vs. MRO

In the above definition the translational structural order parameter  $t$  is defined globally. However, as shown in the following, it can be useful to define  $t$  locally.

$$t = \int_{r_1}^{r_2} |g(r) - 1| dr \quad (12.4)$$

The advantage of this definition is that the order parameter, by changing the integration limits, can be defined on specific length scales. The resulting order parameters now quantify the evolution of translational ordering on the length scale considered, and a comparison of order parameters defined at different length scales can reveal information on where the order is formed.

The structural order parameter for short-range ordering,  $t_{SRO}$ , is obtained by integrating the first two peaks of  $g(r)$ , corresponding to an upper integration limit of about 6.8 Å, while the medium-range translation structural order parameter  $t_{MRO}$  is calculated from 6.8 Å to 30 Å (cf. figure 12.8). This choice is based on the fact that pair correlations of individual atomic clusters, e.g. icosahedra, only contribute to the first two peaks of  $g(r)$ . The higher  $r$ -range is excluded due to scattering in the data. The results of this analysis are summarized in figure 12.9.

The relative contribution of the TSOPs defined locally with respect to  $t_{total}$  gives insights on the length scale where the order is formed. Both  $t_{SRO}$  and  $t_{MRO}$  increase with decreasing temperature and show an additional, unexpected increase in the temperature region of the LLT (cf. figure 12.9). However, the relative contribution of the two local parameters to the overall increase  $t_{total}$  changes upon cooling, as shown by the evolution of  $t_{MRO}/t_{total}$ . Evidently,  $t_{SRO}/t_{total} = 1 - t_{MRO}/t_{total}$ . At the liquidus, illustrated by the dashed line at 1170 K,  $t_{MRO}$  makes about 13 % of  $t_{total}$ , while about 87 % stem from short-range correlations. With decreasing temperature the relative contribution of translational medium-range ordering,  $t_{MRO}/t_{total}$ , continuously increases. Within the region of the LLT (shaded region) a marked increase in  $t_{MRO}/t_{total}$  can be noticed.

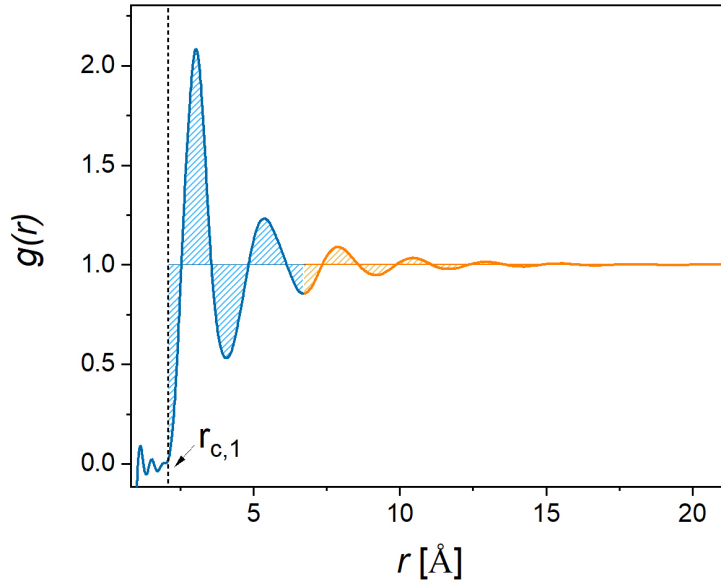


Figure 12.8: Definition of length-scale dependent translational structural order parameters. To evaluate the length-scale dependence of the formation of translational structural ordering, the definition of the TSOP is applied section-wise. The boundary is set at the second minimum of  $g(r)$  corresponding to the end of the second coordination shell. Integration from the lower limit  $r_{c,1}$  up to this boundary yields the short-range translational structural ordering parameter  $t_{SRO}$  (blue), while integration beyond yields the medium-range translational structural ordering parameter  $t_{MRO}$  (orange).



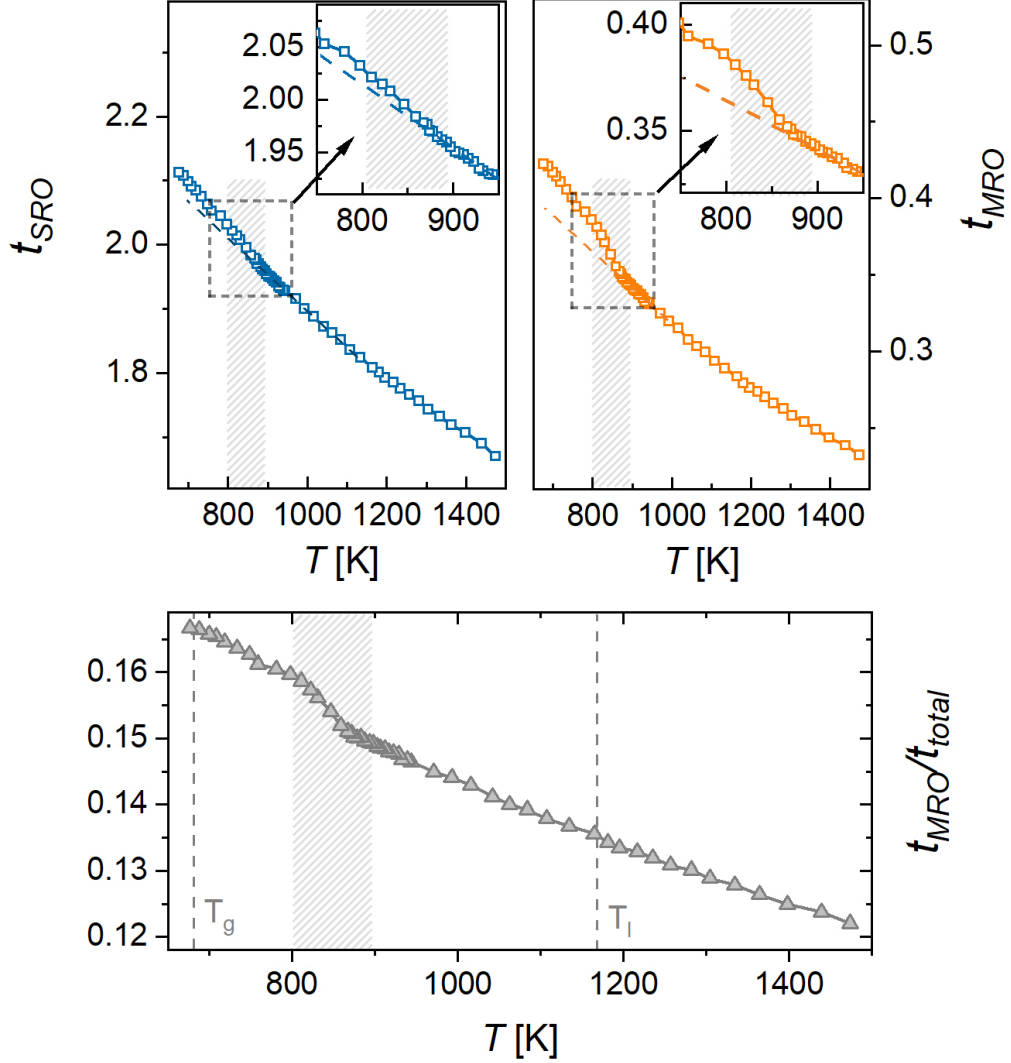


Figure 12.9: Contribution of short-range and medium-range or extended-range translational ordering to the overall translational ordering during cooling (lower panel). The upper panels show the evolution of the locally defined structural order parameters. The formation of translational order on length scale associated with short-range ordering is characterized by  $t_{SRO}$ , while  $t_{MRO}$  measures the formation of structural order on length scales associated with medium- and extended-range ordering. The dashed area is the temperature regime where evidences of a LLT are found.

Below the LLT,  $t_{MRO}/t_{total}$  further increases until the onset of glass transition during cooling is reached (dashed line at around 680 K).

Further analysis shows that within the LLT region the majority of the additional changes in  $t_{total}$  stem from atomic correlations exceeding the length scale associated to short-range ordering. Compared to their initial values at 900 K, the additional increase in  $t_{MRO}$  as a consequence of the LLT is significantly larger than for  $t_{SRO}$ . For  $t_{SRO}$  the additional increase between 800 K and 900 K is about 0.017 compared to an initial value of about 1.95, corresponding to a relative increase of less than 1 % only. On the other hand the additional increase of  $t_{MRO}$  is about 0.021 compared to an initial value of about 0.34, i.e. relative increase of about 6.2 %. The low additional increase in  $t_{SRO}$  implies that short-range translational ordering is only minor affected during the LLT, suggesting that local cluster structures chemically and topological remain almost unaffected. On the other hand the pronounced relative increase in  $t_{MRO}$  implies that the structural changes associated with the LLT mainly occur on length scales corresponding to medium- or extended-range ordering, in line with the increase in the correlation length obtained from the Ornstein-Zernike analysis performed in chapter 11. Together these findings might be taken as further evidence that the LLT structurally goes ahead with an extension of medium-range ordering by an aggregation of solute-centered atomic clusters.

Accepting that the TSOPs are appropriate measures of the translational structural ordering on the specific length scales, the current analysis implies that (I) translational structural ordering increases at all length scales (SRO and MRO) upon cooling as expected, (II) the major part, i.e. roughly 85 %, of the translational structural order parameter stem from atomic pair correlations on the length-scale associated to short-range ordering, while 15 % stem from atomic pair correlations associated to medium- or extended range ordering, (III) during cooling the contribution of medium- or extended-range ordering to the overall translational order increases, (IV) during the LLT a preferential increase of medium-range translational structural ordering occurs.

## 12.5 Implications to the dynamics

The evolution of the heat capacity and the increase of the translational order parameter  $t$  observed in the experimental data of the *Vit106a* alloy are qualitatively similar to numerical results obtained by Xu et al. from simulations of liquids modeled with the Jagla ramp potential [112] (cf. figure 12.5). When the Jagla liquid passes its Widom line, a liquid-liquid transition occurs, manifesting as a smeared peak in  $c_p$ , with noticeable changes in the structure characterized by the changes in two order parameters  $t$  and  $Q_6$ . The simulation of Xu et al. further show that the transition from the less ordered, low density structure of the high temperature liquid (LDL) to the more ordered, high density structure of

the low temperature liquid (HDL) has direct implications on the dynamics. As shown in figure 12.4 the increase in the translational structural order parameters goes along with a marked change in the dynamic behavior. If the HDL is heated at  $P < P_c$  towards the coexistence line (path  $\gamma$ ) an Arrhenius-like temperature dependence of the diffusion is obtained, indicating a strong dynamic behavior. In contrast, if the LDL at  $P > P_c$  is cooled towards the coexistence line (path  $\beta$ ), the diffusivity data indicate a more fragile behavior, characterized by a pronounced temperature-dependence of the activation energy for diffusion at lower temperatures in accordance with a VFT behavior. If the LDL is cooled at  $P > P_c$  (path  $\alpha$ ), the diffusivity data first follows the LDL data until it deviates from its initial trend and approaches the HDL data. Accordingly, the diffusivity data indicate a dynamic crossover behavior when the liquid passes its Widom line. Applying these findings to the present case, the observed additional increase in the translational structural order parameter  $t_{total}$  of the *Vit106a* bulk metallic glass forming alloy in the temperature region of the anticipated LLT, implies a fragile-to-strong transition in agreement with the experimental data (cf. figure 10.16). Moreover, the observed course of  $t_{total}$  is reminiscent to a Jagla-liquid that traverses its Widom-line, suggesting that the LLT in *Vit106a* is a smeared order-disorder transition above its liquid-liquid-critical point.

## 12.6 Correlations between translational order parameters and the correlation length

The curves shown in figure 12.7 and figure 12.9 are reminiscent of the evolution of the correlation length extracted from the Ornstein Zernike analysis of the long-range decay behavior of  $g(r)$ , which in turn is found to scale with the temperature-induced changes on the inverse of the FWHM,  $\gamma^{-1}$  (cf. chapter 11). A corresponding correlation analysis shows that all translational structural order parameters, correlate well with the correlation length  $\xi$ , and hence with  $\gamma^{-1}$ . Plotting the TSOPs against  $\xi$  yields almost ideal linear correlations with  $R^2 > 0.997$  over the entire temperature range including the LLT as shown in figure 12.10. The observation that  $t_{MRO}$  correlates with  $\xi$  and  $\gamma^{-1}$  is reasonable, considering that  $\xi$  and  $\gamma^{-1}$  are quantities describing the decay of long range oscillations in  $g(r)$ . However, the almost perfect linear correlations found for  $t_{total}$  or  $t_{SRO}$  may rather be surprising, as both quantities strongly depend on short-ranged atomic pair correlations, that are actually excluded from the Ornstein-Zernike analysis.

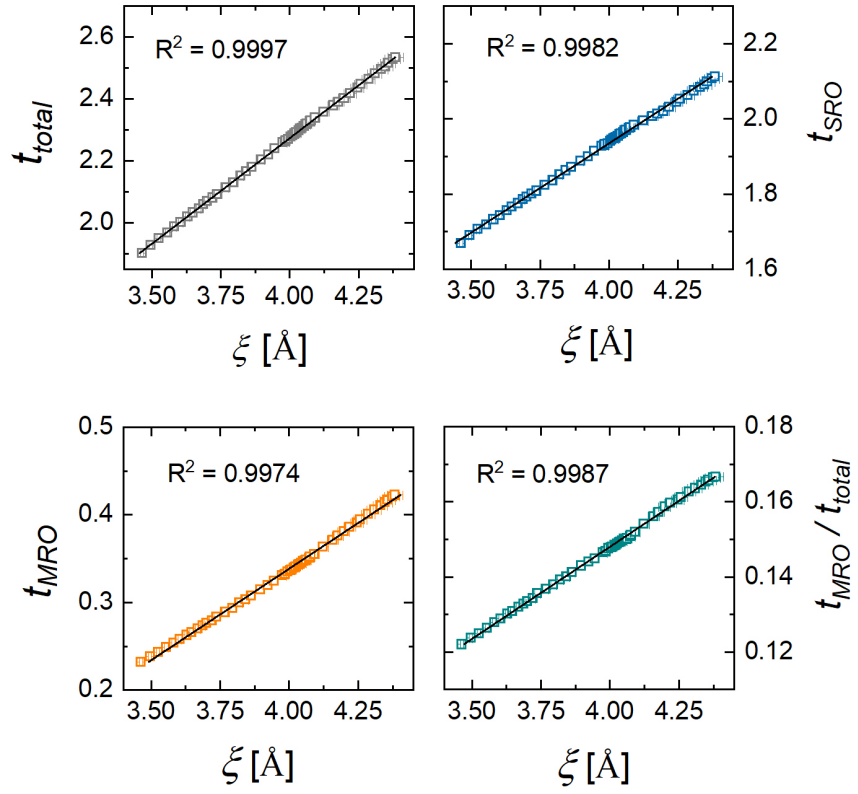


Figure 12.10: Correlation between translational structural order parameters,  $t_{total}$ ,  $t_{SRO}$ , and  $t_{MRO}$  and the correlation length  $\xi$  extracted from the Ornstein Zernike analysis.

## 12.7 TSOP analysis of BMG formers around the glass transition

The analysis of translational structural ordering presented above is now applied to the structural real space data of the *Pt42* and *Vit106a* bulk metallic glass formers in their glassy state and during the glass transition. The corresponding results are shown in figure 12.11 and figure 12.12. As expected from the strong correlations between the TSOPs and the decay exponent  $\xi$  (shown in figure 12.10), the TSOPs derived from the real-space data mirror the course of  $\xi$ , which in turn shows a strong correlation to the FWHM derived directly from the reciprocal space data  $S(Q)$  (cf. figure 11.15). In the glassy state  $t_{total}$ ,  $t_{SRO}$ , and  $t_{MRO}$  show a less pronounced negative decrease than in the supercooled liquid state, in line with the conception that the supercooled liquid is characterized by a more pronounced increase in structural disorder on all length scales. Like  $\xi$  the TSOPs show a maximum around the glass transition, reminding on a  $\lambda$ -peak, which stems from the fact that a re-increase of the TSOPs occurs at roughly  $0.9T_g$ . This re-increase is rather surprising as it implies that translational structural ordering increases(!) when the system is heated through its glass transition, while actually one might expect that the TSOPs gradually bend downwards and change in slopes when the structure relaxes towards its metastable liquid states. A  $\lambda$ -transition-like behavior could be expected for a real thermodynamic continuous order-disorder transition, however, in the present case the (laboratory) glass transition is actually a purely kinetic phenomenon arising from the crossing of the structural relaxation time and the time scale of observation. One might also tend to relate the re-increase in  $\xi$  and the TSOPs to structural relaxation or recovery effects that lead to an increase in (translational) structural order in the glass when the systems move towards its metastable equilibrium states. However, a comparison with the DSC traces in figure 12.11 and figure 12.12 obtained from samples with the same thermal history does not corroborate this idea. First, structural relaxation as indicated by an exothermic heat release prior to the glass transition usually starts at temperatures much lower than  $0.9T_g$ , where the TSOPs are still decreasing. This can be seen in particular for the *Vit106a* glass former (cf. figure 12.12), where an exothermic heat release in the DSC trace, i.e. a negative deviation from the “0-line” starts at around 200 °C, while the re-increase of the TSOPs occurs much later at around 350 °C. Second, recovery effects, normally manifesting as pronounced overshoots in the DSC signal during the glass transition, are only small (*Pt42*) or absent (*Vit106a*). Furthermore, recovery effects are limited to the beginning of the supercooled liquid region only, while at higher temperatures in the supercooled liquid, the system is able to reach its equilibrium states due to the rapid decrease of the structural relaxation time with increasing temperature. If the observed re-increase in the TSOPs indeed would correspond to recovery effects, one might expect that at higher temperatures in the supercooled liquid

region, where the system is in equilibrium, the value of the TSOPs should be lower than in the glass. While this seems to be the case for the *Pt42* alloy, that shows indications of a recovery in its DSC trace on the beginning of the supercooled liquid, in the *Vit106a*, where no indications for recovery are seen in the DSC traces, this is apparently not the case. Here the TSOPs (as well as  $\xi$ ) exhibit values larger than in the glass, which opposes the conception that the equilibrated supercooled liquid should be characterized by a more pronounced (translational) structural disorder. Based on this, structural relaxation below  $T_g$  or recovery effects during the glass transition can hardly be made responsible for the observed re-increase in the TSOPs (or  $\xi$ ). The origin of the observed course of the TSOPs and  $\xi$ , reminiscent of a  $\lambda$ -transition, remains to be explored.

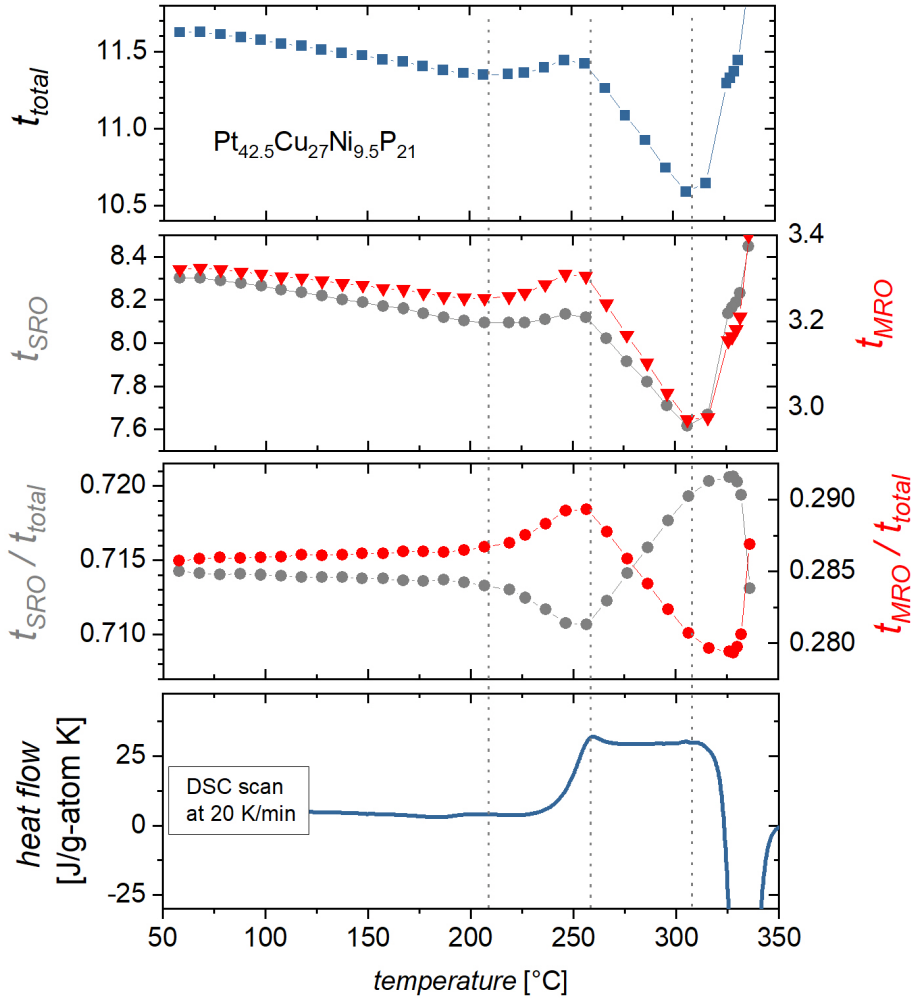


Figure 12.11: Translational structural order parameter analysis in the *Pt42* bulk metallic glass forming alloy during the glass transition.

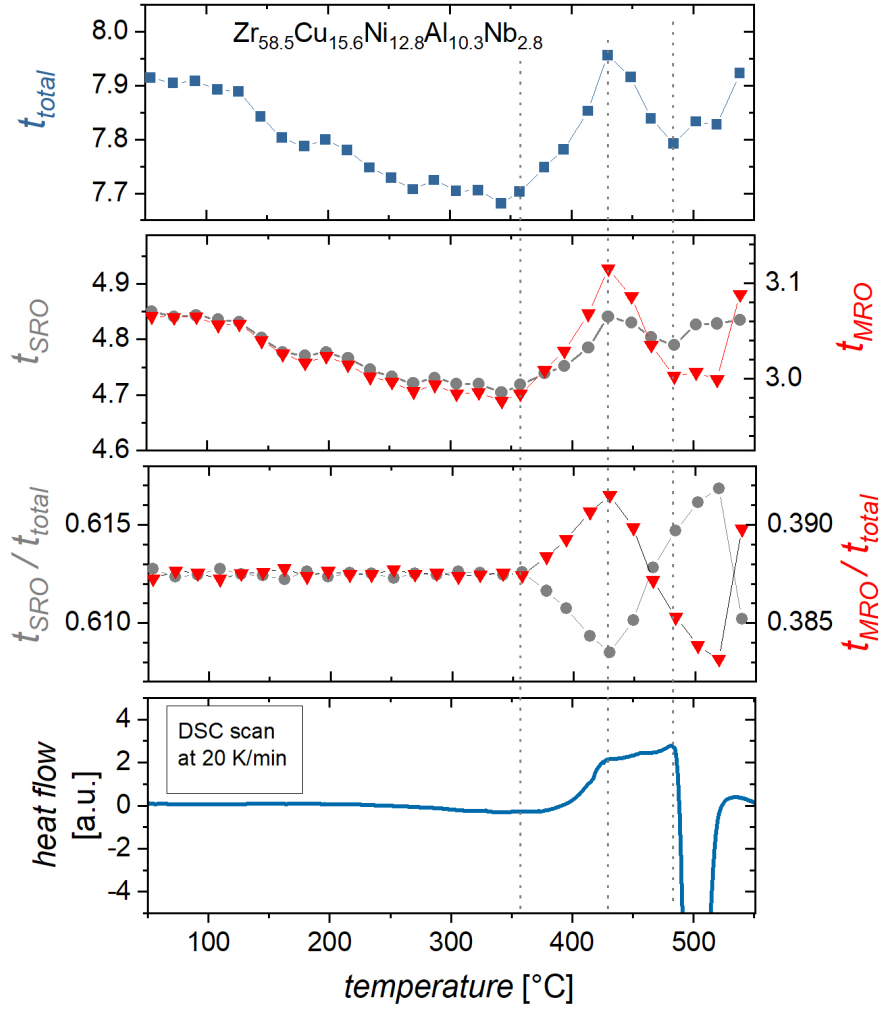


Figure 12.12: Translational structural order parameter analysis in the *Vit106a* bulk metallic glass forming alloy during the glass transition.

Another interesting observation is made by the present TSOP analysis, when looking at the relative contributions of  $t_{SRO}$ , characterising the increase in translational structural order on the length scale of short-range order, and  $t_{MRO}$ , characterising the increase in translational structural order on length scales corresponding to medium- or extended-range translational structural ordering, to the overall increase in translational structural ordering  $t_{total}$ . At lower temperatures in the glass,  $t_{SRO}/t_{total}$  and  $t_{MRO}/t_{total}$  remain essentially constant for both alloys. However, in the temperature range where the re-increase the TSOPs and  $\xi$  is observed,  $t_{MRO}/t_{total}$  increases at the expense of  $t_{SRO}/t_{total}$ . Once the end of the glass transition is reached and the system has restored its equilibrium this trend inverses. Note that the latter is in accordance with the behavior observed in figure 12.9. This implies that the re-increase in the TSOPs and  $\xi$  is accom-

panied by a preferential increase in atomic pair correlations on the length scale corresponding to medium- or extended range ordering, when the structure starts to unfreeze. Once the system is unfrozen, the formation of disorder preferentially occurs on the length-scales corresponding to medium- or extended range order, explaining why  $t_{MRO}/t_{total}$  increases at the expense of  $t_{SRO}/t_{total}$ . The latter might be taken as indication that the formation of structural disorder in the deeply undercooled liquid state arises from a destruction of atomic cluster aggregates or network structures, while short range ordering, appears to be less affected. This is further corroborated by the observation that the relative change in the slopes of  $t_{MRO}$  between the supercooled liquid region and the glass is much more pronounced than for  $t_{SRO}$  which shows a much less pronounced change in its temperature dependence between the supercooled liquid and glass. In particular in the kinetically stronger alloy (*Vit106a*) the temperature dependence of  $t_{SRO}$  in the supercooled liquid appears to be similar to the glassy state, suggesting that short-range ordering is not markedly “destroyed” in the deeply undercooled liquid. In case of the kinetically more fragile liquid, a stronger temperature dependence of  $SRO$  in the deeply undercooled liquid compared to the glass is observed, implying that the formation of disorder also affects short-range ordering to a larger degree. Still, as mentioned above, the destruction of translational structural order in the equilibrium liquid seems to preferentially occur on the length scales beyond short-range ordering, as indicated by the increase of  $t_{MRO}/t_{total}$  at the expense of  $t_{SRO}/t_{total}$ .

## 12.8 Summary

In summary, the present order parameter study indicates that translational structural order increases at all length scales when the system is cooled towards the glass transition. Defining length-scale dependent translational structural order parameters, it is found that the relative contribution of medium- and extended-range pair correlations to the overall translational structural order increases continuously with decreasing temperature. Moreover, an additional increase of translational structural ordering is observed in the temperature range of the anticipated LLT. This increase mainly stems from pair correlations on the length scale associated to medium- and extended-range ordering, while atomic correlations corresponding to short-range ordering only exhibit a minor additional increase. All together, the observations made in the present chapter in addition to the findings obtained in the previous chapters, i.e. the course of the heat capacity shown in figure 10.8, the increase in the correlation length  $\xi$  shown in figure 11.16, as well as the dynamic behavior illustrated in 10.16, are in agreement with the simulations of Xu et al. performed on liquids modeled with a two-ramp Jagla potential above their liquid-liquid critical point in the phase diagram [112]. This supports the conception that the LLT in the *Vit106* bulk metallic glass forming



alloy is a continuous, smeared order-disorder transition in which a kinetically stronger liquid is formed from a more fragile liquid when the system is cooled over its Widom line.

## Chapter 13

# Summarizing Remarks and Outlook

The present study on the thermal expansion behavior of bulk metallic glass forming alloys indicates that the Ehrenfest relation, assuming  $v_m \propto Q_1^{-3}$ , with  $v_m$  being the atomic volume and  $Q_1$  being the position of the principal diffraction peak, holds for the glassy state but breaks down in the liquid state. In the glasses the thermal expansion coefficients derived from x-ray diffraction data assuming a validity of the Ehrenfest relation are in agreement with those derived from volume measurements, which in turn are found to be mirrored by the thermal-induced shift of peak positions of the (reduced) pair distribution function  $G(r)$  beyond the 3<sup>rd</sup> coordination shell. In the liquid state the situation is more complex, and a much less pronounced correlation between the shift of the principal diffraction peak (PDP) and the volumetric expansion is observed. Although a modification of the Ehrenfest relation by an adaption of the exponent  $\xi$ , linking  $v_m$  and  $Q_1$  via  $v_m \propto Q_1^{-\xi}$ , to a value of 2.31 seems to improve the correlation, a clear functional relation between the thermal-induced shift of  $Q_1$  and macroscopic volume changes is not apparent from the present analysis.

Irrespective of that, the current structural reciprocal space analysis of the bulk metallic glass formers reveals a correlation between the thermal-induced shift of the principal peak position and fragility. While no correlation exists in the glassy state, the shift of the PDP in the supercooled liquid close to the glass transition is found to correlate with the fragility steepness index  $m$ . An improved correlation is found if the difference between the the liquid and glass is considered. Taking into account that, irrespective of the exact functional dependence, there is a trend of increasing thermal dilatation with a more pronounced shift in the liquid state, and that the thermal expansion in the glass obeys the Ehrenfest relation, the present findings are in line with the conception that a larger difference in the thermal expansion between the liquid and the glassy state results in a more pronounced increase in free volume upon heating and thus correlates with a higher fragility in agreement with the free volume model of the viscous slowdown. Nonetheless,

it would be interesting to determine the volume expansion of the liquid phase of the alloys near their glass transitions by dilatometric methods.<sup>1</sup>

The present structural analysis of real-space data shows that with the transition to the (undercooled) liquid state the thermal dilatation between the different coordination shells, as derived from the shift of peak positions in  $g(r)$ , diverges, suggesting a length-scale dependent dilatation of the liquid structure. The fragility is found to correlate with thermal-induced structural changes on distinct length scales. More fragile liquids are found to exhibit less pronounced negative shifts in their first coordination shell, along with pronounced thermal shifts at length scales of  $\approx 1$  nm. The former observation is in accordance with the conception that softer repulsion goes along with a stronger (less fragile) dynamic behavior [149, 150], an observation also made for colloid glasses [150]. Moreover, a strong empirical correlation between the local dilatation on the length scale in between 0.7 to 1 Å and the fragility of numerous bulk metallic glass forming alloys is found. According to this correlation, more fragile liquids are characterized by a pronounced dilation on this length scale, while stronger metallic glass forming liquids display almost no dilatation on this length scale. Applied to the structural changes during a liquid-liquid transition (LLT) in the deeply undercooled melt of the *Vit106a* BMG forming alloy, the correlation predicts a dynamic crossover in agreement with experimental viscosity data.

The existence of the LLT in the *Vit106a* bulk metallic glass forming alloy is anticipated from the occurrence of several anomalies including thermodynamic as well as structural data. An additional exothermic heat release, corresponding to peak in the specific heat capacity over emissivity is found in the deeply undercooled liquid between 800 K and 900 K, coinciding with unexpected shifts in the principal diffraction peak, its full-width at half maximum, as well as several irregularities in the reduced pair distribution function. The change in entropy associated with the transition from the less-ordered high temperature phase to the more ordered low temperature phase is estimated to be about 7% of the entropy of fusion in accordance with earlier studies performed on a similar bulk glass forming liquid [152]. Considering the similarity of the observation made for the two systems, it appears that order-driven LLTs are not a peculiarity but rather a common feature of dense-packed bulk metallic glass forming liquids that show a tendency towards chemical and topological ordering during undercooling. Additional experiments on other alloys could strengthen this idea. With the transition to alloy systems whose glass forming ability is less prone to contamination

---

<sup>1</sup>The author has attempted to measure the thermal expansion in the supercooled liquid region of the alloy near the glass transition using classical dilatometry. However, the data acquired by this approach appear to be not reliable. In particular for the fragile glass formers the influence due to structural softening, leading to an underestimation of the thermal expansion coefficients, cannot be excluded and is detrimental for the derivation of the real thermal expansion in the supercooled liquid region. Consequently only the volume data obtained from electrostatic levitation studies are reported.

from atmospheres, aerodynamic levitation techniques could be used, providing much higher cooling rates and enabling to investigate glass formers with higher critical cooling rates.

The fact that no marked changes in the specific volume or the thermal expansion coefficients are observed during the LLT in *Vit106a* and *Vit1* implies that the transition is driven rather by chemical than by topological ordering towards higher density states. The latter is conceivable by recognizing that (I) strong bulk metallic glass former such as *Vit106a* and *Vit1* exhibit high packing densities already in the equilibrium liquid, which also explains their high melt viscosities and high glass forming ability, and (II) the non-directional bonding character of metals energetically does not favor considerably less-dense packed atomic configurations, in contrast to system with more directional bonding (e.g. water or silicon). The observation that the two alloys exhibit a unusual shift in the position of the PDP although no marked change in the molar volume  $v_m$  is observed further corroborates that a clear functional dependence between  $Q_1$  and  $v_m$  in the liquid state is missing. Accordingly, care must be taken when relating changes in  $Q_1$  to changes in the macroscopic density of multi-component system.

The current analysis of the structural changes on the length scale associated to short-range ordering shows that the observed evolution of the second-to-first peak position ratio  $r_2/r_1$  in the high-temperature liquid of *Vit106a* above the LLT is basically in accordance with an increasing concentration of energetically-favored icosahedra-like solute-centered  $Zr$ -clusters, as predicted from structural models [57]. In the temperature regime of the LLT, the  $r_2/r_1$  data deviate from their initial trend and slightly bend downwards. This predominantly stems from a more negative shift of  $r_1$  in the low temperature liquid, as indicative for a more pronounced atomic redistribution towards the repulsive part of the interatomic potential.

The present study further shows that the Ornstein-Zernike approach yields an adequate description of the long-range decay of density fluctuations in multicomponent bulk metallic glass forming liquids. This holds irrespective of whether the classical Ornstein-Zernike approach or a cluster-adapted fractal approach is used. It is found that the description of structural data, i.e. the quality of the fits, is better for the liquid phase and improves further with increasing temperatures. At lower temperatures closer to the glass transition or below, the fits progressively struggle to mirror the shape of the peaks corresponding to the lower coordination shells. The latter might be related to the formation of specific structural ordering schemes on the length scale of medium-range order, whose peculiarities are no longer captured by the Ornstein-Zernike description, similar to the situation of short-range ordering. In this context it would be interesting to investigate if a temperature dependent change in the dimensionality  $D_f$  during undercooling may improve the fitting. The latter could be taken as indication of the possible formation of a fractal cluster structure at lower temperatures and in the glassy state. However, it turns out that the extraction  $D_f$  from direct fitting of the

experimental  $g(r)$  data is difficult due to mutual dependencies among the fit parameters. To extract  $D_f$  from the fits, the number of fit parameters needs to be reduced. Possible steps towards this directions can be deduced from the current findings.

According to the present Ornstein Zernike analysis (OZA) the correlation length of the *Vit106a* liquid continuously increases during cooling from above its liquidus down into the glassy state in agreement with a continuously increasing structural coherence. In the region of the LLT an additional increase in the correlation length is observed. Given that the viscosity of a liquid increases with an increasing correlation length, this suggests a transition towards a stronger dynamic liquid phase in agreement with the experimental viscosity data, as well as the evolution of the dynamics predicted from the structural data based on the local dilatation on a length scale of 0.7 nm and 1 nm. If properly adapted, the OZA can be performed on  $G(r)$  instead of  $g(r)$ , provided that the fit parameter serving as the amplitude is left as free parameters, and provided that its temperature dependence scales appropriately with the temperature dependence of the number density. The latter is of particular importance if one is interested in comparing different alloys, as otherwise their different thermal expansion may affect the value and temperature dependence of the extracted correlation length. In general, the correlation length determined from the OZA shows a strong linear correlation with the full width at half maximum (FWHM) of  $S(Q)$ . This holds for the glassy as well as the liquid state, although a stronger correlation is found for the liquid state. Extending the OZA to lower temperatures, it is found that the correlation length starts to deviate from its initial negative trend in the glass and turns into a positive trend before the onset of the calorimetric glass transition is reached, resulting in a peak-like maximum of the correlation length at the end of the glass transition. The origin of the re-increase of the correlation length during heating towards the glass transition, and the maximum observed at the end of the glass transition remains open.

A translational structural order parameter (TSOP) analysis of the LLT in *Vit106a* qualitatively replicates previous findings obtained from simulations on Jagla liquids [112]. Like the Jagla liquid the *TSOP* derived from experimental structural data shows a step-like increase during the LLT, indicating an increase in translational structural order. Whether this goes ahead with an increase in the bond-orientational order parameter (BOOP) cannot be answered, as the latter is not directly accessible from diffraction studies. Simulations could help to prove a possible change in the BOOP during cooling and reveal the nature of the lower-energetic structural motifs that are formed during undercooling, providing deeper insights on the nature of the LLT. For Jagla liquids the changes in the order parameters are accompanied by a dynamic transition from a low-density, more fragile, high-temperature liquid phase towards a high-density, stronger, low-temperature liquid phase. Applied to the present analysis of the *Vit106a* bulk metallic glass forming alloy the observed course of the TSOP is thus in agree-

ment with a dynamic crossover from a more fragile towards a stronger liquid phase during cooling, in accordance with viscosity measurements that indicate a discrepancy of the high and low temperature fragilities.

By adapting the definition of the TSOP, the formation of translational order at different length scales can be studied. The current analysis performed for the structural data of the *Vit106a* alloy show that (I) translational structural order continuously increases with decreasing temperature on all length scales, (II) the LLT is accompanied by an additional increase in translational order, (III) the density fluctuations on the length scale of short-range ordering ( $1^{st}$  and  $2^{nd}$  peak) contribute to about 85 % to the overall translational structural ordering, while only about 15 % stem from density fluctuation on the length scales associated to medium- or extended-range ordering ( $3^{rd}$  peak and beyond), (IV) the relative contribution of density fluctuations beyond the length scale of short-range ordering increases with decreasing temperature, and (V) all translational order parameters correlate well with the correlation length extracted from the OZA, which in turn is found to correlate well with the full width at half maximum (FWHM) of  $S(Q)$ . It would be interesting to see how the present analysis applies to other bulk metallic glass forming liquids. Considering that more fragile liquids are characterized by a more pronounced decrease of configurational entropy upon heating, it may be anticipated that they show a more pronounced decrease of translational structural. In particular, it might be asked whether the different fragilities observed among different alloys are related to the formation of translational structural order on specific length scales. For example, it would be interesting to test whether the formation of the total translational structural ordering is correlated with the temperature-sensitivity of the dynamics, i.e. fragility. Similarly, it could be tested whether the ratio between the formation of short-ranged translational ordering or medium- or extended-range structural ordering is related to the fragility. These studies could help to reveal further insights on the structural origin of the different fragilities that are observed among bulk metallic glass forming liquids near their glass transitions.

# Bibliography

- [1] “[www.mindat.org](http://www.mindat.org) (date accessed: 2017-02-22).”
- [2] D. Turnbull and J. C. Fisher, “Rate of Nucleation in Condensed Systems,” *The Journal of Chemical Physics*, vol. 17, pp. 71–73, jan 1949.
- [3] D. Turnbull, “Correlation of Liquid-Solid Interfacial Energies Calculated from Supercooling of Small Droplets,” *The Journal of Chemical Physics*, vol. 18, pp. 769–769, may 1950.
- [4] D. Turnbull, “Kinetics of Solidification of Supercooled Liquid Mercury Droplets,” *The Journal of Chemical Physics*, vol. 20, pp. 411–424, mar 1952.
- [5] D. Turnbull, “Under what conditions can a glass be formed?,” *Contemporary Physics*, vol. 10, pp. 473–488, sep 1969.
- [6] P. Klement, W. ; Willens, R.H., Duwez, “Non-Crystalline Structure in Solidified Gold-Silicon Alloys,” *Nature*, vol. 187, pp. 869–870, 1960.
- [7] M. Telford, “The case for bulk metallic glasses,” *materialstoday*, pp. 36–43.
- [8] Y. Q. Cheng, E. Ma, and H. W. Sheng, “Alloying strongly influences the structure, dynamics, and glass forming ability of metallic supercooled liquids,” *Applied Physics Letters*, vol. 93, no. 11, pp. 12–15, 2008.
- [9] Y. Q. Cheng and E. Ma, “Atomic-level structure and structure-property relationship in metallic glasses,” *Progress in Materials Science*, vol. 56, no. 4, pp. 379–473, 2011.
- [10] S. Pauly, L. Löber, R. Petters, M. Stoica, S. Scudino, U. Kühn, and J. Eckert, “Processing metallic glasses by selective laser melting,” *Materials Today*, vol. 16, no. 1-2, pp. 37–41, 2013.
- [11] X. P. Li, M. P. Roberts, S. O’Keeffe, and T. B. Sercombe, “Selective laser melting of Zr-based bulk metallic glasses: Processing, microstructure and mechanical properties,” *Materials and Design*, vol. 112, no. September, pp. 217–226, 2016.

- [12] Y. Shen, Y. Li, C. Chen, and H. L. Tsai, "3D printing of large, complex metallic glass structures," *Materials and Design*, vol. 117, pp. 213–222.
- [13] E. Williams and N. Lavery, "Laser processing of bulk metallic glass: A review," *Journal of Materials Processing Technology*, vol. 247, pp. 73–91, sep 2017.
- [14] P. Bordeenithikasem, M. Stolpe, A. Elsen, and D. C. Hofmann, "Glass forming ability, flexural strength, and wear properties of additively manufactured Zr-based bulk metallic glasses produced through laser powder bed fusion," *Additive Manufacturing*, vol. 21, pp. 312–317.
- [15] P. Bordeenithikasem, Y. Shen, H. L. Tsai, and D. C. Hofmann, "Enhanced mechanical properties of additively manufactured bulk metallic glasses produced through laser foil printing from continuous sheetmetal feedstock," *Additive Manufacturing*, vol. 19, pp. 95–103, 2018.
- [16] J. Schroers, "The superplastic forming of bulk metallic glasses," *Jom*, vol. 57, pp. 35–39, 2005.
- [17] C. A. Schuh, T. C. Hufnagel, and U. Ramamurty, "Mechanical behavior of amorphous alloys," *Acta Materialia*, vol. 55, no. 12, pp. 4067–4109, 2007.
- [18] F. Spaepen, "A microscopic mechanism for steady state inhomogeneous flow in metallic glasses," *Acta Metallurgica*, vol. 25, pp. 407–415, 1977.
- [19] A. Argon, "Plastic deformation in metallic glasses," *Acta Metallurgica*, vol. 27, pp. 47–58, jan 1979.
- [20] M. Stolpe, J. Kruzic, and R. Busch, "Evolution of shear bands, free volume and hardness during cold rolling of a Zr-based bulk metallic glass," *Acta Materialia*, vol. 64, pp. 231–240, 2014.
- [21] M. H. Turnbull, D. ; Cohen, "Free Volume Model of the Amorphous Phase: Glass Transition," *The Journal of Chemical Physics*, vol. 34, no. 1, pp. 120–125, 1961.
- [22] D. Klaumuenzer, A. Lazarev, R. Maaß, F. H. Dalla Torre, A. Vinogradov, and J. F. Loeffler, "Probing shear-band initiation in metallic glasses," *Physical Review Letters*, vol. 107, no. 18, pp. 1–5, 2011.
- [23] J. Bokeloh, S. V. Divinski, G. Reglitz, and G. Wilde, "Tracer measurements of atomic diffusion inside shear bands of a bulk metallic glass," *Physical Review Letters*, vol. 107, no. 23, pp. 1–5, 2011.



- [24] H. Roesner, M. Peterlechner, C. Kuebel, V. Schmidt, and G. Wilde, “Density changes in shear bands of a metallic glass determined by correlative analytical transmission electron microscopy,” *Ultramicroscopy*, vol. 142, pp. 1–9, jul 2014.
- [25] B. Yang, M. L. Morrison, P. K. Liaw, R. A. Buchanan, G. Wang, C. T. Liu, and M. Denda, “Dynamic evolution of nanoscale shear bands in a bulk-metallic glass,” *Applied Physics Letters*, vol. 86, no. 14, pp. 1–3, 2005.
- [26] D. Klaumuenzer, R. Maaß, and J. F. Loeffler, “Stick-slip dynamics and recent insight into shear banding in metallic glasses,” *Journal of Materials Research*, vol. 26, no. 12, pp. 1453–1463, 2011.
- [27] F. Spaepen, “Must shear bands be hot ?,” *Nature Materials*, vol. 5, no. January, pp. 7–8, 2006.
- [28] D. C. Hofmann, J.-Y. Suh, A. Wiest, G. Duan, M.-L. Lind, M. D. Demetriou, and W. L. Johnson, “Designing metallic glass matrix composites with high toughness and tensile ductility,” *Nature*, vol. 451, pp. 1085–1089, 2008.
- [29] J. Schroers, T. M. Hodges, G. Kumar, H. Raman, A. J. Barnes, Q. Pham, and T. A. Waniuk, “Thermoplastic blow molding of metals,” *Materials Today*, vol. 14, no. 1-2, pp. 14–19, 2011.
- [30] H. M. Chiu, G. Kumar, J. Blawdziewicz, and J. Schroers, “Thermoplastic extrusion of bulk metallic glass,” *Scripta Materialia*, vol. 61, no. 1, pp. 28–31, 2009.
- [31] G. Kumar, P. A. Staffier, J. Blawdziewicz, U. D. Schwarz, and J. Schroers, “Atomically smooth surfaces through thermoplastic forming of metallic glass,” *Applied Physics Letters*, vol. 97, no. 10, pp. 95–98, 2010.
- [32] G. Kumar, H. X. Tang, and J. Schroers, “Nanomoulding with amorphous metals,” *Nature*, vol. 457, no. 7231, pp. 868–872, 2009.
- [33] J. Heinrich, R. Busch, and B. Nonnenmacher, “Processing of a bulk metallic glass forming alloy based on industrial grade Zr,” *Intermetallics*, vol. 25, pp. 1–4, jun 2012.
- [34] R. P. Sear, “Nucleation: theory and applications to protein solutions and colloidal suspensions,” *Journal of Physics: Condensed Matter*, vol. 19, no. 3, p. 33101, 2007.
- [35] D. Xu and W. L. Johnson, “Crystallization kinetics and glass-forming ability of bulk metallic glasses Pd<sub>40</sub> Cu<sub>30</sub> Ni<sub>10</sub> P<sub>20</sub> and Zr<sub>41.2</sub> Ti<sub>13.8</sub> Cu<sub>12.5</sub>

- Ni<sub>10</sub> Be<sub>22.5</sub> from classical theory,” *Physical Review B - Condensed Matter and Materials Physics*, vol. 74, no. 2, pp. 10–14, 2006.
- [36] M. Fanfoni, M. ; Tomellini, “The Johnson-Mehl-Avrami-Kolmogorov model: A brief review,” *Il nuovo cimento*, vol. 20, no. 7-8, pp. 1171–182, 1998.
  - [37] W. Kauzmann, “The Nature of the Glassy State and the Behavior of Liquids at Low Temperatures,” *Chemical Reviews*, vol. 43, no. 2, 1948.
  - [38] P. G. Debenedetti and F. H. Stillinger, “Supercooled liquids and the glass transition,” *Nature*, vol. 410, no. 6825, pp. 259–267, 2001.
  - [39] H. Tanaka, “General view of a liquid-liquid phase transition,” *Physical Review E - Statistical Physics, Plasmas, Fluids, and Related Interdisciplinary Topics*, vol. 62, no. 5, pp. 6968–6976, 2000.
  - [40] H. Tanaka, “Origin of the excess wing and slow beta relaxation of glass formers: A unified picture of local orientational fluctuations,” *Physical Review E*, vol. 69, p. 021502, feb 2004.
  - [41] M. D. Ediger, “Spatially Heterogeneous Dynamics in Supercooled Liquids,” *Annu. Rev. Phys. Chem.*, vol. 51, pp. 99–128, 2000.
  - [42] T. Kawasaki, T. Araki, and H. Tanaka, “Correlation between dynamic heterogeneity and medium-range order in two-dimensional glass-forming liquids,” *Physical Review Letters*, vol. 99, no. 21, pp. 2–5, 2007.
  - [43] J. D. Bernal, “Geometry of the structure of monatomic liquids,” *Nature*, vol. 185, no. 4706, pp. 68–70, 1960.
  - [44] J. D. Bernal, “Bakerian lecture 1962,” *Proceedings of the Royal Society London Series A - Math Phys Sci*, vol. 280, no. 138, p. 299, 1964.
  - [45] G. D. Scott, “Packing of equal spheres,” *Nature*, vol. 188, no. 4754, pp. 908–909, 1960.
  - [46] J. L. Finney, “Random packing and structure of simple liquids 1. Geometry of random close packing,” *Proceedings of the Royal Society London Series A - Math Phys Sci*, vol. 319, no. 1539, p. 479, 1970.
  - [47] J. L. Finney, “Random packings and structure of simple liquids 2. Molecular geometry of simple liquids,” *Proceedings of the Royal Society London Series A - Math Phys Sci*, vol. 319, no. 1539, p. 495, 1970.
  - [48] D. R. Nelson, “Order, frustration, and defects in liquids and glasses,” *Physical Review B*, vol. 28, no. 10, pp. 5515–35, 1983.

- [49] F. C. Frank, “Supercooling of liquids,” *Proceedings of the Royal Society London Series A - Math Phys Sci*, vol. 215, no. 1120, pp. 43–46, 1952.
- [50] H. Tanaka, “Relationship among glass-forming ability, fragility, and short-range bond ordering of liquids,” *Journal of Non-Crystalline Solids*, vol. 351, no. 8-9, pp. 678–690, 2005.
- [51] T. Schenk, D. Holland-Moritz, V. Simonet, R. Bellissent, and D. M. Herlach, “Icosahedral short-range order in deeply undercooled metallic melts,” *Physical Review Letters*, vol. 89, no. 7, p. 075507, 2002.
- [52] S. Klein, D. Holland-Moritz, D. M. Herlach, N. A. Mauro, and K. F. Kelton, “Short-range order of undercooled melts of PdZr<sub>2</sub> intermetallic compound studied by X-ray and neutron scattering experiments,” *Europhysics Letters*, vol. 102, p. 36001, 2013.
- [53] N. Mattern, P. Jovari, I. Kaban, S. Gruner, A. Elsner, V. Kokotin, H. Franz, B. Beuneu, and J. Eckert, “Short-range order of Cu-Zr metallic glasses,” *Journal of Alloys and Compounds*, vol. 485, no. 1-2, pp. 163–169, 2009.
- [54] S. Holland-Moritz, D. ; Schenk, T. ; Simonet, V.; Bellissent, R. ; Funkoshi, K. ; Merino, J. M. ; Buslaps, T. ; Reutzel, “Short-range order in undercooled Co melts,” *Journal of Non-Crystalline Solids*, vol. 312, pp. 47–51, 2002.
- [55] D. S. Lee, G. W. ; Gangopadhyay, A. K. ; Kelton, K. F. ; Hyers, R. W. ; Rathz, T. J. ; Rogers, J. R. ; Robinson, “Difference in Icosahedral Short-Range Order in Early and Late Transition Metal Liquids,” *Physical Review Letters*, vol. 93, p. 037802, 2004.
- [56] A. Jakse, Noël ; Pasturel, “Local Order of Liquid and Supercooled Zirconium by Ab Initio Molecular Dynamics,” *Physical Review Letters*, vol. 91, no. 19, p. 195591, 2003.
- [57] D. B. Miracle, “A structural model for metallic glasses,” *Nat Mater*, vol. 3, no. 10, pp. 697–702, 2004.
- [58] D. B. Miracle, D. V. Louzguine-Luzgin, L. V. Louzguina-Luzgina, and A. Inoue, “An assessment of binary metallic glasses: correlations between structure, glass forming ability and stability,” *International Materials Reviews*, vol. 55, no. 4, pp. 218–256, 2010.
- [59] L. Ward, D. Miracle, W. Windl, O. N. Senkov, and K. Flores, “Structural evolution and kinetics in Cu-Zr metallic liquids from molecular dynamics simulations,” *Physical Review B - Condensed Matter and Materials Physics*, vol. 88, no. 13, pp. 1–10, 2013.

- [60] A. Hirata, P. Guan, T. Fujita, Y. Hirotsu, A. Inoue, A. R. Yavari, T. Sakurai, and M. Chen, “Direct observation of local atomic order in a metallic glass,” *Nature Materials*, vol. 10, no. 1, pp. 28–33, 2011.
- [61] R. Kuball, Alexander ; Gross, Oliver ; Bochtler, B. ; Busch, “Sulfur-bearing metallic glasses: A new family of bulk glass-forming alloys,” *Scripta Materialia*, vol. 146, pp. 73–76, 2018.
- [62] H. W. Sheng, W. K. Luo, F. M. Alamgir, J. M. Bai, and E. Ma, “Atomic packing and short-to-medium-range order in metallic glasses,” *Nature*, vol. 439, no. 7075, pp. 419–425, 2006.
- [63] A. Hirata, L. J. Kang, T. Fujita, B. Klumov, K. Matsue, M. Kotani, A. R. Yavari, and M. W. Chen, “Geometric frustration of icosahedron in metallic glasses,” *Science*, vol. 341, no. 6144, pp. 376–379, 2013.
- [64] G. Adam and J. H. Gibbs, “On the Temperature Dependence of Cooperative Relaxation Properties in Glass-Forming Liquids,” *The Journal of Chemical Physics*, vol. 43, no. 1, p. 139, 1965.
- [65] I. Gallino, J. Schroers, and R. Busch, “Kinetic and thermodynamic studies of the fragility of bulk metallic glass forming liquids,” *Journal of Applied Physics*, vol. 108, no. 6, 2010.
- [66] J. Ding, Y. Q. Cheng, H. Sheng, and E. Ma, “Short-range structural signature of excess specific heat and fragility of metallic-glass-forming supercooled liquids,” *Physical Review B - Condensed Matter and Materials Physics*, vol. 85, no. 6, pp. 1–5, 2012.
- [67] S. G. Hao, C. Z. Wang, M. J. Kramer, and K. M. Ho, “Microscopic origin of slow dynamics at the good glass forming composition range in  $\text{Zr}_{1-x}\text{Cu}_x$  metallic liquids,” *Journal of Applied Physics*, vol. 107, no. 5, 2010.
- [68] S. G. Hao, C. Z. Wang, M. Z. Li, R. E. Napolitano, and K. M. Ho, “Dynamic arrest and glass formation induced by self-aggregation of icosahedral clusters in  $\text{Zr}_{1-x}\text{Cu}_x$  alloys,” *Physical Review B - Condensed Matter and Materials Physics*, vol. 84, no. 6, pp. 1–4, 2011.
- [69] L. Berthier, G. Biroli, J.-P. Bouchaud, L. Cipelletti, D. El Masri, D. L’Hôte, F. Ladieu, and M. Pierno, “Direct experimental evidence of a growing length scale accompanying the glass transition,” *Science (New York, N.Y.)*, vol. 310, no. 5755, pp. 1797–1800, 2005.
- [70] L. Berthier, “Dynamic Heterogeneity in Amorphous Materials,” *Physics*, vol. 4, 2011.

- [71] P. Zhang, J. J. Maldonis, Z. Liu, J. Schroers, and P. M. Voyles, “Spatially heterogeneous dynamics in a metallic glass forming liquid imaged by electron correlation microscopy,” *Nature Communications*, vol. 9, no. 1, pp. 1–7, 2018.
- [72] Y. Marcus, “On the compressibility of liquid metals,” *Journal of Chemical Thermodynamics*, vol. 109, pp. 11–15, 2017.
- [73] G. Tarjus and D. Kivelson, “Breakdown of the Stokes-Einstein relation in supercooled liquids,” *The Journal of Chemical Physics*, vol. 103, no. 8, pp. 3071–3073, 1995.
- [74] A. Meyer, J. Wuttke, W. Petry, O. Randl, and H. Schober, “Slow Motion in a Metallic Liquid,” *Physical Review Letters*, vol. 80, no. 20, pp. 4454–4457, 1998.
- [75] F. Yang, T. Unruh, and A. Meyer, “Coupled relaxation processes in a glass forming ZrTiNiCuBe liquid,” *EPL (Europhysics Letters)*, vol. 107, no. 2, 2014.
- [76] A. Bartsch, K. Rätzke, A. Meyer, and F. Faupel, “Dynamic arrest in multi-component glass-forming alloys,” *Physical Review Letters*, vol. 104, no. 19, pp. 1–4, 2010.
- [77] S. Wei, Z. Evenson, M. Stolpe, P. Lucas, and C. A. Angell, “Breakdown of the Stokes-Einstein Relation Above the Melting Temperature in a Liquid Phase-Change Material,” *arXiv*, pp. 1–23, 2018.
- [78] R. Kohlrausch, “Theorie des elektrischen Rueckstandes in der Leidner Flasche,” *Annalen der Physik und Chemie*, vol. 91, no. 56-82, pp. 179–213, 1854.
- [79] D. C. Williams, G. ; Watts, “Non-symmetrical dielectric relaxation behavior arising from a simple empirical decay function,” *Transactions of the Faraday Society*, vol. 66, pp. 80–85, 1970.
- [80] B. Ruta, G. Baldi, G. Monaco, and Y. Chushkin, “Compressed correlation functions and fast aging dynamics in metallic glasses,” *The Journal of Chemical Physics*, vol. 138, no. 5, p. 054508, 2013.
- [81] B. Ruta, G. Baldi, Y. Chushkin, B. Rufflé, L. Cristofolini, A. Fontana, M. Zanatta, and F. Nazzani, “Revealing the fast atomic motion of network glasses,” *Nature Communications*, vol. 5, p. 3939, may 2014.

- [82] B. Ruta, Y. Chushkin, G. Monaco, L. Cipelletti, E. Pineda, P. Bruna, V. M. Giordano, and M. Gonzalez-Silveira, “Atomic-Scale Relaxation Dynamics and Aging in a Metallic Glass Probed by X-Ray Photon Correlation Spectroscopy,” *Physical Review Letters*, vol. 109, p. 165701, oct 2012.
- [83] Z. Evenson, B. Ruta, S. Hechler, M. Stolpe, E. Pineda, I. Gallino, and R. Busch, “X-ray photon correlation spectroscopy reveals intermittent aging dynamics in a metallic glass,” *Physical Review Letters*, vol. 115, no. 17, 2015.
- [84] B. Gallino, Isabella; Cangialosi, Daniele; Evenson, Zach; Schmitt, Lisa; Hechler, Simon; Ruta, “Hierarchical aging pathways and reversible fragile-to-strong transition upon annealing of a metallic glass former,” *Acta Materialia*, vol. 144, pp. 400–410, 2018.
- [85] H. Faupel, Franz; Frank, Werner; Macht, Michael-Peter; Mehrer, Helmut; Naundorf, Volker, Raetzke, Klaus; Schober, Herbert R.; Sharma, Suman K.; Teichler, “Diffusion in metallic glasses and supercooled liquids,” *Reviews of Modern Physics*, vol. 75, no. 1, p. 237, 2003.
- [86] A. Meyer, J. Horbach, W. Kob, F. Kargl, and H. Schober, “Channel formation and intermediate range order in sodium silicate melts and glasses,” *Physical Review Letters*, vol. 93, no. 2, pp. 027801–1, 2004.
- [87] H. B. Yu, W. H. Wang, H. Y. Bai, and K. Samwer, “The  $\beta$ -relaxation in metallic glasses,” *National Science Review*, vol. 1, no. 3, pp. 429–461, 2014.
- [88] M. Johari, G. P.; Goldstein, “Viscous liquids and glass transition 2 . Secondary relaxations in glasses of rigid polymers,” *Journal of Chemical Physics*, vol. 53, pp. 2372–88, 1970.
- [89] M. Johari, G. P.; Goldstein, “Viscous liquids and glass transition 3. Secondary relaxations in aliphatic alcohols and other nonrigid molecules,” *Journal of Chemical Physics*, vol. 55, pp. 4245–52, 1971.
- [90] Z. Evenson, S. E. Naleway, S. Wei, O. Gross, J. J. Kruzic, I. Gallino, W. Possart, M. Stommel, and R. Busch, “ $\beta$  relaxation and low-temperature aging in a Au-based bulk metallic glass : From elastic properties to atomic-scale structure,” vol. 174204, pp. 1–14, 2014.
- [91] F. H. Stillinger, “A Topographic View of Supercooled Liquids and Glass Formation,” *Science*, vol. 267, pp. 1935–1939, mar 1995.
- [92] J. D. Stevenson and P. G. Wolynes, “A universal origin for secondary relaxations in supercooled liquids and structural glasses,” *Nature Physics*, vol. 6, p. 62, nov 2009.

- [93] P. S. Salmon and A. Zeidler, “Identifying and characterising the different structural length scales in liquids and glasses: An experimental approach,” *Physical Chemistry Chemical Physics*, vol. 15, no. 37, pp. 15286–15308, 2013.
- [94] C. A. Angell, “Relaxation in liquids, polymers and plastic crystals - strong/fragile patterns and problems,” *Journal of Non-Crystalline Solids*, vol. 131-133, pp. 13–31, 1991.
- [95] H. Eyring, “Viscosity, Plasticity, and Diffusion as Examples of Absolute Reaction Rates,” *The Journal of Chemical Physics*, vol. 4, no. 4, pp. 283–291, 1936.
- [96] P. J. Fox, T.G. ; Flory, “Second order transition temperatures and related properties of polystyrene,” *Journal of Applied Physics*, vol. 21, p. 581, 1950.
- [97] A. K. Doolittle, “Studies in Newtonian Flow. II. The Dependence of the Viscosity of Liquids on Free Space,” *Journal of Applied Physics*, vol. 22, p. 1471, 1951.
- [98] Z. J. Evenson, *On the thermodynamic and kinetic properties of bulk glass forming metallic systems*. PhD thesis, 2012.
- [99] G. S. . C. M. H. Grest, “Liquids, Glasses, and the Glass Transition: A Free-Volume Approach,” *Advances in Chemical Physics*, vol. 48, p. 455, 1981.
- [100] E. S. Park and D. H. Kim, “Correlation between volumetric change and glass-forming ability of metallic glass-forming alloys,” *Applied Physics Letters*, vol. 92, no. 9, p. 091915, 2008.
- [101] A. S. Argon, “Plastic deformation in metallic glasses,” *Acta Metallurgica*, vol. 27, pp. 47–58, 1978.
- [102] J. C. Mauro, Y. Yue, A. J. Ellison, P. K. Gupta, and D. C. Allan, “Viscosity of glass-forming liquids,” *Proceedings of the National Academy of Sciences of the United States of America*, vol. 106, no. 47, pp. 19780–19784, 2009.
- [103] T. Hecksher, A. I. Nielsen, N. B. Olsen, and J. C. Dyre, “Little evidence for dynamic divergences in ultraviscous molecular liquids,” *Nature Physics*, vol. 4, no. 9, pp. 737–741, 2008.
- [104] L.-M. Martinez and C. a. Angell, “A thermodynamic connection to the fragility of glass-forming liquids,” *Nature*, vol. 410, pp. 663–667, apr 2001.

- [105] M. Goldstein, “Viscous liquids and the glass transition. V. Sources of the excess specific heat of the liquid,” *The Journal of Chemical Physics*, vol. 64, no. 11, p. 4767, 1976.
- [106] M. Goldstein, “Viscous liquids and the glass transition: A potential energy barrier picture,” *Journal of Chemical Physics*, vol. 51, no. 9, pp. 3728–3739, 1969.
- [107] C. A. Angell, “Glass-Formers and Viscous Liquid Slowdown since David Turnbull : Enduring Puzzles and New Twists,” *MRS Bulletin*, vol. 33, no. May, pp. 544–555, 2008.
- [108] C. A. Angell, “Glass formation and glass transition in supercooled liquids, with insights from study of related phenomena in crystals,” *Journal of Non-Crystalline Solids*, vol. 354, no. 42-44, pp. 4703–4712, 2008.
- [109] L. Xu, P. Kumar, S. V. Buldyrev, S. H. Chen, P. H. Poole, F. Sciortino, and H. E. Stanley, “Relation Between the Widom line and the Strong-Fragile Dynamic Crossover in Systems with a Liquid-Liquid Phase Transition,” *Proceedings of the National Academy of Sciences of the United States of America*, vol. 102, no. 46, pp. 16558–16562, 2005.
- [110] L. Xu, S. V. Buldyrev, C. A. Angell, and H. E. Stanley, “Thermodynamics and dynamics of the two-scale spherically symmetric Jagla ramp model of anomalous liquids,” *Physical Review E - Statistical, Nonlinear, and Soft Matter Physics*, vol. 74, no. 3, pp. 1–10, 2006.
- [111] H. E. Stanley, P. Kumar, G. Franzese, L. Xu, Z. Yan, M. G. Mazza, S. V. Buldyrev, S. H. Chen, and F. Mallamace, “Liquid polyamorphism: Possible relation to the anomalous behaviour of water,” *European Physical Journal: Special Topics*, vol. 161, no. 1, pp. 1–17, 2008.
- [112] L. Xu, S. V. Buldyrev, N. Giovambattista, and H. E. Stanley, “Liquid-Liquid Phase Transition and Glass Transition in a Monoatomic Model System,” *International Journal of Molecular Sciences*, vol. 11, pp. 5184–5200, dec 2010.
- [113] T. Egami and S. J. L. Billinge, *Unterneath the Bragg Peaks: Structural Analysis of Complex Materials*. Pergamon, Oxford, 1 ed., 2003.
- [114] S. Bluegel, *Scattering Theory: Born Series*. Schriften des Forschungszentrums Juelich, scattering ed., 2012.
- [115] NIST, “<http://physics.nist.gov/PhysRefData/FFast/Text2000/sec02.html> (date accessed 2017-03-05).”



- [116] H. Reimers, Walter; Pyzalla, Anke Rita; Schreyer, Andreas ; Clemens, ed., *Neutrons and Synchrotron Radiation in Engineering Materials Science*. WILEY-VCH Verlag GmbH Co. KGaA, Weinheim, 2008.
- [117] S. J. L. Qiu, Xiangyun; Thompson, Jeroen W. ; Billinge, “PDFgetX2: a GUI-driven program to obtain the pair distribution function from X-ray powder diffraction data,” *Journal of Applied Crystallography*, vol. 37, no. 4, p. 678, 2004.
- [118] “Online Dictionary of Crystallography (<http://reference.iucr.org/dictionary/Lorentz-polarization-correction>) date accessed 2017-07-05.”
- [119] A. J. C. Wilson, *International Tables for Crystallography*. Dordrecht: Kluwer Academic Press, 1995.
- [120] D. A. Keen, “A comparison of various commonly used correlation functions for describing total scattering,” *Journal of Applied Crystallography*, vol. 34, no. 2, pp. 172–177, 2001.
- [121] O. Warren, B. E. ; Krutter, H. ; Morningstar, “FOURIER ANALYSIS OF X-RAY PATTERNS OF VITREOUS SiO<sub>2</sub> and B<sub>2</sub>O<sub>3</sub>,” *Journal of the American Ceramic Society*, vol. 19, no. 1-12, pp. 202–206, 1936.
- [122] SNI, “[www.sni-portal.de](http://www.sni-portal.de) (date accessed 2018-05-20).”
- [123] ESRF, “[www.esrf.eu](http://www.esrf.eu) (date accessed 2017-12-03).”
- [124] Lightsources.org (date accessed 2018-01-20), “<https://lightsources.org/>.”
- [125] T. Kordel, D. Holland-Moritz, F. Yang, J. Peters, T. Unruh, T. Hansen, and A. Meyer, “Neutron scattering experiments on liquid droplets using electrostatic levitation,” *Physical Review B*, vol. 83, pp. 1–9, 2011.
- [126] A. P. Hammersley, “FIT2D V9.129 Reference Manual V3.1,” 1998.
- [127] S. Wei, M. Stolpe, O. Gross, Z. Evenson, I. Gallino, W. Hembree, J. Bednarcik, J. J. Kruzic, and R. Busch, “Linking structure to fragility in bulk metallic glass-forming liquids,” *Applied Physics Letters*, vol. 106, no. 18, 2015.
- [128] H.-J. Hoehne, G. W. H. ; Hemminger, W. F. ; Flammersheim, *Differential Scanning Calorimetry*, vol. 84. Springer-Verlag Berlin Heidelberg New York, 2nd editio ed., 2003.
- [129] H. E. Hagy, “Experimental Evaluation of Beam-Bending Method of Determining Glass Viscosities in the Range 10<sup>8</sup> to 10<sup>15</sup> Poises,” *Journal of the American Ceramic Society*, vol. 46, no. 2, pp. 93–97, 1963.

- [130] I. Jonas, *Thermophysical and structural properties of the equilibrium and undercooled melt of bulk metallic glasses investigated by electrostatic levitation*. PhD thesis, Saarland University, 2016.
- [131] S. R. Elliott, “The Origin of the 1st Sharp Diffraction Peak in the Structure Factor of Covalent Glasses and Liquids,” *Journal of Physics-Condensed Matter*, vol. 4, no. 38, pp. 7661–7678, 1992.
- [132] A. R. Yavari, A. L. Moulec, A. Inoue, N. Nishiyama, N. Lupu, E. Matsubara, W. J. Botta, G. Vaughan, M. D. Michiel, and Å. Kvik, “Excess free volume in metallic glasses measured by X-ray diffraction,” *Acta Materialia*, vol. 53, pp. 1611–1619, apr 2005.
- [133] T. C. Hufnagel, R. T. Ott, and J. Almer, “Structural aspects of elastic deformation of a metallic glass,” *Physical Review B - Condensed Matter and Materials Physics*, vol. 73, no. 6, pp. 1–8, 2006.
- [134] D. Ma, A. D. Stoica, and X. L. Wang, “Power-law scaling and fractal nature of medium-range order in metallic glasses,” *Nature Materials*, vol. 8, no. 1, pp. 30–34, 2009.
- [135] N. Mattern, M. Stoica, G. Vaughan, and J. Eckert, “Thermal behaviour of Pd<sub>40</sub>Cu<sub>30</sub>Ni<sub>10</sub>P<sub>20</sub> bulk metallic glass,” *Acta Materialia*, vol. 60, pp. 517–524, 2012.
- [136] J. Bednarcik, S. Michalik, M. Sikorski, C. Curfs, X. D. Wang, J. Z. Jiang, and H. Franz, “Thermal expansion of a La-based bulk metallic glass: Insight from insitu high-energy x-ray diffraction,” *Journal of Physics Condensed Matter*, vol. 23, no. 25, 2011.
- [137] A. K. Gangopadhyay, M. E. Blodgett, M. L. Johnson, A. J. Vogt, N. A. Mauro, and K. F. Kelton, “Thermal expansion measurements by x-ray scattering and breakdown of Ehrenfest’s relation in alloy liquids,” *Applied Physics Letters*, vol. 104, no. 19, 2014.
- [138] R. O. Simmons and R. W. Balluffi, “Measurements of equilibrium vacancy concentrations in aluminum,” *Physical Review*, vol. 117, no. 1, pp. 52–61, 1960.
- [139] A. Guinier, *X-Ray Diffraction in Crystals, Imperfect Crystals, and Amorphous Bodies*,. W. H. Freeman and Company, San Francisco and London, 1963.
- [140] X. D. Wang, J. Bednarcik, K. Saksl, H. Franz, Q. P. Cao, and J. Z. Jiang, “Tensile behavior of bulk metallic glasses by in situ x-ray diffraction,” *Applied Physics Letters*, vol. 91, no. 8, pp. 91–93, 2007.

- [141] Q. Zeng, Y. Kono, Z. Zeng, J. Wang, S. Sinogeikim, C. Park, Y. Meng, W. Yang, H.-K. Mao, and W. L. Mao, “Universal Fractional Noncubic Power Law for Density of Metallic Glasses,” *Physical Review Letters*, vol. 112, no. 185502, 2014.
- [142] J. Ding, M. Asta, and R. O. Ritchie, “On the question of fractal packing structure in metallic glasses,” *Proceedings of the National Academy of Sciences*, vol. 114, pp. 8458–8463, aug 2017.
- [143] H. F. Poulsen, J. A. Wert, J. Neuefeind, V. Honkimäki, and M. Daymond, “Measuring strain distributions in amorphous materials,” *Nature Materials*, vol. 4, no. 1, pp. 33–36, 2005.
- [144] H. Tanaka, R. Kurita, and H. Matakai, “Liquid-liquid transition in the molecular liquid triphenyl phosphite,” *Physical review letters*, vol. 92, no. 2, p. 025701, 2004.
- [145] N. Mattern, J. Bednarcik, M. Stoica, and J. Eckert, “Temperature dependence of the short-range order of Cu<sub>65</sub>Zr<sub>35</sub>metallic glass,” *Intermetallics*, vol. 32, pp. 51–56, 2013.
- [146] J. Ding, M. Xu, P. F. Guan, S. W. Deng, Y. Q. Cheng, and E. Ma, “Temperature effects on atomic pair distribution functions of melts,” *The Journal of chemical physics*, vol. 140, no. 6, p. 064501, 2014.
- [147] H. Lou, X. Wang, Q. Cao, D. Zhang, J. Zhang, T. Hu, H.-k. Mao, and J.-Z. Jiang, “Negative expansions of interatomic distances in metallic melts,” *Proceedings of the National Academy of Sciences of the United States of America*, vol. 110, no. 25, pp. 10068–10072, 2013.
- [148] R. Boehmer, K. L. Ngai, C. A. Angell, and D. J. Plazek, “Nonexponential relaxations in strong and fragile glass formers,” *The Journal of Chemical Physics*, vol. 99, no. 5, p. 4201, 1993.
- [149] J. Krausser, K. H. Samwer, and A. Zacccone, “Interatomic repulsion softness directly controls the fragility of supercooled metallic melts,” *Proceedings of the National Academy of Sciences*, vol. 112, no. 45, pp. 13762–13767, 2015.
- [150] A. E. Lagogianni, J. Krausser, Z. Evenson, K. Samwer, and A. Zacccone, “Unifying interatomic potential,  $g(r)$ , elasticity, viscosity, and fragility of metallic glasses: Analytical model, simulations, and experiments,” *Journal of Statistical Mechanics: Theory and Experiment*, vol. 2016, no. 8, 2016.
- [151] R. Soklaski, Z. Nussinov, Z. Markow, K. F. Kelton, and L. Yang, “Connectivity of icosahedral network and a dramatically growing static length scale in Cu-Zr binary metallic glasses,” *Physical Review B - Condensed Matter and Materials Physics*, vol. 87, no. 18, pp. 1–8, 2013.

- [152] S. Wei, F. Yang, J. Bednarcik, I. Kaban, O. Shuleshova, A. Meyer, and R. Busch, “Liquid-liquid transition in a strong bulk metallic glass-forming liquid,” *Nature communications*, vol. 4, no. May, p. 2083, 2013.
- [153] M. Stolpe, I. Jonas, S. Wei, Z. Evenson, W. Hembree, F. Yang, A. Meyer, and R. Busch, “Structural changes during a liquid-liquid transition in the deeply undercooled Zr<sub>58.5</sub> Cu<sub>15.6</sub> Ni<sub>12.8</sub> Al<sub>10.3</sub> Nb<sub>2.8</sub> bulk metallic glass forming melt,” *Physical Review B*, vol. 93, no. 1, pp. 1–7, 2016.
- [154] S. Aasland and P. . F. McMillan, “Density-driven liquid-liquid phase separation in the system Al<sub>2</sub>O<sub>3</sub>-Y<sub>2</sub>O<sub>3</sub>,” *Nature*, vol. 369, p. 4, 1994.
- [155] Y. Katayama, Y. Inamura, T. Mizutani, M. Yamakata, W. Utsumi, and O. Shimomura, “Macroscopic Separation of Dense Fluid Phase and Liquid Phase of Phosphorus Macroscopic Separation of Dense Fluid Phase and Liquid Phase of Phosphorus,” *Science (New York, N.Y.)*, vol. 306, 848, 2004.
- [156] M. H. Bhat, V. Molinero, E. Soignard, V. C. Solomon, S. Sastry, J. L. Yarger, and C. A. Angell, “Vitrification of a monatomic metallic liquid,” *Nature*, vol. 448, no. 7155, p. 787, 2007.
- [157] S. Sastry, “The relationship between fragility, configurational entropy and the potential energy landscape of glass-forming liquids,” *Nature*, vol. 409, no. 6817, pp. 164–167, 2001.
- [158] V. Molinero, S. Sastry, and C. A. Angell, “Tuning of tetrahedrality in a silicon potential yields a series of monatomic (Metal-like) glass formers of very high fragility,” *Physical Review Letters*, vol. 97, no. 7, pp. 1–4, 2006.
- [159] I. Saika-Voivod, P. H. Poole, and F. Sciortino, “Fragile-to-strong transition and polyamorphism in the energy landscape of liquid silica,” *Nature*, vol. 412, no. 6846, pp. 514–517, 2001.
- [160] J. L. Yarger and G. H. Wolf, “Polymorphism in Liquids,” *Science (New York, N.Y.)*, vol. 306, no. 820, 2004.
- [161] H. W. Sheng, H. Z. Liu, Y. Q. Cheng, J. Wen, P. L. Lee, W. K. Luo, S. D. Shastri, and E. Ma, “Polyamorphism in a metallic glass,” *Nature materials*, vol. 6, no. 3, pp. 192–197, 2007.
- [162] O. Mishima, “Volume of supercooled water under pressure and the liquid-liquid critical point,” *Journal of Chemical Physics*, vol. 133, no. 14, 2010.
- [163] J. R. Errington and P. G. Debenedetti, “Relationship between structural order and the anomalies of liquid water,” *Nature*, vol. 409, pp. 318–321, jan 2001.

- [164] K.-i. Murata and H. Tanaka, “Liquid liquid transition without macroscopic phase separation in a water glycerol mixture,” *Nature Materials*, vol. 11, no. 5, pp. 436–443, 2012.
- [165] M. Hemmati, C. T. Moynihan, and C. Austen Angell, “Interpretation of the molten BeF<sub>2</sub> viscosity anomaly in terms of a high temperature density maximum, and other waterlike features,” *Journal of Chemical Physics*, vol. 115, no. 14, pp. 6663–6671, 2001.
- [166] R. Kurita and H. Tanaka, “Critical-Like Phenomena Associated with Liquid Liquid Transition in a Molecular Liquid,” *Science (New York, N.Y.)*, vol. 306, no. 5697, pp. 845–848, 2004.
- [167] H. Poole, Peter, T. Grande, C. A. Angell, and F. McMillan, Paul, “Polymorphic Phase Transitions in Liquids and Glasses,” *Science (New York, N.Y.)*, vol. 275, no. 5298, pp. 322–323, 1997.
- [168] C. Zhang, L. Hu, Y. Yue, and J. C. Mauro, “Fragile-to-strong transition in metallic glass-forming liquids,” *Journal of Chemical Physics*, vol. 133, no. 1, 2010.
- [169] J. Orava, D. W. Hewak, and A. L. Greer, “Fragile-to-Strong Crossover in Supercooled Liquid Ag-In-Sb-Te Studied by Ultrafast Calorimetry,” *Advanced Functional Materials*, vol. 25, no. 30, pp. 4851–4858, 2015.
- [170] C. Way, P. Wadhwa, and R. Busch, “The influence of shear rate and temperature on the viscosity and fragility of the Zr<sub>41.2</sub>Ti<sub>13.8</sub>Cu<sub>12.5</sub>Ni<sub>10.0</sub>Be<sub>22.5</sub> metallic-glass-forming liquid,” *Acta Materialia*, vol. 55, pp. 2977–2983, may 2007.
- [171] S. Wei, I. Gallino, R. Busch, and C. A. Angell, “Glass transition with decreasing correlation length during cooling of Fe<sub>50</sub>Co<sub>50</sub> superlattice and strong liquids,” *Nature Physics*, vol. 7, no. 2, pp. 178–182, 2011.
- [172] Z. Evenson, *Thermodynamic and Kinetic Properties of Bulk Glass Forming Metallic Systems*. Saarbrücken: Shaker Verlag, 35 ed., 2012.
- [173] C. C. Hays, J. Schroers, W. L. Johnson, T. J. Rathz, R. W. Hyers, J. R. Rogers, and M. B. Robinson, “Vitrification and determination of the crystallization time scales of the bulk-metallic-glass-forming liquid Zr<sub>58.5</sub>Nb<sub>2.8</sub>Cu<sub>15.6</sub>Ni<sub>12.8</sub>Al<sub>10.3</sub>,” *Applied Physics Letters*, vol. 79, no. 11, pp. 1605–1607, 2001.
- [174] I. Gallino, M. B. Shah, and R. Busch, “Enthalpy relaxation and its relation to the thermodynamics and crystallization of the Zr<sub>58.5</sub>Cu<sub>15.6</sub>Ni<sub>12.8</sub>Al<sub>10.3</sub>Nb<sub>2.8</sub> bulk metallic glass-forming alloy,” *Acta Materialia*, vol. 55, no. 4, pp. 1367–1376, 2007.

- [175] G. N. Greaves, M. C. Wilding, S. Fearn, D. Langstaff, F. Kargl, S. Cox, Q. V. Van, O. Majérus, C. J. Benmore, R. Weber, C. M. Martin, and L. Hennet, “Detection of first-order liquid/liquid phase transitions in yttrium oxide-aluminum oxide melts,” *Science (New York, N.Y.)*, vol. 322, no. 5901, pp. 566–570, 2008.
- [176] J. C. Bendert, M. E. Blodgett, A. K. Gangopadhyay, and K. F. Kelton, “Measurements of volume, thermal expansion, and specific heat in  $\text{Zr}_{57}\text{Cu}_{15.4}\text{Ni}_{12.6}\text{Al}_{10}\text{Nb}_5$  and  $\text{Zr}_{58.5}\text{Cu}_{15.6}\text{Ni}_{12.8}\text{Al}_{10.3}\text{Nb}_{2.8}$  liquids and glasses,” *Applied Physics Letters*, vol. 102, no. 21, p. 211913, 2013.
- [177] M. Leocmach and H. Tanaka, “Roles of icosahedral and crystal-like order in the hard spheres glass transition,” *Nature Communications*, vol. 3, pp. 1–8, 201.
- [178] Y. Zhang, F. Zhang, C. Z. Wang, M. I. Mendelev, M. J. Kramer, and K. M. Ho, “Cooling rates dependence of medium-range order development in  $\text{Cu}_{64.5}\text{Zr}_{35.5}$  metallic glass,” *Physical Review B*, vol. 91, no. 6, p. 064105, 2015.
- [179] N. A. Mauro, M. Blodgett, M. L. Johnson, A. J. Vogt, and K. F. Kelton, “A structural signature of liquid fragility,” *Nature Communications*, vol. 5, pp. 1–7, 2014.
- [180] C. A. Angell, “Formation of Glasses from Liquids and Biopolymers,” *Science (New York, N.Y.)*, vol. 267, pp. 1924–1935, mar 1995.
- [181] W. Nolting, *Grundkurs Theoretische Physik 6 - Statistische Physik*. Springer Spektrum, 2014.
- [182] P. Chirawatkul, A. Zeidler, P. S. Salmon, S. Takeda, Y. Kawakita, T. Usuki, and H. E. Fischer, “Structure of eutectic liquids in the Au-Si, Au-Ge, and Ag-Ge binary systems by neutron diffraction,” *Physical Review B - Condensed Matter and Materials Physics*, vol. 83, no. 1, 2011.
- [183] Z. Yan, S. V. Buldyrev, N. Giovambattista, and H. E. Stanley, “Structural Order for One-Scale and Two-Scale Potentials,” *Physical Review Letters*, vol. 95, p. 130604, sep 2005.
- [184] S. Torquato, T. M. Truskett, and P. G. Debenedetti, “Is Random Close Packing of Spheres Well Defined?,” *Physical Review Letters*, vol. 84, pp. 2064–2067, mar 2000.
- [185] P. J. Steinhardt, D. R. Nelson, and M. Ronchetti, “Bond-orientational order in liquids and glasses,” *Physical Review B*, vol. 28, pp. 784–805, jul 1983.